博士論文

Physical Chemistry on B Removal from Si Using Si-Sn-Cu Solvent with Zr Addition

(Zr 添加 Si-Sn-Cu 溶媒を用いた Si からの B 除去に関する物理化学)

任　永生

Table of Contents

Chapter I. Introduction

1.1. Background

Since the second industrial revolution in the 1860s, the rapid development of mankind has promoted the prosperity of the global economy, but has also led to the serious deterioration of the environment and the depletion of non-renewable resources. As the nonrenewable sources coal, oil and gas, the irrefragable pollution of the environment is the biggest problem. Therefore, it is imperative to change the energy structure, meet the requirements of sustainable development, and develop renewable and clean energy.

Among all renewable energy sources, solar energy is undoubtedly the best choice, because it is inexhaustible and inexhaustible, and it will hardly cause serious pollution problems. In the field of solar energy applications, photovoltaic (PV) technology is the most widely used, so research on the production of solar cells has become the focus of attention around the world. By 2019, silicon is still the preferred basic material, because Si reserves are abundant, accounting for about 85-90% of the entire PV market. [1-1]

However, the supply of Si cannot meet the requirements for large-scale use of solar cells. The main reason behind this is that the technology used has caused environmental pollution and its cost is still high. Although the preparation methods of single crystal Si materials can meet the requirements of solar cells, since these preparation methods were originally developed for the semiconductor industry, there are many limitations in large-scale applications. Therefore, the research and development of low-cost, low-environmental pollution Si materials has become one of the research hotspots in the world today.

1.1.1. Global Energy Crisis

The energy crisis is a major bottleneck for an economy's energy supply. In the literature, it usually refers to one of the energy sources used at a certain time and place, especially those used to power the national grid or used as fuel for

automobiles. Most energy crises are caused by local shortages, wars and market manipulation. With the economic globalization and the rapid development of industry, global energy depletion and environmental pollution are the two main culprits that restrict the sustainable development of human society. Therefore, the development of new energy has become the basic trend of major countries in the world. Solar energy, wind energy, ocean energy, geothermal energy, biomass energy and hydrogen energy are called green energy sources. The development and utilization of these green energy sources has great potential for solving the current energy depletion and environmental pollution problems.

At the beginning of this century, the trend chart of primary energy consumption was predicted, as shown in Fig. 1-1.[1-2] It can be seen that from 2030, PV power generation will begin to occupy a larger proportion of primary energy use, and will occupy an absolute advantage in 2100. Moreover, the current development situation (2019) has exceeded the forecast for that year (2003). Therefore, it is foreseeable that the future development speed will be faster. In addition, from the perspective of the development of the world's PV industry, as the cost of solar PV power generation is much higher than that of conventional hydropower and thermal power, the survival and development of the PV industry market currently mainly benefits from policy support. However, in the long run, the increasing proportion of the PV industry in the energy structure is still the general trend.

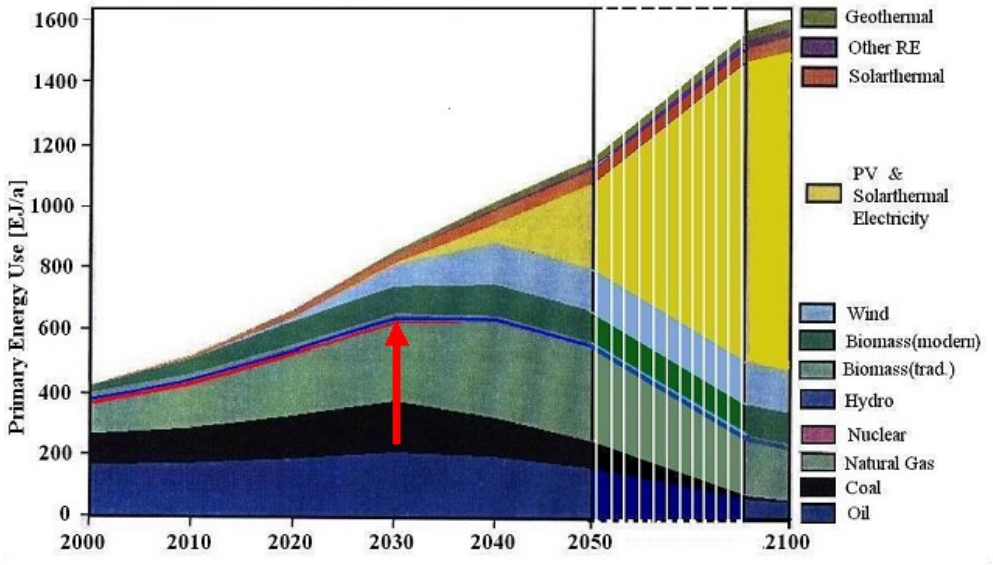

Fig. 1-1. Energy consumption forecast map. [1-2]

1.1.2. Current Situation of Photovoltaic Industry

PV is a method of directly converting solar radiation into electrical energy using semiconductors, which have a PV effect. At present, it has become one of the most practical and clean power generation methods, and has great development prospects. In the last two decades, the PV industry has developed rapidly, especially in Asia, as can be seen from the cumulative global PV installation in Fig. 1-2.

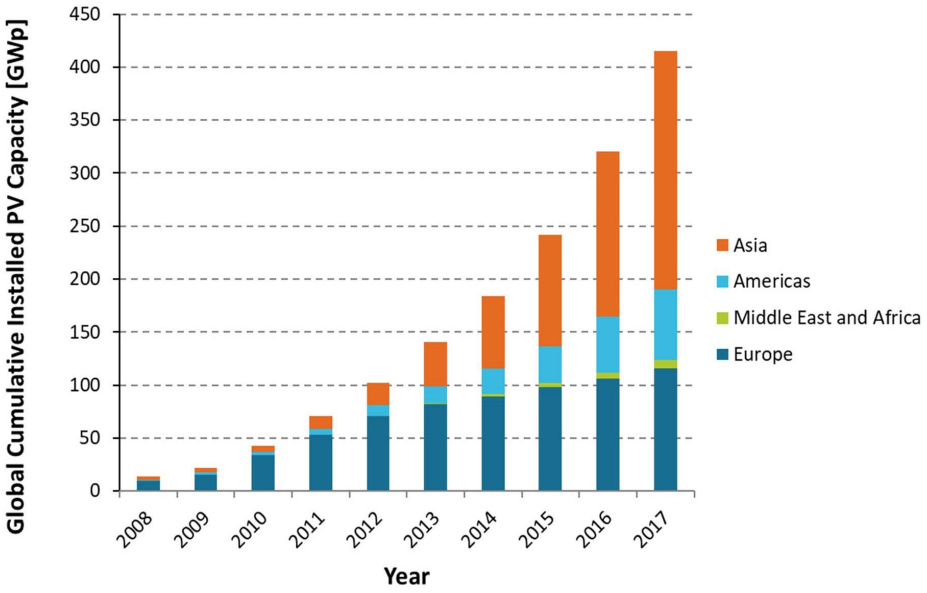

Fig. 1-2. Global Cumulative PV Installation until 2017. [1-3]

PV power generation employs solar panels composed of various solar cells using PV materials. The PV materials presently used include mono-crystalline Si, polycrystalline Si, amorphous Si, cadmium telluride, and copper indium gallium selenide/sulphide. Currently, most of the PV materials in use for solar cells production are crystalline Si because of its relatively high conversion efficiency and established production process. Si-wafer based PV technology accounted for about 95% of the total production in 2017. The share of polycrystalline Si technology is now about 62% of total production as shown in Fig. 1-3. [1-3]

With the increasing demand for renewable energy, the manufacturing industry of solar cells and PV arrays has made great progress in recent years. The continuous development of PV industry has led to the high demand for low-cost Si solar cells. It is widely predicted that solar grade silicon (SOG-Si) with required chemical purity will become the dominant material for large-scale production of Si solar cells.

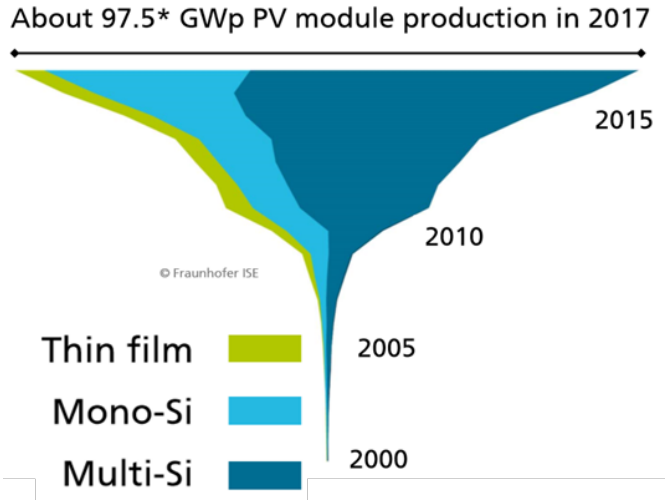

Fig. 1-3. Global Annual PV Production by Technology (in GWp). [1-3]

1.2. Impurities in SOG-Si and Their Effects on the Conversion Efficiency

1.2.1. Impurities and Their Allowable Content for SOG-Si

Since Si is the main raw material of solar cells, the quantity of its production output determines the degree of industrialization. Purity requirement of solar grade silicon (SOG-Si) is higher than 99.9999% (6N).

The current supply of raw materials is mainly from two sources: one is the offcut and scrap of the electronic grade (EG: 9-12 N) Si, which is used in the semiconductor industry, and the other is SOG material obtained from the metallurgical grade (MG: 2-3 N) Si after the purification process (contains many different metallurgical treatment procedures).

Impurities in SOG-Si can be divided into 3 main categories: (i) Dopants (e.g., P and B) that affect resistivity; (ii) light elements (e.g., O, C, and N) that can form inclusions (e.g., SiO2, SiC, and Si3N4) above the solubility limits and can create structure loss in the Czochralski (CZ) Process and instability in the MC process; and (iii) metals (e.g., Fe, Ti, Cu, Cr, and Al) that can reduce the lifetime of carriers and cell efficiency.

Their allowable content for SOG-Si are listed in Table 1-1.

Table 1-1. Allowable content for MG-Si and SOG-Si. [1-4, 5]

Element	Content of MG-Si(ppmw)	Segregation coefficient	Maximum content for solidification once (ppmw)	Maximum content for solidification twice (ppmw)	Allowable content for SOG-Si (ppmw)
B	3.00×10^{1}	8.00×10^{-1}	3.75×10^{-1}	4.69×10^{-1}	3.00×10^{-1}
P	3.00×10^{1}	3.50×10^{-1}	2.86×10^{-1}	8.16×10^{-1}	1.00×10^{-1}
C	1.00×10^{3}	5.00×10^{-2}	1.00×10^{2}	2.00×10^{3}	5.00
O	1.00×10^{2}	1.25	4.00	3.20	5.00
Al	5.00×10^{2}	2.80×10^{-3}	2.51	8.95×10^{2}	7.02×10^{-3}
Fe	8.00×10^{2}	6.40×10^{-6}	1.29×10^{2}	2.02×10^{7}	8.26×10^{-4}
Ti	4.00×10^{1}	2.00×10^{-6}	3.69	1.94×10^{6}	7.37×10^{-6}
Cu	1.00	8.00×10^{-4}	1.93×10^{3}	2.41×10^{6}	1.54
Ni	1.00×10^{-1}	1.30×10^{-4}	1.34×10^{2}	1.03×10^{6}	1.74×10^{-2}
Pd	1.00×10^{-5}	5.00×10^{-5}	6.42×10^{2}	1.28×10^{7}	3.21×10^{-2}
Co	1.00×10^{-1}	2.00×10^{-5}	1.92×10^{2}	9.58×10^{6}	3.83×10^{-3}
Mn	1.00×10^{1}	1.30×10^{-5}	4.50×10^{1}	3.46×10^{6}	5.85×10^{-4}
Cr	1.00	1.10×10^{-5}	3.64×10^{1}	3.31×10^{6}	4.00×10^{-4}
Au	1.00×10^{-5}	2.50×10^{-5}	5.12	2.05×10^{5}	1.28×10^{-4}
V	1.00	4.00×10^{-6}	1.88	4.71×10^{5}	7.53×10^{-6}
Nb	1.00×10^{-1}	4.40×10^{-7}	2.00×10^{1}	4.54×10^{7}	8.79×10^{-6}
Mo	1.00×10^{-1}	4.50×10^{-8}	7.56×10^{1}	1.68×10^{9}	3.40×10^{-6}
W	1.00×10^{-1}	1.70×10^{-8}	7.65×10^{2}	4.50×10^{10}	1.30×10^{-5}
Ta	1.00×10^{-5}	2.10×10^{-8}	1.17×10^{2}	5.58×10^{9}	2.46×10^{-6}
Zr	1.00	1.60×10^{-8}	1.21×10^{2}	7.58×10^{9}	1.94×10^{-6}

1.2.2. Effect of Impurities on the Conversion Efficiency

The most common solar cell is a large-area p-n junction made from Si. A p-n junction is the boundary or interface between p-type and n-type semiconductor materials in a semiconductor single crystal. The "p" (positive) side contains extra

holes and the "n" (negative) side contains extra electrons, which are located in the shell of an electrically neutral atom. This allows current to flow through the connector in only one direction. The p-n junction is formed by a dopant.

Si containing Group V elements such as P is called n-type semiconductor. In n-type semiconductor, Group V elements can act as donors, providing extra free electrons to serve as majority carriers. On the contrary, Si containing Group III elements such as B is called p-type semiconductor. In p-type semiconductor, Group III elements can be considered as acceptors that lacks electrons to generate free holes. It can be shown in Fig. 1-4.

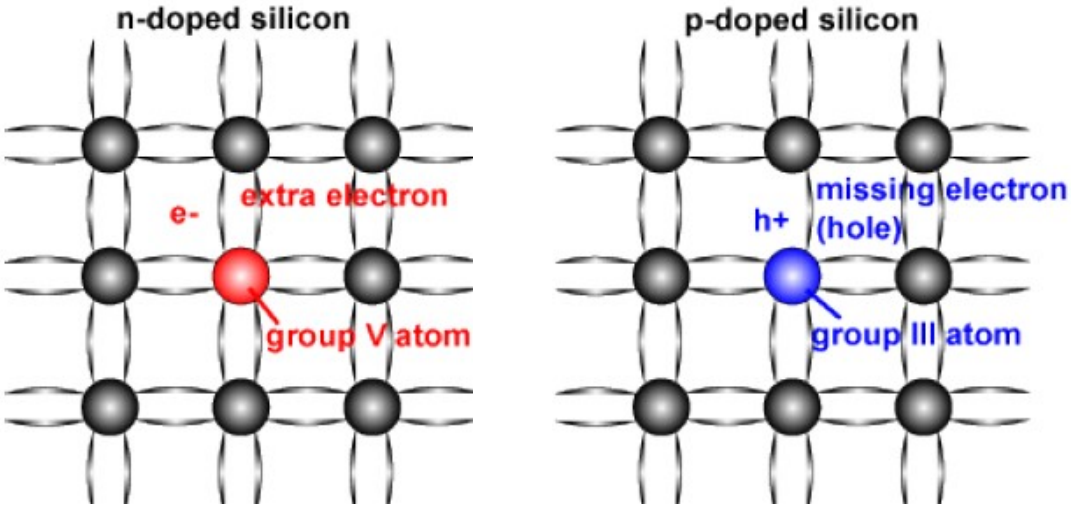

Fig.1-4. Schematic of a Si crystal lattice doped with impurities to produce n-type and p-type semiconductor material. [1-6]

Since the semiconductor performances of Si are highly affected by impurity elements, the content of impurities must be precisely controlled. The allowable content of the impurities in SOG-Si is significantly different. As mentioned, B and P are important elements responsible for the electrical characteristics of Si. Therefore, the allowable content of B and P is set to meet the general requirements for crystalline Si solar cells, that is, the electrical resistance value of $1.0 \pm 0.5 \times 10^{-2}$ (Ω・m). On the other hand, many metal impurities can lead to the formation of impurity states in the band gap, especially Fe, Ti, Ni, and Cr can form active impurity states near the center of the band gap, which may cause p-n junction leakage and reduce solar cell life. Therefore, they are called life-killer elements, and great efforts have been made to remove them during the Si refining process. [1-7]

By measuring the I-V data of Si solar cells, the effects of various impurities (single and composite impurities) on the performance of Si solar cells were studied by Davis *et al.* [1-8]. The conversion efficiencies of p- or n-type solar cells as a function of impurity contents are shown in Fig. 1-5.

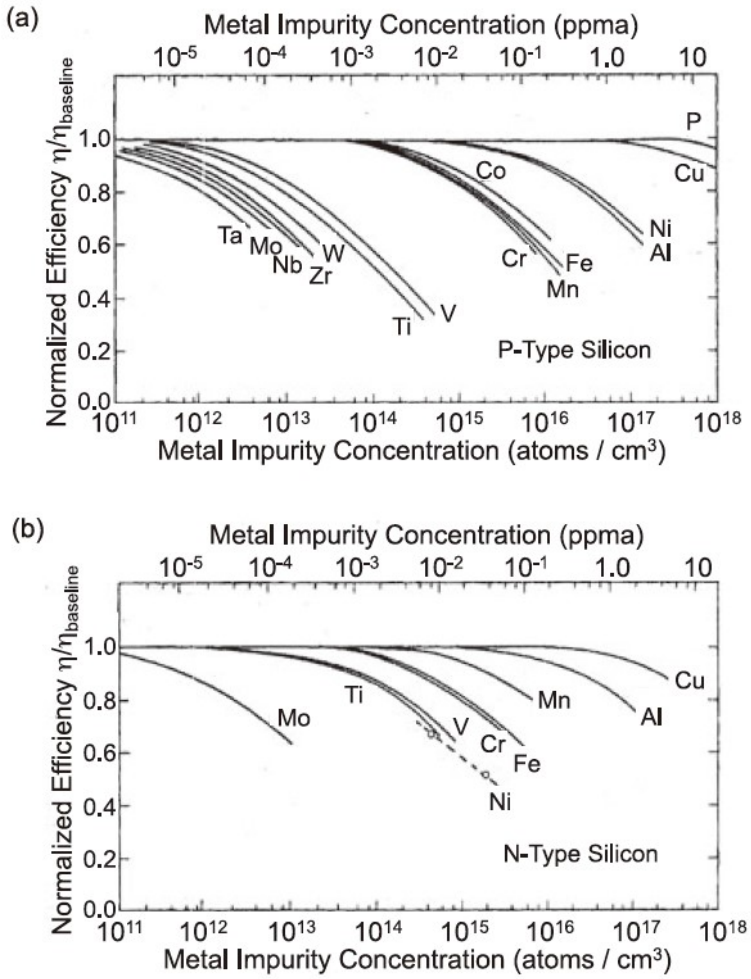

Fig. 1-5. Solar-cell efficiencies versus impurity content for (a) 4-Ω·cm p-base devices and for (b) 1.5-Ω·cm n-base devices. [1-8]

The effect of the metal impurity elements is remarkable, and excessive addition of the dopant elements such as B and P may lower the carrier mobility, leading to the reduction in conversion efficiency.

The content of impurities in raw materials is directly related to the performance of solar cells. For PV applications, the purity of Si is required to be at least 6N (99.9999%). High-purity Si with this purity is called solar-grade silicon (SOG-Si). Therefore, the precise control of the impurity content in SOG-Si is very important for the development of the PV industry.

1.3. SOG-Si Feedstock

SOG-Si and EG-Si can be used to produce solar cells, while they usually started from using MG-Si as the raw material to upgrade. Table 1-2 lists the content of impurities in these 3 grades Si. [1-9]

Table 1-2. Maximum content of impurities in MG-Si, SOG-Si, and EG-Si. [1-9]

Elements		Fe	Al	Ca	Ti	Mg	Mn	Cr	V	Zr	Cu	B	P	C	O
MG-Si	‰	5	2	1	1.6	0.1	0.05	0.05	0.01	0.01	0.01	0.08	0.05	0.6	3
SOG-Si	ppmw	0.1	0.1	0.3	0.01	0.1	0.1	0.1	0.1	0.1	0.1	0.3	0.1	3	10
EG-Si	ppmb	0.2	0.8	0.01	0.2	0.2	0.2	0.2	0.2	0.2	0.2	0.2	0.8	0.5	−

Previously, EG-Si scrap, offcut, and rejected material were the main supply channels for SOG-Si production. However, with the rapid growth of the PV market in the past few decades, there is insufficient waste, and the current main source is non-quality polysilicon, which is deliberately produced by operating conventional processes (e.g., improved Siemens processes: chlorosilane and hot filament; Union Carbide and Komatsu Process: monosilane and hot filament; and Ethyl Corporation process: silane and fluidized bed reactor) with more economical parameters (e.g., higher production efficiency, lower energy consumption, and higher impurity grades, *etc*). [1-10]

1.3.1. Production of MG-Si

Si accounts for about 27% of the earth's crust, and is the second largest element after oxygen. It exists in combination with oxygen forming silicates.

Metallurgical grade silicon (MG-Si), also called industrial silicon, has a typical purity of 98% and is produced by a carbon-thermal reduction method in a submerged arc furnace.

The overall reaction takes place by the following equation:

$$SiO_{(s)} + 2C_{(s)} = Si_{(l)} + 2CO_{(g)} \quad (1\text{-}1)$$

The Si production plant is shown in Fig. 1-6. [1-11] MG-Si are most commonly used for the alloying raw materials for aluminum, steel metal, and the feedstock for the PV and semiconductor industry.

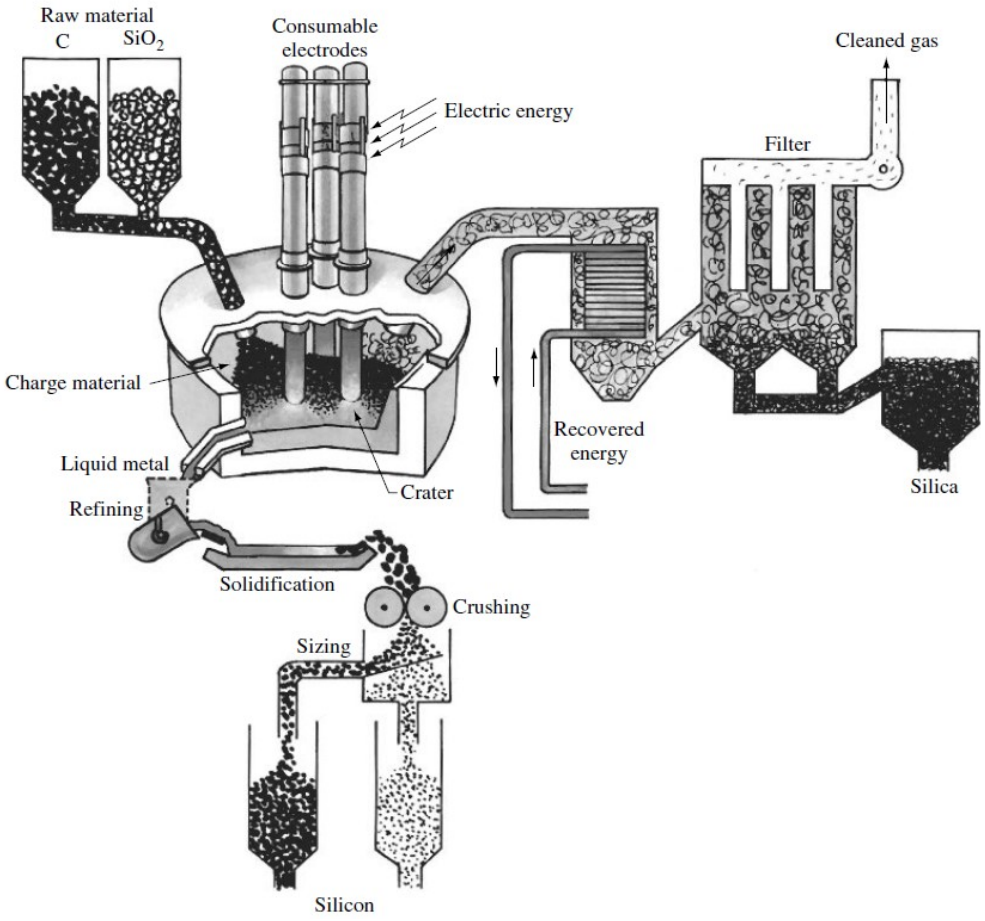

Fig. 1-6. Schematic representation of a furnace for production of MG-Si. [1-11]

1.3.2. Production of SOG-Si

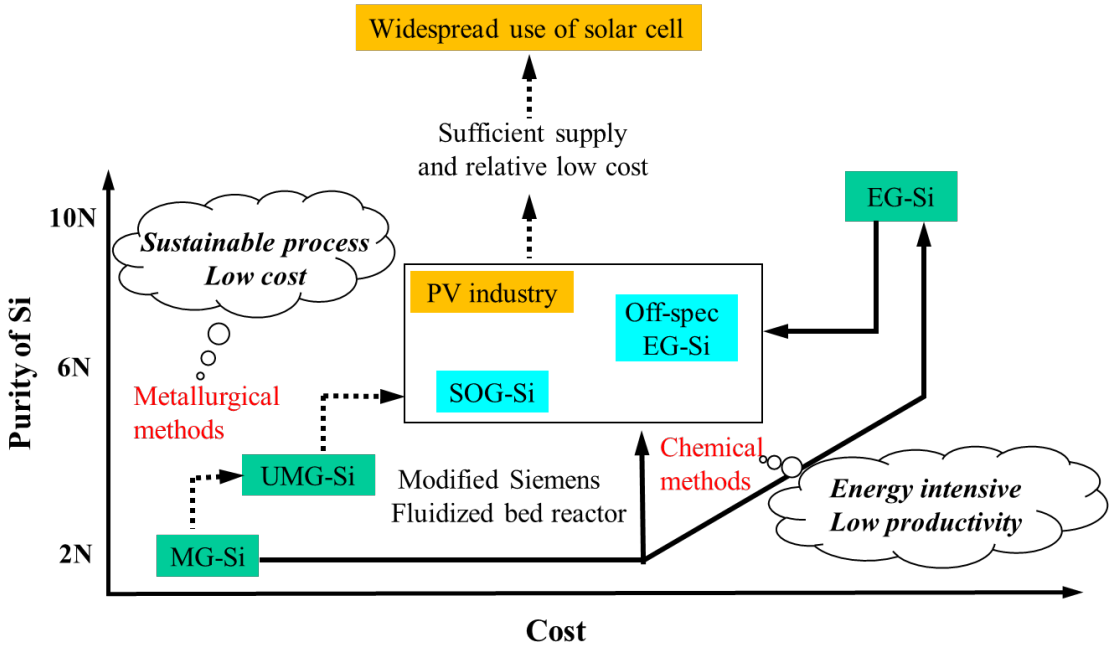

Fig. 1-7. Supply route for SOG-Si.

For PV industry, SOG-Si is the main feedstock. Currently, the modified-Siemens method is the mainstream technique to produce SOG-Si. But it is considered as energy-intensive process with low productivity and high cost.

Metallurgical refining process has long been considered as a promising way to purify the industrial Si directly. It has benefits in mass productivity and relative low cost. So if the remaining challenge can be solved, it will make the widespread use for solar cells. The supply route for SOG-Si can be summarized as in Fig. 1-7.

A) Modified Siemens Process

Most polysilicon is produced by the Siemens process. In this process, trichlorosilane (TCS) is first prepared by hydrochlorination of MG-Si in a fluidized reactor. The purified TCS and hydrogen are mixed after distillation and enter a reactor. The reactor is equipped with a base plate and multiple Si rods in a bell-jar. The Si rods are electrically heated to about 1373 K. A schematic of the Siemens reactor is shown in Fig. 1-8.

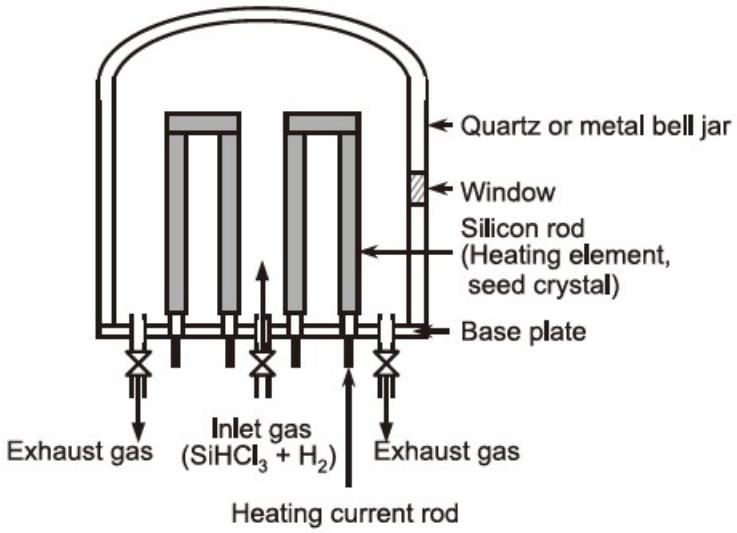

Fig. 1-8. Schematic representation of the traditional Siemens reactor. [1-12]

The chemical reactions of hydrogen, chlorine, and silicon at the deposition temperature and amount are quite complicated, which can be simplified as follows:

$$2SiHCl_3=SiH_2Cl_2+SiCl_4 \quad (1\text{-}2)$$

$$SiH_2Cl_2=Si+2HCl \quad (1\text{-}3)$$

$$HCl+SiHCl_3=H_2+SiCl_4 \quad (1\text{-}4)$$

$$H_2+SiHCl_3=Si+3HCl \quad (1\text{-}5)$$

The Siemens process is highly energy consuming, in which a major part of the energy is dispersed and lost in cooling the inner wall. In addition, large amount of by-product is generated during the chemical vapor deposition (CVD) of Si. In order to reduce the cost, modified Siemens process has been developed. The by-product is recycled through closed-loop process. The Si can be deposited at a higher yield and in a larger surface.

B) Fluidized Bed Reactor Process

Another important method to produce the high purity of Si is based on the thermal decomposition of purified silane. The reaction can be expressed as follow:

$$SiH_4=Si+2H_2 \quad (1\text{-}6)$$

A fluidized bed reactor is used to replace the bell-jar reactor, which is shown in Fig. 1-9. Instead of using static Si seed rods in a bell-jar reactor, the Si particles are continuously charged into the reactor and sustained by a gas stream of SiH_4 and hydrogen. The energy losses and energy consumption are considerably reduced, because decomposition takes place at around 1073 K and cooling the bell jar is not required.

On the other hand, the Si productivity can be considerably improved. The end products are small granules of polysilicon. Subsequently, they are needed to be casted into multi-crystalline Si ingots by directional solidification or grown into monocrystalline Si ingots by Czochralski method.

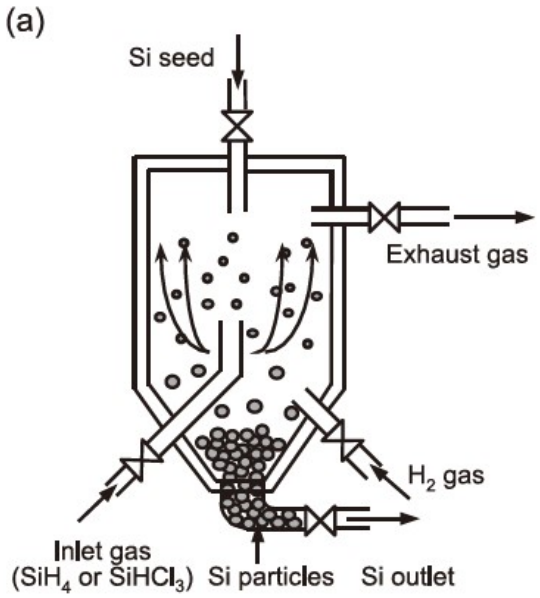

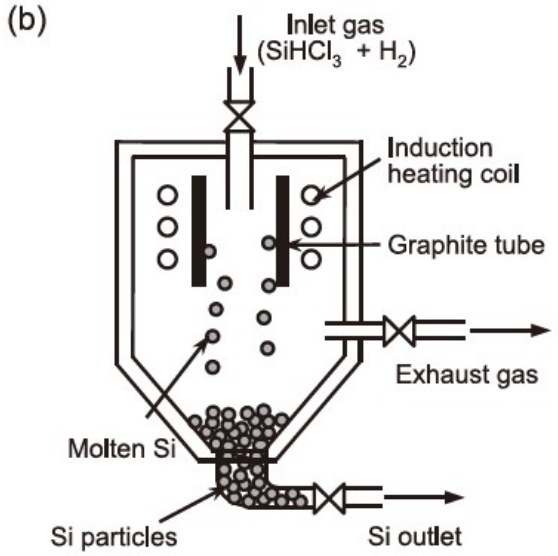

Fig. 1-9. Schematic representation of a fluidized bed reactor. [1-12]

Historically, the PV industry relied on off-spec electronic-grade Si as its primary raw material. That Si, produced through the Siemens process, is both costly and far purer than that required for Si solar cells. With the rapid growth of PV industry, the shortage of Si feedstock occurred, which once became the bottleneck to limit the development of PV industry. Currently, the modified Siemens process and a fluidized bed reactor process have been developed to overcome the cost and energy problems associated with the conventional Siemens process.

However, the cost reduction potential of these processes is limited because of low Si productivity due to converting Si into gaseous compounds such as $SiHCl_3$ and SiH_4, followed by distillation, reduction and deposition into solid Si. The insatiable desire for energy and the political will of many countries to reduce CO_2 emissions assures that demand for PV industry will continue to increase. The realization of widespread use of solar cells will be based on the availability of abundant and low-cost SOG-Si feedstock.

C) Metallurgical Production of SOG Polysilicon

To improve the economic cost and mass productivity of SOG-Si production, an alternative way, namely metallurgical refining process that purify MG-Si directly, is considered as a promising method for reducing the production cost further and being specialized in terms of producing SOG-Si on a large scale.

The metallurgical route has many advantages, such as energy-saving, environmentally-friendly, and continuous. Also, life cycle assessments (LCAs) have been carried out to the polysilicon production by the metallurgical route. [1-13 ~ 16]

A representative metallurgical method is shown in Fig. 1-10, including slag treatment, [1-17] hydrometallurgical leaching, [1-18] vacuum evaporation, [1-19] directional solidification, [1-20] electron beam, [1-21] and plasma [1-22].

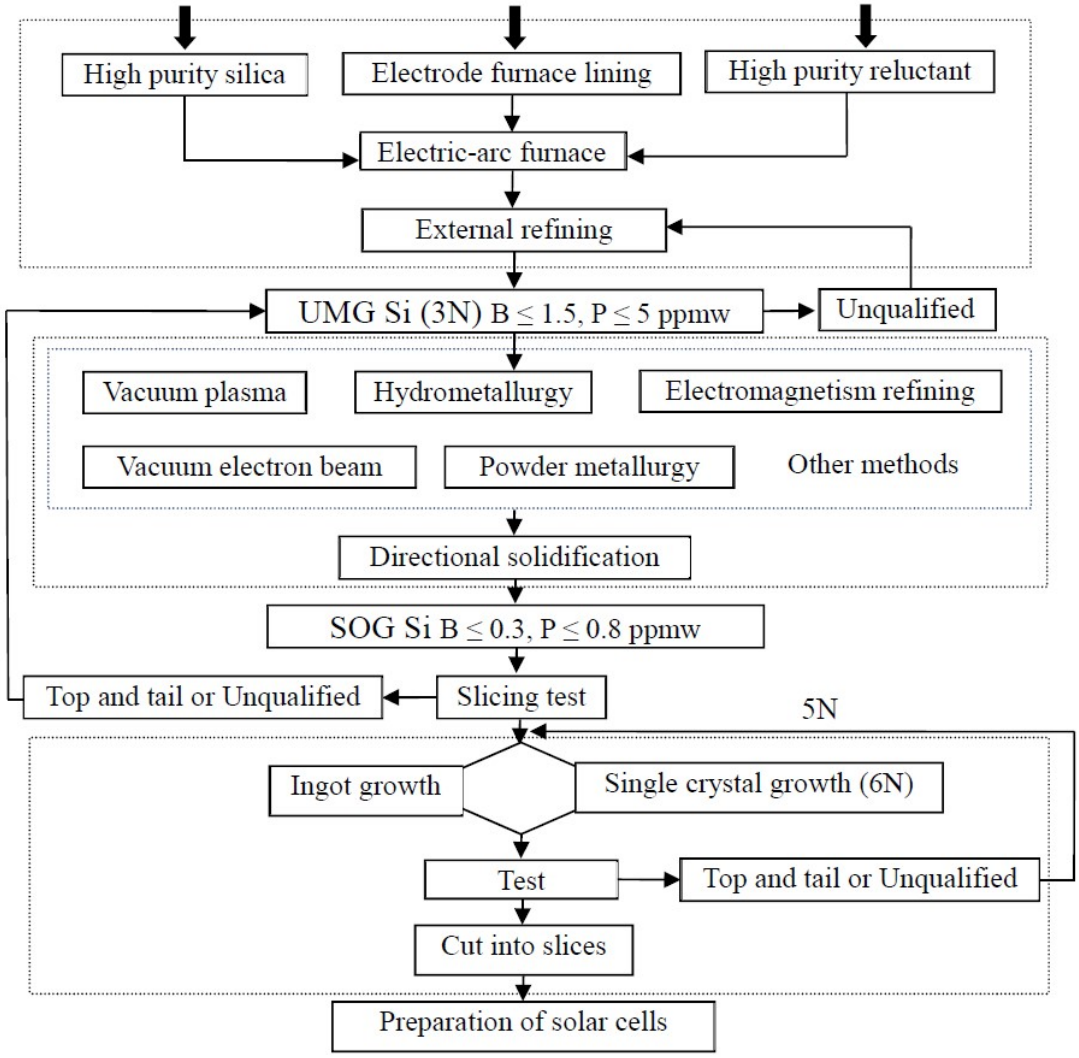

Fig. 1-10. Flowchart of metallurgical route for production of SOG-Si.

Generally, metal impurities can be removed by directional solidification and acid leaching, and electron beam is an effective method to vaporize P and O. [1-23] However, the biggest difficulty of this method is the removal of B due to its large segregation coefficient (0.8 at 1687 K) [1-24] and low vapor pressure [1-25].

1.4. Properties of B in Si and Si-based Solvent

In order to remove B effectively, the properties of B in Si and Si-based solvent should be clear at first. The various properties are summarized below.

1.4.1. Solubility of B in Si

A thermochemical database for the solar cell Si materials covering 33 elements has been established by Tang *et al.*. [1-26] The Si-B binary system is shown in Fig. 1-11.

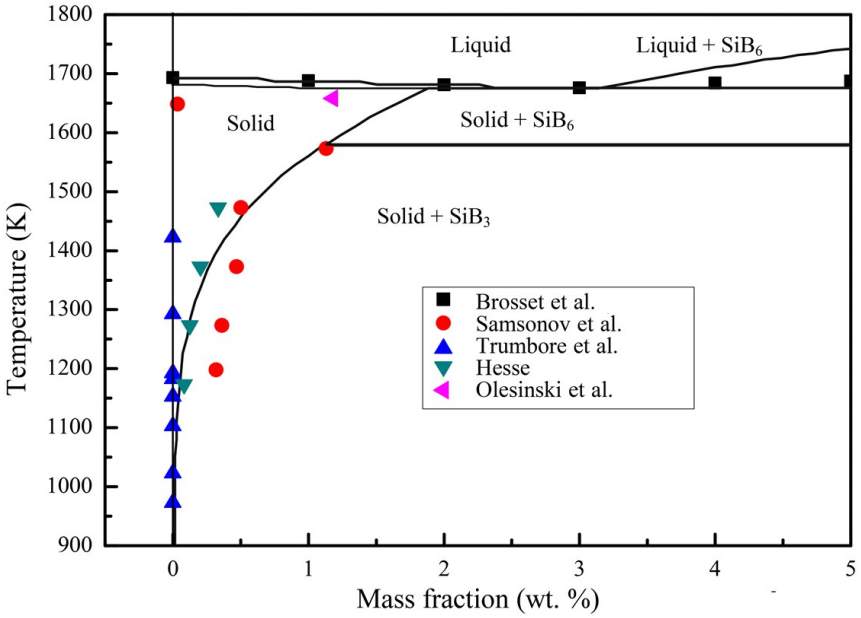

Fig. 1-11. Phase equilibria in the Si-rich Si-B system. [1-158]

The B content in SOG-Si is generally between ppm and several percentage points. [1-27 ~ 31] However, it should be noted that when these data are used in binary alloy system, they should be used carefully considering their verification.

1.4.2. Diffusivity of B in Si

For Si purification of solar cells, dissolved state B should be at the level of ppb ~ ppm. Therefore, mass transfer of B from bulk Si to the reaction surface / interface is an important step in the refining process. Diffusion coefficients, especially experimentally measured ones, are an urgent need for kinetic discussion and model building.

Fig. 1-12 shows the estimated diffusivity of B in solid and liquid Si as a function of temperature. [1-32 ~ 42]

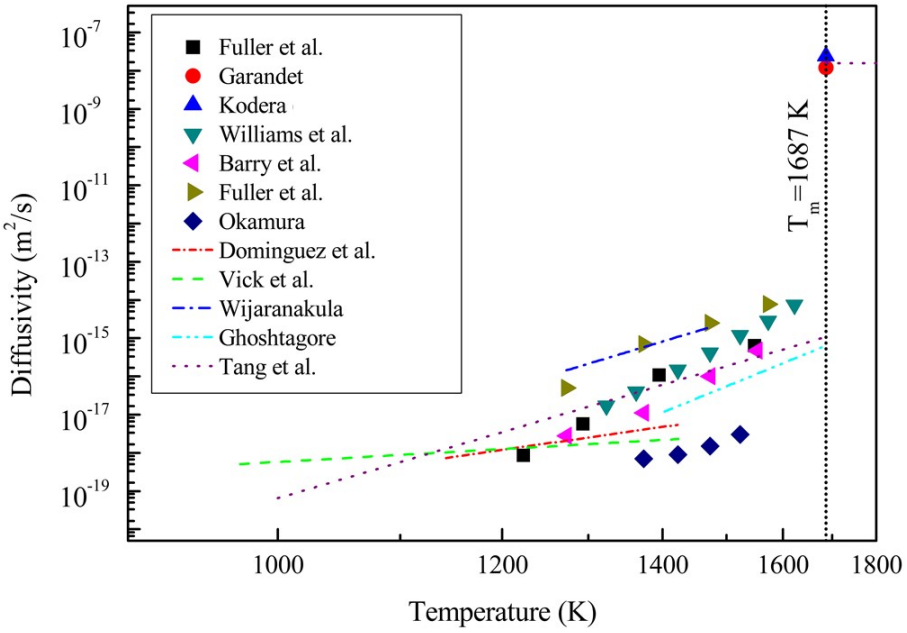

Fig. 1-12. Diffusion coefficients of B in Si. [1-158]

Here, the results of Tang *et al.* [1-43] which give a relationship between the diffusivity of B and temperature, was recommended to use, as shown in Eq. (1-7).

$$\lg D = \begin{cases} \dfrac{-10373}{T} - 8.81, & 1000\ \mathrm{K} < T < 1678\ \mathrm{K} \\ -7.77\left(\pm 0.15\right), & 1687\ \mathrm{K} < T \end{cases} \tag{1-7}$$

1.4.3. Diffusion and Mass Transfer Coefficients of B in Si and Slags

Slag treatment can remove B from MG-Si with a relatively high removal fraction. However, single-stage slag treatment cannot produce sufficiently low B-content Si, and the removal rate depends on the reactor / process design. Therefore, it is interesting to determine the rate-limiting step of removing B from MG-Si by slag treatment. During the slag refining process, the mass transfers of both boron [B] in molten Si and boron oxide ($BO_{1.5}$) in the slag will affect the removal rate of B, the results are listed in Table 1-3.

Table 1-3. Diffusion coefficients and mass transfer rates. [1-44 ~ 54]

Slag (mass fraction)	D_{Si}	D_S	β_{Si}	β_S	δ_{Si}	δ_S	Temperature	Reference
Unit	10^{-8} m^2·s^{-1}	10^{-9} m^2·s^{-1}	10^{-6} m·s^{-1}	10^{-7} m·s^{-1}	mm	mm	K	-
0.37CaO-0.63SiO_2		5.24		62		0.85	1723	Wang *et al.*
0.4CaO-0.4SiO_2-0.2K_2CO_3				243			1823	Wu *et al.*
0.5CaO-0.5SiO_2	1.46		170	31.6	0.086		1823	Wu *et al.*
0.20CaO-0.17SiO_2-0.63$CaCl_2$		8.46		250		0.34	1723	Wang *et al.*
0.63Na_2O-0.37SiO_2				3.66			1973	Fang *et al.*
0.2CaO-0.6SiO_2-0.1CaF_2-0.1Al_2O_3			6.85	1.01			2073	Zhang *et al.*
0.55CaO-0.45SiO_2				14			1823	Nishimoto *et al.*
0.4CaO-0.4SiO_2-0.2MgO				43			1923	Krystad *et al.*
-	2.7						1687	Tang *et al.*
-	1.2						1687	Garandet
-	2.4 ± 0.7						1687	Kodera

D_{Si} and D_S are the diffusion coefficients of B in Si and $BO_{1.5}$ in slag, respectively. β_{Si} and β_S are the mass transfer coefficients of B in Si and $BO_{1.5}$ in slag, respectively. δ_{Si} and δ_S are boundary layer thicknesses in Si and slag, respectively.

1.4.4. Activity Coefficients of B in Si and Slags

In the study of B removal, it is important to clarify the mechanism and kinetics of the removal process to improve the removal efficiency. Activity is also one of the thermodynamic properties for numerical simulation and model building.

The activity coefficient of B is determined by using the first-order interaction coefficients, as expressed in Eq. (1-8)

$$\lg\gamma_B = \lg\gamma_B^0 + \sum_1^{i=n} \varepsilon_B^i x_i \tag{1-8}$$

Where γ_B^o is the activity coefficient of B in molten Si for an infinite dilute solution relative to the pure liquid state; x_i and ε_B^i are the mole fraction of *i* species

and the interaction coefficient between i species and B in molten Si, respectively.

Noguchi *et al.* [1-55] reported the activity coefficient in Si melt determined by equilibrating solid BN and liquid Si under a N_2 atmosphere from 1723 to 1923 K, as expressed in Eq. (1-9).

$$\lg \gamma_B^0 = -\frac{1.11\times10^4}{T} + 5.82, \ (1723\ \mathrm{K} < T < 1923\ \mathrm{K}) \tag{1-9}$$

Tanahashi *et al.* [1-56] measured the activity coefficient in molten Si by equilibrating the Si-B melt with solid BN and/or Si_3N_4 at 1723 and 1773 K, as expressed in Eq. (1-10).

$$\ln \gamma_B^0 = \begin{cases} 2.5 \pm 0.2, \ (1723\ \mathrm{K}) \\ 2.3 \pm 0.2, \ (1773\ \mathrm{K}) \end{cases} \tag{1-10}$$

Inoue *et al.* [1-57] studied the effect of calcium on thermodynamic properties of B in molten Si, and got the activity coefficient, as expressed in Eq. (1-11).

$$\ln \gamma_B^0 = 2.27(\pm0.01), \ (1723\ \mathrm{K}) \tag{1-11}$$

Yoshikawa *et al.* [1-58] determined the activity coefficient by equilibrating molten Si with solid Si_3N_4 and BN at 1693 and 1923 K, as expressed in Eq. (1-12). Eq. (1-13) is the activity coefficient of B in solid Si measured by the segregation behavior of B between solid Si and Si-Al melt. [1-59]

$$\lg \gamma_B^0 = \frac{289(\pm450)}{T} + 1.19(\pm0.25), \ \ (1693\ \mathrm{K} < T < 1923\ \mathrm{K}) \tag{1-12}$$

$$\ln \gamma_B^0 = \frac{14073(\pm276.6)}{T} - 5.73(\pm0.19), \ (1273\ \mathrm{K} < T < 1473\ \mathrm{K}) \tag{1-13}$$

Khajavi *et al.* [1-60] used activity coefficients of B in Si-Fe alloy to evaluate that in solid Si, as expressed in Eq. (1-14).

$$\ln \gamma_B^0 = \frac{16317(\pm282)}{T} - 7.06(\pm0.18), \ \ (1483\ \mathrm{K} < T < 1583\ \mathrm{K}) \tag{1-14}$$

A possible reason why the data from Noguchi *et al.* deviate from those from other researchers is that they did not take the formation of Si_3N_4 into consideration, and when ignored these data, the activity coefficient of B can be represented by Eq. (1-15).

$$\ln \gamma_B^0 = \frac{17450}{T} - 8.15, \ \ (1173 < T < 1923\ \mathrm{K}) \tag{1-15}$$

Interaction coefficients between various species and B in molten Si are listed in

Table 1-4, and the self-interaction coefficients of B in Si can be fitted by Eq. (1-16).

$$\varepsilon_{\mathrm{B}}^{\mathrm{B}} = \frac{2153860}{T} - 1435.47, \quad (1273 < T < 1773\ \mathrm{K}) \tag{1-16}$$

Table 1-4. Interaction coefficients between various species and B in Si. [1-55 ~ 61]

Interaction coefficient	Result	Reference
$\varepsilon_{\mathrm{B}}^{\mathrm{Ca}}$	-3.08±0.84 (1723 K)	Inoue *et al*.
$\varepsilon_{\mathrm{B}}^{\mathrm{B}}$	370±140 (1273 K), 120±40 (1373 K), and 67±20 (1473 K); -159±45 (1483 K), -111±28 (1533 K), and -96±12 (1583 K); -164±8 (1723 K), and -105±8 (1773 K)	Yoshikawa *et al.*, Khajavi *et al.*, and Tanahashi *et al.*
$\varepsilon_{\mathrm{B}}^{\mathrm{Al}}$	1313 (1173 K), 970 (1273 K), 610 (1373 K), and 400 (1473 K)	Yoshikawa *et al.*
$\varepsilon_{\mathrm{B}}^{\mathrm{Sn}}$	2506 ± 143 (1173 K)	Xu et al.
$\varepsilon_{\mathrm{B}}^{\mathrm{N}}$	240 (1723 K), 80±20 (1723 K), 73±1 (1773 K)	Noguchi *et al.*, and Tanahashi *et al.*

Teixeira *et al*. [1-62] investigated the basicity (the ratio of mass fraction between CaO and SiO_2, defined as R) and the activity coefficients of $BO_{1.5}$ for CaO- SiO_2 and CaO-SiO_2-CaF_2 slags at 1823 K, as shown in Eq. (1-17).

$$\ln \gamma_{\mathrm{BO}_{1.5}} = -4.00R + 3.67, \quad (1823\ \mathrm{K}) \tag{1-17}$$

1.4.5. Segregation Coefficients of B between Solid Si and Solvent

During solidification, there will be a clear interface between solid Si and liquid eutectic. At the solid/liquid interface, the content of B in solidified Si is in equilibrium with that in solvent.

For example, for the solidification of Si-60mol% Al melt, the first precipitated phase is solid Si, which is called primary Si. The solubility of B in liquid is higher than that in solid Si, so it can be effectively removed by solvent recrystallization. Of course, the primary Si contains Al, which must be removed later.

The segregation coefficient of B (k_B) can be expressed as Eq. (1-18).

$$k_B = \frac{x_B^S}{x_B^L} = \frac{\gamma_B^L}{\gamma_B^S} \exp\left(\frac{\Delta G_B^0}{RT}\right) \quad (1\text{-}18)$$

Where x_B^S and x_B^L are the molar fractions of B in the solid and liquid phase, respectively. γ_B^S and γ_B^L are the corresponding activity coefficients. ΔG_B^0 refers to the Gibbs energy of the fusion of B.

Eq. (1-19) shows the k_B between the solid Si and Si-Al melt measured by Temperature-Gradient Zone Melting method. [1-58]

$$\ln k_B = 4.23 - 7300 / T \quad (1\text{-}19)$$

The values of k_B for various solvents are listed in Table 1-5.

Table 1-5. Segregation coefficients of B between solid Si and eutectics. [1-59, 60, 63 ~ 66]

Alloy	Result	Reference
Si	0.8	Hall
Si-Al	0.22 (1273 K), 0.32 (1373 K), and 0.49 (1473 K)	Yoshikawa *et al.*
Si-17 wt% Fe	0.07 (1480 K)	Esfahani *et al.*
Si-20 wt% Fe	0.33 ± 0.04 (1483 K), 0.41 ± 0.03 (1533 K), and 0.49 ± 0.01 (1583 K)	Khajavi *et al.*
Si-Sn	0.038 (1500 K, calculated)	Zhao *et al.*
Si-34 wt%Ni	20-65	Yin *et al.*

1.5. Past Researches on B Removal

When the B content in Si solar cells is greater than 0.3 ppmw, the lifetime of minority carriers decreases sharply with the appearance of B-O defects, which determines the photoelectric conversion efficiency. [1-67] Directional solidification and vacuum melting cannot remove B effectively.

At present, the main processes of B removal include slag refining, gas blowing, high-temperature plasma, acid leaching, and low-temperature Si-based solvent refining. [1-68] In order to effectively reduce the B content in large-scale SOG-Si production, it is important to review the development of the B refining process.

1.5.1. Slag Refining

The multi-component slag composed of oxides can absorb or enrich impurities in refining process to prevent Si from contamination. B can be oxidized by slag at the phase boundary. After sufficient refining time, the interface reaction will reach equilibrium. Si with low impurity content is separated from refining slag. This process can be divided into 5 steps: (1) mass transfer from Si bulk phase to the metal boundary layer, (2) diffusion through the metal boundary layer to interface, (3) interfacial reaction at the interface between metal and slag, (4) diffusion through the slag boundary layer from the interface, and (5) mass transfer from the slag boundary layer to slag bulk phase. [1-69]

The interfacial reaction is shown as Eq. (1-20), and its equilibrium constant K is given by Eq. (1-21).

$$\mathrm{B} + 3/4\,\mathrm{SiO_2} = \mathrm{BO_{1.5}} + 3/4\,\mathrm{Si} \tag{1-20}$$

$$K = \frac{\gamma_{(\mathrm{BO_{3/2}})} x_{(\mathrm{BO_{3/2}})} a_{[\mathrm{Si}]}^{3/4}}{\gamma_{[\mathrm{B}]} x_{[\mathrm{B}]} a_{(\mathrm{SiO_2})}^{3/4}} \tag{1-21}$$

Where x_i, a_i, and γ_i are the molar fraction, activity, and activity coefficient of i species, respectively.

Distribution coefficient (L_B) is always used to present the removal efficiency, as shown in Eq. (1-22).

$$L_\mathrm{B} = \frac{x_{(\mathrm{BO_{1.5}})}}{x_{[\mathrm{B}]}} = K \cdot \frac{\gamma_{[\mathrm{B}]} \cdot a_{(\mathrm{SiO_2})}^{3/4}}{\gamma_{(\mathrm{BO_{1.5}})} \cdot a_{[\mathrm{Si}]}^{3/4}} \tag{1-22}$$

The L_B should be as high as possible to minimize the amount of slag needed for refining, because twice or more times slag treatments are not conducive to industrial application. Unfortunately, typical values of L_B range from 1 to 2, and the highest value of L_B reported by Teixeira *et al.* [1-62] is around 5.5. It means that a large ratio of amount between slag and Si (μ) is needed to refine Si.

There are many types of slag for B removal from Si, such as CaO-SiO_2-CaF_2, CaO-SiO_2-TiO_2,[1-70] SiO_2-CaO-Al_2O_3,[1-71] Al_2O_3-BaO-SiO_2,[1-72] CaO-SiO_2-Na_2O-Al_2O_3, [1-73] as shown in Table 1-6.

Table 1-6. Different slag systems for B removal. [1-74 ~ 89]

Slag	Result	Reference
CaO-SiO_2, CaO-SiO_2-MgO	→ < 3 ppmw	Liaw *et al.*
CaO-SiO_2-MgO	L_B=1.7 (R=0.95)	Noguchi *et al.*
CaO-SiO_2-CaF_2	L_B=1.6 (R=2)	
CaO-SiO_2	7.6→0.3 ppmw	Fujiwara *et al.*
CaO-SiO_2	L_B=5.5-4.3 (R=0.55-1.21)	Teixeira *et al.*
CaO-SiO_2	18→1.8 ppmw (R=1.5, μ=2.5, 1873 K, 3 h); L_B=1.57	Wu *et al.*
CaO-SiO_2	22→4.73 ppmw; L_B=0.72-1.58	Wei *et al.*
SiO_2-NaO	10.6→0.65 ppmw (R=0.8, 1973 K, 0.5 h); 0.4→0.2 ppmw (R=2, 1973 K, 0.5 h)	Fang *et al.*
CaO-SiO_2-Al_2O_3	1.5→0.2 ppmw (1823 K, 2 h)	Luo *et al.*
CaO-SiO_2-Al_2O_3	$\lg(L_B)$=0.66-1.8	Jung *et al.*
CaO-SiO_2-Al_2O_3	$L_B=(2.1\text{-}2.4)\{x(SiO_2)/[x(Al_2O_3)+x(SiO_2)]\}$	Jakobsson *et al.*
CaO-SiO_2-NaO	30→5 ppmw (R=1.1, 1873 K, 1 h)	Safarian *et al.*
CaO-SiO_2-K_2CO_3	22→1.8 ppmw (1823 K, 6 h); L_B=2.08	Wu *et al.*
Li_2O–SiO_2–CaF_2	8.6→0.46 ppmw (1973 K, 0.5 h)	Lai *et al.*
CaO-SiO_2-ZnO	12.94→2.18 ppmw (1823 K, 1 h)	Wang *et al.*
CaO-SiO_2-Li_2O	18→1.3 ppmw (R=1.5, μ=4, 1873 K, 3 h)	Wu *et al.*
CaO-SiO_2-LiF	22→1.3 ppmw (R=0.8, μ=4, 1823 K, 2 h); L_B=1.6-2.7	Ding *et al.*
CaO-SiO_2-Al_2O_3-CaF_2	25→4.4 ppmw (μ=1, 2073 K, 2 h);	Li *et al.*
CaO-MgO-Al_2O_3-SiO_2	L_B=1-1.8 (1873 K)	Johnston *et al.*
CaO-SiO_2-$CaCl_2$	148→21 ppmw (R=1.3, μ=3, 1723 K, 0.5 h); 75→5 ppmw (R=1.3, μ=2, 1823 K, 0.5 h)	Wang *et al.*

Khattak *et al.* [1-90] proved that B content in MG-Si can be decreased from 18 to 1 ppmw by the CaO-SiO_2 slag. Johnston *et al.* [1-91] and Cai *et al.* [1-92] observed the

effects of basicity of Al_2O_3-CaO-MgO-SiO_2, Al_2O_3-BaO-SiO_2, CaO-SiO_2-CaF_2, and CaO-SiO_2-Al_2O_3 slag on B removal.

The efficiency of B removal from molten Si by slag treatment depends on several parameters (e.g., reaction kinetics, diffusivity, and partition ratio), which are determined by the structure of slag. [1-93]

The L_B in Eq. (1-22), the determinant of the removal efficiency, is dependent on the activity coefficient and reaction temperature. There is a maximum value of L_B, because chemical equilibrium and steady state can always reach in the treatment process for nearly all slag systems without volatiles.

How to improve L_B and/or break the steady state is the key to B removal. There are 3 ways to achieve it: (1) adding volatile substances, (2) partly or totally replacing CaO with other oxides with higher abilities of oxidization, and (3) gas blowing.

As for the first, the introduction of volatile substances can facilitate the removal of boron oxides from the slag into gaseous phase. The representative one of volatile substances is $CaCl_2$, and Mellström *et al*. [1-94] proposed this idea firstly in 1989, by which the B content decreased from 17 to 5 ppmw after 0.5 h. Wang *et al.* [1-95, 96] researched this ternary CaO-SiO_2-$CaCl_2$ slag system comprehensively, followed by Lu *et al*. [1-97, 98] and Huang *et al.* [1-99]. The introduction of chlorination can transform $BO_{1.5}$ in the slag to BOCl/BCl_3 that can be evaporated at high temperatures.

1.5.2. Gas Blowing

The gas blowing can be defined as the process of blowing oxidation gases (e.g., H_2O, O_2, and H_2) into liquid Si (or slag phase when combined with slag treatment) at high temperature. B contained in Si is oxidized to oxides (e.g., BO, B_2O_3, B_2O, BO_2, and B_2O_2), or hydroxide gases (e.g., BHO, BHO_2, BH_2O_2, and BH_3O_3) formed under a humid atmosphere (Ar-H_2O-O_2). These gaseous products can easily evaporate because their equilibrium partial pressures are 10^5-10^{10} times than the oxidizing gases mentioned above.

Generally, the oxidants needed for oxidative refining reactions can be introduced either as a gas (in the form of air by gas-blowing through a nozzle, or a lance installed on the top of a crucible, or plugged in the bottom), or the slag containing

$CaO-SiO_2$. Gas-blowing is usually combined with the addition of some kinds of slags (e.g., CaO, MgO, and CaF_2), which also act as oxidizing agents. In a broad sense, plasma treatment can also be regarded as an oxidative refining process.

From the point of view of equilibrium, the oxidation of Si is more favorable than that of B, and SiO vapor is more likely to be formed above 873 K, which makes the refining process more complicated. By thermodynamic calculation, the main products when B in liquid Si reacts with the water vapor are BOH, BH_2, BO, and B_2O_2. [1-100] One problem for gas injection is that Si can also be oxidized by the water vapor, which may cause some loss of Si.

Since the work published by Theuerer *et al.* in 1956, [1-101] it has been known that liquid Si can be purified with respect to B when brought in contact with a gas mixture of $Ar-H_2-H_2O$. After that, various gas systems have been studied, including Cl_2, [1-50] O_2, [1-102] H_2, H_2O, [1-103] and HCl [1-104]. Research data of various researchers are listed in Table 1-7.

Table 1-7. Different gas systems for B removal. [1-105 ~ 113]

Gas	Result	Reference
$HCl-H_2O$	20-60→0.3 ppma	Khattak *et al.*
H_2O	24.8→2.01 ppmw	Safarian *et al.*
H_2O	10→2 ppmw (solar furnace, 3473 K, 50 min);	Flamant *et al.*
O_2	35→1.8 ppmw	Wu *et al.*
H_2O-O_2	35→1.8 ppmw	Wu *et al.*
H_2O-O_2, O_2	18→2 ppmw;	Wu *et al.*
H_2-H_2O	→<1 ppmw (induction heating, 2-3 h);	Nordstrand *et al.*
H_2-H_2O	64→0.5 ppmw	Sortland *et al.*
H_2-H_2O	10-25→about 0.1 ppmw	Safarian *et al.*
NH_3-N_2	120→<1 ppmw (1823 K, 6 h)	Chen *et al.*

It can be obviously seen that the injection of $H_2O_{(g)}$, H_2, and O_2 can improve the removal efficiency. However, saturated vapor pressures of nearly all compounds of B are very low, and this limits the reaction rate of B removal.

1.5.3 Plasma Treatment

Although the volatility of B is lower than that of Si, B can react with O, Cl and H at high temperature to form volatile substances, such as BHO, BO, and BH_2. To increase the temperature of Si melt, plasma heating has been employed in laboratory experiments.

The thermal plasma treatment can improve the dynamics of B removal from liquid Si. In the plasma treatment, gaseous boron oxides (e.g., BO, B_2O, B_2O_3) are expected to form at the temperature higher than 2300 K, and among these boron oxides, BO has a relatively high vapor pressure. Ar-H_2O, [1-114] Ar-CO_2, [1-115] Ar-H_2-H_2O, [1-116] Ar-H_2-O_2, [1-117] and Ar-He-H_2O [1-118] were chosen as plasma gases to oxidize and/or hydrogenate B in liquid Si. The schematic diagram of plasma process is shown in Fig. 1-13. [1-119]

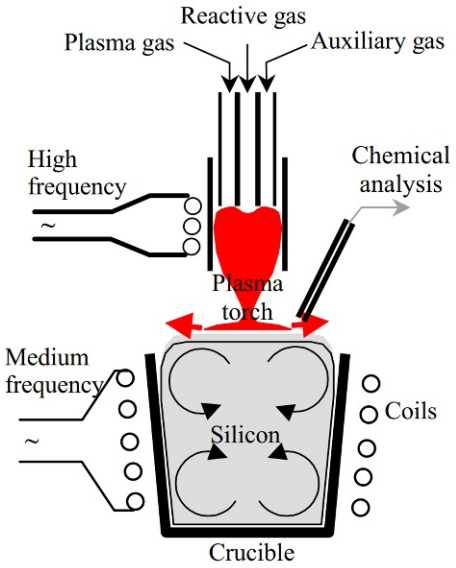

Fig. 1-13. Schematic diagram of plasma process. [1-119]

The merits of plasma treatment are high refining temperature, high activities of chemical reactions, and high abilities to degas. Lee *et al.* [1-120] reported that the plasma of Ar-H_2-H_2O can removal B in the forms of BO and HBO. Yuge *et al.* [1-121] reduced the B content in MG-Si from 10 to 0.1 ppmw by 50.6% H_2-4.6% H_2O plasma refining. Clearly, the results of plasma treatment listed in Table 1-8 are much better than that of normal gas blowing, but there are also many shortcomings limiting its development of the industrial application, such as expensive equipment for production, high energy consumption, and intermittent production.

Table 1-8. Different plasma systems for B removal. [1-122 ~ 126]

Plasma system	Result	Reference
Ar + H_2O	12→1 ppmw	Ikeda *et al.*
Ar + H_2O	22→0.2 ppmw	Cai *et al.*
Ar + H_2O	37.5→4 ppmw	Suzuki *et al.*
H_2 + H_2O	5-10→0.1 ppmw	Nakamura *et al.*
Ar + H_2	10→0.1 ppmw	Nakamura *et al.*
H_2 + O_2	15→2 ppmw	Alemany *et al.*
Ar + H_2 + O_2	64→0.3 ppmw	Rousseau *et al.*

1.5.4. Acid Leaching

Metal impurities can form intermetallic phases (such as silicides and silicates) with Si, which often precipitate at the grain boundary. Acid leaching has a long history of hydrometallurgical modification of Si. Elkem Silgrain process still produce MG-Si commercially; the powders of 90FeSi alloy (90% Si) are immerged in an acid solution of HCl-$FeCl_3$, in which continuous grain boundaries react with the acid mixture and then disintegrate. [1-127]

This process is particularly efficient in the removal of transition metal (e.g., Fe, Cu) because these impurities have very low segregation coefficients in Si.

Surface treatment (or leaching) of HF acid or HCl / HF mixture is also known to wash away residual impurities as oxides or silicates. Grinding Si before pickling to increase surface exposure is a way to improve purity. [1-128, 129]

Sun *et al.* [1-130] reported the effects of the concentration of HF acid and particle size of Si on the removal efficiency. After the calcination treatment at 1273 K for 2 h, quenching at 373 K for 2 h under vacuum, and HNO_3+HF acid leaching at 323 K for 80 minutes, the B content of Si powders (particle size: 44 ~ 74 μm) decreased from 128 to 10.9 ppmw. In addition, the B content of Si powders (particle size: 74 ~ 154 μm) decreased from 8.6 to 3.0 ppmw for the duration (2 h) of HF + H_2O_2 + $(CH_2OH)_2$ acid leaching at 328 K. [1-131]

However, it must be emphasized that this method can not make the B content below the solubility limit in the corresponding curing component in practice.

Fortunately, B, as an additional phase of the solidified MG-Si phase at the grain boundaries, can be removed by extrusion and subsequent etching, leaving the Si grains at about 2 mm. [1-132]

1.5.5. Solvent Refining

Solvent refining, proposed as a new concept, has become the focus of researchers for Si purification in recent decades. It can be applied at a relatively low temperature for refining MG-Si, which is more conducive to the B removal. The recrystallization of primary Si from Si-based alloy melt results in the redistribution of impurities in Si. Simultaneously, the enrichment of primary Si can be controlled, and the impurity content can be reduced to meet the standard of SOG.

Solvent refining is on the basis of fractional crystallization. Si alloying with metals which have low melting points (e.g., Al, Sn, Cu, and Zn), and in the process of directional solidification, impurity of B gathers in molten eutectic phases (e.g., Si-Al, [1-133] Si-Sn, [1-134] Si-Cu, [1-135] and Si-Al-Sn [1-136]) because the liquid melt has a higher solubility than solid Si. During directional solidification with a micro-convex front rather than a flat front, a clear interface was observed between the solid Si and the liquid melt. By definition, ideal solvents are those with a low melting point and / or low solubility in Si. According to Aluminum Company of America and Union Carbide Corporation's patents, Cu, Cu-Al, or Al solvent can be used to upgrade MG-Si. [1-137, 138] They predicted an effective removal of metallic impurities, but did not reveal an opportunity for B removal, but did not reveal the possibility for B removal. Since 2003, thermodynamics on SOG-Si refining with the Si-Al melt at a low temperature has been investigated by Yoshikawa *et al*., [1-139] and a novel concept of low-temperature solidification refining of Si with a Si-based solvent has accordingly been proposed. [1-140] B cannot be effectively removed by conventional directional solidification, while decreased from 56 ppmw to 0.88 ppmw when using Al-Si alloy treatment. [1-141]

Many papers have been published for Si purification using solvent, [1-142, 143] the results are listed in Table 1-9. From which it can be seen that Si-Al solvent is the most selected, the reason is that the k_B between solid Si and Si-Al eutectic is lowest and the Si-Al binary phase diagram is relatively simple without intermediate phase.

Table 1-9. Different alloy systems for B removal. [1-144 ~ 156]

Solvent	Result	Reference
Si-Al	→0.8-1.9 ppmw; *RF* *=95%	Yoshikawa *et al.*
Si-Al	*RF* =74.3%	Li *et al.*
Al–Si (with rotating magnetic field)	65→4.67 ppmw	Zou *et al.*
Si-Al (additive: Ti)	170→1.1 ppmw; precipitate: TiB_2	Yoshikawa *et al.*
Si-Al (additive: 575 ppma Ti)	295→12 ppma; precipitate: TiB_2	Ban *et al.*
Si-Al (additive: Zn)	14.8→2.4 ppmw	Li *et al.*
Si-Al (additive: Hf)	→1.2 ppmw	Lei *et al.*
Si-Al (additive: Zr, Hf, and Ti)	12→1.2 ppmw	Lei *et al.*
Si-Al (additive: V)	506→74 ppma	Chen *et al.*
Si-Sn (twice refining)	15→0.12 ppmw	Zhao *et al.*
Si-Al-Sn	14.8→3.9 ppmw	Li *et al.*
Si-Cu (additive: Ca)	*RF* =44.4%	Fang *et al.*
Si-Cu (with acid leaching)	*RF* =58.7%	Huang *et al.*
Si-Fe	27→2 ppmw	Esfahani *et al.*
Si-Na	9.1→0.3 ppmw	Morito *et al.*
Si-Ga	*RF* =83.3%	Li *et al.*

**RF* is the abbreviation of Removal Fraction

According to thermodynamic calculation, the precipitates (e.g., ZrB_2, HfB_2, and TiB_2) are easier to form, because the standard free energy values of formation of these precipitates are much lower than other borides (e.g., AlB_2, AlB_{12}, and SiB_6). [1-157, 158]

As summarized previously, the schematic diagram of the solvent refining process and basic steps can be shown in Fig. 1-14: (i) Melting process: one or more metals, with low melting point, are pre-melted together with MG-Si to form a Si-rich alloy; (ii) Recrystallization process: Si crystals, with less pollutant, recrystallized from the Si-based alloy melt by cooling down; (iii) Enrichment and purification process: moving out the melt from heating zone, the primary Si will be enriched at one side,

and the impurities are driven and enriched to the other side (residual alloy side) simultaneously. This process can be continued until the temperature reaches the eutectic point of the Si alloy; (iv) Separation process: separate the enriched Si crystals (purified) from the solidified alloy sample.

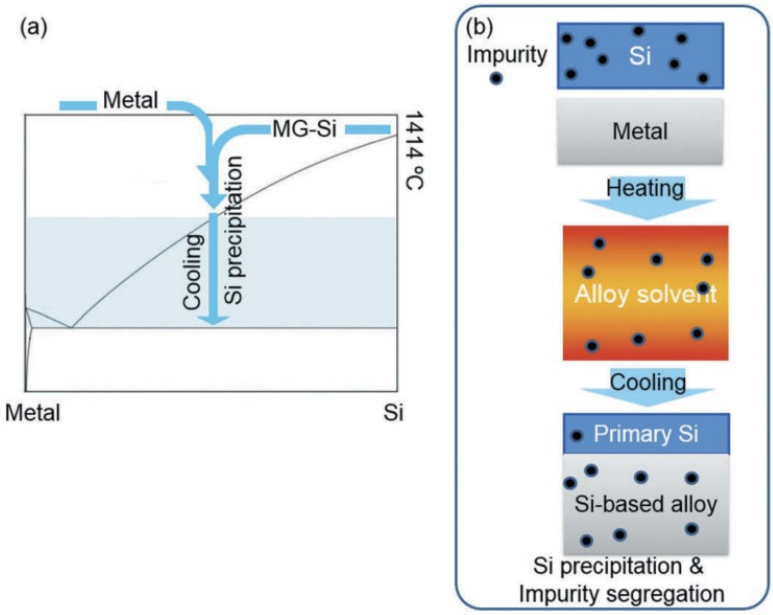

Fig. 1-14. (a) Si-based binary phase diagram
(b) schematic diagram of the solvent refining process. [1-159]

Firstly, thermodynamic research relating to solidification of Si from solvent has been carried out by Yoshikawa *et.al* mainly on the Si-Al. For Si-Al system, it was confirmed to be effective for the removal of impurities, especially for B and P. Because the segregation coefficient of B and P were decreased one order of magnitude, as shown in Fig. 1-15. [1-59] However, based on the comparable density between solidified Si and liquid Si-Al ($\rho_{Si(300\ K)}$ = 2.33 g/cm^3, [1-160] $\rho_{Al(1173\ K)}$ = 2.33 g/cm^3 [1-161]), the growth rate of bulk Si was inadequate and the enrichment and separation of solidified Si from the Si-Al melt have to be achieved through special technologies, such as electromagnetic fields, [1-141, 162] supergravity fields, [1-163] and powder metallurgy techniques [1-164].

Thereafter, Sn and Cu were tried by the other two members (Dr. Ma [1-165] and Mr. Ohshima [1-166]) of our Lab, their merits can be summarized as: (i) the growth rate of Si increased which have been confirmed by their experimental results; (ii) Sn and Cu are electrical inactivity elements in the solar cell, so it can tolerate the relative high

content of them, as shown in Fig. 1-16 [1-4] ; (iii) the significant density difference between solidified Si and Sn/Cu melt ($\rho_{Sn(1555\ K)}$ = 6.32 g/cm^3, [1-167] $\rho_{Cu\ (1358\ K)}$ = 8.96 g/cm^3 [1-168]), it will cause large buoyancy force, thus making the primary Si grow up and float upwards easily to get bulk Si; (iv) they have higher vapor pressure than Si, as shown in Fig. 1-17, [1-25] so they can be removed by vacuum melting; (v) B becomes more unstable in the Si-Sn alloy melt because of the higher γ_B, as shown in Fig. 1-18; [1-165] (vi) both of Sn and Cu have very small solid solubilities in Si, as shown in Fig. 1-19. [1-5]

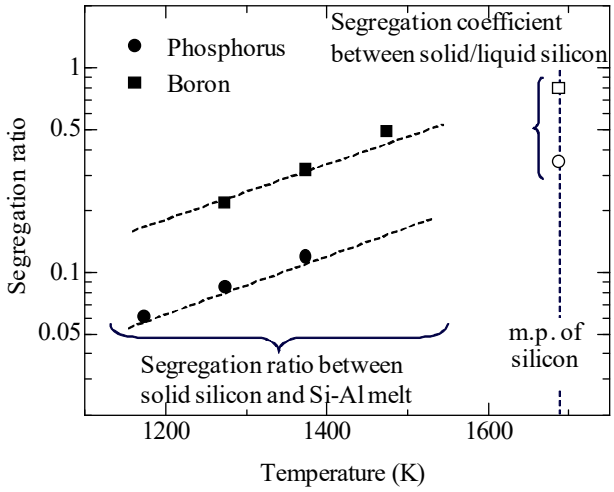

Fig. 1-15. Temperature dependence of segregation ratios of phosphorus and boron between solid Si and Si-Al melt. [1-59]

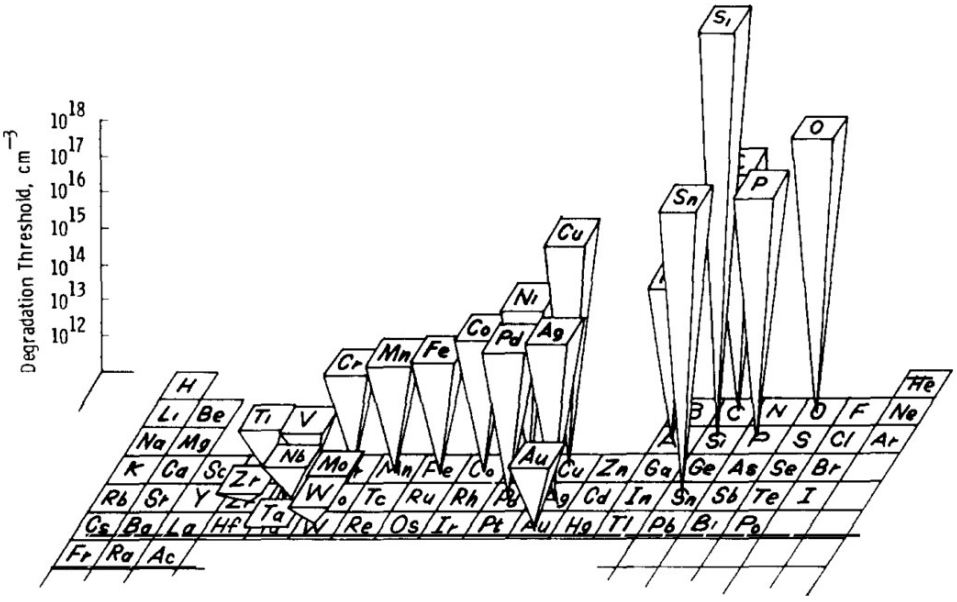

Fig. 1-16. Threshold impurity contents for cell performance reduction. [1-4]

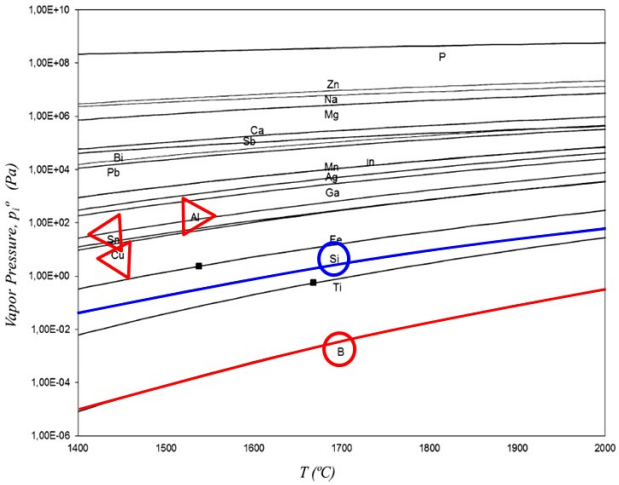

Fig. 1-17. Saturated vapor pressure of each substance. [1-25]

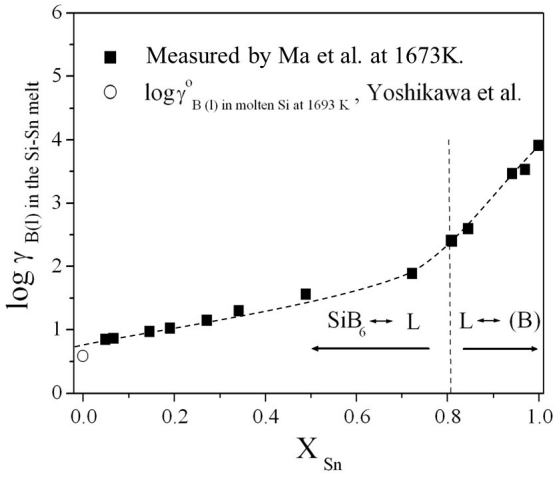

Fig. 1-18. Activity coefficient of B in the Si-Sn melt at 1673 K. [1-165]

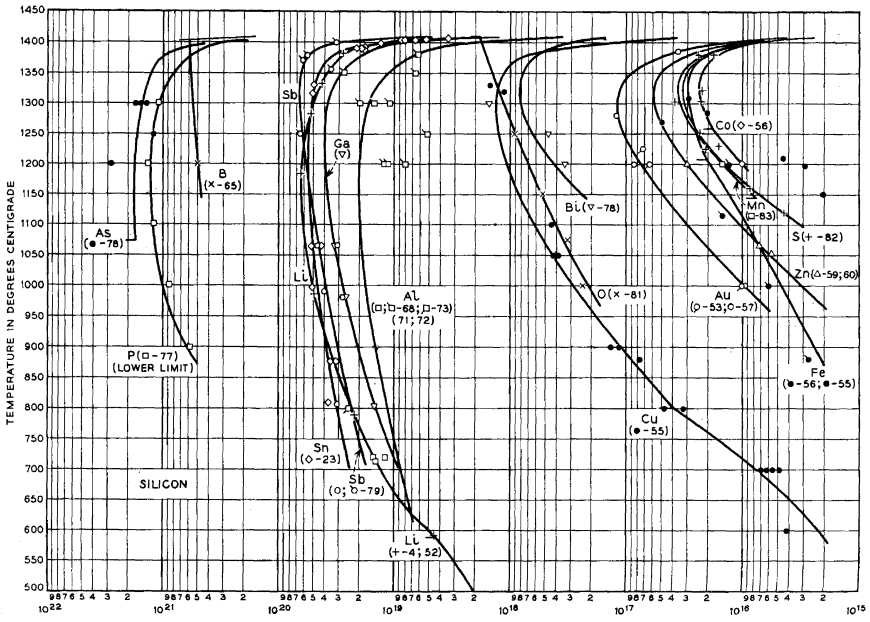

Fig. 1-19. Solid solubility of impurities in silicon (atoms/cm^3). [1-5]

The conversion between the two units can be done by the following equation,

$$A = \frac{B}{5\times10^{22}}\times10^{6} \quad (1\text{-}23)$$

Where A is ppma, B is atoms/cm^3.

Moreover, Ti was tried to use as additive to further enhance the formation and precipitation of boride by Yoshikawa *et al.* in the Si-Al melts, formed a thermodynamically stable compound, TiB_2 [1-169]. The B content in refined Si was reduced from 170 to 1.1 ppma by 933 ppma Ti addition. Similarly, Zr was verified as a more effective additive in improving B removal than Ti in Si-Al melts by Lei *et al.*. [1-170]

With the above discussion, Zr or Ti also can be attempted as impurity getters in Si-Sn and Si-Cu solvents, owing to the following merits: (i) they have strong affinity for B, [1-171] which enhance the formation of boride; (ii) their segregation coefficients are very small (Zr $\rightarrow 1.6\times10^{-8}$, Ti $\rightarrow 2.0\times10^{-6}$ at 1687 K); [1-4, 169, 170] and (iii) their solid solubilities in Si are negligible (less than 0.0001 ppma below 1273 K). [1-5, 172] Hence, it can be eliminated simultaneously with other impurities during the Si directional solidification process and will hardly contaminate the primary Si.

1.6. Objective of This Study

As previously reviewed and discussed, Sn and/or Cu can be considered as better solvents; and Zr or Ti can be employed as suitable impurity getters owing to their corresponding merits. Therefore, to explore a more efficient process for realizing the mass production of SOG-Si with relative low cost, the aim of present work is to clarify the mechanism of (i) separation of bulk Si by flotation based on the significant density difference, and (ii) enhancing B-removal fraction by using additives (Zr, Ti *etc*) in the solidification process of Si with the Si-Sn(-Cu) solvent.

This dissertation contains 7 Chapters with appendix: the first Chapter is introduction. This Chapter mainly summarized the development status of PV industry, the progress of B removal by metallurgy method and their advantages and disadvantages. The significance and feasibility of this research are put forward.

In Chapter 2, in order to confirm whether the upwards or downwards motion

generated better Si enrichment results, the growth control and enrichment of Si crystals from the Si-50.0 at.% Sn melt were conducted in the 1605–1505 K temperature range, under different moving directions, and at different rates ranging from 0.01-0.10mm/min.

In Chapter 3, after determining the advantage of the upwards motion in the separation of bulk Si during the directional solidification process, the effect of Zr/Ti addition on B removal fraction was compared. The B-removal mechanism is discussed from the aspects of theoretical analysis and experimental design. The effects of different variables, such as the moving direction, moving rate, Zr/Ti addition content, and initial Sn content in Si-Sn alloys, on the B-removal fraction were observed. Furthermore, the solubility product of the B-Zr compound in the Si-Sn melt was measured using equilibrium technology.

In Chapter 4, after confirming that Zr is a better additive than Ti and not significant B-removal fraction in Si-Sn system, Si-Cu solvent was considered as a superior solvent based on the conclusion that a lower temperature is more conducive to the formation of boride. An attempt to remove B from Si using Zr as a trapping agent *via* a Si-Cu solvent was developed because of (i) the low liquidus temperature of Si-Cu systems, (ii) low solubility of Cu in solid Si, and (iii) strong affinity of Zr to B for the enhanced boride formation.

In Chapter 5, after confirming that B in a Si-Cu melt can be reduced by precipitating ZrB_2 *via* Zr addition, the solidification refining of Si using Si-Cu solvent with Zr addition was studied. A series of experiments of directional solidification refining were carried out. The B-removal fraction, bulk Si enrichment percentage, and residual Cu content in refined Si were investigated.

In Chapter 6, to further enhancing B removal fraction and make full use of the advantages of aforementioned Si-Sn and Si-Cu system, using Si-based ternary alloy (Si-Sn-Cu) as refining solvent was tried. The separation of Si and B removal fraction were investigated using Si-25at.% Sn-25at.% Cu alloy as solvent.

Chapter 7 summarized the important findings in this research and the outlook for the future research work.

In Appendix, the new concept of using high entropy alloy (ZrTiHfCuNi) as additive for B removal from Si was put forward.

References

1-1 PVinsights. *Weekly Solar PV Snapshot*, 21 August, 2019.

1-2 Mitglieder des Wissenschaftlichen Beirats der Bundesregierung Globale Umweltveränderungen (Stand: 21. März 2003).

1-3 Photovoltaics Report, Fraunhofer Institute for Solar Energy Systems, *ISE,* 2018.

1-4 R. H. Hopkins and A. Rohatgi, Impurity effects in silicon for high efficiency solar cells, *J. Cryst. Growth*, 75 (1986) 67-79.

1-5 F. A. Trumbore, Solid Solubilities of Impurity Elements in Germanium and Silicon. *Bell Syst. Tech. J.*, 39 (1960) 206-233.

1-6 PV EDUCATION.ORG: http://www.pveducation.org/pvcdrom/doping

1-7 森田一樹, 吉川健: まてりあ, 46 (2007) 133-136.

1-8 J. R. Davis, A. Rohatgi, R. H. Hopkins, P. D. Blais, P. Rai-Choudhury, J. R. McCormick and H. C. Mollenkopf: Impurities in Silicon Solar Cells, *IEEE Transactions of Electrodevices,* ED-27 (1980) 677-687.

1-9 F. Chigondo, From metallurgical-grade to solar-grade silicon: an overview, *Silicon,* 10 (2018) 789-798.

1-10 G. Bye, B. Ceccaroli, Solar grade silicon: Technology status and industrial trends, *Sol. Energy Mater. Sol. Cells,* 130 (2014) 634-646.

1-11 A. Schei, J. Tuset and H. Tveit, Production of High Silicon Alloys, *Chap. 12*, Tapir forlag, Trondheim (1998).

1-12 Kouji YASUDA, Kazuki MORITA, Toru H. OKABE, Production processes of Solar Grade Silicon by Hydrogen Reduction and/or Thermal Decomposition, *Journal of MMIJ*, 126 (2010) 115-123.

1-13 Z. Yu, W. Ma, K. Xie, G. Lv, Z. Chen, J. Wu, J. Yu, Life cycle assessment of grid-connected power generation from metallurgical route multi-crystalline silicon photovoltaic system in China, *Appl. Energ.,* 185 (2017) 68-81.

1-14 R. Gløckner, J.O. Odden, G. Halvorsen, R. Tronstad, M.J. de Wild-Scholten, Environmental life cycle assessment of the Elkem Solar metallurgical process route to solar grade silicon with focus on energy consumption and greenhouse gas emissions, *Silicon for the chemical and solar industry IX, Oslo, Norway* (2008).

1-15 M.J. De Wild-Scholten, R. Gløckner, J.O. Odden, G. Halvorsen, R. Tronstad,

LCA comparison of the Elkem Solar metallurgical route and conventional gas routes to solar silicon. In *Proceedings of the 23rd European photovoltaic solar energy conference, Valencia, Spain* (2008, Sep.) 1-5.

1-16 M.M. Lunardi, J.P. Alvarez-Gaitan, N.L. Chang, R. Corkish, Life cycle assessment on PERC solar modules, *Sol. Energy Mater. Sol. Cells,* 187 (2018) 154-159.

1-17 M.D. Johnston, L.T. Khajavi, M.Li, S. Sokhanvaran, M. Barati, High-temperature refining of metallurgical-grade silicon: A review, *JOM*, 64 (2012) 935-945.

1-18 H. Lai, L. Huang, C. Gan, P. Xing, J. Li, X. Luo, Enhanced acid leaching of metallurgical grade silicon in hydrofluoric acid containing hydrogen peroxide as oxidizing agent, *Hydrometallurgy*, 164 (2016) 103-110.

1-19 Q. Wang, W. Dong, Y. Tan, D. Jiang, C. Zhang, X. Peng, Impurities evaporation from metallurgical-grade silicon in electron beam melting process, *Rare Metals,* 30 (2011) 274.

1-20 S. Hu, Y. Dai, A. Gagnoud, Y. Fautrelle, R. Moreau, Z. Ren, Z. Ren, K. Deng, X. Li, Effect of a magnetic field on macro segregation of the primary silicon phase in hypereutectic Al-Si alloy during directional solidification, *J. Alloy Compd.,* 722 (2017) 108-115.

1-21 J.C.S. Pires, J. Otubo, A.F.B. Braga, P.R. Mei, The purification of metallurgical grade silicon by electron beam melting, *J. Mater. Process. Tech.,* 169 (2005) 16-20.

1-22 B.P. Lee, H.M. Lee, D.H. Park, J.S. Shin, T.U. Yu, B.M. Moon, Refining of MG-Si by hybrid melting using steam plasma and EMC, *Sol. Energy Mater. Sol. Cells,* 95 (2011) 56-58.

1-23 S.S. Zheng, T.A. Engh, M. Tangstad, X.T. Luo, Separation of phosphorus from silicon by induction vacuum refining, *Sep. Purif. Technol.,* 82 (2011) 128-137.

1-24 Morita, K.; Miki, T. Thermodynamics of solar-grade-silicon refining. *Intermetallics*, 11 (2003) 1111–1117.

1-25 Safarian, J.; Tangstad, M. Vacuum refining of molten silicon. *Metall. Mater. Trans. B*, 43B (2012) 1427–1445.

1-26 K.Tang, E.J. Øvrelid, G. Tranell, M. Tangstad, A thermochemical database for the solar cell silicon materials, *Mater. Trans.,* 50 (2009) 1978-1984.

1-27 G.V. Samsonov, V.M. Sleptsov, Investigation of the solubility of boron in silicon, *J. Inorg. Chem.,* 8 (1963) 1047-1048. (Crys Structure, Equi Diagram; Experimental)

1-28 C. Brosset, B. Magnusson, The silicon-boron system, Nature, 187 (1960) 54.

1-29 F.A. Trumbore, P.E. Freeland, R.A. Logan, Distribution coefficient of antimony in silicon from solvent evaporation experiments, *J. Electrochem. Soc.,* 108 (1961) 458-460.

1-30 J. Hesse, Loeslichkeit und Ausscheidungskinetik von Bor in polykristallinem Silizium, *Z. Met*., 59 (1968) 499-503.

1-31 R.W. Olesinski, G.J. Abbaschian, The B-Si (boron-silicon) system, *Bulletin of alloy phase diagrams*, 5 (1984) 478-484.

1-32 C.S. Fuller, J.A. Ditzenberger, Diffusion of donor and acceptor elements in silicon, *J. Appl. Phys.,* 27 (1956) 544-553.

1-33 J.P. Garandet, New determinations of diffusion coefficients for various dopants in liquid silicon, *Int. J. Thermophys.,* 28 (2007) 1285-1303.

1-34 H. Kodera, Diffusion coefficients of impurities in silicon melt, *Jpn. J. Appl. Phys.,* 2 (1963) 212.

1-35 E.L. Williams, Boron diffusion in silicon, *J. Electrochem. Soc.,* 108 (1961) 795-798.

1-36 M.L. Barry, P. Olofsen, Doped Oxides as diffusion sources I. Boron into silicon, *J. Electrochem. Soc.,* 116 (1969) 854-860.

1-37 C.S. Fuller, J.A. Ditzenberger, Diffusion of boron and phosphorus into silicon, *J. Appl. Phys.,* 25 (1954) 1439-1440.

1-38 M. Okamura, Boron diffusion into silicon using elemental boron, *Jpn. J. Appl. Phys.,* 8 (1969) 1440.

1-39 E. Dominguez, M. Jaraiz, A non-Fickian model of the boron in silicon diffusion from BN sources, *J. Electrochem. Soc.,* 133 (1986) 1895-1900.

1-40 G.L. Vick, K.M. Whittle, Solid solubility and diffusion coefficients of boron in silicon, *J. Electrochem. Soc.,* 116 (1969) 1142-1144.

1-41 W. Wijaranakula, An anomalous enhanced tail diffusion of boron in directly bonded samples of heavily and lightly doped silicon, *Jpn. J. Appl. Phys.,* 32 (1993) 3872.

1-42 R.N. Ghoshtagore, Donor diffusion dynamics in silicon, *Phys. Rev. B,* 3 (1971) 397.

1-43 K. Tang, E.J. Øvrelid, G. Tranell, M. Tangstad, Thermochemical and kinetic databases for the solar cell silicon materials, *Crystal growth of Si for solar cells,* Springer, Berlin, Heidelberg, 2009, p. 219-251.

1-44 F. Wang, J. Wu, W. Ma, Y. Lei, K. Wei, B. Yang, Experimental determination of diffusion and mass transfer of boron oxide in molten slag for metallurgical grade silicon purification, *J. Chem. Thermodyn*., 118 (2018) 215-224.

1-45 J. Wu, F. Wang, W. Ma, Y. Lei, B. Yang, Thermodynamics and kinetics of boron removal from metallurgical grade silicon by addition of high basic potassium carbonate to calcium silicate slag, *Metall. Mater. Trans. B,* 47 (2016) 1796-1803.

1-46 J. Wu, F. Wang, Z. Chen, W. Ma, Y. Li, B. Yang, Y. Dai, Diffusion and mass transfer of boron in molten silicon during slag refining process of metallurgical grade silicon, *Fluid Phase Equilibr*., 404 (2015) 70-74.

1-47 Y. Wang, K. Morita, Reaction mechanism and kinetics of boron removal from molten silicon by CaO-SiO_2-$CaCl_2$ slag treatment, *J. Sustain. Metall.,* 1 (2015) 126-133.

1-48 M. Fang, C. Lu, L. Huang, H. Lai, J. Chen, X. Yang, J. Li, W. Ma, P. Xing, X. Luo, Multiple slag operation on boron removal from metallurgical-grade silicon using Na_2O-SiO_2 slags, *Ind. Eng. Chem. Res*., 53 (2014) 12054-12062.

1-49 L. Zhang, Y. Tan, J. Li, Y. Liu, D. Wang, Study of boron removal from molten silicon by slag refining under atmosphere, *Mat. Sci. Semicon. Proc.,* 16 (2013) 1645-1649.

1-50 H. Nishimoto, Y. Kang, T. Yoshikawa, K. Morita, The rate of boron removal from molten silicon by CaO-SiO_2 slag and Cl_2 treatment, *High Temp. Chem. Proc.,* 31 (2012) 471–477.

1-51 E. Krystad, K. Tang, G. Tranell, The kinetics of boron transfer in slag refining of silicon, *JOM,* 64 (2012) 968-972.

1-52 K. Tang, E.J. Øvrelid, G. Tranell, M. Tangstad, Critical assessment of the impurity diffusivities in solid and liquid silicon, *JOM,* 61 (2009) 49-55.

1-53 J.P. Garandet, New determinations of diffusion coefficients for various dopants in liquid silicon, *Int. J. Thermophys*., 28 (2007) 1285-1303.

1-54 H. Kodera, Diffusion coefficients of impurities in silicon melt, *Jpn. J. Appl. Phys*., 2 (1963) 212.

1-55 R. Noguchi, K. Suzuki, F. Tsukihashi, N. Sano, Thermodynamics of boron in a silicon melt, *Metall. Mater. Trans. B,* 25 (1994) 903-907.

1-56 M. Tanahashi, T. Fujisawa, C. Yamauchi, Activity of boron in molten silicon, *Journal of the mining and materials processing institute of Japan,* 114 (1998) 807-812.

1-57 G. Inoue, T. Yoshikawa, K. Morita, Effect of calcium on thermodynamic properties of boron in molten silicon, *High Temp. Chem. Proc.,* 22 (2003) 221-226.

1-58 T. Yoshikawa, K. Morita, Thermodynamic property of B in molten Si and phase relations in the Si-Al-B system, *Mater. Trans.,* 46 (2005) 1335-1340.

1-59 T. Yoshikawa, K. Morita, Removal of B from Si by solidification refining with Si-Al melts, *Metall. Mater. Trans. B,* 36 (2005) 731-736.

1-60 L.T. Khajavi, K. Morita, T. Yoshikawa, M. Barati, Thermodynamics of boron distribution in solvent refining of silicon using ferrosilicon alloys, *J. Alloy Compd.,* 619 (2015) 634-638.

1-61 F. Xu, S. Wu, Y. Tan, J. Li, Y. Li, Y. Liu, Boron removal from metallurgical silicon using Si-Al-Sn ternary alloy, *Sep. Sci. Technol.,* 49 (2014) 305-310.

1-62 L.A.V. Teixeira, K. Morita, Removal of boron from molten silicon using CaO-SiO2 based slags, *ISIJ Int.,* 49 (2009) 783-787.

1-63 R.N. Hall, Segregation of impurities during the growth of germanium and silicon, *J. Phys. Chem. A,* 57 (1953) 836-839.

1-64 S. Esfahani, M. Barati, Purification of metallurgical silicon using iron as impurity getter, part II: extent of silicon purification, *Met. Mater. Int*., 17 (2011) 1009-1015.

1-65 L. Zhao, W. Zhi, Z. Guo, C. Li, Low-temperature purification process of metallurgical silicon, *Trans. Nonferrous Met. Soc. China,* 21 (2011) 85-1192.

1-66 Z. Yin, A. Oliazadeh, S. Esfahani, M. Johnston, M. Barati, Solvent refining of silicon using nickel as impurity getter, *Can. Metall. Quart.,* 50 (2011) 166-172.

1-67 T. Shimoda, T. Masuda, Liquid silicon and its application in electronics, *Jpn. J. Appl. Phys.,* 53 (2014) 02B-A01.

1-68 R. Al-khazraji, Y. Li, L. Zhang, Application of slag refining technique to

metallurgical grade silicon purification process: A review, *Funct. Mater.,* 25 (2018) 364-370.

1-69 J.A.T. Jones, B. Bowman, P.A. Lefrank, The Making, shaping, and treating of steel-Steelmaking and refining volume, The AISE Steel Foundation, Pittsburgh, PA, 1998, p. 281-304.

1-70 H. Bjerke, Removal of boron from silicon by slag treatment and by evaporation of boron from slag in hydrogen atmosphere, *Master's thesis, Institutt for materialteknologi*, 2012.

1-71 E.J. Jung, B.M. Moon, S.H. Seok, D.J. Min, The mechanism of boron removal in the CaO-SiO_2-Al_2O_3 slag system for SoG-Si, *Energy,* 66 (2014) 35-40.

1-72 M.D. Johnston, M. Barati, Metallurgical refining of silicon for solar applications by slagging of impurity elements, *Materials challenges in alternative and renewable energy*, 2011, p. 207-224.

1-73 M. Li, T. Utigard, M. Barati, Removal of boron and phosphorus from silicon using CaO-SiO_2-Na_2O-Al_2O_3 flux, *Metall. Mater. Trans. B,* 45 (2014) 221-228.

1-74 H.M. Liaw, F.S. d'Aragona, Purification of metallurgical-grade silicon by slagging and impurity redistribution, *Sol. Cells,* 10 (1983) 109-118.

1-75 H. Fujiwara, R. Otsuka, K. Wada, T. Fukuyama, Silicon purifying method, slag for purifying silicon and purified silicon, 2005, *U.S. Patent Application No. 10/503,304*.

1-76 L.A.V. Teixeira, Y. Tokuda, T. Yoko, K. Morita, Behavior and state of boron in CaO-SiO_2 slags during refining of solar grade silicon, *ISIJ int.,* 49 (2009) 777-782.

1-77 J. Wu, Y. Li, K. Wei, B. Yang, Y. Dai, Boron removal in purifying metallurgical grade silicon by CaO-SiO_2 slag refining, *Trans. Nonferrous Met. Soc. China,* 24 (2014) 1231-1236.

1-78 K. Wei, H. Lu, W. Ma, Y. Li, Z. Ding, J. Wu, Y. Dai, Boron removal from metallurgical grade silicon by CaO-SiO_2 slag refining, *Rare Metals,* 34 (2015) 522-526.

1-79 D. Luo, L. Ning, Y. Lu, G. Zhang, T. Li, Removal of boron from metallurgical grade silicon by electromagnetic induction slag melting, *Trans. Nonferrous Met. Soc. China,* 21 (2011) 1178-1184.

1-80 L.K. Jakobsson, M. Tangstad, Distribution of boron between silicon and

$CaO-MgO-Al_2O_3-SiO_2$ slags, *Metall. Mater. Trans. B,* 45 (2014) 1644-1655.

1-81 J. Safarian, G. Tranell, M. Tangstad, Boron removal from silicon by $CaO-Na_2O-SiO_2$ ternary slag, *Metall. Mater. Trans. E,* 2 (2015) 109-118.

1-82 H. Lai, L. Huang, C. Lu, M. Fang, W. Ma, P. Xing, J. Li, X. Luo, Reaction mechanism and kinetics of boron removal from metallurgical-grade silicon based on Li_2O-SiO_2 slags, *JOM,* 68 (2016) 2371-2380.

1-83 F. Wang, J. Wu, W. Ma, M. Xu, Y. Lei, B. Yang, Removal of impurities from metallurgical grade silicon by addition of ZnO to calcium silicate slag, *Sep. Purif. Technol.,* 170 (2016) 248-255.

1-84 J. Wu, W. Ma, B. Jia, B. Yang, D. Liu, Y. Dai, Boron removal from metallurgical grade silicon using a $CaO-Li_2O-SiO_2$ molten slag refining technique, *J. Non-Cryst. Solids*, 358 (2012) 3079-3083.

1-85 Z. Ding, W. Ma, K. Wei, J. Wu, Y. Zhou, K. Xie, Boron removal from metallurgical-grade silicon using lithium containing slag, *J. Non-Cryst. Solids,* 358 (2012) 2708-2712.

1-86 J. Li, L. Zhang, Y. Tan, D. Jiang, D. Wang, Y. Li, Research of boron removal from polysilicon using $CaO-Al_2O_3-SiO_2-CaF_2$ slags, *Vacuum*, 103 (2014) 33-37.

1-87 M.D. Johnston, M. Barati, Distribution of impurity elements in slag-silicon equilibria for oxidative refining of metallurgical silicon for solar cell applications, *Sol. Energy Mater. Sol. Cells,* 94 (2010) 2085-2090.

1-88 Y. Wang, X. Ma, K. Morita, Evaporation removal of boron from metallurgical-grade silicon using $CaO-CaCl_2-SiO_2$ Slag, *Metall. Mater. Trans. B,* 45 (2014) 334-337.

1-89 H. Chen, Y. Wang, W. Zheng, Q. Li, X. Yuan, K. Morita, Model implementation of boron removal using $CaCl_2-CaO-SiO_2$ slag system for solar-grade silicon, *Metall. Mater. Trans. B,* 48 (2017) 3219-3227.

1-90 C.P. Khattak, K.V. Ravi (Eds.), Silicon processing for photovoltaics II (Vol. 6), Elsevier, 2012.

1-91 M.D. Johnston, M. Barati, Effect of slag basicity and oxygen potential on the distribution of boron and phosphorus between slag and silicon, *J. Non-Cryst. Solids,* 357 (2011) 970-975.

1-92 J. Cai, J. Li, W. Chen, C. Chen, X. Luo, Boron removal from metallurgical

silicon using CaO-SiO_2-CaF_2 slags, *Trans. Nonferrous Met. Soc. China,* 21 (2011) 1402-1406.

1-93 A. Hosseinpour, L.T. Khajavi, Slag refining of silicon and silicon alloys: a review, *Min. Proc. Ext. Met. Rev.,* 39 (2018) 308-318.

1-94 R. Mellström, O. Andersson, G. Åhlund, I. Johansson, Method for the purification of silicon, 1989, *Intl. Patent. WO8902415 (A1). 1989-03-23.*

1-95 Y. Wang, K. Morita, Measurement of the phase diagram of the SiO_2-$CaCl_2$ system and liquid area study of the SiO_2-CaO-$CaCl_2$ system, *Metall. Mater. Trans. B,* 47 (2016) 1542-1547.

1-96 Y. Wang, K. Morita, Measurement of CaO-SiO_2-$CaCl_2$ slag density by an improved Archimedean method, *J. Min. Metall. B,* 51 (2015) 113-116.

1-97 C. Lu, L. Huang, H. Lai, M. Fang, W. Ma, P. Xing, L. Zhang, J. Li, X. Luo, Effects of slag refining on boron removal from metallurgical-grade silicon using recycled slag with active component, *Sep. Sci. Technol.,* 50 (2015) 2759-2766.

1-98 C. Lu, T. Tang, Z. Sheng, P. Xing, X. Luo, Improved removal of boron from metallurgical-grade Si by CaO-SiO_2-$CaCl_2$ slag refining with intermittent $CaCl_2$ addition, *Vacuum,* 143 (2017) 7-13.

1-99 L. Huang, H. Lai, C. Gan, H. Xiong, P. Xing, X. Luo, Separation of boron and phosphorus from Cu-alloyed metallurgical grade silicon by CaO-SiO_2-$CaCl_2$ slag treatment, *Sep. Purif. Technol.,* 170 (2016) 408-416.

1-100 C. Alemany, C. Trassy, B. Pateyron, K.I. Li, Y. Delannoy, Refining of metallurgical-grade silicon by inductive plasma, *Sol. Energy Mater. Sol. Cells,* 72 (2002) 41-48.

1-101 H.C. Theuerer, Removal of boron from silicon by hydrogen water vapor treatment, *JOM,* 8 (1956) 1316-1319.

1-102 J. Wu, B. Yang, Y. Dai, K. Morita, Boron removal from metallurgical grade silicon by oxidizing refining, *Trans. Nonferrous Met. Soc. China,* 19 (2009) 463-467.

1-103 E.F. Nordstrand, M. Tangstad, Removal of boron from silicon by moist hydrogen gas, *Metall. Mater. Trans. B,* 43 (2012) 814-822.

1-104 A. Yvon, E. Fourmond, C. Ndzogha, Y. Delannoy, C. Trassy, Inductive plasma process for refining of solar grade silicon, *In EPM 2003 4th international*

conference on electromagnetic processing of materials, Forum Editions, 2003 September, p. 125-130.

1-105 C.P. Khattak, F. Schmid, D.B. Joyce, E.A. Smelik, M.A. Wilkinson, Production of solar-grade silicon by refining of liquid metallurgical-grade silicon, *In AIP conference proceedings,* 462 (1999) 731-736.

1-106 C.P. Khattak, D.B. Joyce, F. Schmid, A simple process to remove boron from metallurgical grade silicon, *Sol. Energy Mater. Sol. Cells,* 74 (2002) 77-89.

1-107 J. Safarian, K. Tang, K. Hildal, G. Tranell, Boron removal from silicon by humidified gases, *Metall. Mater. Trans. E,* 1 (2014) 41-47.

1-108 G. Flamant, V. Kurtcuoglu, J. Murray, A. Steinfeld, Purification of metallurgical grade silicon by a solar process, *Sol. Energy Mater. Sol. Cells,* 90 (2006) 2099-2106.

1-109 J. Wu, W. Ma, Y. Li, B. Yang, D. Liu, Y. Dai, Thermodynamic behavior and morphology of impurities in metallurgical grade silicon in process of O_2 blowing, *Trans. Nonferrous Met. Soc. China,* 23 (2013) 260-265.

1-110 J. Wu, Y. Li, W. Ma, K. Liu, K. Wei, K. Xie, B. Yang, Y. Dai, Impurities removal from metallurgical grade silicon using gas blowing refining techniques, *Silicon,* 6 (2014) 79-85.

1-111 Ø.S. Sortland, M. Tangstad, Boron removal from silicon melts by H_2O/H_2 gas blowing: mass transfer in gas and melt, *Metall. Mater. Trans. E,* 1 (2014) 211-225.

1-112 J. Safarian, K. Tang, J.E. Olsen, S. Andersson, G. Tranell, K. Hildal, Mechanisms and kinetics of boron removal from silicon by humidified hydrogen, *Metall. Mater. Trans. B,* 47 (2016) 1063-1079.

1-113 Z. Chen, K. Morita, Iron-catalyzed boron removal from molten silicon in ammonia, *Metall. Mater. Trans. E,* 3 (2016) 228-233.

1-114 K. Suzuki, T. Kumagai, N. Sano, Removal of boron from metallurgical-grade silicon by applying the plasma treatment, *ISIJ int*., 32 (1992) 630-634.

1-115 K. Suzuki, K.S. Akaguchi, T. Nakagiri, N. Sano, Gaseous removal of phosphorus and boron from molten silicon, *J. Jpn. I. Met.,* 54 (1990) 161-167.

1-116 H.C. Theuerer, Removal of boron from silicon by hydrogen water vapor

treatment, *JOM,* 8 (1956) 1316-1319.

1-117 D. Morvan, J. Amouroux, F. Slootman, N. Madigou, T. Roger, Control of the plasma refining of materials by computer analysis using an optical fiber, spectrometer and O.M.A., *The 8th international symposium on plasma chemistry, ISPC-8*, Tokyo, Japan. 3 (1987) 1868-1873.

1-118 H. Baba, N. Yuge, Y. Sakaguchi, M. Fukai, F. Aratani, Y. Habu, Removal of boron from molten silicon by argon-plasma mixed with water vapor, *In tenth EC photovoltaic solar energy conference*, Springer, Dordrecht, 1991 p. 286-289.

1-119 Y. Delannoy, C. Alemany, K.I. Li, P. Proulx, C. Trassy, Plasma-refining process to provide solar-grade silicon, *Sol. Energy Mater. Sol. Cells,* 72 (2002) 69-75.

1-120 B.P. Lee, H.M. Lee, D.H. Park, J.S. Shin, T.U. Yu, B.M. Moon, Refining of MG-Si by hybrid melting using steam plasma and EMC, *Sol. Energy Mater. Sol. Cells,* 95 (2011) 56-58.

1-121 N. Yuge, H. Baba, Y. Sakaguchi, K. Nishikawa, H. Terashima, F. Aratani, Purification of metallurgical silicon up to solar grade, *Sol. Energy Mater. Sol. Cells,* 34 (1994) 243-250.

1-122 T. Ikeda, M. Maeda, Elimination of boron in molten silicon by reactive rotating plasma arc melting, *Mater. Trans.*, *JIM,* 37 (1996) 983-987.

1-123 J. Cai, C. Lu, J. Li, W. Ma, X. Luo, Boron removal from metallurgical silicon by plasma melting using electromagnetic induction, *Trans. Nonferrous Met. Soc. China,* 12 (2012) 033.

1-124 N. Nakamura, H. Baba, Y. Sakaguchi, Y. Kato, Boron removal in molten silicon by a steam-added plasma melting method, *Mater. Trans.,* 45 (2004) 858-864.

1-125 N. Nakamura, H. Baba, Y. Sakaguchi, S. Hiwasa, Y. Kato, Boron removal in molten silicon with steam added plasma melting method, *J. Jpn. I. Met.,* 67 (2003) 583-589.

1-126 S. Rousseau, M. Benmansour, D. Morvan, J. Amouroux, Purification of MG silicon by thermal plasma process coupled to DC bias of the liquid bath. *Sol. Energy Mater. Sol. Cells,* 91 (2007) 1906-1915.

1-127 M.D. Díez, M. Fjeld, E. Andersen, B. Lie, Validation of a compartmental population balance model of an industrial leaching process: The Silgrain® process,

Chem. Eng. Sci., 61 (2006) 229-245.

1-128 S. Pizzini, Solar grade silicon as a potential candidate material for low-cost terrestrial solar cells, *Sol. Energy Mater.,* 6 (1982) 253-297.

1-129 J. Dietl, Hydrometallurgical purification of metallurgical-grade silicon, *Sol. Cells,* 10 (1983) 145-154.

1-130 Y. Sun, Q. Ye, C. Guo, H. Chen, X. Lang, F. David, Q. Luo, C. Yang, Purification of metallurgical-grade silicon via acid leaching, calcination and quenching before boron complexation, *Hydrometallurgy,* 139 (2013) 64-72.

1-131 H. Lai, L. Huang, C. Gan, P. Xing, J. Li, X. Luo, Enhanced acid leaching of metallurgical grade silicon in hydrofluoric acid containing hydrogen peroxide as oxidizing agent, *Hydrometallurgy,* 164 (2016) 103-110.

1-132 T. Shimpo, T. Yoshikawa, K. Morita, Thermodynamic study of the effect of calcium on removal of phosphorus from silicon by acid leaching treatment, *Metall. Mater. Trans. B,* 35 (2004) 277-284.

1-133 T. Yoshikawa, K. Morita, Solid solubilities and thermodynamic properties of aluminum in solid silicon, *J. Electrochem. Soc.,* 150 (2003) G465-G468.

1-134 X. Ma, T. Yoshikawa, K. Morita, Removal of boron from silicon-tin solvent by slag treatment, *Metall. Mater. Trans. B*, 44 (2013) 528-533.

1-135 A.M. Mitrašinović, T.A. Utigard, Refining silicon for solar cell application by copper alloying, *Silicon*, 1 (2009) 239-248.

1-136 Y. Li, Y. Tan, J. Li, Q. Xu, Y. Liu, Effect of Sn content on microstructure and boron distribution in Si-Al alloy, *J. Alloy Compd.,* 583 (2014) 85-90.

1-137 P.S. Kotval, H.B. Strock, Process for the production of improved refined metallurgical silicon, 1980, *U.S. Patent No. 4,193,975*, Washington, DC: U.S. Patent and Trademark Office.

1-138 R.K. Dawless, Silicon purification method using copper or copper-aluminum solvent metal, 1989, *U.S. Patent No. 4,822,585*, Washington, DC: U.S. Patent and Trademark Office.

1-139 T. Yoshikawa, K. Morita, Removal of phosphorus by the solidification refining with Si-Al melts, *Sci. Technol. Adv. Mat.,* 4 (2003) 531.

1-140 T. Yoshikawa, K. Morita, An evolving method for solar-grade silicon production: solvent refining, *JOM*, 64 (2012) 946-951.

1-141 T. Yoshikawa, K. Morita, Refining of Si by the solidification of Si-Al melt with electromagnetic force, *ISIJ Int.,* 45 (2005) 967-971.

1-142 J.L. Gumaste, B.C. Mohanty, R.K. Galgali, U. Syamaprasad, B.B. Nayak, S.K. Singh, P.K. Jena, Solvent refining of metallurgical grade silicon, *Sol. Energy Mater.,* 16 (1987) 289-296.

1-143 R.K. Dawless, R.L. Troup, D.L. Meier, A. Rohatgi, Production of extreme-purity aluminum and silicon by fractional crystallization processing, *J. Cryst. Growth,* 89 (1988) 68-74.

1-144 K. Morita, and T. Yoshikawa, Thermodynamic evaluation of new metallurgical refining processes for SOG-silicon production, *Trans. Nonferrous Met. Soc. China,* 21 (2011) 685-690.

1-145 Y. Li, Y. Tan, P. Cao, J. Li, P. Jia, Y. Liu, Study on redistribution of boron during silicon solidification refining process in Si-Al melts, *Mater. Res. Innov.,* 19 (2015) 81-85.

1-146 Q. Zou, J. Jie, J. Sun, T. Wang, Z. Cao, T. Li, Effect of Si content on separation and purification of the primary Si phase from hypereutectic Al-Si alloy using rotating magnetic field, *Sep. Purif. Technol.,* 142 (2015) 101-107.

1-147 T. Yoshikawa, K. Morita, Thermodynamics on the solidification refining of silicon with Si-Al melts, *In EPD congress-TMS 2005 annual meeting and exhibition*, San Francisco, 2005, p. 549-558.

1-148 B. Ban, J. Li, X. Bai, Q. He, J. Chen, S. Dai, Mechanism of B removal by solvent refining of silicon in A l-Si melt with Ti addition, *J. Alloy Compd.,* 672 (2016) 489-496.

1-149 Y. Li, Y. Tan, J. Li, K. Morita, Si purity control and separation from Si-Al alloy melt with Zn addition, *J. Alloy Compd.,* 611 (2014) 267-272.

1-150 Y. Lei, W. Ma, L. Sun, J. Wu, Y. Dai, K. Morita, Removal of B from Si by Hf addition during Al-Si solvent refining process, *Sci. Technol. Adv. Mat.,* 17 (2016) 12-19.

1-151 Y. Lei, W. Ma, J. Wu, K. Wei, S. Li, K. Morita, Impurity phases and their removal in Si purification with Al-Si alloy using transition metals as additives, *J. Alloy Compd.,* 734 (2018) 250-257.

1-152 K. Chen, X. Chen, Y. Lei, W. Ma, J. Han, Z. Yang, Mechanism of

enhancing B removal from Si with V addition using Al-Si as the refining solvent, *Sep. Purif. Technol.,* 203 (2018) 168-177.

1-153 M. Fang, C. Lu, H. Lai, L. Huang, J. Chen, W. Ma, Z. Sheng, J. Shen, J. Li. X. Luo, Effect of solidification rate on representative impurities distribution in Si-Cu alloy, *Mater. Sci. Tech-Lond.,* 29 (2013) 861-867.

1-154 L. Huang, H. Lai, C. Lu, M. Fang, W. Ma, P. Xing, J. Li, X. Luo, Enhancement in extraction of boron and phosphorus from metallurgical grade silicon by copper alloying and aqua regia leaching, *Hydrometallurgy,* 161 (2016) 14-21.

1-155 H. Morito, T. Karahashi, M. Uchikoshi, M. Isshiki, H. Yamane, Low-temperature purification of silicon by dissolution and solution growth in sodium solvent, *Silicon*, 4 (2012) 121-125.

1-156 J. Li, B. Ban, Y. Li, X. Bai, T. Zhang, J. Chen, Removal of impurities from metallurgical grade silicon during Ga-Si solvent refining, *Silicon,* 9 (2017) 77-83.

1-157 J. Wu, D. Yang, M. Xu, W. Ma, Q. Zhou, Z. Xia, Y. Lei, K. Wei, S. Li, Z. Chen, K. Xie, Boron removal from silicon using secondary refining techniques by metallurgical method, *Sep. Purif. Rev.,* 00 (2018) 1-21.

1-158 Chen, H., et al. Boron removal for solar-grade silicon production by metallurgical route:A review. *Sol. Energy Mater. Sol. Cells*, 203 (2019) 110169.

1-159 Li, Y. and L. Zhang, Application of Si-Based Solvents to the Purification of Metallurgical Grade-Silicon. *Sep. Purif. Rev.,* 00 (2019) 1-24.

1-160 http://www.rsc.org/periodic-table/element/14/silicon (accessed November 6, 2019).

1-161 M.J. Assael, K. Kakosimos, R. M. Banish, J. Brillo, I. Egry, R. Brooks, P.N. Quested, K.C. Mills, A. Nagashima, Y. Sato and W.A. Wakeham, Reference Data for the Density and Viscosity of Liquid Aluminum and Liquid Iron. *J. Phys. Chem. Ref. Data*, 35 (2006) 285-300.

1-162 W. Yu, W. Ma, G. Lv, H. Xue, S. Li, Y. Dai, Effect of electromagnetic stirring on the enrichment of primary silicon from Al–Si melt, *J. Cryst. Growth*, 405 (2014) 23-28.

1-163 J. Li, Z. Guo, H. Tang, Z. Wang, S. Sun, Si purification by solidification of Al–Si melt with super gravity. *Trans. Nonferrous Met. Soc. China*, 22 (2012) 958-963.

1-164 X. Gu, X.G. Yu, D.R. Yang: Low-cost solar grade silicon purification process with Al–Si system using a powder metallurgy technique, *Sep. Purif. Technol.,* 77 (2011) 33-39.

1-165 X.D. Ma, Doctoral Dissertation, The University of Tokyo, 2012.

1-166 大嶋 陽介: 東京大学修士論文 (2012).

1-167 B.B. Alchagirov and A.M. Chochaeva, Temperature dependence of the density of liquid tin. *High Temp.,* 38 (2000) 44-48.

1-168 http://www.rsc.org/periodic-table/element/29/copper (accessed November 6, 2019).

1-169 Yoshikawa, T.; Arimura, K.; Morita, K. Boron removal by titanium addition in solidification refining of silicon with Si-Al melt. *Metall. Mater. Trans. B,* 36B (2005) 837–842.

1-170 Y. Lei, K. Morita, *et al.*, B removal by Zr addition in electromagnetic solidification refinement of Si with Si-Al melt. *Metall. Mat. Trans. B*, 47 (2016) 27-31.

1-171 I. Barin, Thermochemical Data of Pure Substances, *VCH, Weinheim,* (1989) 1384, 1523, 1708.

1-172 Y. Lei, W.H. Ma, L.E. Sun, J.J. Wu, K. Morita, Effects of small amounts of transition metals on boron removal during electromagnetic solidification purification of silicon with Al-Si solvent. *Separ. Purif. Technol.,* 162 (2016) 20-23.

Chapter II. Growth Control of Si Crystals from Si-Sn Melt

2.1. Introduction

For solvent refining, the most critical first step is to enrich and separate large area of primary Si from Si-based alloy melt. Therefore, the research content of this Chapter is mainly concentrated on growth control of Si crystals from Si-Sn melt by directional solidification. The current study was aimed at clarifying the growth control and enrichment of Si crystals from the Si-Sn melt under different moving directions and at different rates. The optimal conditions for crystal growth and enrichment were determined. Moreover, a model was established encompassing the crystal growth process and enrichment mechanism of the Si-Sn melt during directional solidification.

2.2. Experiment

2.2.1. Experimental Materials and Equipment

The materials used in experiments in this research are listed in Table 2-1,

Table 2-1. Various materials used in the experiment.

Material	Specification/Purity	Company name
Sn grain	>99.9%	Kojundo chemical laboratory Co., Ltd, Japan
SOG-Si	100.00%	------
Graphite crucible	High-purity dense	Nikkato Co., Ltd, Japan
Alumina crucible	High-purity	Nikkato Co., Ltd, Japan
Ar gas	99.99%	Sumitomo Seika Chemicals Co., Ltd, Japan
Ethanol, acetone	------	FUJIFILM Wako Pure Chemical Co., Ltd, Japan
Polishing paper	100, 400, 800, 1200, 2000 mesh	Maruto Instrument Co., Ltd.
Diamond polishing liquid	3, 1, 0.25 μm	Maruto Instrument Co., Ltd, Japan
Colloidal silica	0.06, 0.02 μm	PACE Technologies Co., Ltd, USA
Clay	------	DEBIKA Co., Ltd, Japan
Alumina powder	>99.9%	Rigaku Corp, Japan

And the equipment used in experiments in this research are listed in Table 2-2.

Table 2-2. Various equipment used in the experiment.

Equipment	Company name
Balance	Sartorius Co., Ltd, Germany
Induction furnace	Chino Co., Ltd, Japan
Standard B-type thermocouple	------
Dual-wavelength infrared pyrometer	Chino Co., Ltd, Japan
SiC electric resistance furnace	Nitto Kagaku Co., Ltd, Japan
Temperature measuring instrument	midi LOGGER TYPE GL220, GRAPHTEC Co., Ltd, China
Cutting machine	Maruto Instrument Co., Ltd, Japan
Grinder	Maruto Instrument Co., Ltd, Japan
Stove	Asahi Rika Corporation, Japan
Vacuum pump	ULVAC KIKO, Inc.
SEM-EDS	S4200, Hitachi Corp, Japan
EBSD	Oxford Instruments plc, Britain

2.2.2. Sample Preparation Process

A high frequency induction furnace (50 kHz) was employed to conduct the pre-melting experiments. The schematic of this apparatus is shown in Fig. 2-1.

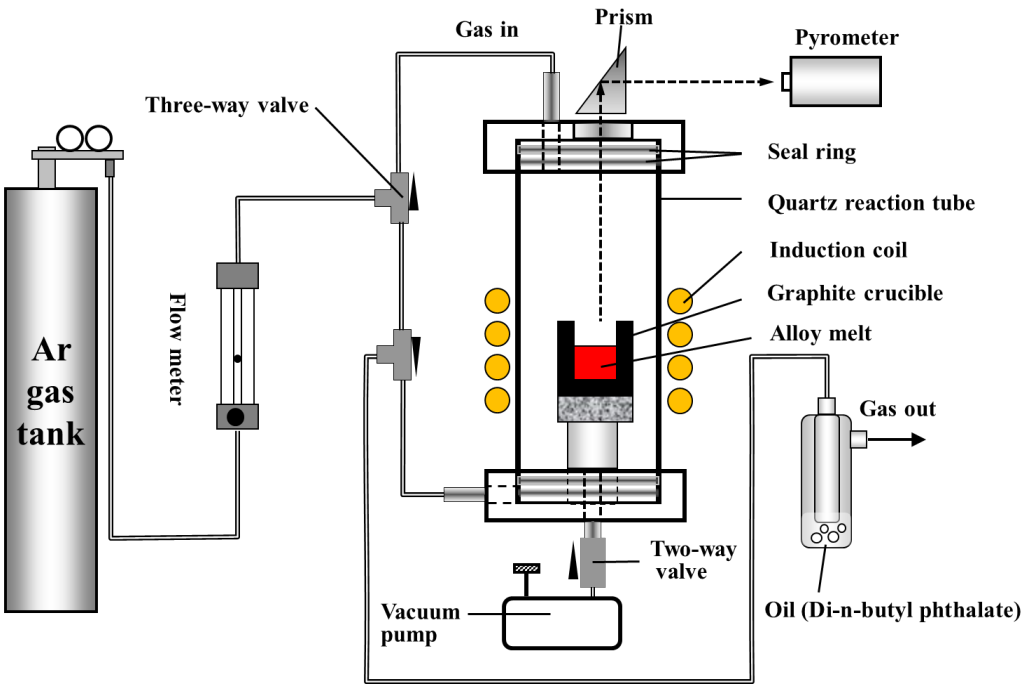

Fig. 2-1. Schematic of the induction furnace for pre-melting experiment.

In total, 30 grams of bulk Si (99.9999 %) and Sn grains (99.9 %) were placed in a high-purity dense graphite crucible (20 mm outer diameter (O.D.), 14 mm inner diameter (I.D.), 70 mm length) to prepare the Si-Sn alloys. To prevent the oxidation of the melt, the quartz chamber (60 mm O.D., 54 mm I.D., 400 mm length) was first evacuated using a vacuum pump (ultimate pressure < 6 Pa). The chamber was then filled with Ar gas (99.99 %) at a flow rate of 200 mL/min. The surface temperature of the Si-Sn melt was monitored through a prism, using a dual-wavelength infrared pyrometer.

Subsequently, directional solidification experiments were conducted as follows. First, the pre-melted alloys were placed into the alumina reaction tube (30 mm O.D., 24 mm I.D., 1000 mm length) of a SiC electric resistance furnace combined with a vertical motion system controlled by a stepping motor, which was used to carry out the directional solidification experiments, as shown in Fig. 2-2. The moisture, CO_2, and O_2 in the Ar gas were removed by passing the gas successively through soda lime, silica gel, magnesium perchlorate, and magnesium turnings heated at 823 K. The sample was subsequently melted and maintained above the liquidus temperature of the alloy for 1 h in an Ar atmosphere for chemical homogenization.

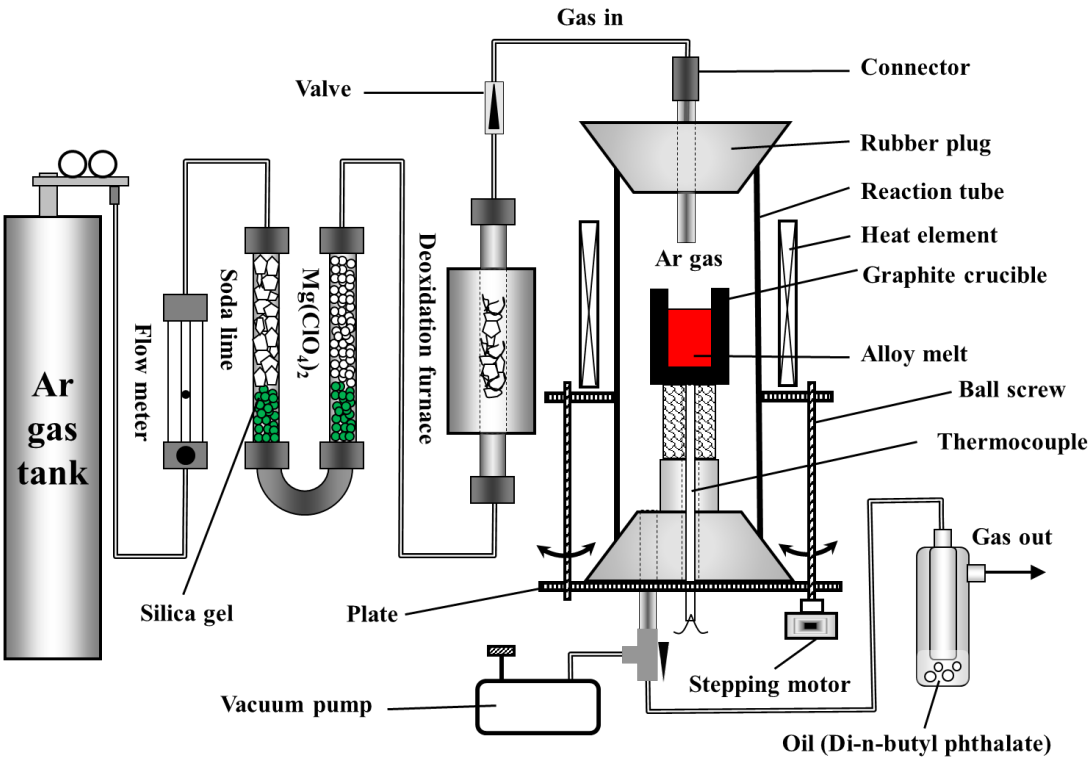

Fig. 2-2. Schematic of the experimental apparatus for directional solidification.

After the above steps were completed, directional solidification was conducted by moving the alumina reaction tube upwards or downwards at a rate of 0.01-0.10 mm/min, respectively. The temperature distribution along the vertical direction is shown in Fig. 2-3. Directional solidification experiments were conducted in the 1605–1505 K temperature range. The alloys solidified continuously from one end to the other due to the furnace cooling caused by moving it upwards or downwards.

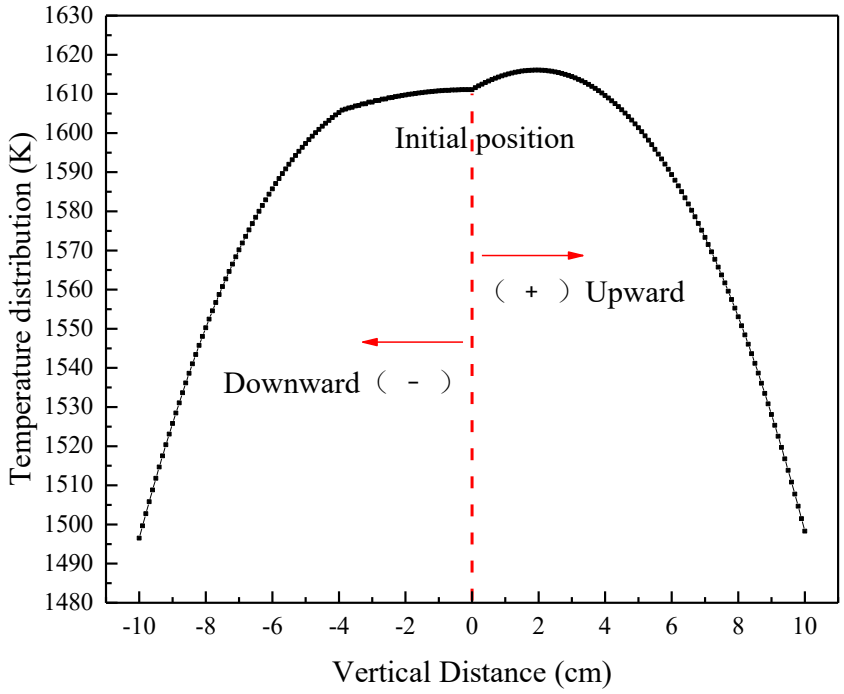

Fig. 2-3. Temperature distribution along the vertical direction.

When the solidification completed, the samples were cut along the longitudinal section, which was parallel to the growth direction of the primary Si crystal. These samples were used to characterize and calculate the Si enrichment.

Part of the samples were ground using SiC paper and polished using standard metallographic techniques before observation. The macro and micro structure of the solidified samples were observed using a digital camera and a scanning electron microscope equipped with an energy dispersive spectrometer (SEM-EDS), respectively.

To obtain detailed data on the Si enrichment percentage, the agglomerated Si part of the solidified sample was cut off along the interface using a diamond sawing machine. The calculation process of Si enrichment percentage is shown in Fig. 2-4.

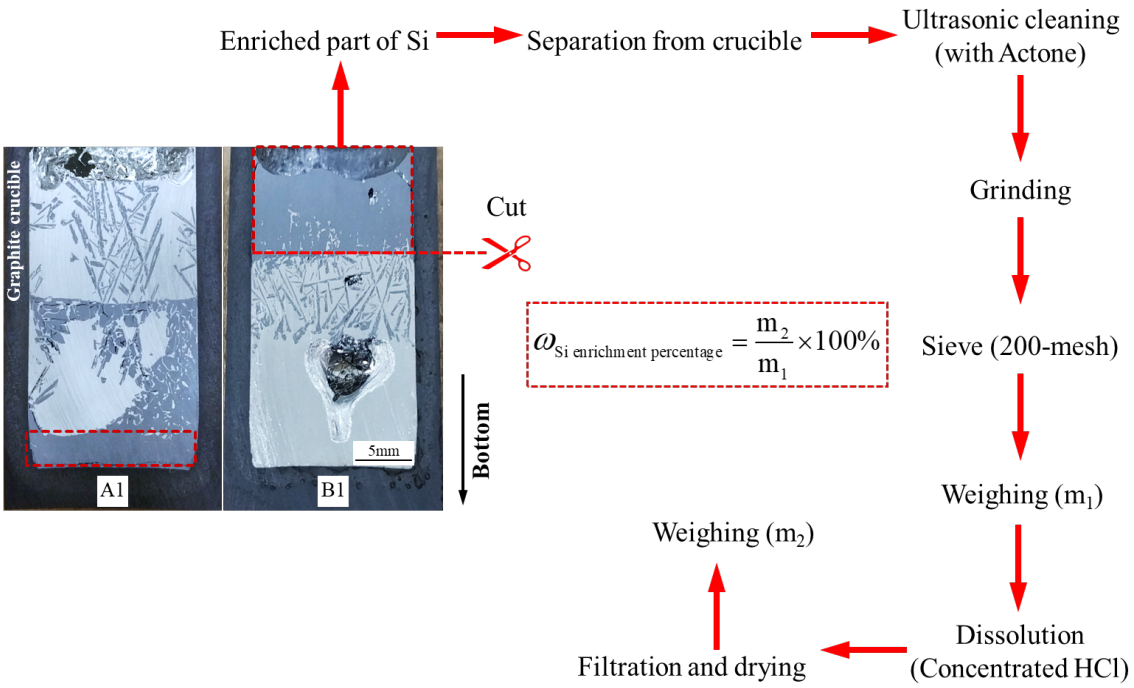

Fig. 2-4. Calculation process of Si enrichment percentage.

The sample was subsequently subjected to ultrasonic cleaning with acetone, ground into powders in an agate mortar, and then sifted using a 200 mesh sieve (particle diameter < 75 μm). Furthermore, the mass of the powder was precisely determined and recorded as m_1. Afterward, the powder was dissolved using concentrated HCl to remove Sn in the intergranular and liquid phases, followed by filtration and drying. The mass of the dried powder was also measured and recorded as m_2. Finally, the enrichment Si percentage could be calculated, using the following formula:

$$\omega = \frac{m_2}{m_1} \times 100\% \quad (2\text{-}1)$$

The dried Si powder was then dissolved using a mixture of HNO_3, H_2SO_4, and HF (HNO_3: H_2SO_4: HF = 5:2:5 in volume ratio, where HF was added dropwise to prevent the drastic reaction between Si and the acids) to analyse the incorporation of Sn into the solid Si using an inductively coupled plasma optical emission spectrometer (ICP-OES).

2.2.3. Analysis and Characterization

2.2.3.1 Microstructure Observation and Phase Composition Measurement by SEM-EDS

The alloy microstructure and composition were characterized by scanning electron microscopy (SEM, FE-SEM-S4200, Hitachi Corp, Japan) coupled with energy dispersive spectrometry (EDS). The picture of this machine is shown in Fig. 2-5, the observation of sample was conducted at 15 kV.

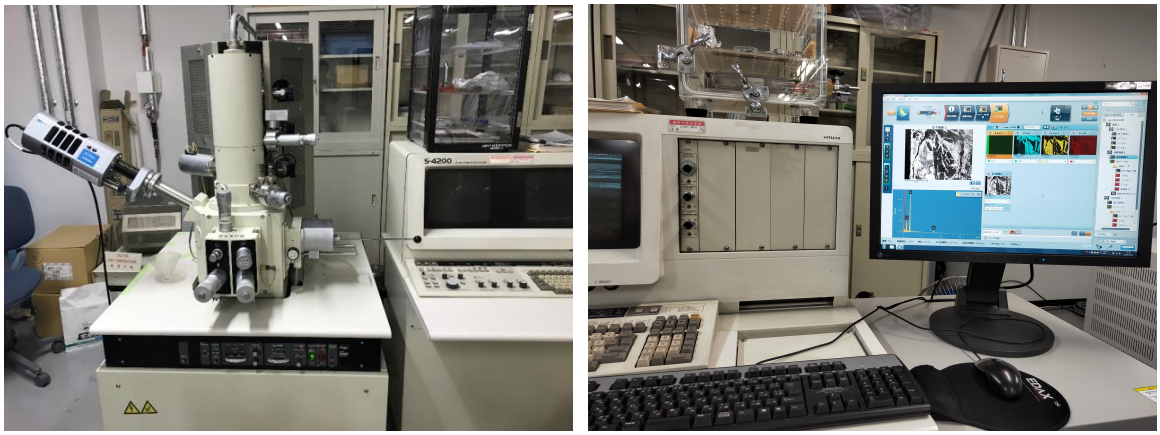

Fig. 2-5. SEM-EDS facility and computer operation window.

The preparation procedure of samples for SEM-EDS observation is described as following:

1. The as-annealed alloy was cut into pieces along the radial cross section to make sure the height of sample meets the requirement of SEM-EDS observation.
2. The sample was polished using a grinder for several times. The sandpapers used in each time were 100 #, 400 #, 800 #, 1200 #, 2000 #, consequently. Afterward, the sample was further polished using polishing cloth with diamond polishing liquid. The diameters of diamond particles were 3 μm, 1 μm, 0.25 μm, consequently.
3. After polishing, the sample was washed in the ultrasonic cleaner for 10 minutes, twice, using water in the first time and ethanol in the second.
4. Then the sample was dried in the stove at 200 ˚C for 10 minutes, in order to have unstable chemical contaminant vaporized.
5. The sample was kept in vacuum chamber for 24 h in order to remove volatile contaminant on the surface.

2.2.3.2 Crystal Orientation by EBSD

The Electron Back-Scattered Diffraction (EBSD) technique is widely used to measure the crystal orientation and local mis-orientation, which provide many useful

information for identifying the phase change process. Particularly, it is very helpful for identifying on which habit plane the grain was grown during solidification. Therefore, the EBSD observation was conducted for bulk Si zone of sample.

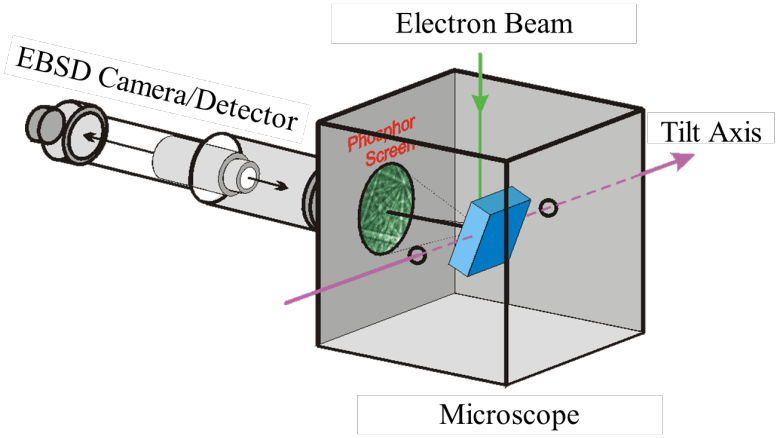

Fig. 2-6. Schematic diagram of working principle. [2-1]

Similar to XRD, the EBSD pattern is formed by diffractions between lattice planes but using electrons rather than X-ray, the working principle is shown in Fig. 2-6. Due to the much weak intensity of diffraction peaks, the EBSD observation requires a smaller surface roughness to prevent the background noise from morphological second electron reflection. Furthermore, the EBSD pattern is very sensitive to residual stress which causes the shift in lattice planes and weaken the diffraction intensity.

(a) **(b)**

Fig. 2-7. (a) Sample on holder in EBSD chamber and (b) observation scene.

Therefore, in order to reduce the surface roughness for a further step while not introducing residual stress, the sample was polished based on SEM samples prepared

afore, using silica polishing liquids, with particle sizes of 0.06 μm, and 0.02 μm, sequentially. The reason why using silica rather than diamond is that, the hardness of diamond is too large, which will introduce residual stress while polishing. After the sample polished, it was washed using ultrasonic cleaner with ethanol for 10 minutes, twice, and then dried on the stage stove at 200 ˚C to remove volatile chemicals contaminants. Fig. 2-7 shows the sample on holder inside EBSD device chamber and the picture of observation scene.

2.3. Results and Discussion

2.3.1. Dependence on Moving Directions and SEM-EDS Analysis

Initially, solidification was performed without moving process, and the primary Si tended to distribute at the upper part, but could not be enriched together so that generated across the whole sample (Fig. 2-8(I)-(O)). Afterwards, directional solidification was performed by moving the samples upwards and downwards at a 0.04 mm/min rate, respectively. This contributed to the distribution of primary Si at the top or bottom end of the samples (Fig. 2-8(I)-(B) and (A), respectively). Compared with Fig. 2-8(I)-(O), I concluded that when directional solidification was absent, primary Si failed to separate from the Sn-Si melt and just dispersed throughout the entire sample, even though there was a big difference in density between primary Si and the Si-Sn melt. It should be noted that one end of the sample would be enriched in Si after moving the sample upwards or downwards at a certain rate. Moreover, it seemed that the upwards directional solidification was more favourable to Si enrichment than the downwards one, based on surface topography.

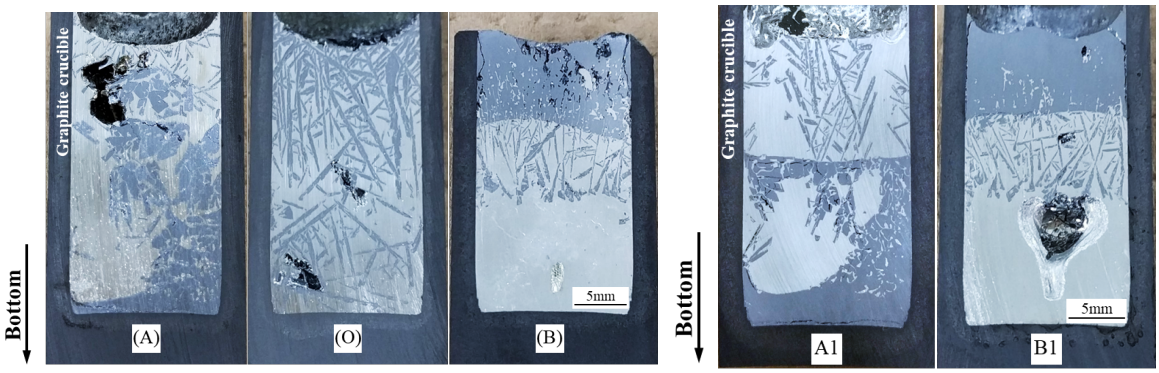

(I) (II)

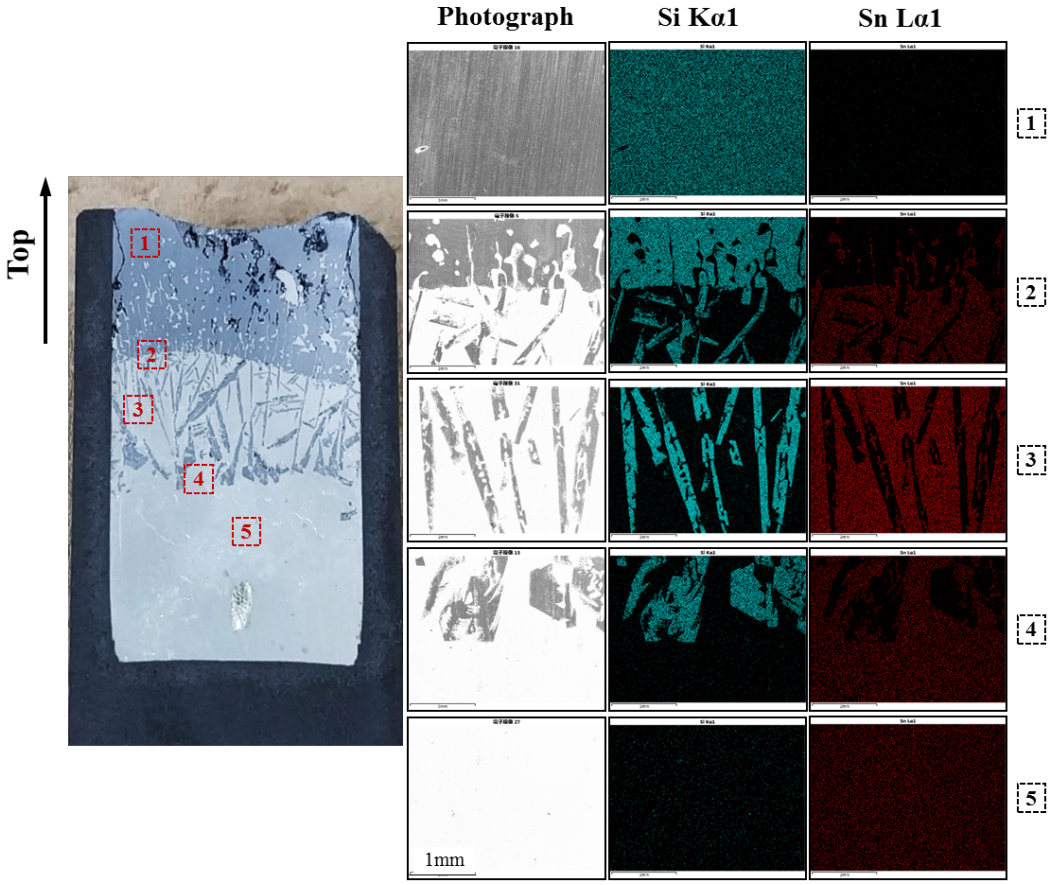

(III)

Fig. 2-8. Cross sections of samples under different moving directions using Si-50 at.% Sn alloy (I): (A) move-down at 0.04 mm/min rate, (O) without moving process, and (B) move-up at 0.04 mm/min rate; (II): (A1) move-down at 0.02 mm/min rate, and (B1) move-up at 0.02 mm/min rate; and (III) specular scanning by SEM at different area from top to bottom (photograph, Si Kα1, and Sn Lα1, respectively).

To confirm whether the upwards or downwards motion generated better enrichment results, upwards and downwards directional solidification experiments at slower moving rates (0.02 mm/min) were carried out. The cross sections of the samples are shown in Fig. 2-8(II)-(B1) and (A1), respectively. The experiment results showed that the amount of precipitated Si increased and Si floated upwards easily due to the buoyancy caused by the significant difference in density between solidified Si and liquid Si-Sn ($\rho_{Si(300\ K)} = 2.33\ g/cm^3$, [2-2] $\rho_{Sn(1555\ K)} = 6.32\ g/cm^3$ [2-3]) during the upwards process. It was difficult for primary Si crystals to grow and enrich during the downwards process, since Si had to overcome buoyancy. This was different from the directional solidification of the Al-Si alloy attributed to the

comparable density between solidified Si and liquid Si-Al ($\rho_{Si(300\ K)}$ = 2.33 g/cm^3, $\rho_{Al(1173\ K)}$ = 2.33 g/cm^3 [2-4]). It should be mentioned that the upwards process also involved a flat interface and a stable mushy-zone compared with the downwards process.

The sample in Fig. 2-8(I)-(B) was analysed using a SEM-EDS instrument to reveal the morphology changes of the solidified alloy. The SEM image and mapping analysis results are presented in Fig. 2-8(III). It was determined that the cross section of the sample consisted of three parts: a Si-rich zone, a mushy-zone (transition region), and a Sn-rich zone.

2.3.2. A Model to Explain the Force Analysis in Upwards and Downwards

Based on the experimental results and those obtained analysing the SEM-EDS images, a model was proposed to explain the crystal growth process and enrichment mechanism during directional solidification, as shown in Fig. 2-9(α) and (β).

According to the definition of Newtonian fluids, Stokes equation can be written as follows:

$$\nu = \frac{2(\rho_1 - \rho_2)gr^2}{9\eta} \tag{2-2}$$

where ν is the floating velocity of the primary Si particle, η is dynamic viscosity of the Si-Sn melt ($\eta_{(T>680K)} \approx$ 0.01268 Poise=0.001268 Pa·s)[2-5], ρ_1 is the density of the Si-Sn melt ($\rho_1 = \rho_{Si\text{-}Sn\ (1605\ K)} \approx$ 6.32 g/cm^3), ρ_2 is the density of the primary Si particle ($\rho_2 = \rho_{Si\ (300\ K)} \approx$ 2.33 g/cm^3), g is the acceleration of gravity, and r is the radius of the primary Si particle (0< r <7.5μm)[2-6].

$$\nu = \frac{2\times(6.32\text{-}2.33)\times10^3 \mathrm{Kg/m^3}\times 9.8\mathrm{m/s^2}\times r^2}{9\times1.27\times10^{-3} Pa\bullet s} \tag{2-3}$$

$$\nu = 0.377\times r^2 (mm/\min) \tag{2-4}$$

Here, the unit of r is μm. So, the floating velocity of Si particle depends on the radius of the primary Si particle is shown in Fig. 2-9(γ). From Fig. 2-9(γ), we can see that the influence of buoyancy is quite large during the solidification process, when the radius of the primary Si particle is 7.5 μm, the floating velocity is about 21mm/min.

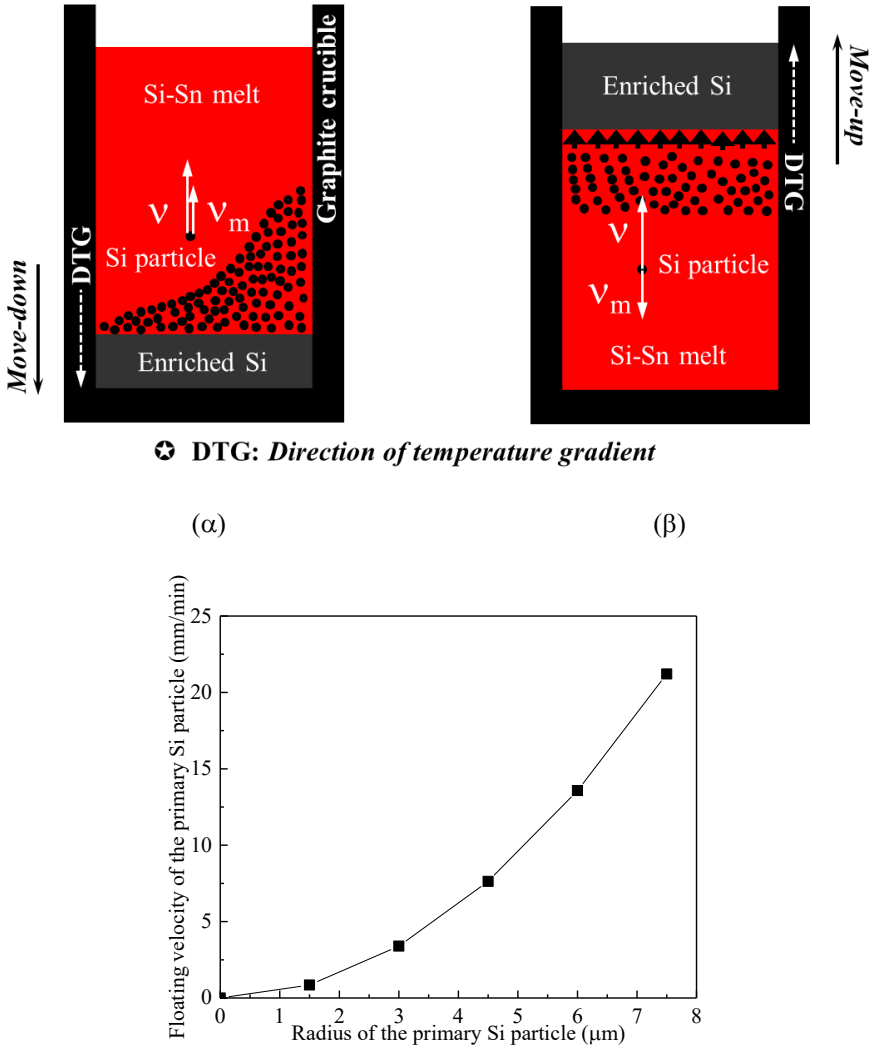

Fig. 2-9. Simulation diagram of enrichment mechanism during the downwards (α), upwards (β) directional solidification process, (γ) the floating velocity of the primary Si particle as a function of radius.

If the Si particle was selected as the research object and the Si-Sn melt as the reference system for the analysis, the following equations can be obtained:

Upwards process: $v_{up} = |v_m - v|$,

Downwards process: $v_{down} = |v_m + v|$ (2-5)

where v_m is the moving rate controlled by the stepping motor and v_{up} and v_{down} are the velocities of the primary Si particle moving back to the melted alloy during the upwards and downwards directional solidification processes, respectively. This shows that during the downwards process, according to the Archimedean principle, although buoyancy is greater in the deeper part of the melt, the critical nucleation

energy is lower in the beginning of the heterogeneous nucleation of C and Si, and the cohesive energy of C-Si is greater than that of Si-Si ($E_{\text{Si-C}}$ = 1.318 eV/atom > $E_{\text{Si-Si}}$ = 1.245 eV/atom). [2-7] Therefore, at the very beginning of the downwards process, Si particles can be concentrated as a thin layer at the bottom of a graphite crucible. In time, with the increase in the radius of the Si particle, the floating velocity became larger that force them to return to the melted alloy, which was detrimental for crystal growth and enrichment, and the Si particles could not be enriched in the front frozen Si layer eventually. This phenomenon was absent in the upwards process.

It should be noted that v_m is an important controllable factor affecting the enrichment rate. Therefore, the natural advantage of the Sn-Si system should be fully used during the upwards directional solidification process.

2.3.3. Dependence on Moving Rates for the Si Enrichment

After determining the advantage of the upwards motion in the separation mechanism and directional solidification process, the effect of the move-up rates on separation and enrichment efficiency was investigated, as shown in Fig. 2-10.

From Fig. 2-10, it can be seen that the samples obtained using the 0.01, 0.02, and 0.04 mm/min moving rates have flat interfaces, however, the interfaces became rough for the samples obtained using the 0.06, 0.08, and 0.10 mm/min moving rates. Meanwhile, the separation effect and enrichment percentage in the top parts of the samples became worse and lower, respectively.

This phenomenon was well consistent with Eq. (2-3), and can be explained as follows. During the directional solidification process, the cooling rate was estimated using the product of the moving rate and temperature gradient, *i.e.* Cooling rate (K/min) = Moving rate (m/min) × Temperature gradient (K/m). As the moving rate was increased from 0.01 to 0.10 mm/min, the cooling rate became higher and constitutional super cooling in the liquid phase was enhanced, which might have caused the nucleation of Si particles ahead of the growth interface.

It should be mentioned that large areas of quasi-bulk Si could be obtained when the upwards moving rates were 0.01 and 0.02 mm/min. Analysing the image in Fig. 2-10 (a) and (b), it can be verified that using the upwards process to obtain quasi-bulk Si from the Si-Sn alloy is feasible.

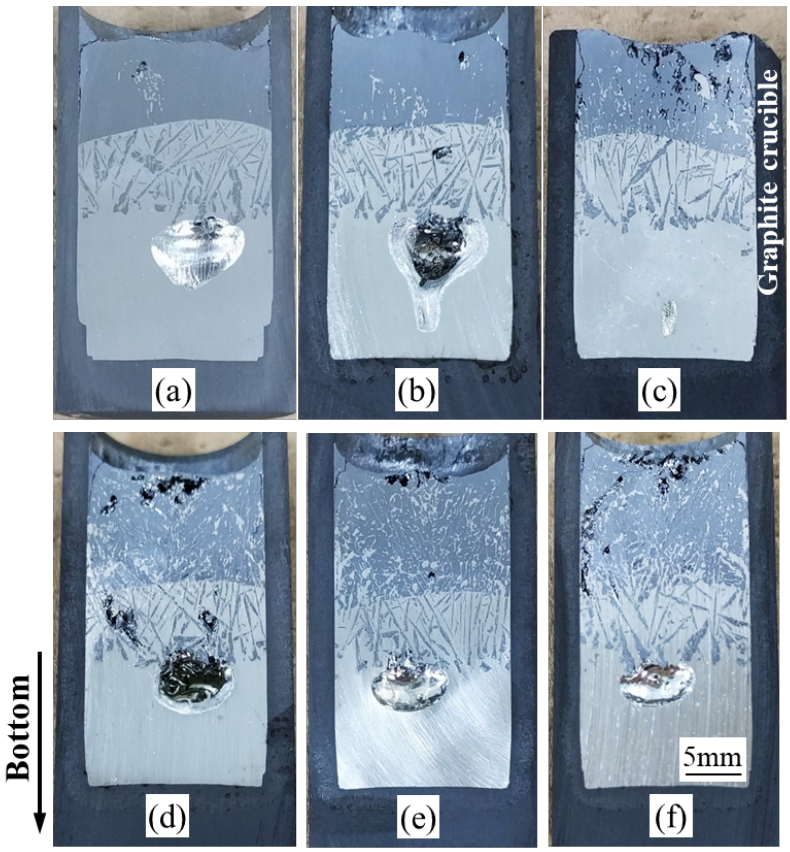

Fig. 2-10. Cross sections of samples at different move-up rates using Si-50 at.% Sn alloy (a) 0.01 mm/min, (b) 0.02 mm/min, (c) 0.04 mm/min, (d) 0.06 mm/min, (e) 0.08 mm/min, and (f) 0.10 mm/min.

2.3.4. Si Enrichment Percentage and Residual Sn Content

The SEM-EDS images before and after HCl leaching are shown in Fig. 2-11(i) and (ii), and detailed data of the Si enrichment percentage and Sn content are listed in Table 2-3.

The feasibility and validity of calculating the Si enrichment percentage by removing Sn from the intergranular and liquid phases using concentrated HCl was demonstrated in Fig. 2-11(i). Based on Fig. 2-11(ii), it can be seen that the Si enrichment percentage increased with the decrease of the moving rates, although the enrichment percentage of the 0.10 mm/min sample was slightly larger than that of the 0.08 mm/min sample. In addition, the upwards and downwards processes generated almost the same Si enrichment percentage at the 0.02 mm/min moving rate: 90.8%.

It should be noted that a bulk-Si area was only observed in the thin bottom section of the downwards sample, while a much larger bulk-Si area was obtained during the upwards process, the amounts of bulk-Si in the two samples being 0.8656 and 1.2670 g, respectively. It can be concluded that the upwards process was more favourable for Si enrichment than the downwards one, which is in agreement with the previous model analysis. Moreover, repeated experiments were also carried out to demonstrate the repeatability of the results, such as S-03 and S-04. Therefore, from an experimental point of view on both the amount of bulk-Si and the Si enrichment percentage, we demonstrated that the upwards process was better than the downwards one. The largest Si enrichment percentage reached was 98.6% at the 0.01 mm/min upwards moving rate.

Table 2-3. Si enrichment ratio and Sn content in enriched Si after HCl leaching under different conditions at temperature range from 1605 to 1505K using Si- 50 at.% Sn alloys.

Sample No.	Moving Rate (mm/min)	Moving Direction	Original Quality m_1(g)	After Dissolution m_2(g)	Si Enrichment Percentage w (%)	Sn content in Enriched Si (ppmw)	Sn molar fraction
S-01	0.01	Up	1.2839	1.2663	98.6	5582	0.00132
S-02	0.02	Up	1.2670	1.1504	90.8	6046	0.00143
S-03	0.04	Up	2.2415	1.7573	78.4	6666	0.00158
S-04	0.04	Up	1.2817	0.9845	76.8	6809	0.00161
S-05	0.06	Up	1.7120	0.9830	57.4	6706	0.00159
S-06	0.08	Up	2.6303	1.3342	50.7	6739	0.00160
S-07	0.10	Up	2.6271	1.4697	55.9	6874	0.00163
S-08	0.02	Down	0.8656	0.7861	90.8	6795	0.00161
S-09	0.04	Down	---	---	---	---	---
S-10	0	No	---	---	---	---	---

"---" No analysis,

S-03 and S-04 are the repeatability test experiments.

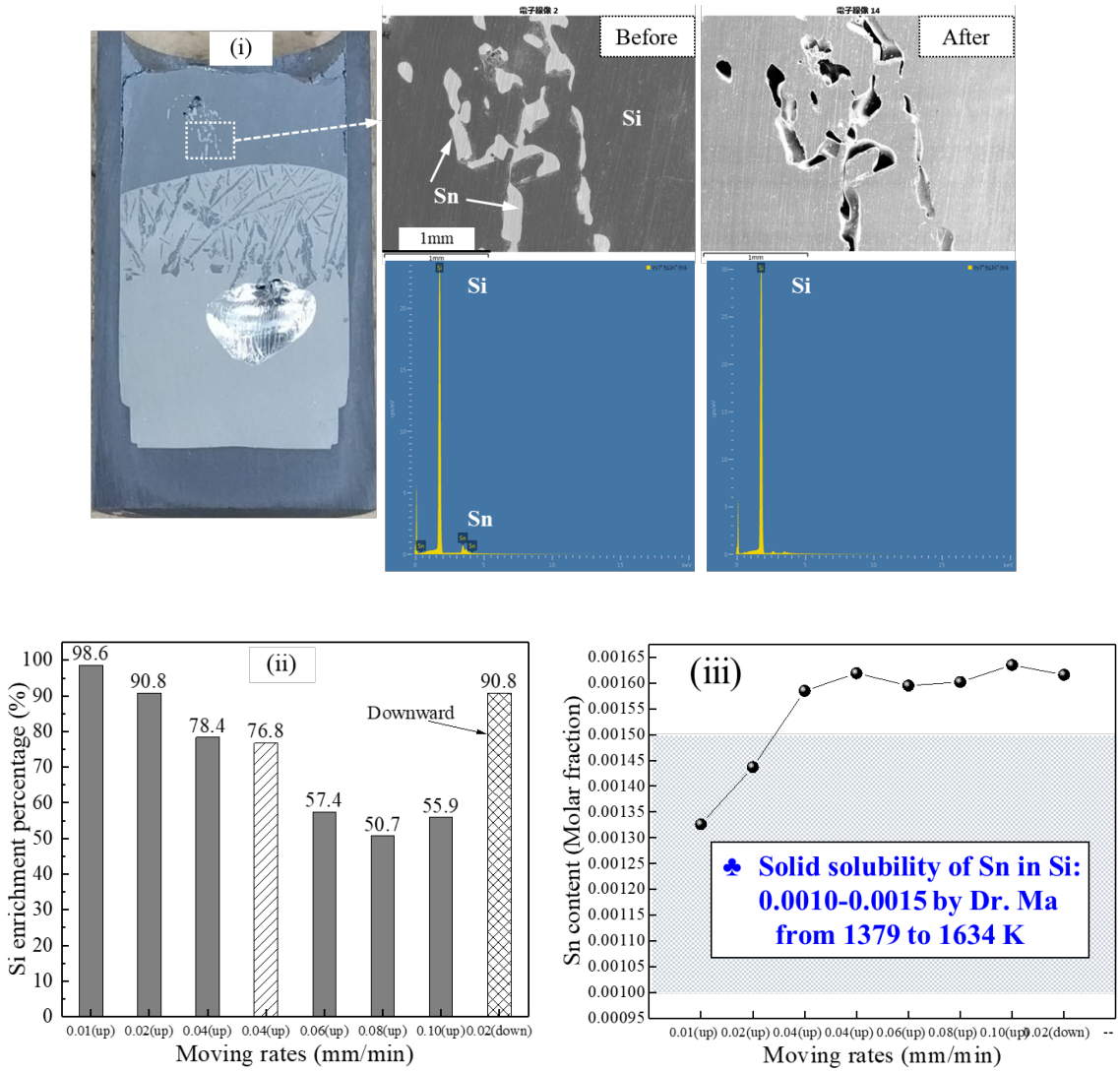

Fig. 2-11. (i) SEM-EDS images before and after HCl leaching, (ii) Si enrichment percentage, and (iii) relationship between the Sn in enriched Si and solid solubility of Sn in Si under different moving directions and at various rates.

Furthermore, the relationship between the Sn content (ppmw) and its molar fraction can be calculated using Eq. (2-6), and the results are shown in Fig. 2-11(iii):

$$\text{Molar fraction of Sn} = \frac{\dfrac{\text{Sn content}}{M_{\text{Sn}}}}{\dfrac{\text{Sn content}}{M_{\text{Sn}}} + \dfrac{\text{1-Sn content}}{M_{\text{Si}}}} \tag{2-6}$$

where $M_{\text{Sn}} = 118.71$ g/mol and $M_{\text{Si}} = 28.09$ g/mol are the molar masses of Sn and Si, respectively.

From Fig. 2-11(iii), it can be seen that the molar fraction of residual Sn in the enriched Si area changed from 0.00132 to 0.00163, which is similar with the solid

solubility of Sn in Si (0.0010-0.0015) as reported by Ma *et al*.. [2-8] This proved that after the HCl leaching of the Si enrichment area, the Sn content can be easily reduced to the level of the solid solubility of Sn in Si.

2.3.5. EBSD Analysis for Enriched Bulk Si

In order to observe the morphology of the obtained bulk Si and determine the orientation of crystal growth, EBSD analysis was carried out after fine polishing (specific sample making process has been introduced in the previous section 2.2.3.2), fine polished sample is shown in Fig. 2-12(a) and SEM image of an area of the sample in Fig. 2-12(b). Firstly, EDS was used to confirm the element distribution of Si and Sn, as shown in Fig. 2-13, it can be seen that the enrichment density of Si is very high. Moreover, the interface and the morphology of crystalline Si in the transition region can be clearly seen.

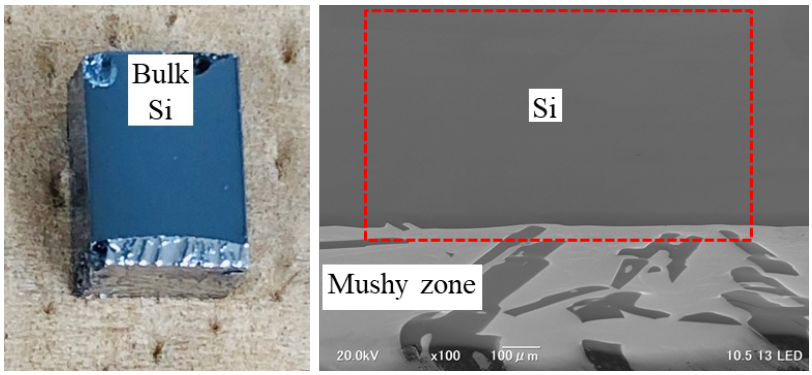

(a) **(b)**

Fig. 2-12. (a) Fine polished sample and (b) SEM image of the sample.

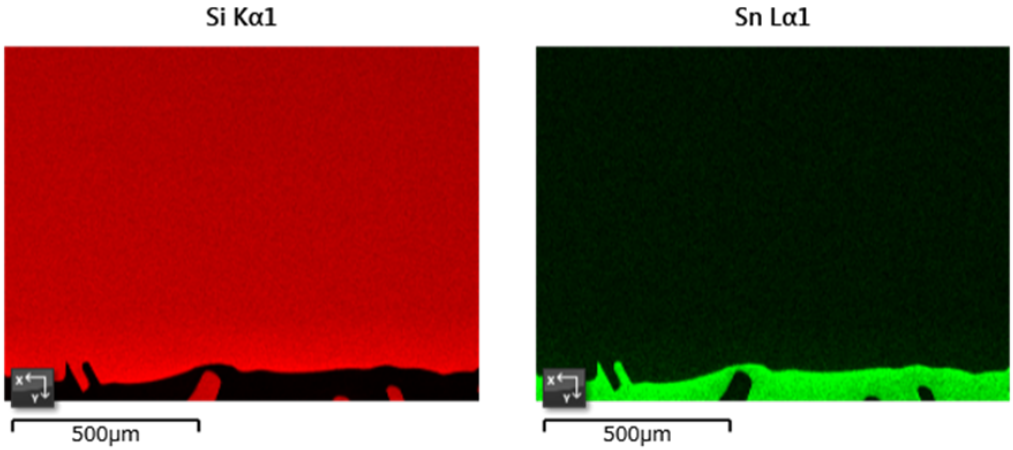

Fig. 2-13. EDS maps of Si and Sn.

Then EBSD maps was obtained, the Inverse Pole Figure (IPF) in Z axis direction is shown in Fig. 2-14. It can be seen that the bulk Si region is anisotropic, because the color difference of the IPF indicates the orientation difference of the crystal. And the preferred orientation of crystal growth is from crucible wall, which is different from the others which growing from Si-Sn alloy melt due to the temperature gradient and constitutional super-cooling. And the Si grain size which grown from the crucible wall direction is much larger. In other words, there are grain boundaries between different orientations, which indicate that the bulk Si obtained by this directional solidification method is polycrystalline Si rather than monocrystalline Si.

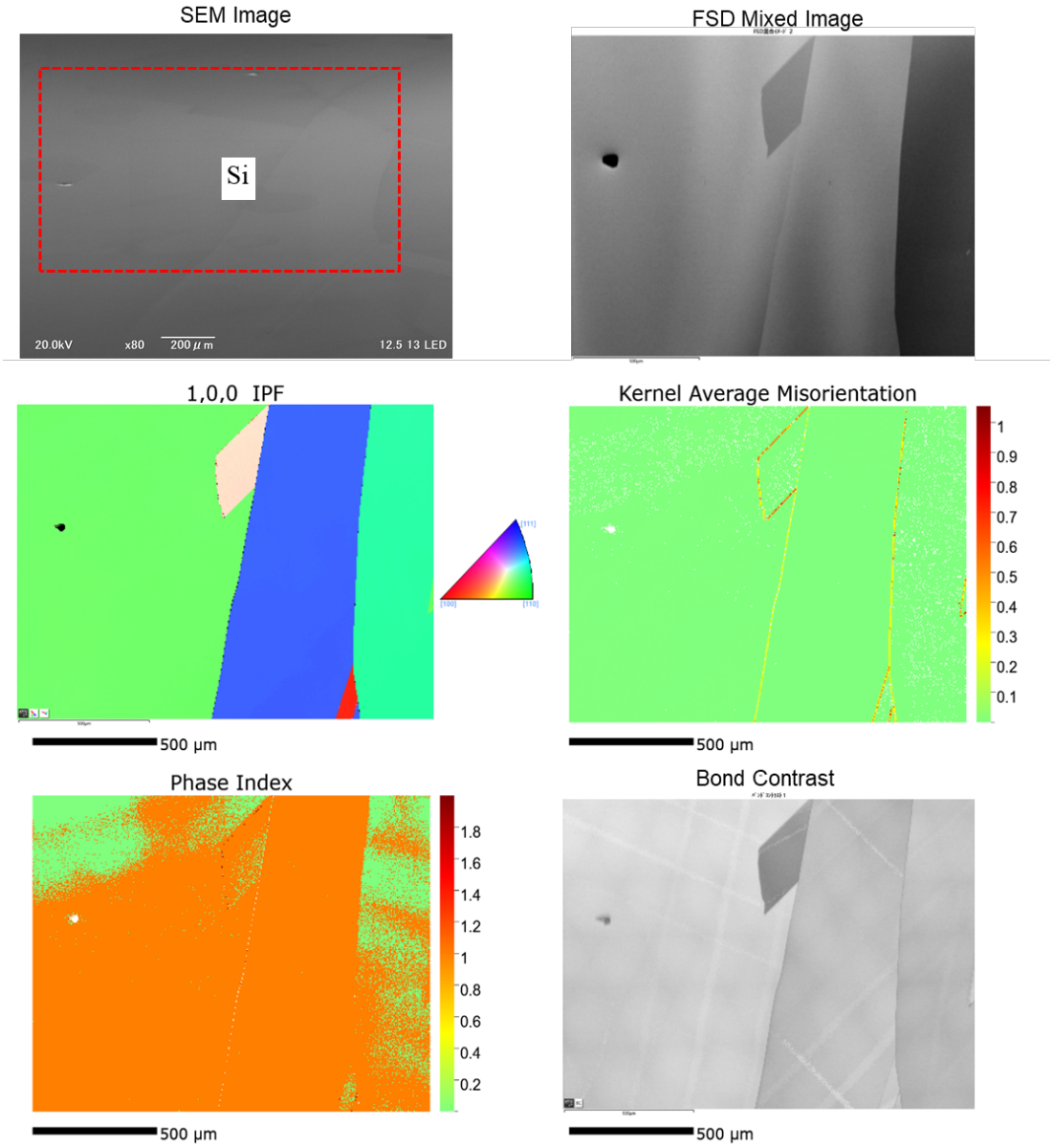

Fig. 2-14. SEM images and EBSD maps of enriched bulk Si zone.

The partial enlarged drawing of IPF and crystal plane of each local positions are shown in the Fig. 2-15 below. It can be concluded from the Fig. 2-15 that the crystal growth plane in the solidification process are [101], [102], [$11\bar{2}$], [001], and [111], based on Fig. 2-15 (i), the intersection angle of locally magnified positions can be determined, detailed shown as in Fig. 2-15 (g) and (h).

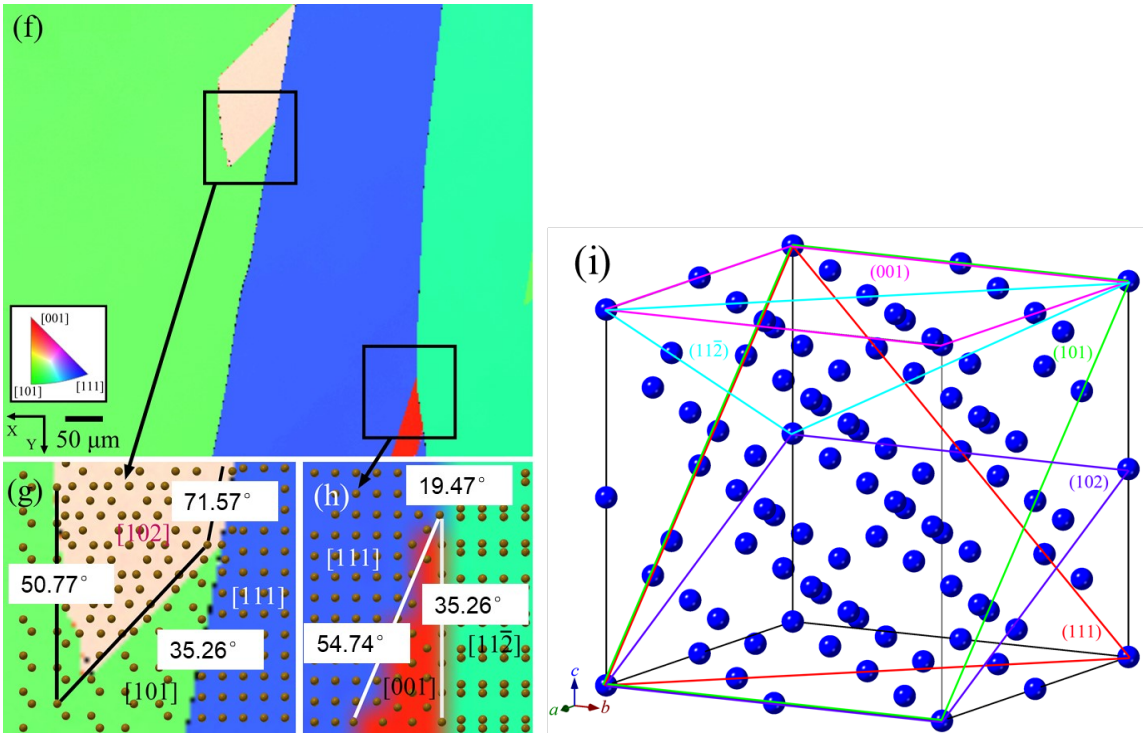

Fig. 2-15. (f) IPF (Inverse Pole Figure) Z Axis, (g) and (h) space lattices and intersection angle of locally magnified positions, (i) crystal plane (determine the intersection angle).

2.4. Simulation Model of Si Growth Process

To better explain the enrichment and growth process of primary Si in the directional solidification process, COMSOL Multiphysics 5.2 software was used to build a model and simulate the process.

The COMSOL Multiphysics is a cross-platform finite element analysis, solver and multiphysics simulation software, which allows conventional physics-based user interfaces and coupled systems of partial differential equations (PDEs). Here, three modules *i.e.*, heat transfer, fluid flow, and phase transition are coupled with each other. The specific equations and parameters of each module in the simulation process are shown in the following details.

2.4.1. Model Description

2.4.1.1. Heat Transfer

Conductive heat transfer was considered for all components of this model. Conduction dominates solid components (Si and crucible) while convection dominates liquid Si-Sn melt. The equation is given as Eq. (2-7); the first term on the left is the Fourier's law, and the following two terms are derived from the heat transfer differential equation and equation of continuity.

$$\rho c_p \frac{\partial T}{\partial t} + \rho c_p \mathbf{u} \cdot \nabla T + \nabla \cdot (-k \nabla T) = Q \tag{2-7}$$

Where ρ, c_p, T, t, $\mathbf{u}$, and k are the density [kg/m^3], specific heat capacity [J/(kg·K)], temperature [K], reaction time [s], two-dimensional axisymmetric velocity field, and thermal conductivity [W/(m·K)], respectively. Radiative transfer among all gray surfaces in the furnace is non-negligible, especially at a high temperature, and it can be represented by Eqs. (2-8) and (2-9), which are derived from the effective radiation formula.

$$\varepsilon(G - \sigma T^4) = -\mathbf{n} \cdot (-k \nabla T) \tag{2-8}$$

$$J = \varepsilon \sigma T^4 + (1 - \varepsilon) G \tag{2-9}$$

Where ε, G, σ, and J are the emissivity, irradiation [W/m^2], Stefan–Boltzmann constant [W/(m^2·K^4)], and radiosity [W/m^2], respectively.

2.4.1.2. Fluid Flow

Melts in the system are assumed to be the Newtonian fluid under laminar flow conditions; thus, according to N-S equations, the governing equations that express the convection of the Si-Sn melt and the velocity profiles are as follows:

$$\rho_i \frac{\partial \boldsymbol{\mu}_i}{\partial t} + \rho(\boldsymbol{\mu}_i \cdot \nabla)\boldsymbol{\mu}_i = \nabla \left[-\rho_i + \mu_i (\nabla \boldsymbol{\mu}_i + (\nabla \boldsymbol{\mu}_i)^T) - \frac{2}{3}(\nabla \cdot \boldsymbol{\mu}_i) \right] + \boldsymbol{F}_i \tag{2-10}$$

$$\frac{\partial \rho_i}{\partial t} + \nabla \cdot (\rho_i \boldsymbol{\mu}_i) = 0 \tag{2-11}$$

The volume force $\boldsymbol{F}$ consists of a gravitational acceleration vector and the temperature of the melt. The Si/crucible and alloy melt/crucible interfaces are rigid boundaries, which means that the crucible constraint is considered strictly.

2.4.1.3. Phase Transition

The release of latent heat was considered through the change in L (enthalpy). In addition, the specific heat capacity c_p also changes considerably during the transition. To account for the latent heat related to the phase transition, the c_p are

$$c_p = \frac{1}{\rho}(\theta_l \rho_l c_{p,l} + \theta_s \rho_s c_{p,s}) + L\frac{\partial \alpha_m}{\partial T} \tag{2-11}$$

and $\theta_l + \theta_s = 1$ (2-12)

where L is the latent heat of the transition and its value is L=1787 [kJ/kg]. α_m is the thermal expansion coefficient.

$$\alpha_m = \frac{1}{2}\frac{\theta_s \rho_s - \theta_l \rho_l}{\theta_l \rho_l + \theta_s \rho_s} \tag{2-13}$$

ρ and k are the density and thermal conductivity of the mixture during the phase transition, respectively, which are both estimated by linear relations:

$$\rho = \theta_l \rho_l + \theta_s \rho_s \tag{2-14}$$

$$k = \theta_l k_l + \theta_s k_s \tag{2-15}$$

In order to directly show the solid/liquid interface, the fraction of liquid phase is given by θ_l,

$$\theta_l = \begin{cases} 1, & T > T_m + \Delta T \\ \dfrac{T - T_m + \Delta T}{2\Delta T}, & T_m - \Delta T \le T \le T_m + \Delta T \\ 0, & T < T_m - \Delta T \end{cases} \tag{2-16}$$

Where T_m is the melting point and ΔT denotes the transition temperature span which in this case is set to 2 K.

2.4.2. Model Setting Conditions and Parameters

The boundary condition of temperature can be set according to the temperature distribution in the furnace, which can be established as Eq. (2-17).

$$\begin{aligned} T(z) = {} & 1611.08794 + 4.96708z - 1.14136z^2 - 0.04834z^3 \\ & -0.006000030690z^4 + 1.99995\times10^{-7}z^5 - 5.20524\times10^{-8}z^6 \\ & +6.95987\times10^{-9}z^7 - 4.69469\times10^{-10}z^8 + 1.26339\times10^{-11}z^9 \end{aligned} \quad (0 \le Z \le 10cm) \tag{2-17}$$

$$Z = (\nu, t) \tag{2-18}$$

Where v can be set as 0.01, 0.02, 0.04, 0.06, 0.08, 0.10 mm/min, which should be consistent with the upwards and downwards moving rates of the experiments, and *t* represents time.

The corresponding liquidus temperature T_m of different components (dependence on ω_{Sn}) are listed in Table 2-4.

Table 2-4. The corresponding liquidus temperature of different components. [2-9]

Temperature (K)	1787	1781	1780	1776	1769	1766	1748	1733	1728	1705
ω_{Sn}	0	0.00735	0.00991	0.0212	0.0364	0.0425	0.2	0.3	0.4	0.5
Temperature (K)	1700	1653	1643	1533	1473	1439	1429	1400	1373	1351
ω_{Sn}	0.6	0.7	0.8	0.9	0.9379	0.944	0.9546	0.9637	0.9699	0.9753
Temperature (K)	1335	1302	1251	1250	1199	1175	1164	1125	1080	505
ω_{Sn}	0.9766	0.9834	0.986	0.9888	0.99222	0.99224	0.9935	0.99609	0.9975	1

Here the relationship equation between the liquidus temperature and Sn composition can be obtained according to the shape of liquidus in different ranges, as shown in Eq. (2-19).

$$T_m\left(w_{Sn}\right)=\begin{cases} -6421.4{w_{Sn}}^3+3294.9{w_{Sn}}^2-593.12w_{Sn}+1687, & 0<w_{Sn}\le 0.2 \\ -3967.8{w_{Sn}}^4+7428.7{w_{Sn}}^3-5039.5{w_{Sn}}^2+1302.7w_{Sn}+1536.7, & 0.2<w_{Sn}\le 0.9 \\ -363809000{w_{Sn}}^5+1705760000{w_{Sn}}^4-3198540000{w_{Sn}}^3 & \\ +2998360000{w_{Sn}}^2-1405120000w_{Sn}+263348000+1940.2, & 0.9<w_{Sn}\le 0.9975 \\ -4.04412\times10^7{w_{Sn}}^2+8.05913\times10^7w_{Sn}-4.01495\times10^7-12, & 0.9975<w_{Sn}\le 1 \end{cases} \quad (2\text{-}19)$$

The properties of various materials involved in this simulation model are listed in Table 2-5 and its following equations.

For the solvent part of the Table 2-5, the properties of each parameter used are shown in the following equations.

$$k_{Sn}=11.43428+0.03384702T-5.119712\times10^{-6}T^2, 505<T<1550$$

$$k_{Si}=58.2+2.5\times10^{-2}\left(T-1730\right), 1687<T<1773$$

$$c_{p,\,Sn}=436.1506-0.8789032T+0.001578736T^2-1.454044\times10^{-6}T^3$$
$$+6.830016\times10^{-10}T^4-1.295004\times10^{-13}T^5, 505<T<1200$$

$$c_{p,\,Si}=908.7393, 1687<T<2000$$

$$\rho_{Sn} = 7319.324 - 0.6191594T - 1.473564\times10^{-4}T^2, 505 < T < 1650$$

$$\rho_{Si} = 3120.45 - 0.35T, 1687 < T < 2000$$

$$\alpha_{Sn} = 2.996454\times10^{-5} + 1.185385\times10^{-8}T + 8.872342\times10^{-16}T^2, 505 < T < 1400$$

$$\alpha_{Si} = 4.032438\times10^{-5} + 2.609376\times10^{-9}T + 4.857503\times10^{-13}T^2, 1687 < T < 2000$$

Table 2-5. The properties of various materials. [2-10 ~ 17]

Material	Thermal conductivity k [W/(m·K)]	Heat capacity at constant pressure c_p [J/(kg·K)]	Density ρ[kg/m³]	Ratio of specific heat γ	Coefficient of thermal expansion α [1/K]	Dynamic viscosity μ [Pa·s]
Graphite	100	1800	1710			
Silicon	393.8803 -0.980598T +9.947652×10^{-4} T^2 -4.55816×10^{-7}T^3 +7.898531×10^{-11}T^4 (900<T<1685)	769.4598 +0.1871751T -3.18396×10^{-5} T^2 (1000<T<1685)	2332.565 +0.003839515T -5.433308×10^{-5}T^2 +4.287211×10^{-8}T^3 -1.366545×10^{-11}T^4 (293<T<1685)	1	5e-5	
Solvent	$\omega_{Sn}\cdot k_{Sn}+\omega_{Si}\cdot k_{Si}$	$\omega_{Sn}\cdot c_{p,Sn}+\omega_{Si}\cdot c_{p,Si}$	$\omega_{Sn}\cdot\rho_{Sn}+\omega_{Si}\cdot\rho_{Si}$	1.1	$\omega_{Sn}\cdot\alpha_{Sn}+\omega_{Si}\cdot\alpha_{Si}$	0.0012

2.4.3. Model Results and Explanation for Solidification Mechanism

When all the parameters are input into the corresponding module, the whole process diagram of Si crystallization and growth can be generated, the final state of phase distribution and flow field distribution during upwards and downwards are shown in Fig. 2-16. The state diagram of the growth and enrichment of primary Si in different days during the 0.01 mm/min upwards moving experiment are shown in Fig. 2-17.

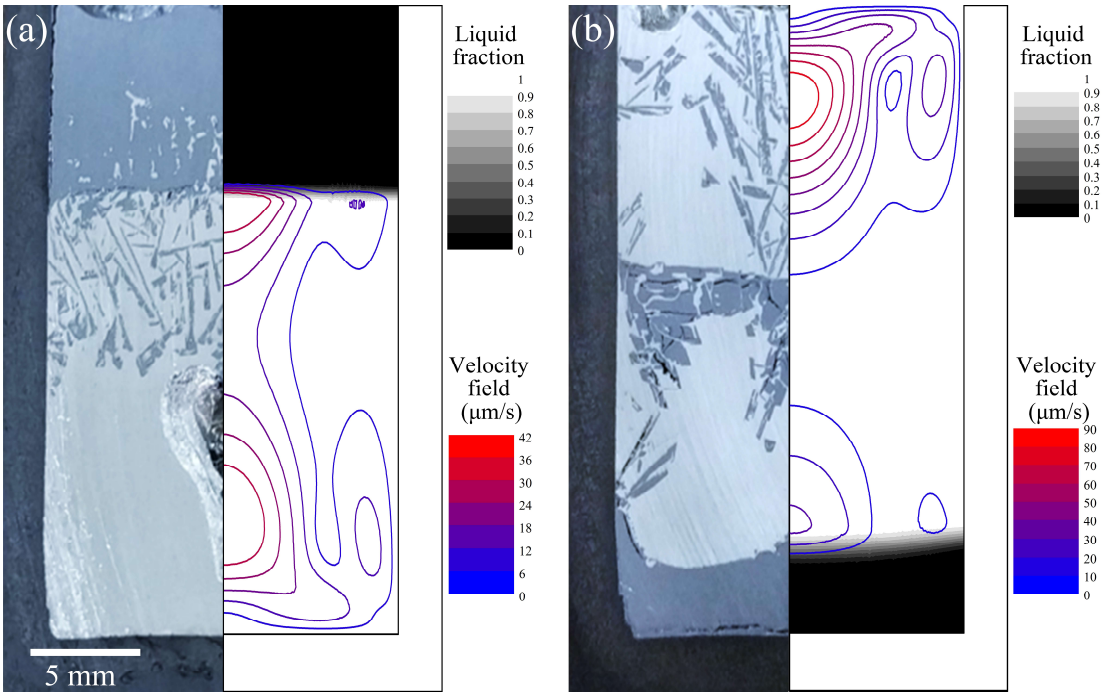

Fig. 2-16. Final state of phase distribution and flow field distribution (a) upward; (b) downward.

Through the comparison of the flow field of the upward and downward shown in Fig. 2-16, it can be seen that the flow rate in the melt during the downward process (90 μm/s) is almost twice of that during the upward process (42 μm/s), which makes it easier for primary Si crystal to be re-entangled into the melt, which is not conducive to Si enrichment to obtain a large area of bulk Si. This is consistent well with the previous experimental results, which also proved that the upwards moving process method is easier to obtain large area of bulk silicon than the downwards moving process from Si-Sn melt from simulation perspective.

Furthermore, through the process simulation diagram Fig. 2-17, it can be seen that when the solid-liquid interface is gradually pushed to the middle of the crucible, the mushy area (*i.e.*, the area where the solid-liquid phase coexists) will become wider, as shown in Fig. 2-17(c). At this time, the interface will become unstable and prone to defects (grain boundaries and dislocations, as shown in the Fig.s 2-14 and -15). If the upwards moving rate is too fast in this process, the mushy area will become larger, and then some liquid Sn will be solidified and remained in the enriched solid Si part because it is too late to return to the melt, resulting in the decrease of the density of the enriched Si (as shown in the Fig. 2-10).

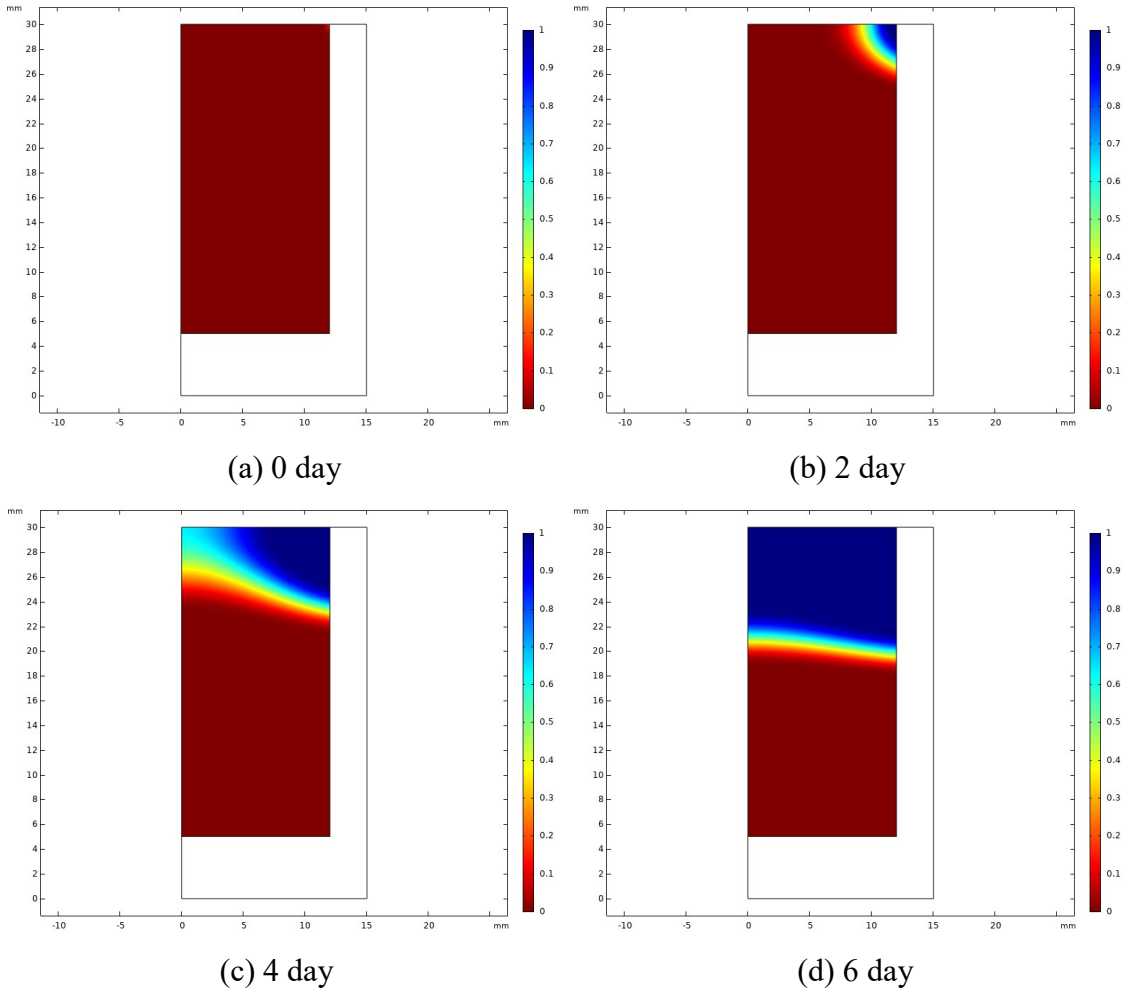

(a) 0 day (b) 2 day

(c) 4 day (d) 6 day

Fig. 2-17. The state diagram of the growth and enrichment of primary Si in different days during the 0.01 mm/min upwards moving experiment.

2.5. Short Summary

In summary, a refining process employing a Si-Sn solvent system using directional solidification was studied for effectively controlling the growth and enrichment of Si crystals. Meanwhile, a model was established to explain the crystal growth process and enrichment mechanism.

The following conclusions were drawn: (1). The upwards process was more favourable than the downwards one: the amount of precipitated Si increased and floated upwards easily due to the buoyancy caused by the significant difference in density between solidified Si and the Si-Sn melt during the upwards process; (2). The Si enrichment percentage increased with the decrease of the moving rates. The largest Si enrichment percentage reached 98.6% at the 0.01 mm/min upwards

moving rate; (3). After HCl leaching, the residual Sn (molar fraction) in the enriched Si area could be easily reduced to the 0.00132-0.00163 range, which was almost the same as the range of the solid solubility of Sn in Si; (4). The obtained bulk Si is polycrystalline Si, and the priority growth direction is from crucible wall; and (5) a model was established to simulate the Si growth process using COMSOL Multiphysics 5.2, which explained the defects (grain boundaries and dislocations) formation and residual Sn content in the enriched Si part dependence on the width of S/L interface, caused by the moving rate.

The most critical first step for using Si based alloy solvent refining to produce SOG-Si was analysed in this study.

References

2-1 https://wenku.baidu.com/view/771a7f51aeaad1f347933f8d.html (accessed November 6, 2019).

2-2 http://www.rsc.org/periodic-table/element/14/silicon (accessed November 6, 2019).

2-3 B.B. Alchagirov and A.M. Chochaeva, Temperature dependence of the density of liquid tin. *High Temp.*, 38 (2000) 44-48.

2-4 M.J. Assael, K. Kakosimos, R. M. Banish, J. Brillo, I. Egry, R. Brooks, P.N. Quested, K.C. Mills, A. Nagashima, Y. Sato and W.A. Wakeham, Reference Data for the Density and Viscosity of Liquid Aluminum and Liquid Iron. *J. Phys. Chem. Ref. Data*, 35 (2006) 285-300.

2-5 H.R. Thresh and A.F. Crawley, The Viscosities of Lead, Tin, and Pb-Sn Alloys, *Metall. Trans.*, 1 (1970) 1531–35.

2-6 R. Wang, W. Lu, and L.M. Hogan, Growth morphology of primary silicon in cast Al–Si alloys and the mechanism of concentric growth, *J. Cryst. Growth*, 207 (1999) 43-54.

2-7 J. Wang, K. Zhang and X. Xie, Pair potentials for C-C, Si-Si and Si-C from inversion of the cohesive energy. *J. Phys.: Condens. Matter*, 6 (1994) 989-996.

2-8 X.D. Ma, Doctoral dissertation, *The University of Tokyo*, 2012, Chapter 2, p. 42-43.

2-9 Landolt-Börnstein, *Group IV Physical Chemistry* 5J, (Pu-Re – Zn-Zr) https://materials.springer.com/lb/docs/sm_lbs_978-3-540-70705-9_2730.

2-10 C.A. Swenson, *Journal of Physical and Chemical Reference Data*, 12 (1983) 179.

2-11 P.D. Desai, *Journal of Physical and Chemical Reference Data*, 15 (1986) 967 and K.K. Kelley, *US Bureau of Mines*, Bulletin No. 476 (1949); available online at pbadupws.nrc.gov/docs/ML1212/ML12124A257.pdf

2-12 W. Hemminger, *High Temperatures-High Pressures*, 17 (1985) 465.

2-13 C.Y. Ho, R.W. Powell and P.E. Liley, *Journal of Physical and Chemical Reference Data*, 1 (1972) 279.

2-14 B.J. McBride, S. Gordon and M.A. Reno, *NASA Technical Paper* (1993) 3287.

2-15 L.B. Pankratz, *US Bureau of Mines* Bulletin (1982) 672.

2-16 W.D. Drotning, *High Temperature Science*, 11 (1979) 265.

2-17 Y.S. Sung, H. Takeya, K. Hirata, K. Togano, *Applied Physics Letters*, 83 (2003) 1122.

Chapter III. Zr/ Ti Addition on B-removal Behavior in Si-Sn Solvent

3.1. Introduction

In Chapter II, the most critical first step for using Si-Sn alloy solvent refining to produce large area of bulk Si has been studied. It is worth mentioning that additives such as Ti and Zr in Si-Sn alloys may affect Si refining, which will be further disscussed in this Chapter.

3.2. Theoretical analysis

Si-Sn solvent was selected because of its unique advantages, which have been elaborated in our previous study. [3-1] More importantly, B became thermodynamically more unstable in the case of Si-Sn alloy melts. [3-2] Therefore, if B can be removed by adding small amounts of additives that have strong affinity for B to enhance the formation and precipitation of intermetallic compounds, it would be more effective and practical.

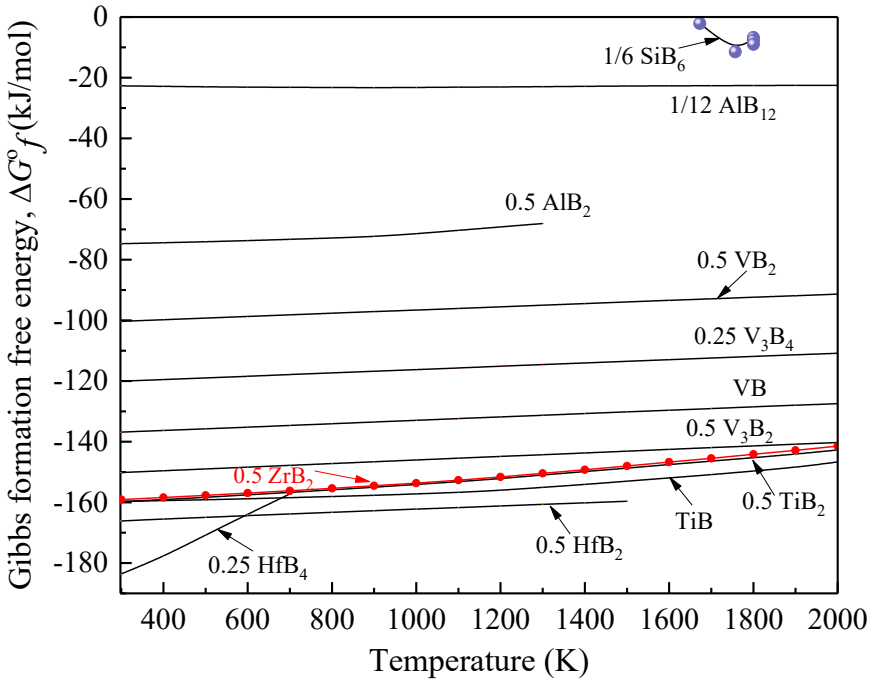

Fig. 3-1. Ellingham diagram for some borides. [3-3]

Note that Ti, discovered by Yoshikawa *et al.*, was proved to work as such an additive in the Si-Al melts, forming a thermodynamically stable compound, TiB_2 [3-4]. The B content in refined Si was reduced from 170 to 1.1 ppma by 933 ppma Ti addition. Similarly, Zr was verified as a more effective additive in improving B removal than Ti in Si-Al melts by Lei *et al.*. [3-5]

With the above background on additives in Si-Al melts, this study employs Zr/Ti as an impurity getters owing to their following merits: (i) they have strong affinity for B, [3-3] as shown in Fig. 3-1, which enhance the formation of boride; (ii) their segregation coefficients are very small (Zr $\rightarrow 1.6 \times 10^{-8}$, Ti $\rightarrow 2.0 \times 10^{-6}$ at 1687 K); [3-6] and (iii) their solid solubilities in Si are negligible (less than 0.0001 ppma below 1273 K) [3-7]. Hence, they can be eliminated simultaneously with other impurities after the Si purification process and will not contaminate the Si. Based on these, this study aims at clarifying the effect of the Zr/Ti additive on B-removal behavior from Si in solidification refining with Si-Sn solvent.

3.3. Experiment

3.3.1. Pre-melting of Si-1 mass% B and Si-1 mass% Zr/Ti Alloys

Initially, a high-frequency induction furnace (50 kHz) was used to pre-melt Si-1 mass% B and Si-1 mass% Zr/Ti alloys. The schematic of this apparatus is shown in Fig. 3-2. Certain amounts of bulk Si, lump B, and shot Zr were accurately weighed in proportion.

The samples were placed in an A-type high-purity dense graphite crucible. Firstly, the air in the quartz chamber was evacuated by a vacuum pump (extreme pressure is below 6 Pa), and then filled with Ar gas at a flow rate of 200 ml/min to prevent the melt from being oxidized. The surface temperature of the Si-1 mass% B and Si-1 mass% Zr/Ti melt was monitored by a dual-wavelength infrared pyrometer through a prism. The compositions of Si-1 mass% B and Si-1 mass% Zr/Ti alloys were reconfirmed using an inductively coupled plasma optical emission spectrometer (ICP-OES). After reconfirmation, these two types of alloys were used as raw materials for subsequent experiments.

The sizes of various materials and purity of various substances used in the experiment are listed in Table 3-1 and 3-2, respectively.

Table 3-1. Sizes of various materials used in the experiment (mm).

Material	Outside diameter	Inside diameter	Length
A-type graphite crucible	30	24	50
B-type graphite crucible	20	14	70
C-type graphite crucible	20	14	50
Quartz chamber	60	54	400
Alumina reaction tube	30	24	1000

Table 3-2. Purity of various substances.

Substance	Form	Purity
Si	Bulk	6N
Sn	Grains	99.9%
B	Lump	99.8%
Zr	Shot	99.6%
Ti	Sponge	99.5%
Ar	Gas	99.99%

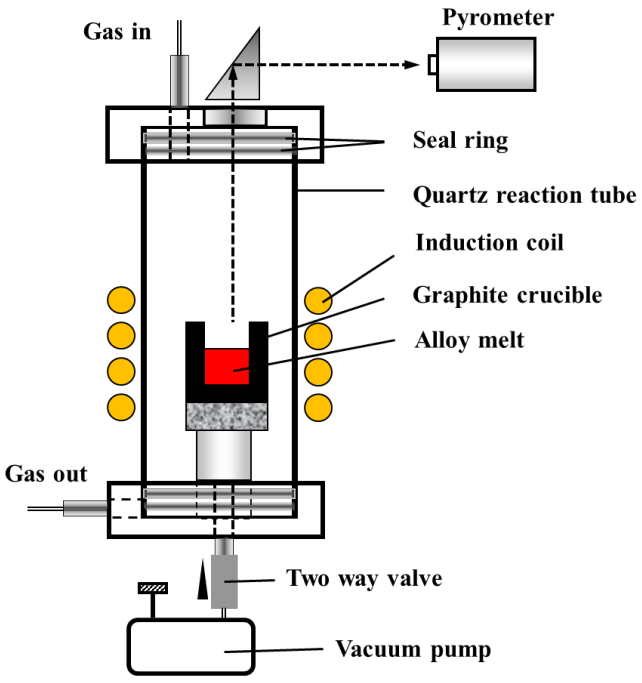

Fig. 3-2. Schematic of the induction furnace for pre-melting experiment.

3.3.2. Directional Solidification Refining of Si from Si-Sn Melt

30 g of bulk Si and Sn grains, together with different amounts of pre-melted Si-1 mass% B and Si-1 mass% Zr/Ti alloys, were placed in a B-type graphite crucible to prepare the Si-Sn alloys. Subsequently, the crucibles were put into an alumina reaction tube of a SiC electric resistance furnace. The furnace combined with a vertical motion system controlled by a stepping motor, which was used to carry out the directional solidification experiments, as shown in Fig. 3-3. The CO_2, H_2O, and O_2 in the Ar gas were eliminated by passing the gas through soda lime, silica gel, magnesium perchlorate, and magnesium turnings (heated at 823 K) successively. The sample in the alumina reaction tube was maintained above the liquidus temperature of alloys for 1 h in an Ar atmosphere to ensure that it was melted uniformly.

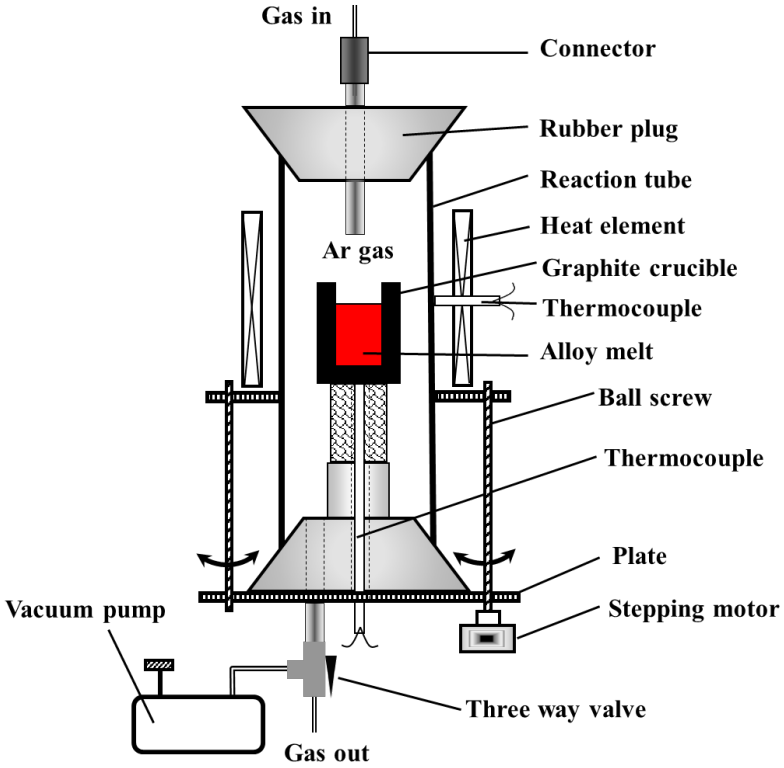

Fig. 3-3. Schematic of the experimental apparatus for directional solidification.

Then, directional solidification was carried out at the rate of 0.01−0.10 mm/min under the temperature gradient of 10^3 K/m. The temperature of the furnace was calibrated with a standard B-type thermocouple, and the temperature profiles during the solidification process are shown in Fig. 3-4.

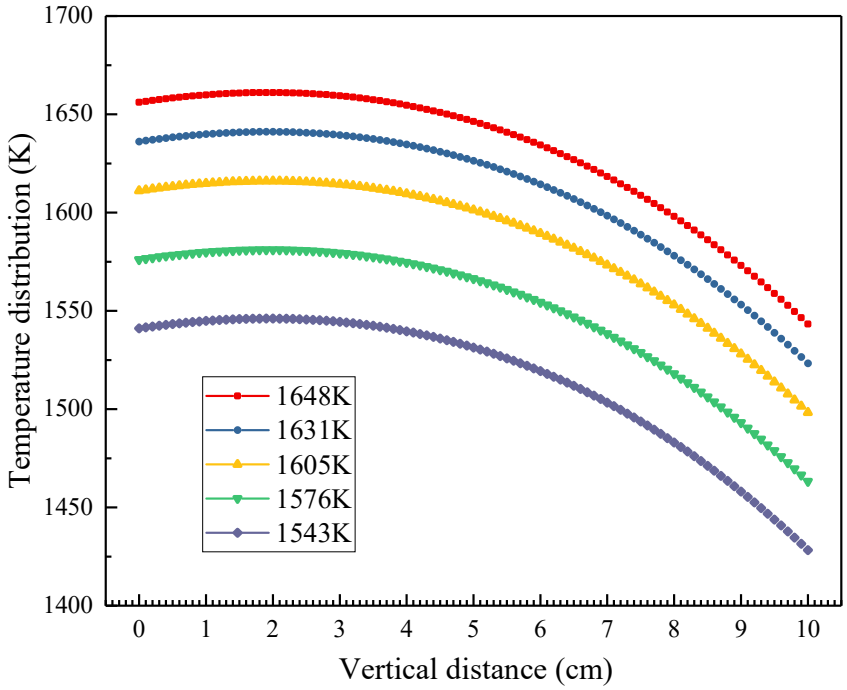

Fig. 3-4. Temperature profiles during solidification process for different Si-Sn alloys.

The samples were cut open along the longitudinal section when the solidification was completed. After polished using standard metallographic techniques, a digital camera and a scanning electron microscope equipped with an energy-dispersive spectrometer (SEM-EDS) were used to observe the macro and micro structures of the solidified samples, respectively.

The enriched Si part was cut off along the interface, subsequently subjected to ultrasonic cleaning with acetone, ground into powders in an agate mortar, and then sifted using a 200-mesh sieve. Furthermore, the powder was pickled using concentrated mixed acids, including HCl and HF (HCl: HF = 1:1 in volume ratio), to remove Sn and impurities (B, Zr/Ti) in the intergranular and liquid phases, followed by filtration and drying.

Afterward, the dried Si powder was dissolved using a mixture of HNO_3, H_2SO_4, and HF (HNO_3: H_2SO_4: HF = 5:2:5 in volume ratio, where HF was added drop by drop to prevent a drastic reaction between Si and the acids) to analyse the B, Zr/Ti, and residual Sn content in the refined Si part using the ICP-OES. The flowchart of the sample analysis is shown in Fig. 3-5.

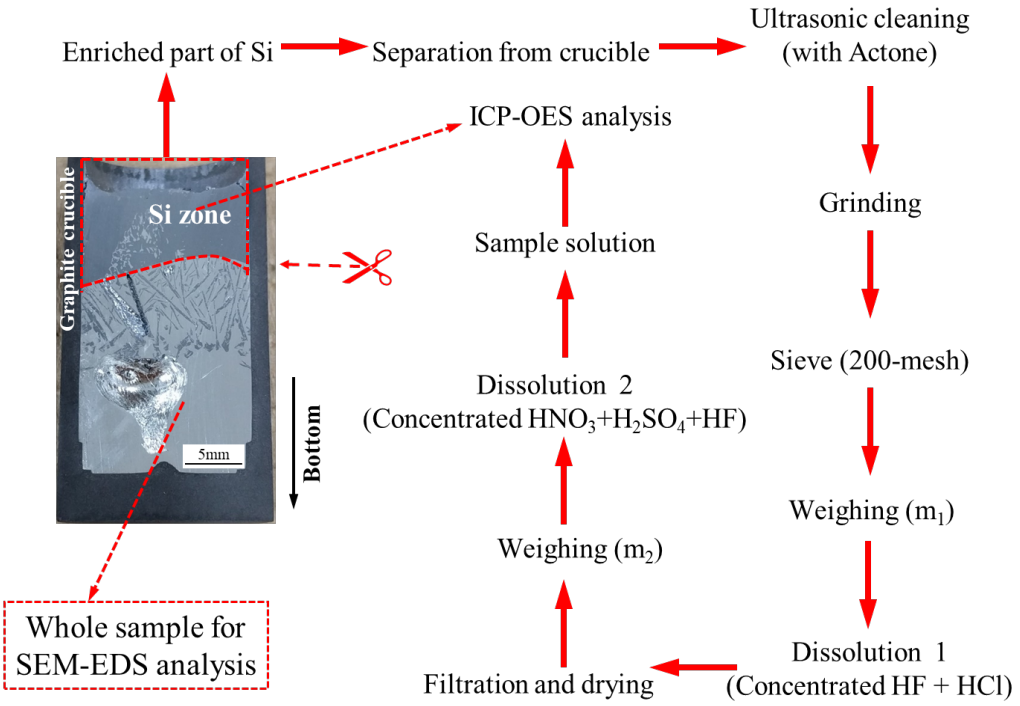

Fig. 3-5. Flowchart of sample analysis.

3.3.3. Measurement of Solubility Product (Ksp) of Zr and B in Si-Sn Melt

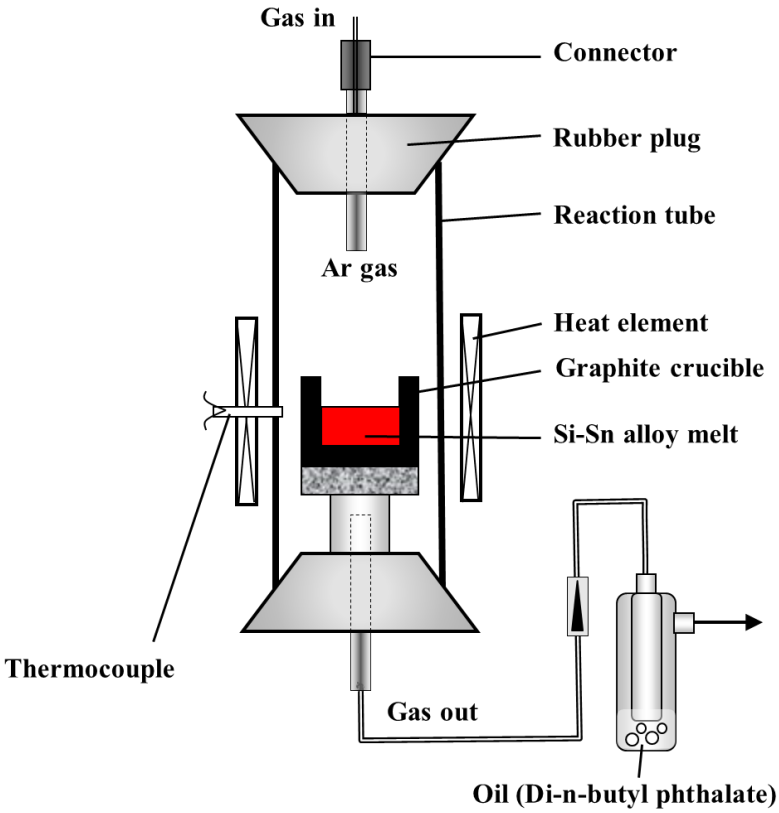

Fig. 3-6. Schematic of the SiC electrical resistance furnace for equilibrium experiment.

The SiC electrical resistance furnace shown in Fig. 3-6 was employed to perform the thermodynamic equilibrium experiments. 20 g of bulk Si and Sn grains, together with different amounts of pre-melted Si-1 mass% B and Si-1 mass% Zr alloys, were placed in a C-type graphite crucible to prepare the Si-Sn alloys containing certain amounts of B and Zr.

Equilibrium was attained by holding the Si-Sn-Zr-B melt at 1605 and 1575 K (Si-50 at.% Sn at 1605 K, and Si-65 at.% Sn at 1575 K to ensure that their liquidus temperature are slightly exceeded), in the Ar atmosphere, for 12 h. The sample was gradually cooled to room temperature, controlled by approximately 200 K/h. Then, SEM-EDS analysis was carried out to observe the B and Zr distribution behavior and ICP-OES analysis was performed to obtain the content of B and Zr in the Si-Sn alloy after equilibrium.

3.4. Results and Discussion of Adding Zr

3.4.1. Relations Among X_B, γ_B, and k_B in Si-Sn Melt

The activity coefficients of Zr and B in Si-Sn melt were calculated by FactSage based on the FT Lite database. Following are the set values of each parameter: temperature at 1687 K (melting point of Si), molarity of Zr (<0.002), and molarity of B (<0.002). Zr and B in the Si-Sn melt in this composition range can be regarded as an ideal dilute solution, which was considered to obey Henry's law. Fig.s 3-7 and 8 are drawn based on the calculated data.

Fig. 3-7 shows that the activity coefficient of B (γ_B) increases significantly, especially when the molar fraction of Sn is higher than 0.9, which can ultimately reach 1225 in pure Sn melt. This is well-consistent with the values measured by Ma *et al.* [3-8].

To clarify the relation of the thermodynamic parameters for each element, I hereby choose B as an example to determine the relations among the solubility of B (X_B), activity coefficient of B (γ_B), and segregation coefficient of B (k_B) in Si-Sn melt.

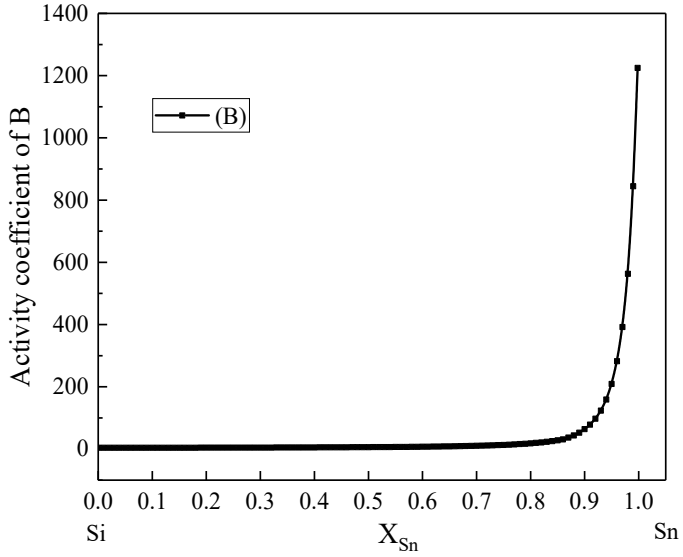

Fig. 3-7. Activity coefficient of B in Si-Sn melt at 1687 K.

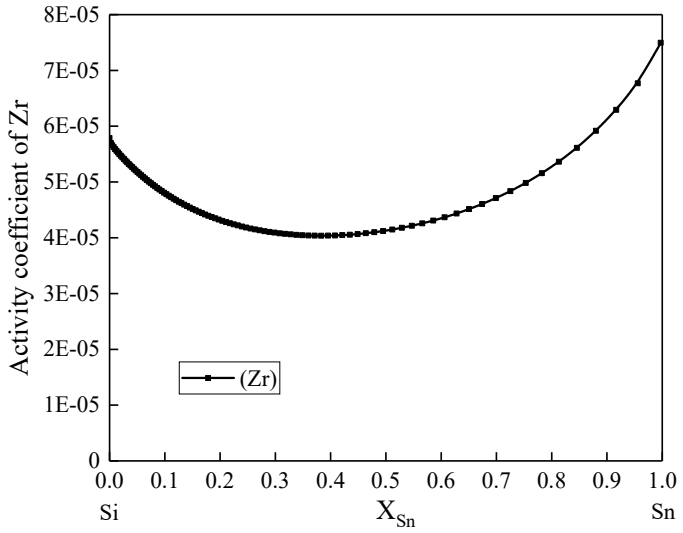

Fig. 3-8. Activity coefficient of Zr in Si-Sn melt at 1687 K.

The fusion reaction of B in the Si-Sn melt can be expressed by Eq.s (3-1) and (3-2). At equilibrium, the chemical potential of B in Si-Sn melt is equal to that in the solid phase, as shown in Eq. (3-3). Eq.s (3-4) can be obtained by deforming Eq. (3-3). Finally, the segregation coefficient of B between solid Si and Si-Sn melt can be expressed as Eq. (3-5).

$$\mathrm{B(s)}_{\text{in solid Si}} = \mathrm{B(l)}_{\text{in Si-Sn melt}} \tag{3-1}$$

$$\Delta G_{\mathrm{l}}^{o\,fus} = 50184 - 21.82T \ (J/mol) \ [3\text{-}9] \tag{3-2}$$

$$G^{\mathrm{o}}_{\mathrm{B\,(s)}} + RT\ln a_{\mathrm{B\,(s)\ in\ solid\ Si}} = G^{\mathrm{o}}_{\mathrm{B\,(l)}} + RT\ln a_{\mathrm{B\,(l)\ in\ Si\text{-}Sn\ melt}} \tag{3-3}$$

$$\Delta G_{\mathrm{l}}^{\mathrm{o}\,fus} = -RT\ln\frac{a_{\mathrm{B(l)\ in\ Si\text{-}Sn\ melt}}}{a_{\mathrm{B(s)\ in\ Solid\ Si}}} = -RT\ln\frac{\gamma_{\mathrm{B(l)\ in\ Si\text{-}Sn\ melt}}\bullet X_{\mathrm{B\ in\ Si\text{-}Sn\ melt}}}{a_{\mathrm{B(s)\ in\ Solid\ Si}}} \quad (3\text{-}4)$$

$$\ln k_{\mathrm{B}} = \ln\frac{X_{\mathrm{B\ in\ Solid\ Si}}}{X_{\mathrm{B\ in\ Si\text{-}Sn\ melt}}} = \frac{\Delta G_m^{\mathrm{o}\,fus}}{RT} + \ln\frac{\gamma_{\mathrm{B(l)\ in\ Si\text{-}Sn\ melt}}}{\gamma_{\mathrm{B(s)\ in\ Solid\ Si}}} \quad (3\text{-}5)$$

Here, $\Delta G_{\mathrm{l}}^{\mathrm{o}\,fus}$ denotes the Gibbs energy change for the fusion of B, where l and s in parenthesis represent the liquid and solid standard states, respectively. In addition, the effect of other elements in the melt on the interaction coefficient of B ($\varepsilon_{\mathrm{B}}^{i}X_{i\ \mathrm{in\ Si\text{-}Sn\ melt}}$, i represents elements such as Zr) is not considered.

From Eq. (3-4), it can be concluded that the activity coefficient of B (γ_{B}) is in anti-correlation with the solubility of B (X_{B}). Therefore, a larger activity coefficient implies a lower solubility of B and *vice versa*, which also agrees well with the B-Sn binary phase diagram. [3-10]

Eq. (3-5) shows that the segregation coefficient of B (k_{B}) becomes larger in Si-Sn melt than that in the pure Si system (0.8 at 1687 K) because of the larger activity coefficient of B (γ_{B}). This implies that it will become more difficult to remove B using Sn as the refining solvent by directional solidification alone.

Under these circumstances, note that I use Zr as an additive that has a strong affinity for B, to enhance the formation and precipitation of boride, thus improving the B-removal fraction during the directional solidification process.

Fig. 3-8 shows that the activity coefficient of Zr is very small in both Si and Sn melt, with a slight difference, which means that Zr has a similar segregation coefficient (k_{Zr}) in Si-Sn melt as that in Si (1.6×10^{-8} at 1687 K). This implies that Zr is expected to be eliminated easily after the directional solidification process and will not contaminate the Si.

3.4.2. Thermodynamic Analysis of the Possibility of Boride Formation

Based on the Zr-B binary system, [3-11] ZrB_2 is the most probable phase in the temperature range of solidification refining. If I consider the ZrB_2 formation reaction, as represented by Eq. (3-6), the Gibbs energy change can be expressed as below. [3-12]

$$\mathrm{Zr(l)} + 2\mathrm{B(l)} = \mathrm{ZrB_2(s)} \quad (3\text{-}6)$$

$$\Delta rG_6^{\mathrm{o}\,f} = -449000 + 76.9T\ (\mathrm{J/mol}) \quad (3\text{-}7)$$

$$\Delta rG_6^{\circ f} = -RT\ln\frac{\alpha_{ZrB_2(s)}}{\alpha_{Zr(l)\text{ in Si-Sn melt}}\cdot\alpha^2_{B(l)\text{ in Si-Sn melt}}} \quad (3\text{-}8)$$

$$\alpha_{Zr(l)\text{ in Si-Sn melt}}\cdot\alpha^2_{B(l)\text{ in Si-Sn melt}} = exp^{(-\frac{54005}{T}+9.25)} \quad (3\text{-}9)$$

Here, $\Delta rG_6^{\circ f}$ denotes the Gibbs energy change for Eq. (3-6) and α_j is the activity of component j and the character in the parenthesis denotes the standard state. If $\alpha_{ZrB_2(s)}$ is considered as unity, the product of $\alpha_{Zr(l)\text{ in Si-Sn melt}}\cdot\alpha^2_{B(l)\text{ in Si-Sn melt}}$ at different temperatures can be obtained using Eq. (3-9), which is deduced by making Eq.s (3-7) and (3-8) simultaneously equal. The detailed data are listed in Table 3-3, which indicates that the formation of ZrB_2 is possible at extremely small α_{Zr} and α_B in theory.

Table 3-3. Product of $\alpha_{Zr(l)\text{ in Si-Sn melt}}\cdot\alpha^2_{B(l)\text{ in Si-Sn melt}}$ at different temperatures.

Temperature (K)	$\alpha_{Zr(l)\text{ in Si-Sn melt}}\cdot\alpha^2_{B(l)\text{ in Si-Sn melt}}$
873	1.42×10^{-23}
973	8.17×10^{-21}
1073	1.44×10^{-18}
1173	1.05×10^{-16}
1273	3.92×10^{-15}
1373	8.61×10^{-14}
1473	1.24×10^{-12}
1573	1.28×10^{-11}
1673	9.96×10^{-11}
1773	6.15×10^{-10}

Under the same conditions, Si_2Zr and Sn_2Zr may form after adding Zr to the Si-Sn melt according to the Si-Zr and Sn-Zr binary phase diagrams. [3-13, 14] However, ZrB_2 is expected to be the most thermodynamically stable compound in the Si-Sn melt considering the following reactions: [3-15]

$$ZrSi_2(s) + 2B(l) = 2Si(l) + ZrB_2(s) \quad (3\text{-}10)$$

$$\Delta rG_{10}^{\circ f} = -163000 + 7.1T\,(J/mol) \quad (3\text{-}11)$$

$$ZrSn_2(s) + 2B(l) = 2Sn(l) + ZrB_2(s) \quad (3\text{-}12)$$

$$\Delta rG_{12}^{\circ f} = -273500 + 83.1T\,(J/mol) \quad (3\text{-}13)$$

3.4.3. Removal of B from Si by Zr Addition in Solidification Refining

Table 3-4. Initial compositions of Si-Sn melt and final compositions of refined Si under different conditions.

No.	Moving Direction	Lifting Rate (mm/min)	Initial Composition of the Si-Sn Melt			Final Composition of Refined Si	
			B (ppma/ppmw)	Zr (ppma/ppmw)	Sn (at.%)	B (ppmw)	Zr (ppmw)
R01	up	0.01	153/120	211/1370	50	42.5	0.0
R02	up	0.02	153/120	211/1370	50	51.3	0.0
R03	down	0.02	153/120	211/1370	50	71.4	0.0
R04	up	0.04	153/120	211/1370	50	54.9	0.0
R05	down	0.04	153/120	211/1370	50	72.0	0.0
R06	up	0.06	153/120	211/1370	50	56.0	0.0
R07	up	0.08	153/120	211/1370	50	59.0	0.0
R08	up	0.10	153/120	211/1370	50	60.3	0.0
R09	up	0.04	153/120	0/0	50	74.5	0.0
R10	up	0.04	153/120	211/1370	50	53.3	0.0
R11	up	0.04	153/120	422/2742	50	48.6	0.0
R12	up	0.04	153/120	633/4114	50	47.3	0.0
R13	up	0.04	153/120	845/5485	50	42.0	1.0
R14	up	0.04	153/120	1057/6857	50	31.2	26.6
R15	up	0.04	153/120	211/1370	20	92.6	0.0
R16	up	0.04	153/120	211/1370	35	90.8	0.0
R17	up	0.04	153/120	211/1370	65	46.9	31.9
R18	up	0.04	153/120	211/1370	80	35.1	38.0
R19	up	0.01	2400/1860	1200/7850	50	733	271

R04 and R10 are the repeatability test experiments.

After elucidation of the thermodynamic characteristics of B and Zr in the Si-Sn system and the feasibility of adding Zr to enhance B removal, conditional experiments under different variables were carried out. Table 3-4 shows the initial composition of the Si-Sn melt and the final composition of refined Si, and Table 3-5 shows the initial and final contents of B and Zr in different positions using the pure Si system. The B content in a typical MG-Si is between 13 and 130 ppma, [3-16]

while the initial B content of the Si-Sn melt in this study was set to 153 ppma [120 ppmw] considering the possible contamination from Sn in the practical refining process. The initial B and Zr contents of the Si-Sn melt were controlled by precisely weighing the powdered Si-1 mass% B and Si-1 mass% Zr alloys, respectively.

Table 3-5. Initial and final contents of B and Zr (ppmw).

No.	Moving Directions	Lifting Rate (mm/min)	Initial Content in Si		Final Content in Refined Si		
			B	Zr	Position	B	Zr
R20	up	0.01	120	1370	top	61.7	4.7
					middle	89.3	8.3
					bottom	113.2	24.6

3.4.3.1. Dependence on Zr Additive Content

The effect of Zr addition on the B-removal fraction at the moving rate of 0.04 mm/min is shown in Fig. 3-9.

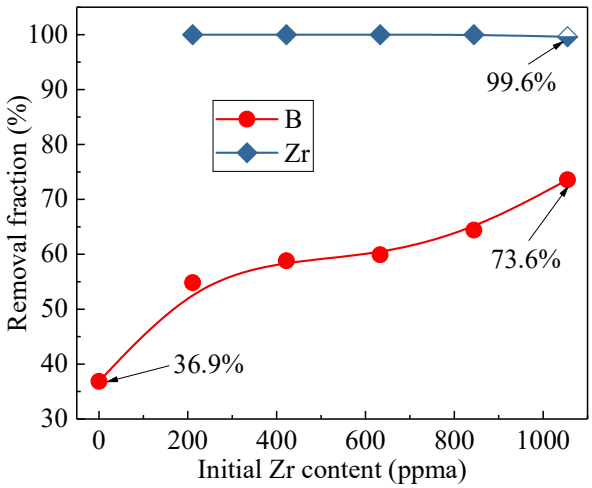

Fig. 3-9. Removal fractions of B and Zr after solidification refining with varying initial Zr additive content.

When the Si-50 at.% Sn melt (containing 120 ppmw B) was used as the refining solvent, the B-removal fraction increased from 36.9% to 73.6% with an increase in Zr content from 0 to 1057 ppma (6857 ppmw), indicating that Zr was critically responsible for the decrease in B content in the refined Si. This is because the activity of B in the Si-Sn melt significantly decreased with an increase in Zr activity, as expressed in Eq. (3-9) and listed in Table 3-3. Besides, the activity of B in the solid Si will decrease according to Eq.s (3-1)-(3-3). The removal fraction of the

added Zr slightly decreased from 100% to 99.6% (26.6 ppmw in refined Si) with an increase in its initial content, because it was difficult for a larger amount of Zr to diffuse sufficiently from the Si grains into the intergranular and liquid phases in a limited time.

3.4.3.2. Dependence on Moving Rate and Direction

The effect of moving rate [related to cooling rate, *i.e.,* cooling rate (K/min) = moving rate (m/min) × temperature gradient (K/m)] on B and Zr removal (Si-50 at.% Sn was the refining solvent containing 120 ppmw B and 1370 ppmw Zr) is shown in Fig. 3-10. The moving rates employed in this study were 0.01, 0.02, 0.04, 0.06, 0.08, and 0.10 mm/min.

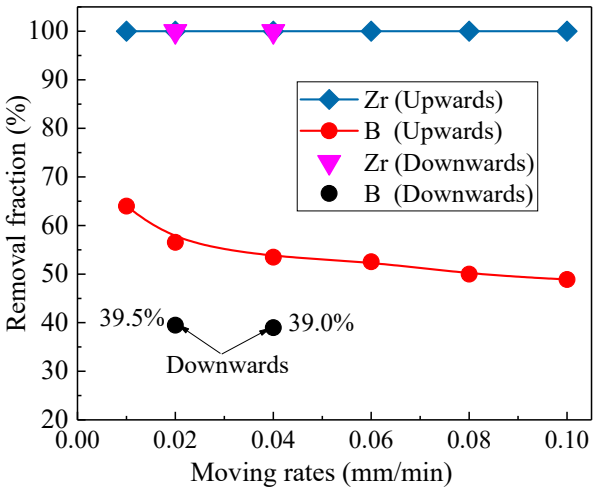

Fig. 3-10. Removal fractions of B and Zr after solidification refining with varying moving rates and directions.

According to Fig. 3-10, the B-removal fraction increased from 48.9% to 64.0% with a decrease in the upward moving rate from 0.10 to 0.01 mm/min, indicating that a lower cooling rate is more favourable for B removal. This is possibly because a lower cooling rate provides more time for the diffusion of B from the solid Si to the intergranular and liquid phases, enabling the refining process to be carried out much closer to its equilibrium. On the other hand, the removal fraction of Zr was 100% even at 0.10 mm/min upward moving rate, which is sufficient for Zr removal owing to its relatively small segregation coefficient (1.6×10^{-8} at 1687 K).

Moreover, the upward directional solidification process had higher removal fraction of B than downward, which were 56.5% and 39.5% at 0.02 mm/min 53.5% and 39.0% at 0.04 mm/min moving rate, indicating that upward is more favourable

for B removal. In the upward directional solidification process, the hot zone was located in the lower part of the crucible, which is beneficial for the mass transfer and thermal convective, and the strong self-miscellaneous ability led to less B impurity residual in crystalline primary Si.

3.4.3.3. Dependence on Sn Content

The effect of melt composition on B removal at the moving rates of 0.04 and 0.01 mm/min is shown in Fig. 3-11(a) and (b).

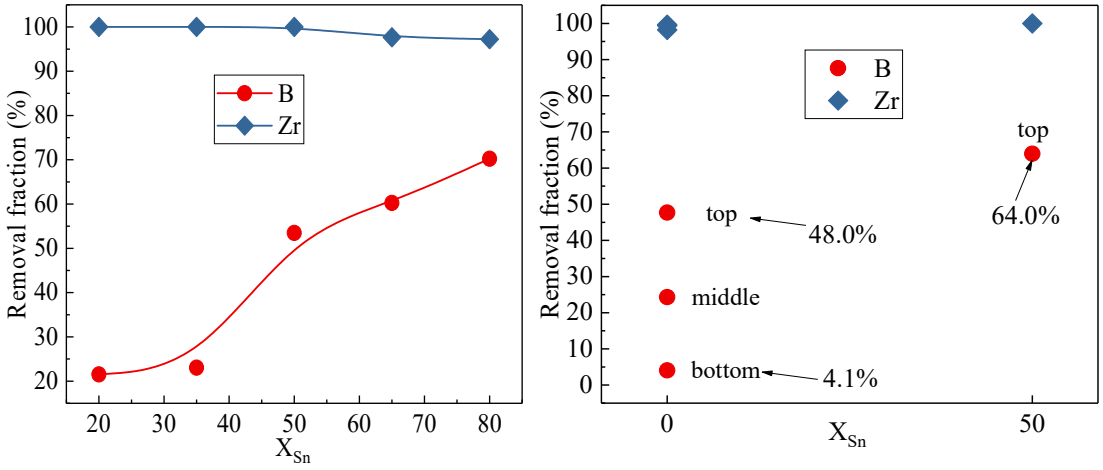

(a) (b)

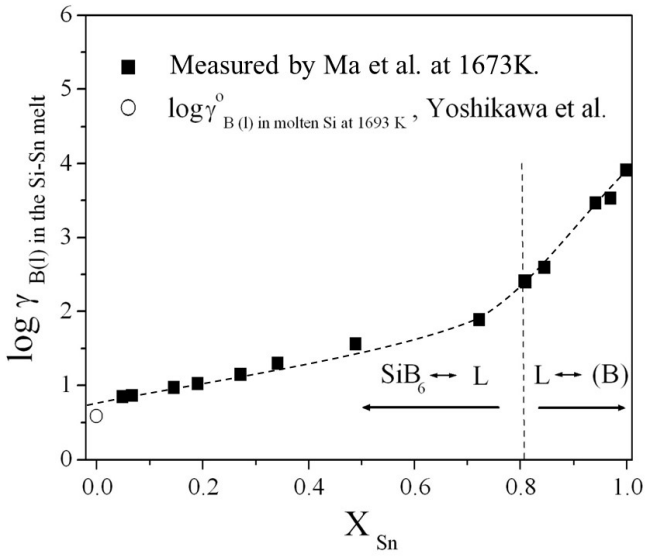

(c)

Fig. 3-11. Removal fractions of B and Zr after solidification refining with varying initial Sn content (a) 0.04 and (b) 0.01 mm/min, (c) activity coefficient of B in the Si-Sn melt at 1673 K. [3-8]

Fig. 3-11(a) shows that the B-removal fraction increased from 21.5% to 70.3% with an increase in the initial Sn content from 20 to 80 at.%. This can be explained as follows: the activity coefficient of B will increase at a higher initial Sn content [3-8], as reported by Ma *et al.* (Fig. 3-11(c)), and the segregation coefficient of B will decrease at a lower temperature. [3-17] Inversely, the Zr removal fraction slightly decreased from 100% to 97.2% with an increase in the initial Sn content from 20 to 80 at.%. Fig. 3-11(b) shows that the Si-50 at.% Sn system has better removal fraction for both B and Zr compared to the pure Si system at 0.01 mm/min upward rate. The removal fractions of B and Zr increased from 48% to 64% and from 99.6% to 100%, respectively. For a pure Si sample, the removal fractions of B (48% → 4.1%) and Zr (99.6% → 98.2%) gradually decreased from top to bottom after directional solidification refining, as detailed in Table 3-5.

3.4.4. Distribution Behavior of B and Zr

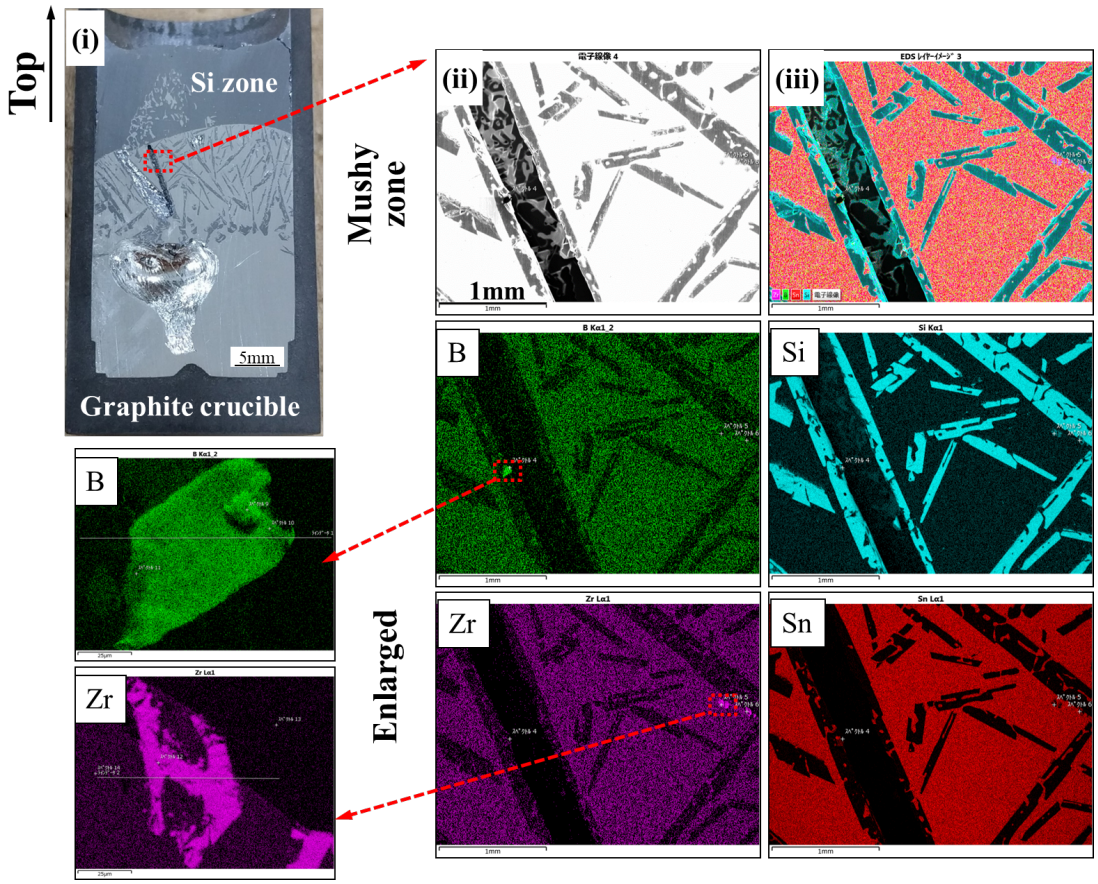

Fig. 3-12. (i) Cross section of a sample using Si-50 at.% Sn alloy, (ii) photograph of the area of the sample, (iii) SEM-EDS analysis of each element.

Although the removal fraction of B has been improved, it is not as significant as expected. To further explain this phenomenon, the distribution behavior of B and Zr in the directional solidification refining process was studied by SEM-EDS.

Fig. 3-12 presents an SEM image and EDS analysis of the region in a solidified sample (No. R19 in Table 3-4). After observing the whole sample, B- and Zr-enriched areas were found only in the mushy zone, and were observed to not combine to form B-Zr intermediate compounds. The initial B and Zr contents in sample No. R19 were 1860 and 7850 ppmw, respectively. While the contents of B and Zr were much higher than those in MG-Si, there was still no reaction to form boride under this condition.

Beyond these analysis, I calculated the cooling process diagram of Si-50 at.% Sn melt under different initial B and Zr contents (No. R19 and R01 in Table 3-4) using the FactSage Equilib module, which are shown in Fig.s 3-13(a) and (b). These figures show that the temperature range of boride formation is 710−1610 K and 770−1350 K, respectively, in case of an ideal equilibrium solidification process. This indicates that the higher the initial B and Zr contents, the higher is the temperature of the corresponding boride formation. Note that the temperature of boride formation under all experimental conditions was not higher than the liquidus temperature of Si-50 at.% Sn (1605 K).

Certainly, during the directional solidification process, as the primary Si crystals continued to precipitate and enriched, the composition of the alloy melt will change and the liquidus temperature will gradually decrease. This may result in decreasing the solubility of B and Zr in the residual Si-Sn melt to promote the possibility of boride formation, which thus improves the removal fraction of B. However, because of the kinetic factors, the boride produced by the reaction may be more limited in size and difficult to detect. All of the above explain why boride was hard to find in Si-Sn melts.

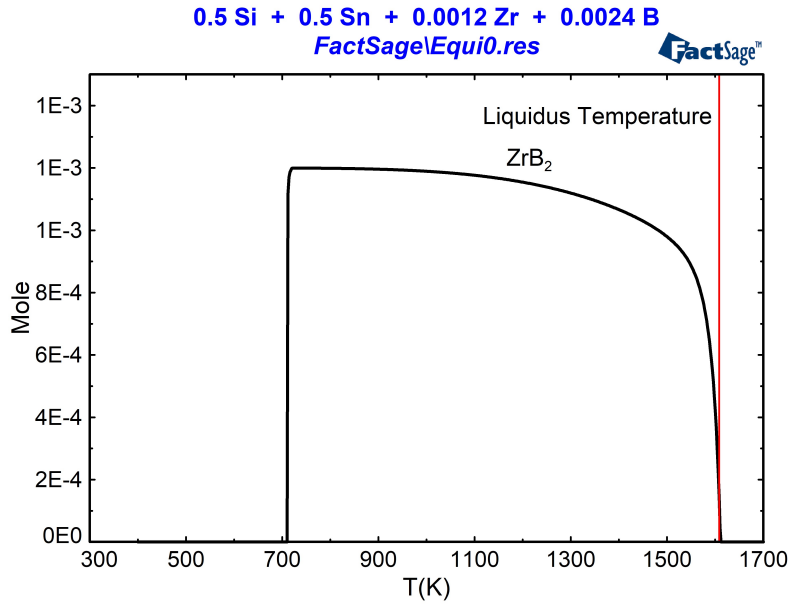

(a)

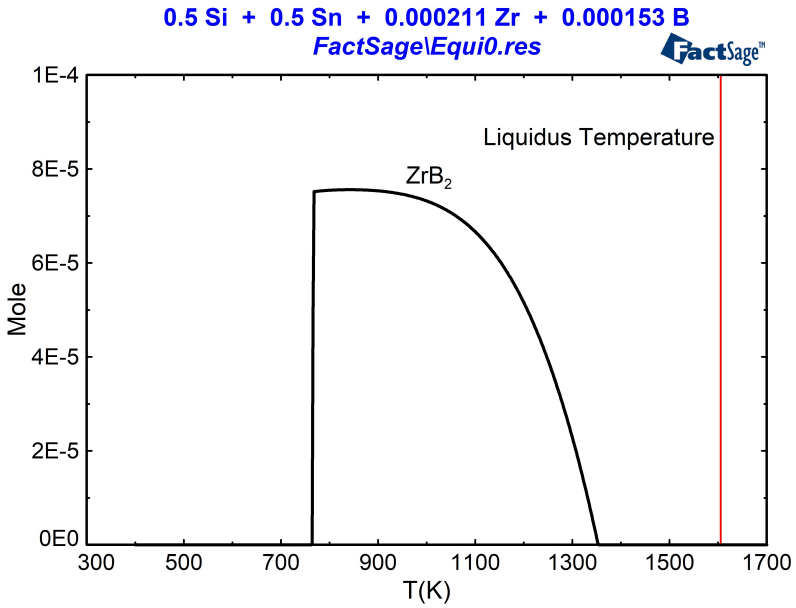

(b)

Fig. 3-13. Cooling process diagram of Si-50 at.% Sn melt: (a) with initial 1200 ppma Zr and 2400 ppma B; (b) with initial 211 ppma Zr and 153 ppma B.

3.4.5. Solubility Product (Ksp) of ZrB_2 in Si-Sn Melt

It is known from the above that several steps should be met for the formation of boride: at the beginning, the B and Zr dissolve in the Si-Sn melt; subsequently, after saturation, they react to form boride (ZrB_2). Therefore, it is necessary to determine the solubility product of ZrB_2 in the Si-Sn melt.

Equilibrium was attained by holding the Si-Sn-Zr-B melt at 1605 and 1575 K (Si-50 at.% Sn at 1605 K, Si-65 at.% Sn at 1575 K to ensure that they are slightly higher than their liquidus temperatures) in the Ar atmosphere for 12 h. After solidification was completed, the Si-Sn alloy sample was cut in half. The contents of B and Zr in the top area were measured by ICP-OES, which are listed in Table 3-6.

Table 3-6. Experimental results of ZrB_2 solubility in the Si-Sn melt.

Sample	Alloy composition Sn (at.%)	Temperature T (K)	Initial Content (ppma)		After Equilibration (ppma)		$X_{Zr\ in\ Si\text{-}Sn\ melt} \cdot X_{B\ in\ Si\text{-}Sn\ melt}^2$
			Zr	B	Zr	B	
S-01	50	1605	211	765	204	786	1.26×10^{-10}
S-02	50	1605	422	765	402	763	2.34×10^{-10}
S-03	50	1605	633	765	617	745	3.42×10^{-10}
S-04	50	1605	845	765	821	722	4.28×10^{-10}
S-05	50	1605	1057	765	997	731	5.33×10^{-10}
S-06	50	1605	1900	765	1826	726	9.62×10^{-10}
S-07	65	1575	211	460	207	456	4.30×10^{-11}
S-08	65	1575	422	460	406	430	7.51×10^{-11}
S-09	65	1575	633	460	621	437	1.19×10^{-10}
S-10	65	1575	845	460	792	443	1.55×10^{-10}
S-11	65	1575	1057	460	986	453	2.02×10^{-10}
S-12	65	1575	1900	460	1874	421	3.32×10^{-10}

Different units between ppmw (values obtained from ICP-OES) and ppma of each element can be converted using Eq. (3-14),

$$\mathrm{ppma}_{(i)} = \frac{\dfrac{\mathrm{ppmw}_{(i)}}{M_{(i)}}}{\dfrac{m_{(Si)}}{M_{(Si)}} + \dfrac{m_{(Sn)}}{M_{(Sn)}} + \dfrac{\mathrm{ppmw}_{(B)}}{M_{(B)}} + \dfrac{\mathrm{ppmw}_{(Zr)}}{M_{(Zr)}}} \tag{3-14}$$

where i in parenthesis represents B or Zr, and $M_{(Si)} = 28.09$ g/mol, $M_{(Sn)} = 118.71$ g/mol, $M_{(B)} = 10.81$ g/mol, and $M_{(Zr)} = 91.22$ g/mol are the molar

masses of Si, Sn, B, and Zr, respectively. Here, it is considered that the alloy composition remains unchanged before and after equilibrium.

Eq. (3-15) can be derived from Eq. (3-8), as follows:

$$\begin{aligned}\Delta rG_6^{of} &= -RT\ln\frac{\alpha_{ZrB_2(s)}}{\alpha_{Zr(l)\text{ in Si-Sn melt}}\cdot\alpha^2_{B(l)\text{ in Si-Sn melt}}}\\ &= -RT\ln\alpha_{ZrB_2(s)} + RT\ln X_{Zr\text{ in Si-Sn melt}}\cdot X_{B\text{ in Si-Sn melt}}{}^2\\ &+ RT\ln\gamma_{Zr(l)\text{ in Si-Sn melt}}\cdot\gamma_{B(l)\text{ in Si-Sn melt}}{}^2\end{aligned} \tag{3-15}$$

Here, the ZrB_2 solubility in the Si-Sn melt at the infinite dilution of Zr and B can be defined as the product of $X_{Zr\text{ in Si-Sn melt}}\cdot X_{B\text{ in Si-Sn melt}}{}^2$.

Table 3-6 shows that the amounts of B and Zr before and after equilibrium did not change significantly, implying that no boride was produced at these two temperatures. Meanwhile, SEM-EDS analysis was carried out for samples S-06 and S-12, and no boride was found.

Therefore, the solubility products can be determined as follows:

$$\begin{aligned}&X_{Zr\text{ in Si-Sn melt}}\cdot X_{B\text{ in Si-Sn melt}}{}^2\\ &\quad\geq 9.62\times10^{-10}\left(1605\text{ K},\ \text{Si}-50\text{ at.\% Sn}\right)\\ &\quad\geq 3.32\times10^{-10}\left(1575\text{ K},\ \text{Si}-65\text{ at.\% Sn}\right)\end{aligned} \tag{3-16}$$

According to Eq. (3-16), the solubility of ZrB_2 in Si-Sn melt increased when the temperature increased, within the scope of FactSage calculation results, which were 3.94×10^{-9} at 1575 K and 4.35×10^{-8} at 1605 K, respectively.

Moreover, these values are 100 times higher than those of using Ti as an additive in the Si-Al system measured by Yoshikawa *et al.* [3-4], as follows:

$$\begin{aligned}&X_{Ti\text{ in Si-Al melt}}\cdot X_{B\text{ in Si-Al melt}}{}^2\\ &\quad= 2.39\times10^{-12}\left(1273\text{ K},\ \text{Si}-60.0\text{ at.\% Al}\right)\\ &\quad= 9.80\times10^{-14}\left(1173\text{ K},\ \text{Si}-64.6\text{ at.\% Al}\right)\end{aligned} \tag{3-17}$$

This indicates that if B was reduced to lower than 10 ppma, the added Ti must be larger than 980 ppma at 1173 K and 23900 ppma at 1273 K in the Si-Al melt system.

In contrast, I can conclude that B and Zr are much more soluble in the Si-Sn system because of the higher liquidus temperature, so the initial content required to form the boride is much higher than that in the Si-Al system.

Therefore, a high refining temperature was responsible for the lower removal fraction of B when Si-Sn alloy was employed as the refining solvent.

3.5. Results and Discussion of Adding Ti

In order to make a comparative test with adding Zr to verify whose boron removal effect is better, a series of Ti addition experiments also have been done subsequently. Since the effect of other factors (such as moving direction, moving rate, different alloy composition, *etc.*) has been clarified previously, in this part, I only investigate the experiments of different Ti addition amount at 0.04mm/min upwards moving rate.

One of the samples obtained and the analysis process are shown in the Fig. 3-14. The experimental results are listed in Table 3-7.

Table 3-7. Initial compositions of Si-Sn melt and final B in refined Si with different additive contents.

No.	Moving Direction	Lifting Rate (mm/min)	Initial Compositions of the Si-Sn Melt			Final B in Refined Si	
			B (ppmw)	Zr/Ti (ppma/ppmw)	Sn (at.%)	B (ppmw)	Removal fraction (%)
T01	up	0.04	120	Ti-211/138	50	71.8	40.0
T02	up	0.04	120	Ti-422/275	50	69.6	42.0
T03	up	0.04	120	Ti-633/413	50	63.6	47.0
T04	up	0.04	120	Ti-845/551	50	57.6	52.0
T05	up	0.04	120	Ti-1057/690	50	69.2	42.0
R09	up	0.04	120	0/0	50	74.5	36.9
R10	up	0.04	120	Zr-211/1370	50	53.3	54.8
R11	up	0.04	120	Zr-422/2742	50	48.6	58.8
R12	up	0.04	120	Zr-633/4114	50	47.3	60.0
R13	up	0.04	120	Zr-845/5485	50	42.0	64.0
R14	up	0.04	120	Zr-1057/6857	50	31.2	73.6

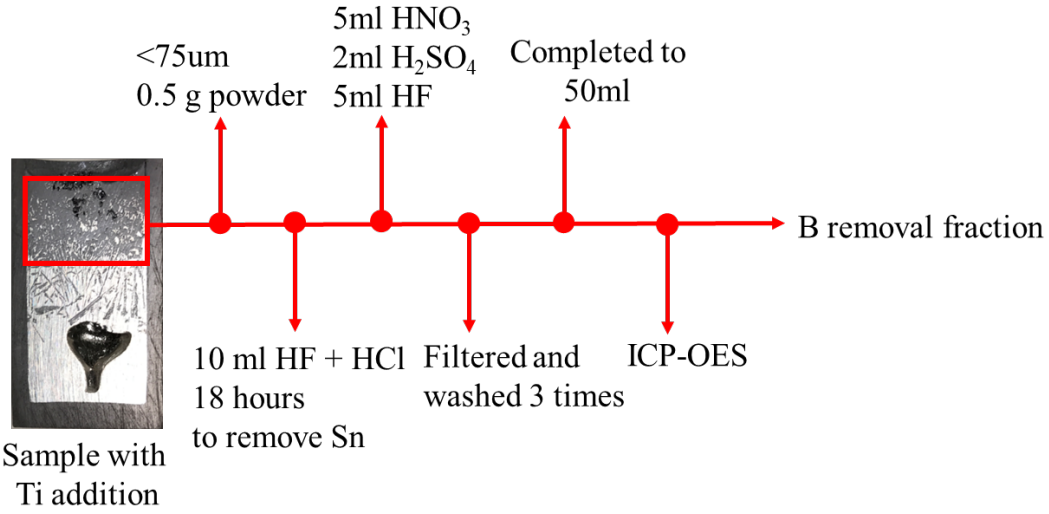

Fig. 3-14. Flowchart of sample analysis.

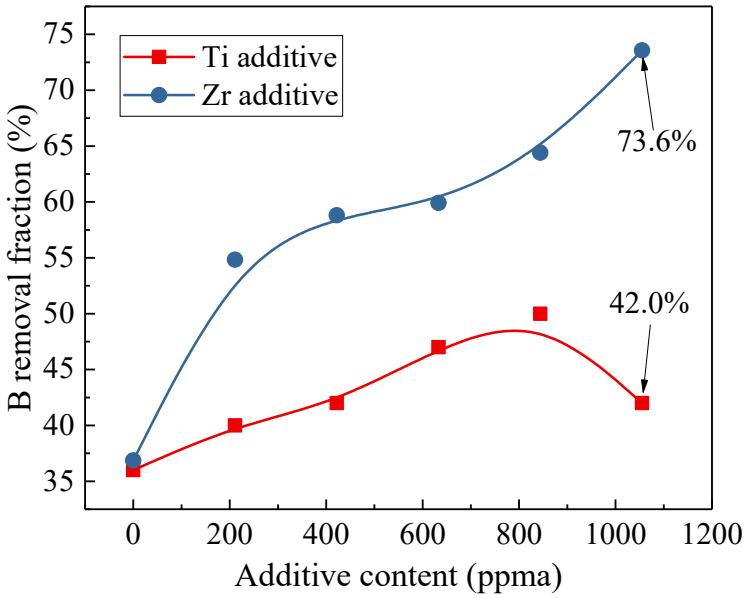

Fig. 3-15. Removal fractions of B after solidification refining with varying initial Zr/Ti additive content (0.04mm/min upwards moving).

When the Si-50 at.% Sn melt (containing 120 ppmw B) was used as the refining solvent, the B-removal fraction increased from 36.9% to 73.6% with an increase in Zr content from 0 to 1057 ppma (6857 ppmw), and increased from 36.9% to 52.0 % then down to 42.0 % with an increase in Ti content from 0 to 1057ppma (690ppmw). The results show that the effect of B removal by adding Ti is very weak, even worse than that by adding Zr. It can be explained as follows:

$$Zr(l) + 2B(l) = ZrB_2(s) \quad (3\text{-}6)$$

$$\Delta rG_6^{of} = -449000 + 76.9T(\text{J/mol}) \quad (3\text{-}7)$$

$$\mathrm{Ti(l)} + 2\mathrm{B(l)} = \mathrm{TiB_2(s)} \quad (3\text{-}18)$$

$$\Delta rG_{18}^{\circ f} = -436000 + 67.3T\,(\mathrm{J/mol}) \quad [3\text{-}18, 19] \quad (3\text{-}19)$$

The results can be shown in Fig. 3-16, from which it can be seen that ZrB_2 is more stable at low temperature. Moreover, it can be inferred that the solubility product constant of ZrB_2 is smaller than TiB_2, based on the activity coefficients of Zr and Ti in Si-Sn melt.

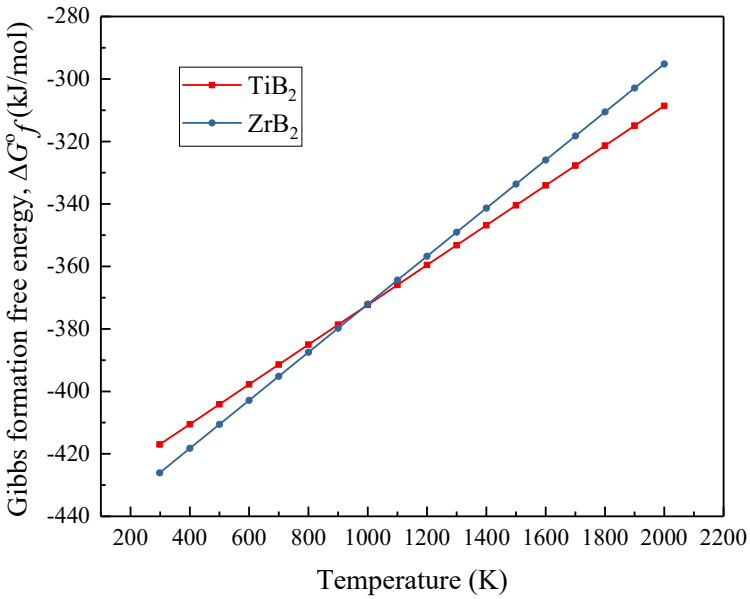

Fig. 3-16. Gibbs formation energy for TiB_2 and ZrB_2 in Si-Sn melt.

3.6. Short Summary

I clarified the relations among the solubility of B (X_B), activity coefficient of B (γ_B), and segregation coefficient of B (k_B) in Si-Sn melt. I found that it is difficult to remove B using Sn as the refining solvent just by directional solidification because of the larger value of k_B. Zr was selected as an additive that has strong affinity for B, to enhance the formation and precipitation of boride, thus expecting to improve the B-removal fraction.

The removal of B from Si by Zr addition in solidification refining was studied under different variables, *i.e.*, Zr additive content, moving direction/rate, and initial Sn content in Si-Sn melt. Based on the experimental results, the B-removal fraction was improved to some extent by adding a small amount of Zr and the refining process would be more effective at a lower cooling rate, upward moving direction, and higher Zr content combined with a lower liquidus temperature.

Finally, the solubility product (Ksp) of Zr and B in Si-Sn melt was also measured. The constants were determined as $\geq 9.62 \times 10^{-10}$ (1605 K, Si-50 at.% Sn) and $\geq 3.32 \times 10^{-10}$ (1575 K, Si-65 at.% Sn), which were 100 times higher than those in the Si-Al melt measured by Yoshikawa *et al.* A high refining temperature was responsible for the lower removal fraction of B when the Si-Sn alloy was employed as the refining solvent. I concluded that the refining process should be carried out at a low temperature, which is more conducive to boride formation.

Finally, a series of comparative experiments were carried out by adding Ti additive. The results show that the effect of B removal by adding Ti is very weak, even worse than that by adding Zr.

Thus, the B-removal experiments using Zr as an additive to Si-Cu and Si-Sn-Cu melts are currently being conducted to reduce the liquidus temperature and the B-removal mechanism will be further studied.

References

3-1 Y. Ren, H. Wang, K. Morita, Growth control and enrichment of Si crystals from Si-Sn melt by directional solidification. *Vacuum*, 158 (2018) 86–92.

3-2 X. Ma, T. Yoshikawa, K. Morita, Purification of metallurgical grade Si combining Si-Sn solvent refining with slag treatment, *Sep. Purif. Technol.,* 125 (2014) 264-268.

3-3 I. Barin, Thermochemical Data of Pure Substances, *VCH, Weinheim*, (1989) 1384, 1523, 1708.

3-4 T. Yoshikawa, K. Arimura, K. Morita, Boron removal by titanium addition in solidification refining of silicon with Si-Al melt. *Metall. Mater. Trans. B*, 36B (2005) 837–842.

3-5 Y. Lei, W.H. Ma, L.E. Sun, Y.N. Dai, K. Morita, B removal by Zr addition in electromagnetic solidification refinement of Si with Si-Al melt, *Metall. Mat. Trans. B*, 47 (2016) 27-31.

3-6 R.H. Hopkins, A. Rohatgi, Impurity effects in silicon for high efficiency solar cells, *J. Cryst. Growth*, 75 (1986) 67–79.

3-7 K. Tang, E.J. Øvrelid, G. Tranell, M. Tangstad, *Thermochemical and kinetic databases for the solar cell silicon materials, in: The Twelfth International Ferroalloys Congress, Sustainable Future*, Helsinki, Finland, (2010).

3-8 X.D. Ma, T. Yoshikawa, K. Morita, Phase relations and thermodynamic property of boron in the silicon-tin melt at 1673 K, *J. Alloys Compd.,* 529 (2012) 12-16.

3-9 E.T. Turkdogan, *Physical Chemistry of High-temperature Technology*, Academic Press, New York, (1980) 5.

3-10 V.P. Itkin, The B-Sn (boron-tin) system, *J. Phase Equilib*. 17 (1996) 129-130.

3-11 H.M. Chen, F. Zheng, H.S. Liu, L.B. Liu, Z.P. Jin, Thermodynamic assessment of B–Zr and Si–Zr binary systems, *J. Alloys Compd.,* 468 (2009) 209-216.

3-12 E.T. Turkdogan, *Physical Chemistry of High-temperature Technology*, Academic Press, New York, (1980) 5, 20, 21, 24.

3-13 H. Okamoto, The Si-Zr (Silicon-Zirconium) system, *Bull. Alloy Phase Diagr.*, 11 (1990) 513-519.

3-14 N. Subasic, Thermodynamic evaluation of Sn-Zr phase diagram, *Calphad,* 22 (1998) 157-165.

3-15 R.J. Pérez, C. Toffolon-Masclet, J.M. Joubert, B. Sundman, The Zr–Sn binary system: New experimental results and thermodynamic assessment. *Calphad,* 32 (2008) 593-601.

3-16 C.P. Khattak, D.B. Joyce, F. Schmid: *Report, Crystal Systems, Inc.*, Massachusetts, December (1999).

3-17 K. Morita, T. Yoshikawa, Thermodynamic evaluation of new metallurgical refining processes for SOG-silicon production, *Trans. Nonferrous Mater. Soc. China*, 21 (2011) 685-690.

3-18 *Phase Diagrams of Binary Titanium Alloys*, J.L. Murray, ed., ASM INTERNATIONAL, Metals Park, OH, 1987.

3-19 *JANAF Thermodynamical Tables*, 3rd ed., M.W. Chase, Jr., C.A. Davles, J.R. Downey, Jr., D.J. Frurip, R.A. McDonald, and A.N. Syverud, eds., American Chemical Society and American Institute of Physics for National Bureau of Standards, New York, NY, 1985.

Chapter IV. Formation Mechanism of ZrB_2 in Si–Cu Melt

4.1. Introduction

In Chapter II and III, the separation of bulk Si and removal of B by adding a small amount of Zr in a Si-Sn solvent were studied systematically. A large amount of bulk poly-Si was obtained [4-1] and no ZrB_2 precipitates were identified. [4-2] The results indicated that Zr and B are much more soluble in a Si-Sn system because of its higher liquidus temperature, meaning the initial content required to form borides is much greater than that in a Si-Al system. [4-3] I concluded that a refining process carried out at a lower temperature is more conducive to the formation of boride.

Based on the results discussed above, Cu can be considered as a superior solvent because (i) it has very small solid solubility in Si, [4-4] (ii) there is a significant density difference between primary Si ($\rho_{Si\ (300\ K)}$ = 2.33 g/cm^3) [4-5] and liquid Si-Cu ($\rho_{Cu\ (1358\ K)}$ = 8.96 g/cm^3) [4-6], and because (iii) it has a much lower liquidus temperature than a Si-Sn system, but a similar liquidus temperature compared to a Si-Al system. For example, when selecting 50.0 at.% Si as a criterion, the liquidus temperatures of Si-Sn, Si-Al, and Si-Cu systems are 1605 K, 1339 K, and 1341 K, respectively. Therefore, this study aimed to clarify the formation mechanisms of ZrB_2 in a Si-Cu melt by using chemical equilibrium technology and to measure important thermodynamic data (such as solubility products).

4.2. Experiment

A SiC electrical resistance furnace was employed to carry out thermodynamic equilibrium experiments. An experimental apparatus schematic is presented in Fig. 4-1 (a). The temperature of the furnace was calibrated using a standard B-type thermocouple. The CO_2, H_2O, and O_2 contents in the Ar gas (99.99%) were eliminated by passing the gas successively through soda lime, silica gel, magnesium perchlorate, and magnesium turnings heated to 823 K. A total of 20 g of bulk Si and Cu powder (99.9%) with different amounts of pre-melted Si-1 mass% Zr and Si-1 mass% B alloys was placed in a high-purity dense graphite crucible (20 mm outer

diameter (OD), 14 mm inner diameter (ID), 50 mm length) to prepare Si-Cu alloys containing certain amounts of Zr and B.

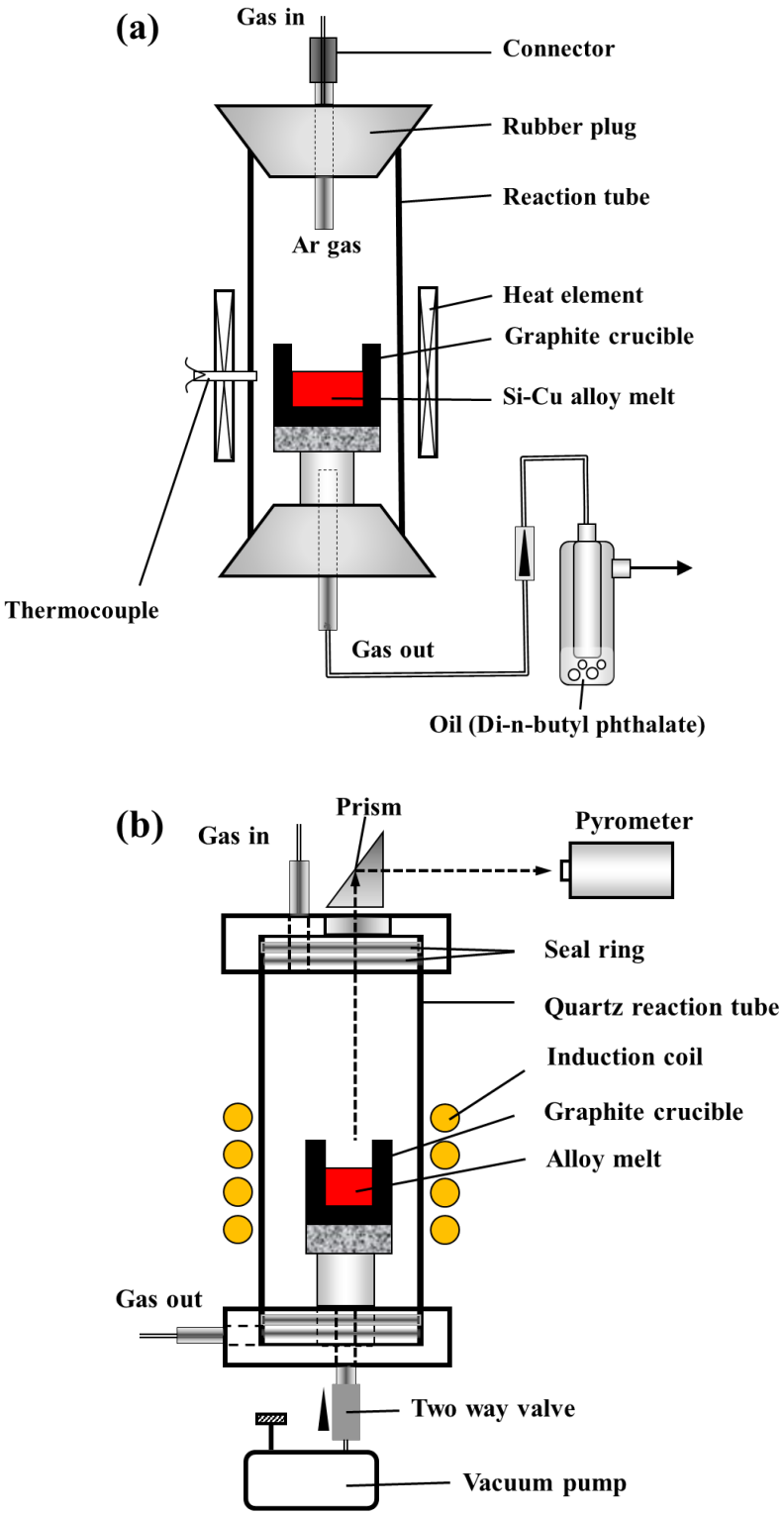

Fig. 4-1. Schematic diagrams of (a) the SiC electrical resistance furnace for equilibrium experiments and (b) induction furnace for pre-melting experiments.

The Si-1 mass% Zr and Si-1 mass% B alloys were prepared using a high-frequency induction furnace (50 kHz). A schematic of this furnace is presented in Fig. 4-1 (b). Specific amounts of bulk Si (99.9999%), shot Zr (99.6%), and lump B (99.8%) were weighed accurately and proportionally. The materials were then placed into a high-purity dense graphite crucible (30 mm OD, 24 mm ID, 50 mm length). To avoid oxidation, the air in the quartz chamber (60 mm OD, 54 mm ID, 400 mm length) was evacuated using a vacuum pump (ultimate pressure < 6 Pa). The chamber was then filled with Ar gas at a flow rate of 200 ml/min to prevent the melt from oxidizing. The surface temperatures of the Si-1 mass% Zr and Si-1 mass% B melts were monitored through a prism using a dual-wavelength infrared pyrometer. After melting and holding at 1873 K for 2 h, the sample was cooled quickly to 298 K by the control program.

Subsequently, they were ground into powders (particle diameter < 75 μm) in an agate mortar to homogenize their compositions. Then, their compositions were confirmed using inductively-coupled plasma optical emission spectroscopy (ICP-OES). Following confirmation, these two types of alloys were used as raw materials for subsequent experiments.

Equilibrium was obtained by holding the Si-Cu-Zr-B melts at 1345 K (Si-50.0 at.% Cu) and 1258 K (Si-57.0 at.% Cu) in an Ar atmosphere for 12 h to ensure that their liquidus temperatures were slightly exceeded. The samples were then gradually cooled to 298 K at a rate of approximately 200 K/h. Following solidification, the samples were cut in half lengthwise using a diamond saw cutting machine.

Next, scanning electron microscopy combined with energy-dispersive spectroscopy (SEM-EDS) and electron probe microanalysis (EPMA) were utilized to observe the Zr and B distribution behaviors in whole samples. Finally, the top portion of the Si-Cu alloy (without ZrB_2) was dissolved using a mixture of HF and HNO_3 (HF: HNO_3 = 1:1 by volume, where HF was added dropwise to prevent drastic reactions) to analyze the Zr and B contents using ICP-OES.

4.3. Results and Discussion

4.3.1. Activity Coefficients of B (γ_B) and Zr (γ_{Zr}) in Si-Cu/Al Melts

First, the activity coefficients of B and Zr in Si-Al/Cu melts were calculated using the FactSage software, based on the FT-Lite database. The set values for each parameter were as follows: temperature of 1687 K (melting point of Si), molarity of B (< 0.002), and molarity of Zr (< 0.002). Si-Al/Cu melts dissolved with B and Zr in this composition range can be regarded as ideal dilute solutions, where B and Zr obey Henry's law. Fig. 4-2 represents the calculated data.

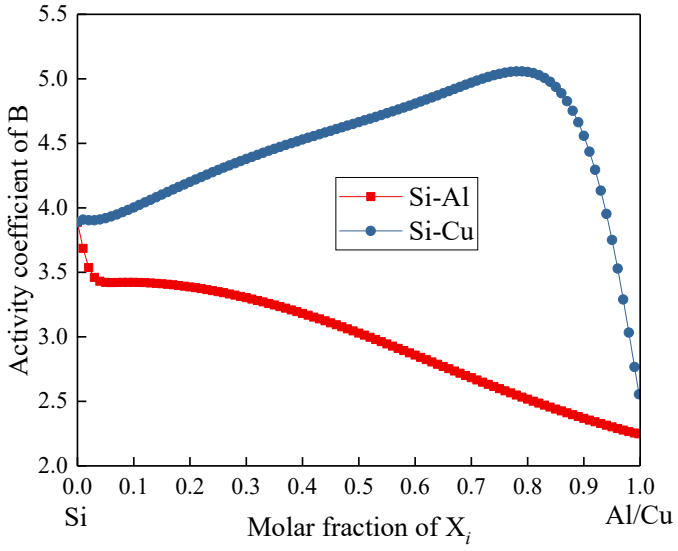

(a)

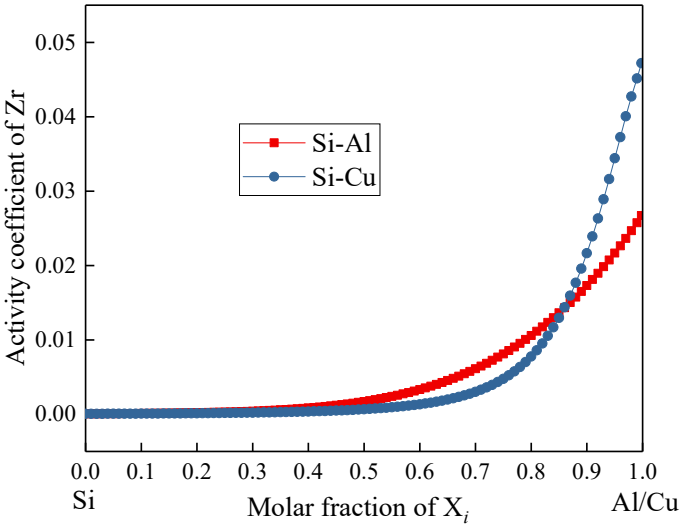

(b)

Fig. 4-2. Activity coefficients of (a) B and (b) Zr in Si-Al/Cu melts at 1687 K.

In a Si-Al system, B removal by adding Zr to form ZrB_2 was confirmed by Lei. [4-7] From Fig. 4-2, one can see that (i) the activity coefficients of B in the two Si-based alloy melts are on the same order of magnitude, but the Si-Cu system has a slightly higher value, and (ii) the activity coefficients of Zr in the two Si-based alloy melts are approximately the same. These results reveal one of the reasons why the Si-Cu system is more desirable for B removal by Zr addition.

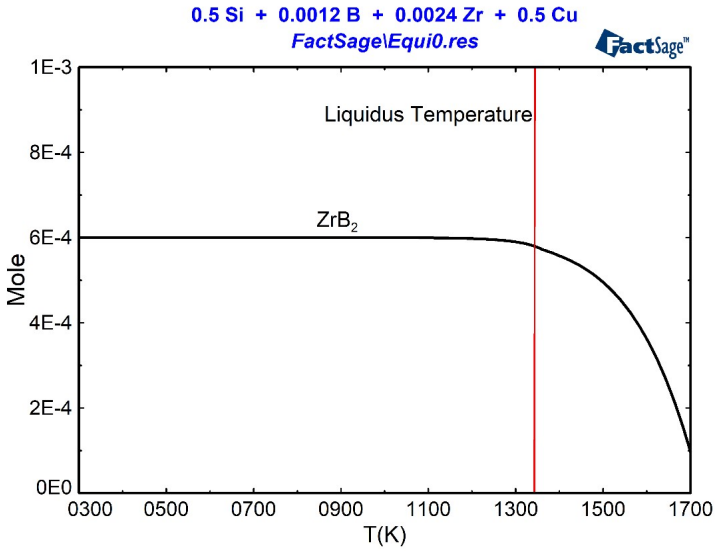

(a)

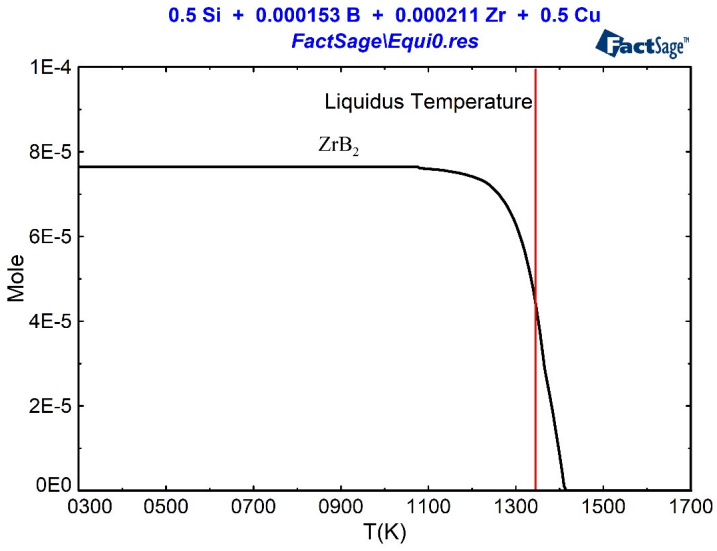

(b)

Fig. 4-3. Cooling process diagram (partially enlarged) of Si-50.0 at.% Cu melt with (a) initial conditions of 1200 ppma B and 2400 ppma Zr, and (b) initial conditions of 153 ppma B and 211 ppma Zr.

In addition to this analysis, cooling process diagrams of Si-50.0 at.% Cu melts with different initial B and Zr contents were calculated using the FactSage Equilib module, as shown in Fig. 4-3. One can see that the liquidus temperature (1341 K) falls within the temperature range of boride formation, even for the Si-50.0 at.% Cu melt with initial conditions of 153 ppma B and 211 ppma Zr (below 1410 K), confirming the formation potential of ZrB_2.

4.3.2. ZrB_2 Precipitation in Si-Cu Alloys

Table 4-1. Experimental results for ZrB_2 solubility in Si-Cu melts at 1345 K and 1258 K.

Sample	Alloy composition Cu (at.%)	Temperature, T (K)	Initial Content (ppma)		After Equilibration (ppma)		$X_{Zr\ in\ Si\text{-}Cu\ melt}^2 \cdot X_{B\ in\ Si\text{-}Cu\ melt}$
			Zr	B	Zr	B	
S-01	50.0	1345	211	460	204	145	4.29×10^{-12}
S-02	50.0	1345	2400	460	1412	57	4.59×10^{-12}
S-03	50.0	1345	422	460	268	123	4.05×10^{-12}
S-04	50.0	1345	633	460	392	110	4.74×10^{-12}
S-05	50.0	1345	845	460	522	87	3.95×10^{-12}
S-06	50.0	1345	1057	460	803	64	3.29×10^{-12}
S-07	50.0	1345	2100	460	1405	55	4.25×10^{-12}
S-08	50.0	1345	3000	460	1420	51	3.69×10^{-12}
Average Value							**4.11×10^{-12}**
K-01	57.0	1258	200	310	104	120.8	1.52×10^{-12}
K-02	57.0	1258	400	310	257	93.9	2.27×10^{-12}
K-03	57.0	1258	600	310	435	71.6	2.23×10^{-12}
K-04	57.0	1258	800	310	624	62.6	3.20×10^{-12}
K-05	57.0	1258	1000	310	776	52.8	3.04×10^{-12}
K-06	57.0	1258	1200	310	974	45.5	3.29×10^{-12}
K-07	57.0	1258	2100	310	1308	40.5	2.36×10^{-12}
K-08	57.0	1258	3000	310	1295	38.1	2.46×10^{-12}
Average Value							**2.55×10^{-12}**

The solubility products of ZrB_2 in a Si-50.0 at.% Cu melt at 1345 K and Si-57.0 at.% Cu melt at 1258 K are listed in Table 4-1. The initial contents of B at 1345 and 1258 K were set to 460 and 310 ppma, respectively. The clear decrease in the B and Zr contents following equilibrium confirms the removal of B *via* Zr addition.

The equilibrium B and Zr contents are considered to be the abscissa and ordinate, respectively, as shown in Fig. 4-4. The slope relationships of −0.514 and −0.463 (analytical errors are ± 0.03) were obtained from the logarithms of the Zr and B contents in the melt. The results indirectly prove that the composition of the boride produced should be ZrB_2 with a theoretically ideal slope of −0.5.

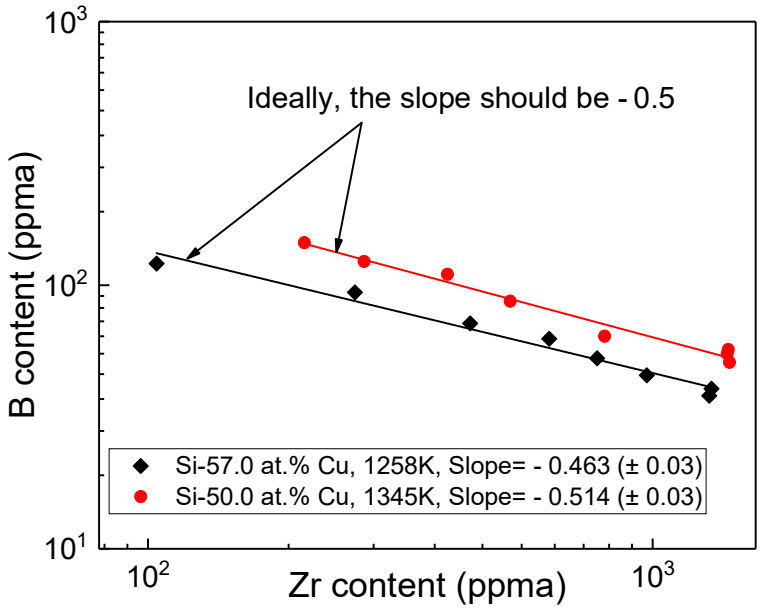

Fig. 4-4. Logarithmic analysis of equilibrium B and Zr contents.

To clarify the morphology of the Si-Cu melt, SEM-EDS and EPMA were conducted on the Si-50.0 at.% Cu alloy sample (S-07 in Table 4-1). The SEM micrographs and EDS results for each of the elements in the sample are presented in Fig.s 4-5 and 4-6. These results reveal that the polygonal precipitates near the bottom of the sample are B-Zr-rich phases (Fig.s 4-6 (e) and 4-6 (f)). The compositions of precipitates (A) and (B) in Fig. 4-6 (a) were measured using EPMA quantitative analysis.

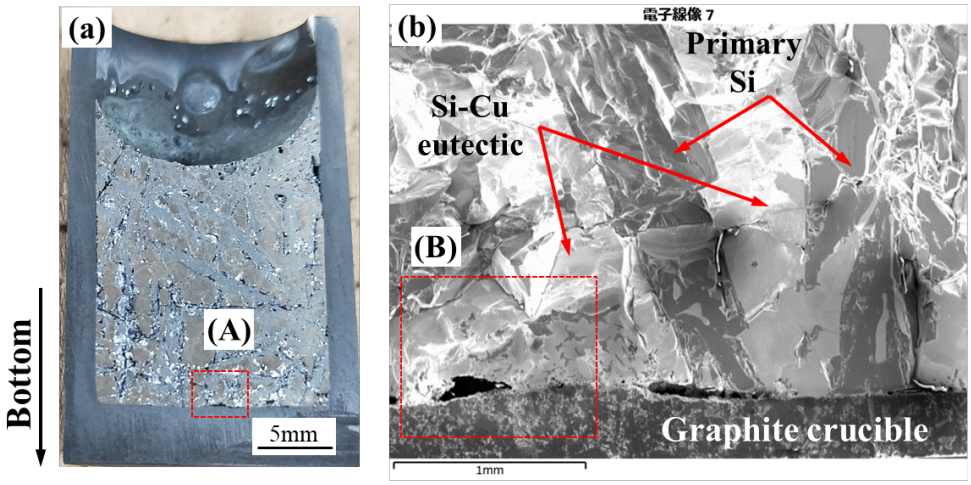

Fig. 4-5. (a) Photograph of a longitudinal section of the Si-50.0 at.% Cu alloy samples (S-07 in Table 4-1) and (b) a SEM image of the (A) region in (a).

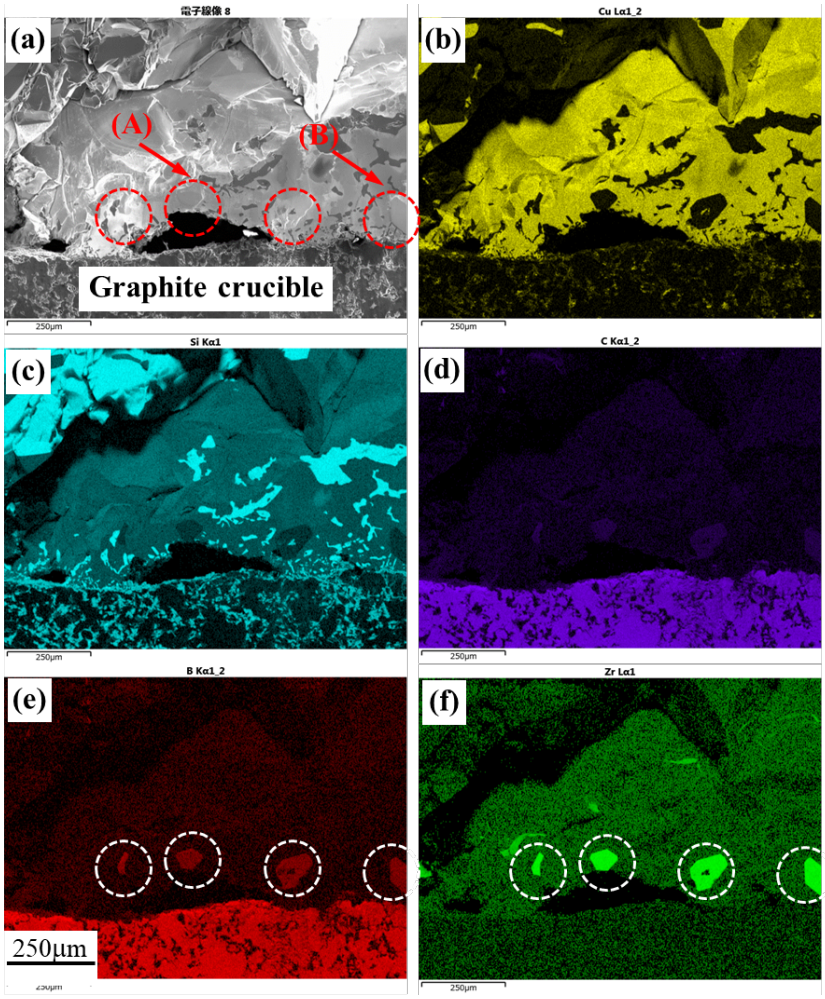

Fig. 4-6. SEM-EDS analysis of a region in Fig. 4-5(b): (a) SEM image; (b), (c), (d), (e) and (f) are the element maps of Cu, Si, C, B, and Zr in (a), respectively.

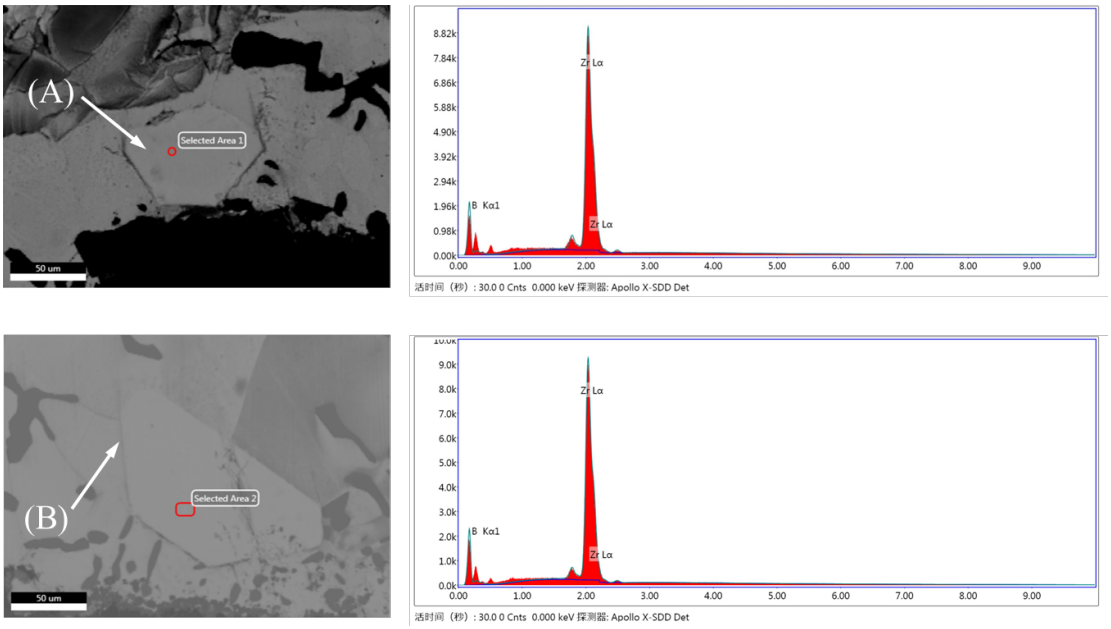

Fig. 4-7. EPMA images and relative intensities of the characteristic X-rays of the components in precipitates (A) and (B) from Fig. 4-6 (a).

Table 4-2. EPMA quantitative analysis results for precipitates (A) and (B) from Fig. 4-6 (a) compared to standard ZrB_2.

Substance	Atomic percent (%)			
	B	Zr	Cu	Si
Precipitate (A) in Fig. 4-6(a)	65.37	34.46	0.06	0.11
Precipitate (B) in Fig. 4-6(a)	68.65	31.18	0.13	0.04
Standard ZrB_2	66.62	33.38	---	---

The relative intensities of the characteristic X-rays of the components of precipitates (A) and (B) from Fig. 4-6 (a) are presented in Fig. 4-7. The detailed values for each element and comparisons to those of pure ZrB_2 (purchased from Shanghai Aladdin Company, Product No. Z131682 | CAS No. 12045-64-6) are listed in Table 4-2. Although trace amounts of Cu and Si dissolution were present in the precipitates, a lack of significant differences in the relative intensities and contents of Zr and B indicates that precipitates (A) and (B) are ZrB_2 intermediate compounds.

Additionally, it provides direct evidence that the B in a Si-Cu melt can be reduced by precipitating ZrB_2 *via* Zr addition. Furthermore, these precipitates appear in the Si-Cu eutectic phase and at the boundaries of Si crystals, as shown in Fig.s 4-6 (a) and (c), indicating that impurities (*i.e.*, Zr and B) are formed in the low-temperature liquid phase (Si-Cu melt) and do not contaminate primary Si crystals.

4.3.3. Solubility Product (Ksp) of ZrB_2 in Si-Cu Melt

It can be concluded that when reaching the solubility limits of Zr and B in a Si-Cu melt at a certain temperature, excessive Zr and B react to form ZrB_2, as represented by Eq. (4-1). The standard Gibbs energy change is expressed by Eqs. (4-2) and (4-3). [4-8]

$$\mathrm{Zr(l)} + 2\mathrm{B(l)} = \mathrm{ZrB_2(s)} \tag{4-1}$$

$$\Delta G^{o}_{f,\mathrm{ZrB_2}} \cong -449000 + 76.9T\ (\mathrm{J/mol}) \tag{4-2}$$

$$\begin{aligned}\Delta G^{o}_{f,\mathrm{ZrB_2}} &= -RT\ln\frac{a_{\mathrm{ZrB_2(s)}}}{a_{\mathrm{Zr(l)\ in\ Si\text{-}Cu\ melt}}\cdot a_{\mathrm{B(l)\ in\ Si\text{-}Cu\ melt}}{}^{2}} \\ &= -RT\ln a_{\mathrm{ZrB_2(s)}} + RT\ln X_{\mathrm{Zr\ in\ Si-Cu\ melt}}\cdot X_{\mathrm{B\ in\ Si-Cu\ melt}}{}^{2} \\ &\quad + RT\ln\gamma_{\mathrm{Zr(l)\ in\ Si-Cu\ melt}}\cdot\gamma_{\mathrm{B(l)\ in\ Si-Cu\ melt}}{}^{2}\end{aligned} \tag{4-3}$$

Here, $\Delta G^{o}_{f,\mathrm{ZrB_2}}$ is the standard Gibbs energy change for ZrB_2 formation. The characters *s* and *l* in parentheses denote the solid and liquid standard state, respectively. α_i, X_i, and γ_i are the activity, mole fraction, and activity coefficient of component *i*, respectively. Since ZrB_2 was precipitated in the Si-Cu melt, the activity of ZrB_2 can be considered as unity. Zr and B in the Si-Cu melt in this composition range obey Henry's law because of their relatively low content, which is verified from the relations of the slope (both closed to -1/2) between the $\ln X_{\mathrm{Zr\ in\ Si-Cu\ melt}}$ and the $\ln X_{\mathrm{B\ in\ Si-Cu\ melt}}$ in Fig. 4-4.

Accordingly, the ZrB_2 solubility in the Si-Cu melt at an infinite dilution of Zr and B can be determined as Eq. [4-4], by averaging the values of $X_{\mathrm{Zr\ in\ Si-Cu\ melt}}\bullet X_{\mathrm{B\ in\ Si-Cu\ melt}}{}^{2}$ of each sample:

$$\begin{aligned}X_{\mathrm{Zr\ in\ Si-Cu\ melt}}\cdot X_{\mathrm{B\ in\ Si-Cu\ melt}}{}^{2} &= 4.11\times10^{-12}\ (1345\mathrm{K},\ \mathrm{Si\text{-}50at.\%Cu}) \\ &= 2.55\times10^{-12}\ (1258\mathrm{K},\ \mathrm{Si\text{-}57at.\%Cu})\end{aligned} \tag{4-4}$$

By substituting these two values into Eq. [4-3], $RT\ln\gamma^{o}_{\mathrm{Zr(l)\ in\ Si-Cu\ melt}}\cdot\gamma^{o}_{\mathrm{B(l)\ in\ Si-Cu\ melt}}{}^{2}$ were determined as Eq. [4-5] at 1345K and 1258K, with the consideration of $\alpha_{\mathrm{ZrB_2(s)}} = 1$. Where the symbol γ^{o}_{i} means the activity coefficient of component *i* at its infinite dilution.

$$RT\ln\gamma^{\circ}_{\text{Zr(l) in Si–Cu melt}}\cdot\gamma^{\circ}{}^{2}_{\text{B(l) in Si–Cu melt}}$$
$$= \text{-52400 (J/mol)} \quad (1345\text{K, Si-50at.\%Cu}) \qquad (4\text{-}5)$$
$$= \text{-73060 (J/mol)} \quad (1258\text{K, Si-57at.\%Cu})$$

Based on the Gibbs-Duhem integration method developed by Toop, [4-9] which can convert the ternary system into a binary system, as expressed in Eq. [4-6].

$$RT\ln\gamma_{2\,(1\text{-}2\text{-}3)} = \left[\frac{x_1}{1-x_2}RT\ln\gamma_{2\,(1\text{-}2)}+\frac{x_3}{1-x_2}RT\ln\gamma_{2\,(2\text{-}3)}\right]_{x_2}-(1-x_2)^2\Delta G^{\text{M.ex}}_{1\text{-}3\,x_1/x_3} \qquad (4\text{-}6)$$

$RT\ln\gamma^{\circ}_{\text{B (l) in Si–Cu melt}}$ and $RT\ln\gamma^{\circ}_{\text{Zr (l) in Si–Cu melt}}$ can be expressed as Eq. [4-7].

$$RT\ln\gamma^{\circ}_{i\text{ (l) in Si–Cu melt}} = X_{\text{Si in Si-Cu melt}}\cdot RT\ln\gamma^{\circ}_{i\text{ (l) in Si melt}}$$
$$+X_{\text{Cu in Si-Cu melt}}\cdot RT\ln\gamma^{\circ}_{i\text{ (l) in Cu melt}}-\Delta G^{\text{M.ex}}_{\text{Si-Cu melt}} \qquad (4\text{-}7)$$

(i : B or Zr)

Here, $\Delta G^{\text{M.ex}}_{\text{Si-Cu melt}}$ denotes the excess Gibbs energy for mixing in the Si-Cu melt. [4-10] It can be calculated by the Redlich-Kister polynomials regarding the melt as a regular solution, as expressed by Eq. [4-8].

$$\Delta G^{\text{M.ex}}_{\text{A-B melt}} = \sum_{i=0}^{j}\Omega^{i}_{\text{A-B}}(\text{X}_\text{A}-\text{X}_\text{B})^{i}\,\text{X}_\text{A}\text{X}_\text{B} \qquad (4\text{-}8)$$

Where $\Omega^{i}_{\text{A-B}}$ represents the binary interaction parameters for A-B system. In this study, the relevant binary interaction parameters for Si-Cu and Si-Zr system, in liquid phase, are provided in Table 4-3.

Table 4-3. The binary interaction parameter for Si-Cu, Cu-Zr systems in liquid phase.

System	Parameter, J/mol
Si-Cu [4-11]	$\Omega^{0}_{\text{Si-Cu}} = \text{-39688+14.275}T$
	$\Omega^{1}_{\text{Si-Cu}} = \text{-49937+29.790}T$
	$\Omega^{2}_{\text{Si-Cu}} = \text{-31810+18.008}T$
Cu-Zr [4-12]	$\Omega^{0}_{\text{Cu-Zr}} = \text{-61685.53+11.29235}T$
	$\Omega^{1}_{\text{Cu-Zr}} = \text{-8830.66+5.04565}T$

Eq. [4-9] can be derived by substituting Eq. [4-7] into $RT\ln\gamma^{\circ}_{\text{Zr(l) in Si−Cu melt}}\cdot\gamma^{\circ}_{\text{B(l) in Si−Cu melt}}{}^{2}$.

$$\begin{aligned} &RT\ln\gamma^{\circ}_{\text{Zr(l) in Si−Cu melt}}\bullet\gamma^{\circ}_{\text{B(l) in Si−Cu melt}}{}^{2} \\ =&X_{\text{Cu in Si-Cu melt}}\bullet RT\ln\gamma^{\circ}_{\text{Zr(l) in Cu melt}}\bullet\gamma^{\circ}_{\text{B(l) in Cu melt}}{}^{2} \\ +&X_{\text{Si in Si-Cu melt}}\bullet RT\ln\gamma^{\circ}_{\text{Zr(l) in Si melt}}\bullet\gamma^{\circ}_{\text{B(l) in Si melt}}{}^{2}-3\Delta G^{\text{M.ex}}_{\text{Si-Cu melt}} \end{aligned} \tag{4-9}$$

Where $RT\ln\gamma^{\circ}_{\text{Zr(l) in Si melt}}\bullet\gamma^{\circ}_{\text{B(l) in Si melt}}{}^{2}$ has been estimated by Chen, as expressed by Eq. [4-10]. [4-13]

$$RT\ln\gamma^{\circ}_{\text{Zr(l) in Si melt}}\bullet\gamma^{\circ}_{\text{B(l) in Si melt}}{}^{2}=251200-244.9T\ \text{(J/mol)} \tag{4-10}$$

Correspondingly, $RT\ln\gamma^{\circ}_{\text{Zr(l) in Cu melt}}\bullet\gamma^{\circ}_{\text{B(l) in Cu melt}}{}^{2}$ can be calculated as Eq. [4-11].

$$RT\ln\gamma^{\circ}_{\text{Zr(l) in Cu melt}}\bullet\gamma^{\circ}_{\text{B(l) in Cu melt}}{}^{2}=-409300+324.0T\ \text{(J/mol)} \tag{4-11}$$

Where $RT\ln\gamma^{\circ}_{\text{Zr(l) in Cu melt}}$ can be treated in Eqs. [4-12] and [4-13]. X_{Cu} was regarded as 1 because of the very low content of Zr.

$$RT\ln\gamma^{\circ}_{\text{Zr(l) in Cu melt}}=\left[\Delta G^{\text{M.ex}}_{\text{Cu-Zr melt}}-X_{\text{Cu}}\frac{\partial\Delta G^{\text{M.ex}}_{\text{Cu-Zr melt}}}{\partial X_{\text{Cu}}}\right]_{X_{\text{Cu}}=1} \tag{4-12}$$

$$\begin{aligned} RT\ln\gamma^{\circ}_{\text{Zr(l) in Cu melt}}=&\sum_{i=0}^{j}\Omega^{i}_{\text{Cu-Zr}}(\text{X}_{\text{Cu}}-\text{X}_{\text{Zr}})^{i}\,\text{X}^{2}_{\text{Cu}} \\ &-2\sum_{i=0}^{j}i\Omega^{i}_{\text{Cu-Zr}}(\text{X}_{\text{Cu}}-\text{X}_{\text{Zr}})^{i-1}\text{X}^{2}_{\text{Cu}}X_{\text{Zr}} \end{aligned} \tag{4-13}$$

Therefore, $RT\ln\gamma^{\circ}_{\text{B(l) in Cu melt}}$ can be derived as Eq. [4-15], based on the Eqs. [4-12]~[4-14].

$$RT\ln\gamma^{\circ}_{\text{Zr(l) in Cu melt}}\bullet\gamma^{\circ}_{\text{B(l) in Cu melt}}{}^{2}=RT\ln\gamma^{\circ}_{\text{Zr(l) in Cu melt}}+2RT\ln\gamma^{\circ}_{\text{B(l) in Cu melt}} \tag{4-14}$$

$$RT\ln\gamma^{\circ}_{\text{B(l) in Cu melt}}=-169400+153.8T\ \text{(J/mol)} \tag{4-15}$$

Substitute Eqs. [4-10] and [4-11] into Eq. [4-9], and combined with $\Delta G^{\text{M.ex}}_{\text{Si-Cu melt}}$ of

different alloy compositions, $RT\ln\gamma^{o}_{\text{Zr(l) in Si–Cu melt}}\cdot\gamma^{o}_{\text{B(l) in Si–Cu melt}}{}^{2}$ can be estimated, correspondingly. Finally, substituted it into Eq. [4-3], $RT\ln X_{\text{Zr in Si–Cu melt}}\cdot X_{\text{B in Si–Cu melt}}{}^{2}$ of the different compositions at corresponding liquidus temperatures can be derived.

The solubility products of ZrB_2 and the relationships between Zr and B contents in Si-Cu melts at corresponding liquidus temperatures were estimated using the equations presented above. The results are presented in Fig.s 4-8 and 9.

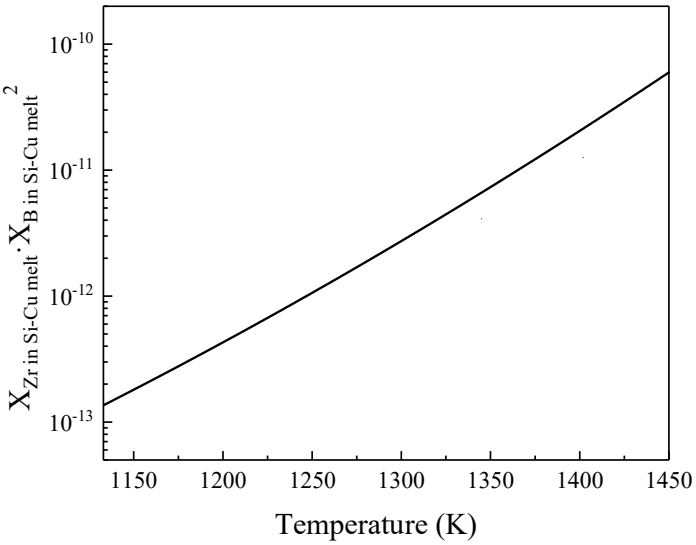

Fig. 4-8. Estimated data for the solubility products of Zr and B in Si-Cu melts at different liquidus temperatures.

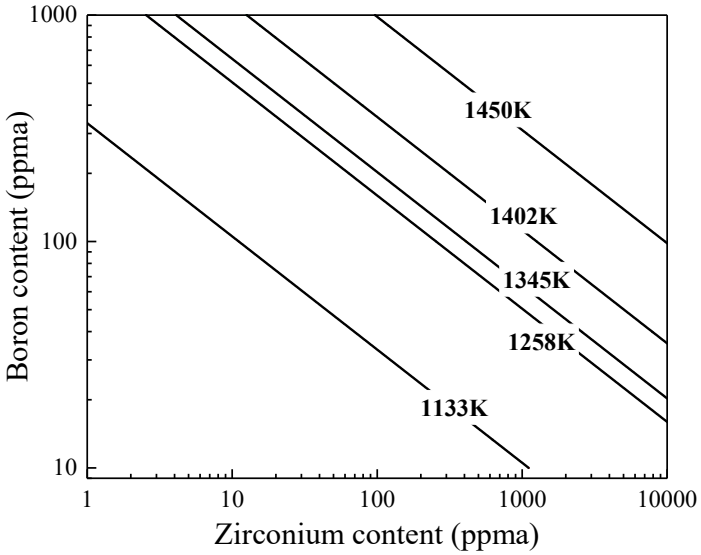

Fig. 4-9. Relations between B and Zr content in a Si-Cu melt based on temperature.

From Fig. 4-8, one can see that the amount of solubility products decreases with a decrease in temperature and vice versa. Furthermore, from Fig. 4-9, it can be concluded that when the initial content is below the corresponding line, the added B and Zr will be completely dissolved in the Si-Cu melt. Otherwise, ZrB_2 will precipitate. In this manner, the Zr and B contents in the Si-Cu melt will eventually converge to the lines in the figure. Furthermore, I can predict that the B content can be reduced in a Si-Cu melt by increasing the Zr content. For example, B in a Si-Cu melt at 1133 K can be reduced to a content less than 10 ppma when adding an amount of Zr greater than 1000 ppma, which is lower than the content estimated by Lei in a Si-Al melt at the same temperature. [4-7] All of the results above indicate that a Si-Cu system forms ZrB_2 more easily than a Si-Al system, which is consistent with the aforementioned FactSage calculation results.

4.4. Short Summary

Based on the activity coefficients of B (γ_B) and Zr (γ_{Zr}) in Si-Cu and Si-Al melts, it was determined that a Si-Cu system forms ZrB_2 more easily than a Si-Al system. Additionally, the potential for boride formation with certain initial contents of B and Zr was predicted using FactSage.

The solubility products (Ksp) of B and Zr in a Si-Cu melt were measured using chemical equilibrium technology. EPMA confirmed that the B-bearing precipitated particles of ZrB_x found at the bottom of the sample were ZrB_2. The solubility product constants were determined to be 4.11×10^{-12} (1345 K, Si-50.0 at.% Cu) and 2.55×10^{-12} (1258 K, Si-57.0 at.% Cu). Additional values were estimated based on thermodynamic calculations at temperatures ranging from 1133 to 1450 K.

This study provided direct evidence for B removal *via* Zr addition to form ZrB_2 in Si-Cu alloys, as well as theoretical support for the subsequent enrichment of large-area low-B-content bulk polycrystalline Si *via* directional solidification. Additionally, it revealed the potential for recycling Si solar cell waste by alloying such waste with Cu in the presence of Zr.

Highlight

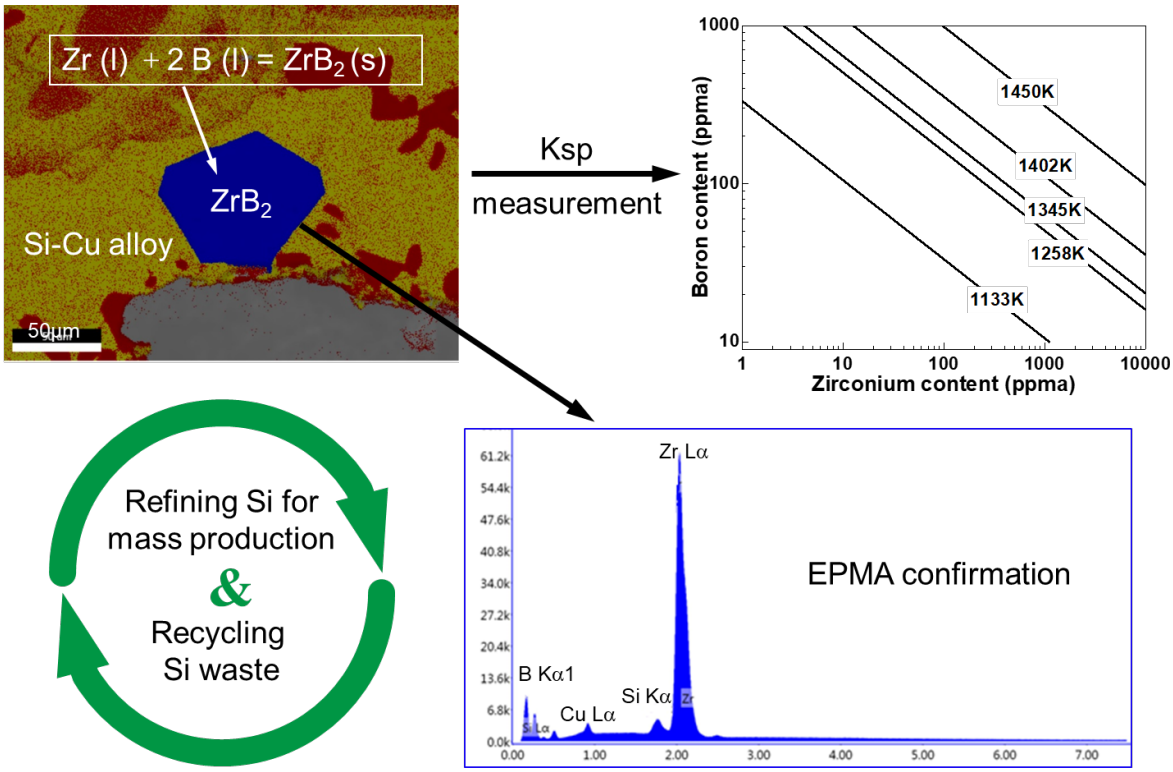

This Chapter highlights the potential for large-scale production of solar-grade Si to promote rapid and sustainable development of the photovoltaic industry.

References

4-1 Ren, Y.; Wang, H.; Morita, K. Growth control and enrichment of Si crystals from Si-Sn melt by directional solidification. *Vacuum*, 158 (2018) 86–92.

4-2 Ren, Y.; Wang, H.; Morita, K. Effect of Zr addition on B-removal behaviour during solidification purification of Si with Si–Sn solvent. *Vacuum*, 167 (2019) 319–328.

4-3 Yoshikawa, T.; Arimura, K.; Morita, K. Boron removal by titanium addition in solidification refining of silicon with Si-Al melt. *Metall. Mater. Trans. B,* 36B (2005) 837–842.

4-4 Trumbore, F.A. Solid solubilities of impurity elements in germanium and silicon. *Bell Syst. Tech. J,* 39 (1960) 206–233.

4-5 http://www.rsc.org/periodic-table/element/14/silicon (accessed November 6, 2019).

4-6 http://www.rsc.org/periodic-table/element/29/copper (accessed November 6, 2019).

4-7 Lei, Y.; et al., Mechanism of ZrB_2 Formation in Al–Si Alloy and Application in Si Purification. *ACS Sustainable Chem. Eng*., 7 (2019) 12990–12996.

4-8 Turkdogan, E.T. Physical Chemistry of High-temperature Technology. Academic Press. New York, 1980, p. 5, 20, 21, 24.

4-9 Toop, G.W. Prediction ternary activities using binary data. *Trans. Met. Soc. AIME,* 233 (1965) 850–855.

4-10 Olesinski, R.W.; Abbaschian, G.J. Bulletin of Alloy Phase Diagrams, 7 (1986) 170–178.

4-11 Shin, D.; Saal, J.E.; Liu Z.K. Thermodynamic Modeling of the Cu-Si System. *CALPHAD*, 32 (2008) 520–526.

4-12 Zeng, K.J.; Hämäläinen, M; Lukas, H.L. A new thermodynamic description of the Cu-Zr system. *JPE,* 15 (1994) 577–586.

4-13 Chen, K, Thermodynamic study of trace transitional metal additives base on refining of Silicon by Al-Si alloy to remove Boron (in Chinese). *Master thesis*, Yunnan University, 2018 (Chapter 3).

Chapter V. Zr Addition to Enhance B Removal in Si-Cu Solvent

5.1. Introduction

In Chapter IV, Electron probe microanalysis (EPMA) confirms that the B-bearing precipitated particles ZrB_x found at the bottom of the sample are ZrB_2. It provides direct evidence that the B in a Si-Cu melt can be reduced by precipitating ZrB_2 *via* Zr addition.[5-1] Furthermore, the solubility product constants were determined as 4.11×10^{-12} (1345 K, Si-50.0 at.% Cu) and 2.55×10^{-12} (1258 K, Si-57.0 at.% Cu), and further estimated by thermodynamic calculation at the temperatures ranging from 1133 to 1450 K.

Therefore, in this Chapter, the solidification refining of Si using Si-Cu solvent with Zr addition will be studied.

5.2. Experiment

20 g of solar grade lump Si (99.9999%) and Cu powder (99.9%), together with different amounts of pre-melted Si-1 mass% B and Si-1 mass% Zr alloys (same raw materials as introduced in Chapter III section 3.3.1), were placed in a high purity dense graphite crucible (A-type: 30 mm outer diameter (OD), 24 mm inner diameter (ID), 50 mm length; B-type: 20 mm outer diameter (OD), 14 mm inner diameter (ID), 70 mm length) to prepare the Si-Cu alloys with different target amount of B and Zr.

Subsequently, the crucibles were put into an alumina reaction tube of a SiC electric resistance furnace. The furnace was equipped with a vertical motion system controlled by a stepping motor, which was used to carry out the directional solidification experiments, as shown in Fig. 5-1. The CO_2, H_2O, and O_2 in the Ar gas were eliminated by passing the gas through soda lime, silica gel, magnesium perchlorate, and magnesium turnings (heated at 823 K) successively. The sample in the alumina reaction tube was maintained above the liquidus temperature of alloys for 1 h in an Ar atmosphere to ensure that it was melted uniformly.

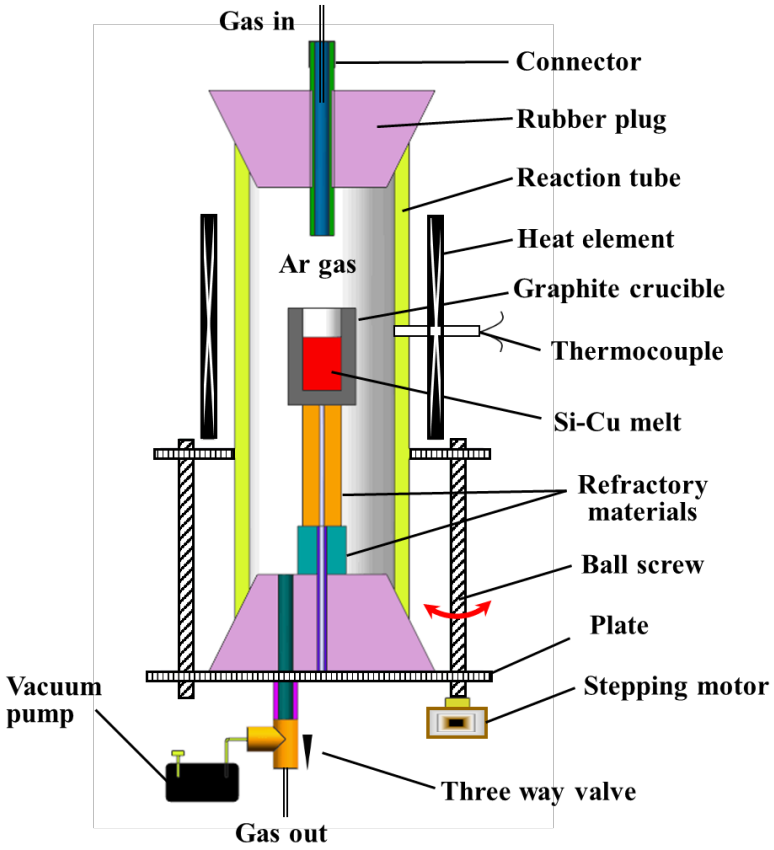

Fig. 5-1. Schematic of the experimental apparatus for directional solidification.

Then, directional solidification was carried out at the rate of 0.01, 0.02 and 0.04 mm/min under the temperature gradient of about 10^3 K/m. The temperature of the furnace was calibrated with a standard B-type thermocouple. The samples were cut open along the longitudinal section when the solidification was completed.

After polished using standard metallographic techniques, a digital camera and a scanning electron microscope equipped with an energy-dispersive spectrometer (SEM-EDS) and electron probe microanalysis (EPMA) were used to observe the macro and micro structures of the solidified samples, respectively.

The enriched Si part was cut off along the interface, subsequently subjected to ultrasonic cleaning with acetone, ground into powders in an agate mortar, and then sifted using a 200 mesh sieve (particle diameter < 75 μm). Furthermore, the mass of the powder was precisely determined and recorded as m_1. Afterward, the powder was dissolved using concentrated mixed acid (HNO_3 + H_2SO_4 + HCl) to remove Cu in the intergranular and liquid phases, followed by filtration and drying. The mass of the dried powder was also measured and recorded as m_2. Finally, the enrichment Si

percentage (ω) could be calculated by $m_2/m_1 \times 100\%$, the calculation process of Si enrichment percentage is shown in Fig. 5-2.

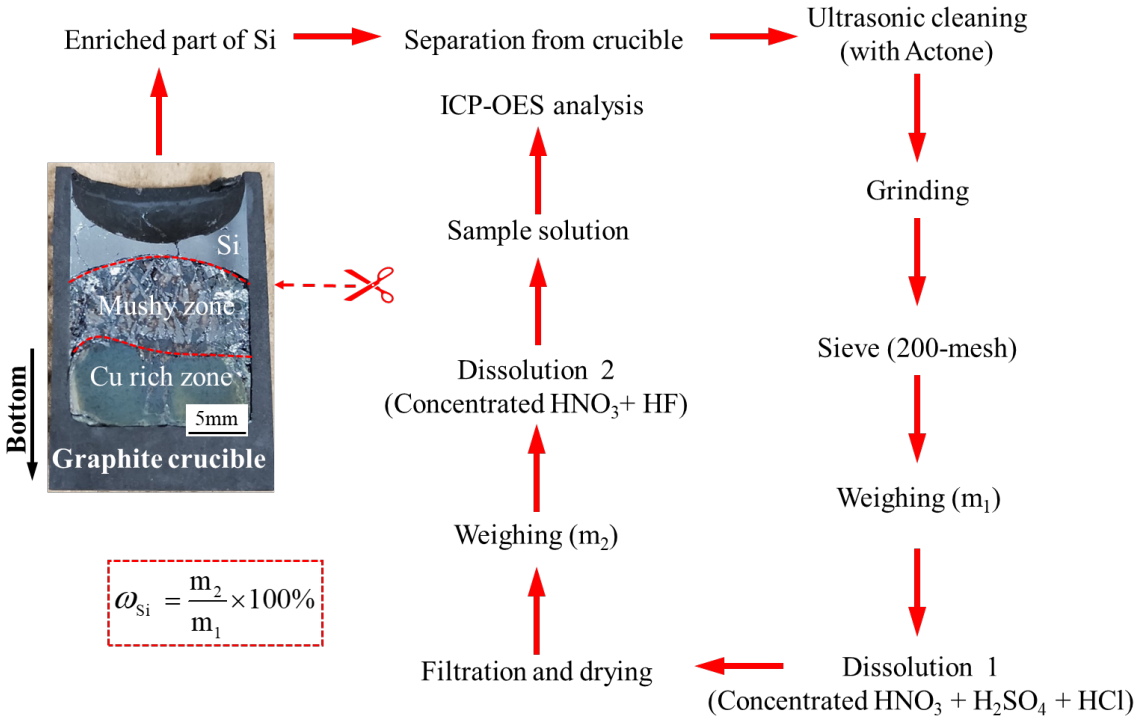

Fig. 5-2. Calculation process of Si enrichment percentage and ICP-OES analysis of enriched Si part.

Finally, the inductively coupled plasma optical emission spectrometer (ICP-OES) was used to analyse the B, Zr, and residual Cu content in the refined Si part, follow the steps outlined below: the dried Si powder was dissolved using a mixture of HNO_3 and HF (HNO_3: HF = 1:1 in volume ratio, where HF was added drop by drop to prevent a drastic reaction between Si and the acids). The ICP-OES analysis of enriched Si part is also shown in Fig. 5-2.

5.3. Results and Discussion

5.3.1. Si Enrichment and Separation

Based on the previous research results in the Si-Sn system, because of the significant density difference between solid Si ($\rho_{Si(300\ K)}$ = 2.33 g/cm^3,) and liquid Si-Sn alloy solution ($\rho_{Sn(1555\ K)}$ = 6.32 g/cm^3,), upwards moving direction is more conducive to obtaining large-area bulk polysilicon.

According to the same principle, the larger density difference between solid Si and liquid Si-Cu alloy solution ($\rho_{Cu\ (1358\ K)}$ = 8.96 g/cm^3) can also be used to obtain large area of bulk polysilicon by upwards. The cross sections of several samples from experiments conducted on different alloy components and different crucible sizes are shown in Fig. 5-3. Here, 0.01mm/min was selected as the rate of the upwards moving process uniformly.

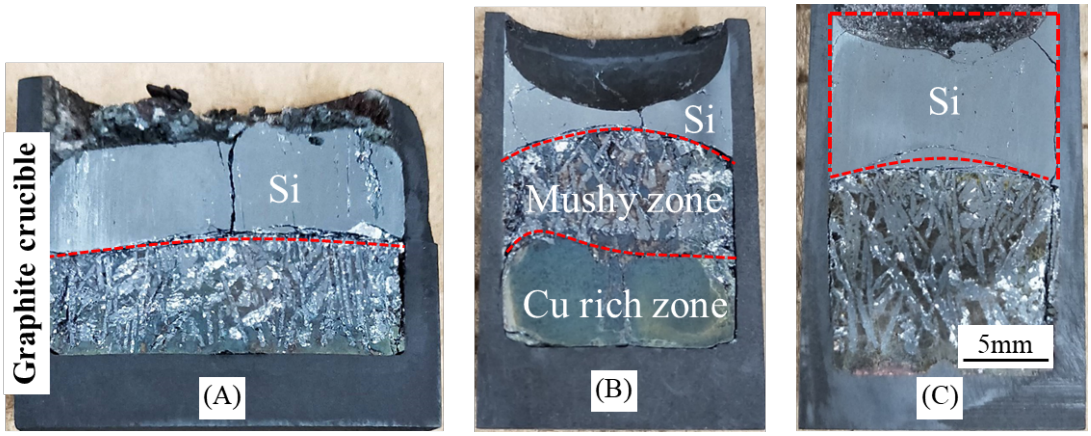

Fig. 5-3. Cross sections of sample under different conditions
(A) Si-50.0 at.% Cu, A-type crucible, (B) Si-50.0 at.% Cu, B-type crucible,
(C) Si-32.5 at.% Cu, B-type crucible.

From Fig. 5-3, it can been clearly seen that upwards moving was also favourable for growth control and enrichment of Si crystal from Si-Cu melt, which includes (i) Large area of bulk Si, (ii) Flat interface, and (iii) Stable mushy zone. The specific values of Si enrichment percentage can be calculated according to the steps shown in Fig. 5-2, the data are listed in Table 5-1.

As can be seen from Table 5-1, under the rate of 0.01mm/min, for samples with different alloy components, the Si enrichment percentage of the obtained bulk Si exceeded 99.0%, and the highest can reach 99.2%. Even under the condition of 0.04mm/min, for the alloy composition of Si-at.% Cu, the enrichment percentage of Si in the bulk Si obtained after directional solidification exceeded 82.0%. Under the same conditions, the percentages of Si are higher than those of the bulk Si obtained by the Si-Sn system (98.6 and 76.8% at 0.01 and 0.04mm/min, respectively).

Table 5-1. Enrichment percentage of Si.

Sample No.	Alloy composition (at.% Cu)	Type of crucible	Moving rate (mm/min)	Before leaching M_1(g)	After leaching M_2(g)	Si enrichment percentage (%)
Y-01	25.0	B-type	0.01	2.0020	1.9820	99.0
Y-02	50.0	B-type	0.01	1.2128	1.2031	99.2
Y-03	50.0	A-type	0.01	1.3459	1.3338	99.1
Y-04	32.5	B-type	0.01	1.5427	1.5306	99.2
Y-05	32.5	B-type	0.04	1.3630	1.1277	82.7
Y-06	32.5	B-type	0.04	1.4351	1.1504	80.2

Y-02 and Y-03 are same alloy composition using different crucible types;

Y-05 and Y-06 are the repeatability test experiments.

5.3.2. Purification (B Removal from Si)

Table 5-2. Initial compositions of Si-Cu melt and final compositions of refined Si.

No.	Moving Direction	Lifting Rate (mm/min)	Initial Composition of the Si-Cu Melt			Final Composition of Refined Si		
			B (ppmw)	Zr (ppmw)	Cu (at.%)	B (ppmw)	Zr (ppmw)	Cu (molar fraction)
R01	up	0.01	80	915	25.0	15.8	0	0.00128
R02	up	0.01	80	915	32.5	17.6	0	0.00135
R03	up	0.04	80	915	32.5	20.7	0	0.00163
R04	up	0.04	80	0	50.0	53.7	0	0.00149
R05	down	0.02	30	0	47.0	28.5	0	0.00228
R06	up	0.01	80	915	50.0	5.3	0	0.00099
R07	up	0.04	80	915	50.0	19.4	0	0.00189
R08	up	0.04	80	305	50.0	26.8	0	0.00174
R09	up	0.04	80	710	50.0	24.6	0	0.00191
R10	up	0.04	80	1220	50.0	14.5	0	0.00166
R11	up	0.04	80	1525	50.0	11.7	0	0.00184

R-04 was carried out without Zr addition, as a blank experiment.

R05 (Si-47at.% Cu) was done by Mr. Ohshima. [5-3]

Table 5-2 shows the initial B and Zr contents of the molten Si-Cu alloy and the residual impurity contents of refined Si. The initial content of B was set at 80 ppmw (153 ppma), since the B content in the MG-Si is 13–130 ppma, [5-2] as well as with the consideration of possible contamination from Cu or Zr additive.

5.3.1. Dependence on Zr Additive Content

The effect of Zr addition on B-removal fraction after solidification refining process at the moving rate of 0.04 mm/min is shown in Fig. 5-4.

When a Si-50.0 at.% Cu melt (containing 80 ppmw B) was employed as the refining solvent, the removal fraction of B increased from 32.9 to 85.4% with the increase in the Zr content from 0 to 1525 ppmw, indicating that Zr was critically responsible for the decrease of B content in the refined Si. In addition, the Zr-removal fraction in all samples is 100%, indicating that there is no Zr residual in the refined Si, this phenomenon can be explained by its very small segregation coefficient (k_{Zr} is 1.6×10^{-8} between solid Si and liquid Si at 1687 K). [5-4]

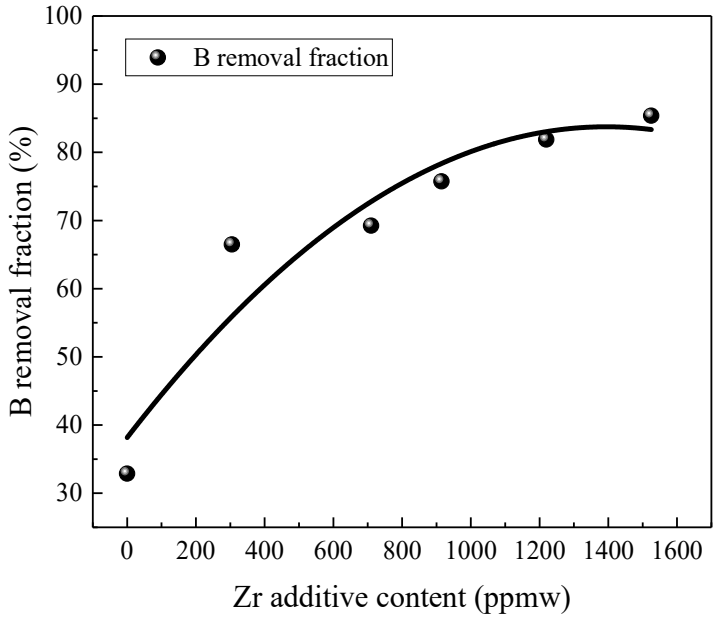

Fig. 5-4. Removal fraction of B after solidification refining with varying initial Zr additive content.

5.3.2. Dependence on Moving rate, Direction and Initial Alloy Compositions

The effect of moving rate/direction and initial alloy compositions on B-removal fraction is shown in Fig. 5-5.

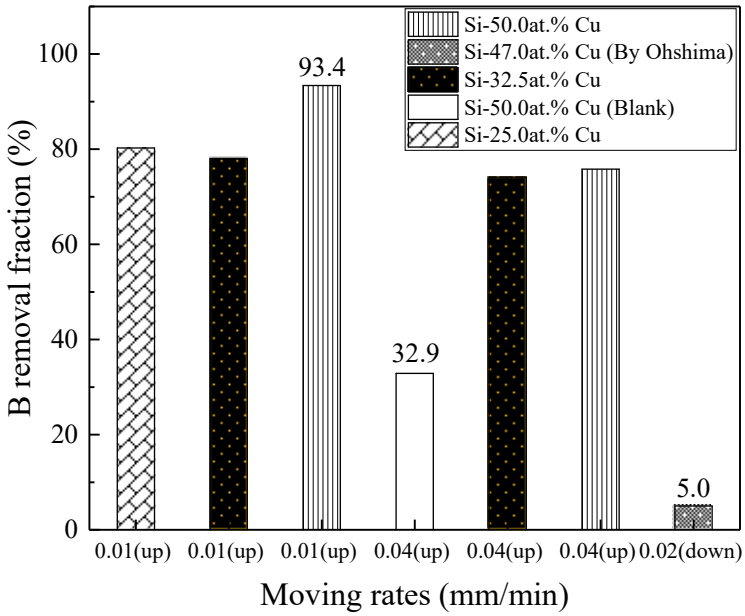

Fig. 5-5. Removal fraction of B with varying initial alloy compositions at different moving rates/directions.

According to Fig. 5-5, the highest removal fraction of B was 93.4 % with Si-50.0 at.% Cu solvent at the 0.01 mm/min upward moving rate, indicating that a higher Cu ratio, a slower cooling rate, and upward moving direction are more favorable for B removal. This result is better than that of adding Ti to the Si-Cu system to remove B, done by Huang *et al.*. [5-5] In their study, the content of B decreased from 624 to 94 ppmw with a removal fraction of 85% when the content of Ti in Si-Cu alloy was 5wt. %. Also, no residual Zr was found in purified Si part of each sample.

5.3.3. Residual Cu in the Refined Si

The residual Cu content in the refined Si of each sample is shown in Fig. 5-6. It can be seen that the molar fraction of residual Cu in the refined Si area changed from 0.00099 to 0.00191. It is lower than 0.00228 which was measured by Ohshima *via* downward moving operation, which can be elucidated as: in the upward directional solidification process, the hot zone was located in the lower part of the crucible, which is beneficial for the mass transfer and thermal convective, and the strong self-miscellaneous ability led to less Cu residual in crystalline primary Si. While, it still slightly higher than the value of solid solubility of Cu in Si, [5-6] which should be further reduced by the subsequent refining process.

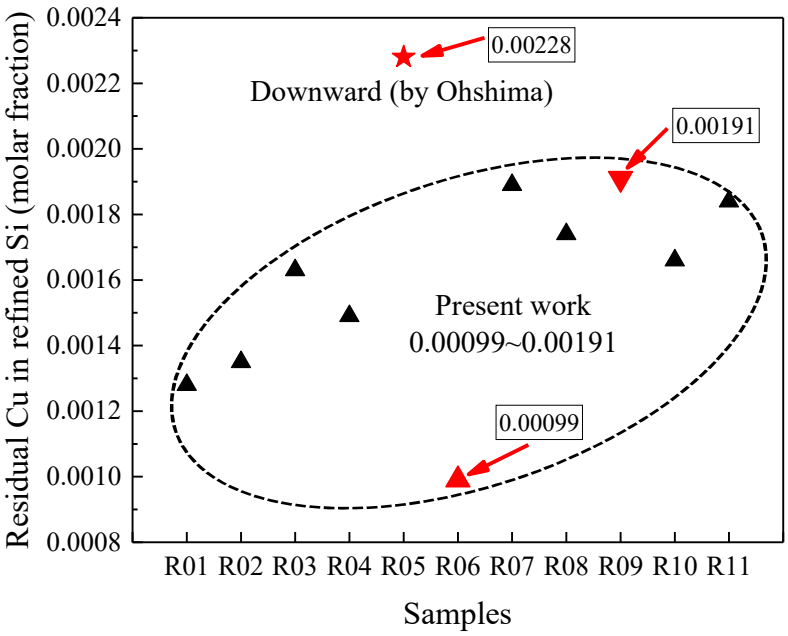

Fig. 5-6. Residual Cu content in refined Si of each sample under different conditions.

5.3.3. Distribution Behavior of Boride

The mechanism of the B removal from Si using the Si-Cu solvent with the Zr addition was clarified by applying an EPMA analysis to the alloy sample (R06 in Table 5-2). Fig. 5-7 (a) shows the longitudinal section of this sample, which showed that the primary Si phase was agglomerated at the top part of the sample, with upwards moving direction. It not only obtains a large area of bulk Si which is beneficial for reducing the consumption of the acid solution to isolate the Si crystals, but also has a stable interface. Previous research [5-7, 8] has conducted in-depth research on this phenomenon why upwards is more suitable for getting large area of bulk Si.

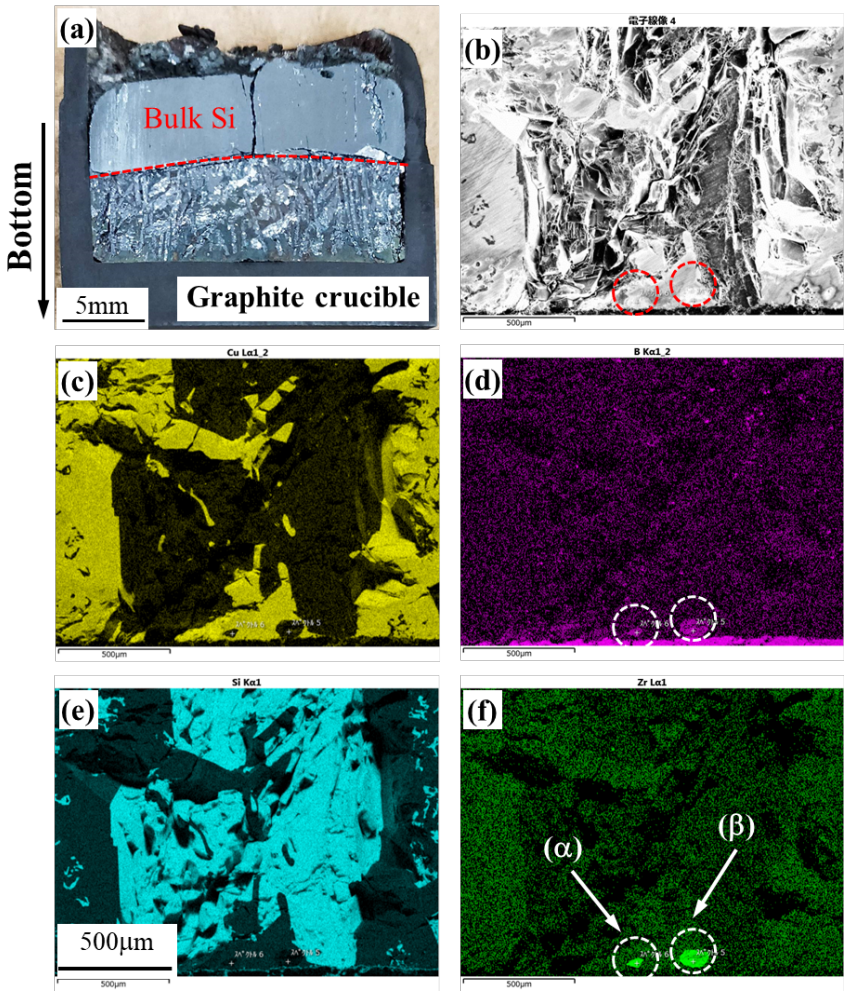

Fig. 5-7. (a) is a photograph section of the Si-50.0at.% Cu alloy after directional solidification refining; (b) is a SEM image of the bottom region in (a); (c), (d), (e) and (f) are the element maps of Cu, B, Si and Zr in (b), respectively.

As shown in Fig. 5-7 (b)-(f), there were some B-Zr rich phases near the bottom of the sample. The detailed value of each element for phases (α) and (β), as well as comparison with those of pure reagent ZrB_2 are listed in Table 5-3. The results also show that phases (α) and (β) are ZrB_2, according to their almost the same ingredients as pure reagent.

Table 5-3. EPMA quantitative analysis for phase (α) and phase (β) in Fig. 5-7(f).

Substance	Atomic percent (%)			
	B	Zr	Cu	Si
Phase (α) in Fig. 5-7(f)	66.74	33.13	0.08	0.05
Phase (β) in Fig. 5-7(f)	70.69	29.12	0.12	0.07
Standard ZrB_2	66.62	33.38	---	---

5.3.4. Segregation Coefficient of B in Si–Cu Melt with Zr Addition

In Chapter IV, it was concluded that the B content in molten Si–Cu gradually decreases with the increasing Zr content. [5-1] It can be employed to predict the precondition for the formation of stable ZrB_2 and the final B content in the molten Si–Cu after Zr addition. Also, experimental results in this paper indicated that B removal from solid Si crystals (not molten Si–Cu) could be significantly enhanced by the addition of Zr, which also confirmed in Si-Al system. [5-9]

The segregation coefficient of B between solid Si and molten Si–Cu is the key factor for predicting the B removal from Si crystals thermodynamically, which can be determined using the following equations.

The segregation coefficient of B between solid Si and molten Si–Cu can be expressed by Eq. (5-7), when the chemical potentials of B in the solid Si and molten Si–Cu are identical at equilibrium, as indicated by Eq. (5-1). Further, $\Delta G_{\mathrm{B}}^{\mathrm{o}\,fus}$ can be expressed as Eq. (5-2), which denotes the Gibbs energy change for the fusion of B. [5-10]

$$\mathrm{B(s)}_{\text{in solid Si}} = \mathrm{B(l)}_{\text{in Si-Cu melt}} \tag{5-1}$$

$$\Delta G_{\mathrm{B}}^{\mathrm{o}\,fus} = 50184 - 21.82T \ (J/mol) \tag{5-2}$$

$$\mu_{\text{B in solid Si}} = \mu_{\text{B in Si-Cu melt}} \tag{5-3}$$

$$G_{\text{B (s)}}^{\mathrm{o}} + RT\ln a_{\text{B (s) in solid Si}} = G_{\text{B (l)}}^{\mathrm{o}} + RT\ln a_{\text{B (l) in Si-Cu melt}} \tag{5-4}$$

$$RT\ln a_{\text{B (s) in solid Si}} = \Delta G_{\mathrm{l}}^{\mathrm{o}\,fus} + RT\ln a_{\text{B (l) in Si-Cu melt}} \tag{5-5}$$

$$\Delta G_{\mathrm{l}}^{\mathrm{o}\,fus} = -RT\ln\frac{a_{\text{B(l) in Si-Cu melt}}}{a_{\text{B(s) in Solid Si}}} = -RT\ln\frac{\gamma_{\text{B(l) in Si-Cu melt}} \bullet X_{\text{B in Si-Cu melt}}}{a_{\text{B(s) in Solid Si}}} \tag{5-6}$$

$$\ln k_{\mathrm{B}} = \ln\frac{X_{\text{B in Solid Si}}}{X_{\text{B in Si-Cu melt}}} = \frac{\Delta G_{\mathrm{l}}^{\mathrm{o}\,fus}}{RT} + \ln\frac{\gamma_{\text{B(l) in Si-Cu melt}}}{\gamma_{\text{B(s) in Solid Si}}} \tag{5-7}$$

As the content of B in the solid Si in this study was very low, the activity coefficient of B can be determined using the first-order interaction parameters, as expressed in Eq. (5-8).

$$\begin{aligned}\ln\gamma_{\text{B(s) in Solid Si}} = {} & \ln\gamma^{0}_{\text{B in Solid Si}} + \varepsilon^{\mathrm{B}}_{\text{B in Solid Si}} \cdot X_{\text{B in Solid Si}} \\ & + \varepsilon^{\mathrm{Zr}}_{\text{B in Solid Si}} \cdot X_{\text{Zr in Solid Si}} + \varepsilon^{\mathrm{Cu}}_{\text{B in Solid Si}} \cdot X_{\text{Cu in Solid Si}}\end{aligned} \tag{5-8}$$

$\varepsilon^{\mathrm{Zr}}_{\text{B in Solid Si}} \cdot X_{\text{Zr in Solid Si}}$ can be ignored, since the solubility of Zr in the solid Si was extremely small. $\varepsilon^{\mathrm{B}}_{\text{B in Solid Si}} \cdot X_{\text{B in Solid Si}}$ for the Zr-saturated Si-Cu melt also can be

ignored because of the small value of $X_{\text{B in Solid Si}}$. For example, it is measured as 5.3 ppmw at 1345 K (53 ± 2 ppma in the Zr-saturated Si-Cu melt at 1345 K, *i.e.*, the average value of S-07 and S-08 in Table 4-1 in Chapter IV). [5-1]

Similarly, the activity coefficient of B in the liquid Si-Cu melt at the liquid stand state can be obtained, as expressed in Eq. (5-9).

$$\begin{aligned}\ln \gamma_{\text{B(l) in Si-Cu melt}} = & \ln \gamma^{0}_{\text{B(l) in Si-Cu melt}} + \varepsilon^{\text{B}}_{\text{B in Si-Cu melt}} \cdot X_{\text{B in Si-Cu melt}} \\ & + \varepsilon^{\text{Zr}}_{\text{B in Si-Cu melt}} \cdot X_{\text{Zr in Si-Cu melt}} + \varepsilon^{\text{Cu}}_{\text{B in Si-Cu melt}} \cdot X_{\text{Cu in Si-Cu melt}}\end{aligned} \tag{5-9}$$

Therefore, the segregation coefficient can be estimated using Eq. (5-10).

$$\begin{aligned}\ln k_{\text{B}} &= \ln \frac{X_{\text{B in Solid Si}}}{X_{\text{B in Si-Cu melt}}} \\ &= \frac{\Delta G_{1}^{\text{o}\,fus}}{RT} + \ln \frac{\gamma_{\text{B(l) in Si-Cu melt}}}{\gamma^{0}_{\text{B(s) in Solid Si}}} - \varepsilon^{\text{Cu}}_{\text{B in Solid Si}} \cdot X_{\text{Cu in Solid Si}}\end{aligned} \tag{5-10}$$

$\ln \gamma^{0}_{\text{B in Solid Si}}$ has been estimated by Yoshikawa et.al. ($\ln \gamma^{0}_{\text{B in Solid Si}} = \frac{14073(\pm 276.6)}{T} - 5.73(\pm 0.19),\ (1273\ \text{K} < T < 1473\ \text{K})$) [5-11] and Khajavi et.al. ($\ln \gamma^{0}_{\text{B in Solid Si}} = \frac{16317(\pm 282)}{T} - 7.06(\pm 0.18),\ (1483\ \text{K} < T < 1583\ \text{K})$) [5-12].

$X_{\text{Cu in Solid Si}}$ at different temperatures can be obtained from Si-Cu binary phase diagram. Although the value of $\varepsilon^{\text{Cu}}_{\text{B in Solid Si}}$ was not reported by previous researchers, it can be speculated to be negative due to the strong affinity of Zr for B. This leads to decrease of k_{B} with the increase of $X_{\text{Zr in Si-Cu melt}}$, indicating that at higher concentrations of Zr, B removal is improved because of decreases in segregation coefficient of B.

Moreover, this can be explained by the followings, the observed continued increase of B removal with higher Zr addition, as the other mechanism (ZrB_2 formation) is expected to level off once $ZrSi_2$ begins to form. Also, when molten Si-Cu was saturated with both Zr and B, both ZrB_2 and $ZrSi_2$ were stable in Si-Cu melt, as indicated by Fig. 5-8 (calculated by FactSage™ Equilib module).

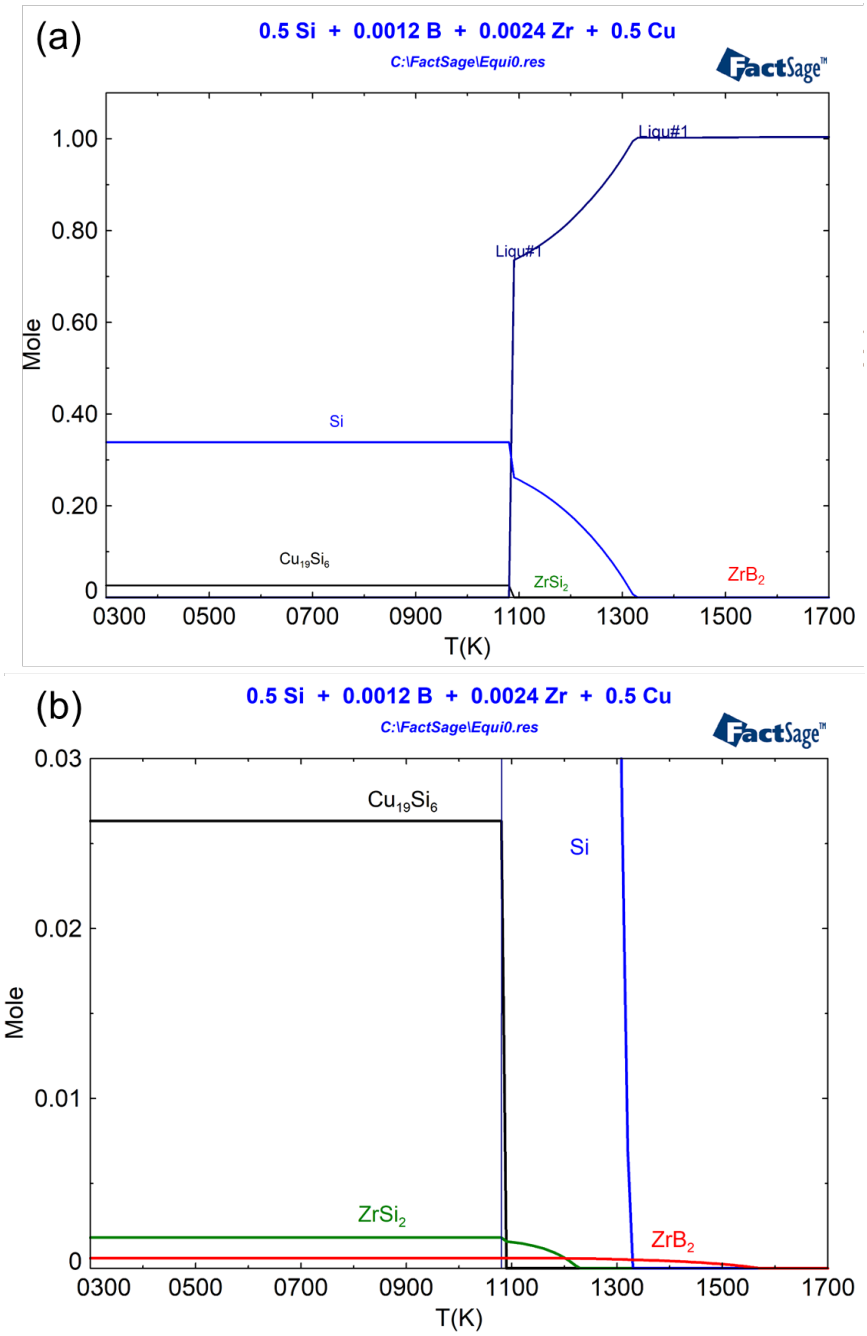

Fig. 5-8. Cooling process diagram of Si-50.0 at.% Cu melt with initial conditions of 1200 ppma B and 2400 ppma Zr calculated using FactSage™: (a) full-scale, (b) partially enlarged.

It can be seen from Fig. 5-8 that the sequence of precipitated phases (exclusive of primary Si phase) in the solidification process is ZrB_2, $ZrSi_2$, and $Cu_{19}Si_6$, respectively. This confirms the aforementioned analysis that boride (ZrB_2) begin to form before the primary Si precipitates, which further proved the feasibility of adding Zr to remove B.

As shown in Fig. 5-9, the crystal structure of the unit cells of Cu_7Si_2, $ZrSi_2$, and ZrB_2 are different. ZrB_2 has a hexagonal structure with lattice parameters of a = 0.3180nm, b = 0.3180nm, and c = 0.3545nm. $ZrSi_2$ has an orthorhombic structure with lattice parameters of a = 0.3686nm, b = 0.3708nm, and c = 0.7629nm. Cu_7Si_2 has a trigonal structure with lattice parameters of a = 0.4085nm, b = 0.4085nm, and c = 0.7587nm. It has been reported that the solubility of Si in the borides as well as silicides is negligible. [5-5] Thereby, the existence of a stable ZrB_2 phase is proposed to be consistent with the experimental results. Moreover, with shorter bond length, the Cu_7Si_2 was more stable than $ZrSi_2$.

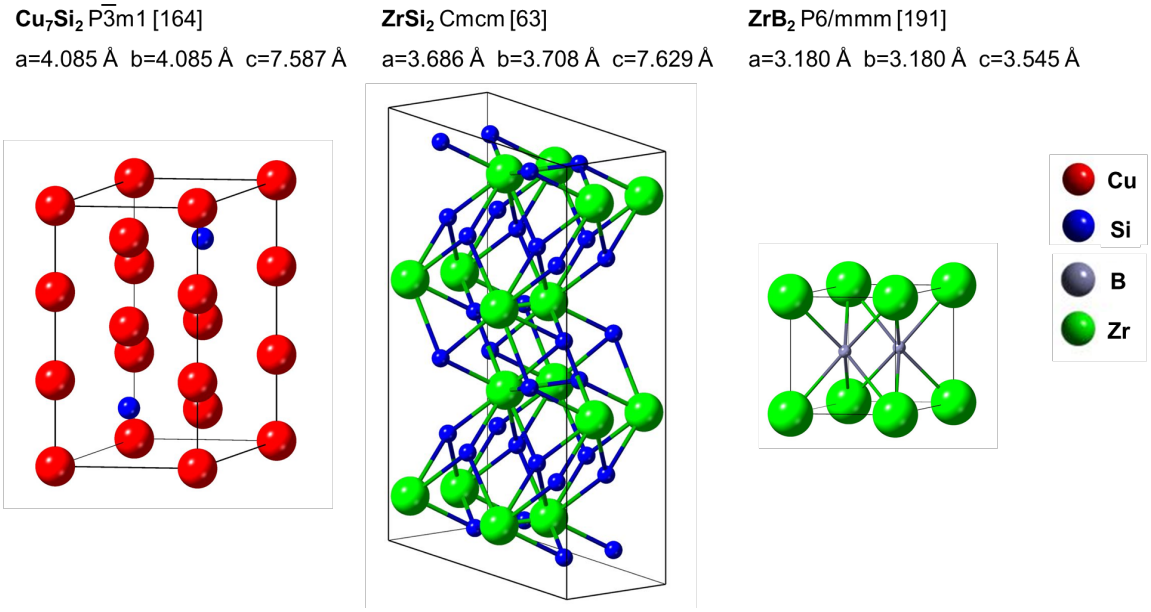

Fig. 5-9. Crystal structure of Cu_7Si_2, $ZrSi_2$, and ZrB_2.

The activities of Zr and B were fixed based on Eq. (5-11) and Eq. (5-14), as the activities of Si, ZrB_2 and $ZrSi_2$ could be regarded as unity (the solubility of Cu in $ZrSi_2$ could be also ignored, same as in ZrB_2). The standard state of Si in Eq. (5-14) can be chosen as liquid or solid, which does not influence the final results. The reaction equations can be seen as follows, [5-13~16]

$$Zr(l) + 2B(l) = ZrB_2(s) \tag{5-11}$$

$$\Delta G^{o}_{ZrB_2} \cong -449000 + 76.9T\,(J/mol) \tag{5-12}$$

$$\Delta G^{o}_{ZrB_2} = -RT \ln \frac{a_{ZrB_2(s)}}{a_{Zr(l)\text{ in Si-Cu melt}} \cdot a^{2}_{B(l)\text{ in Si-Cu melt}}} \tag{5-13}$$

$$Zr(l) + 2Si(s) = ZrSi_2(s) \tag{5-14}$$

$$\Delta G^{\circ}_{ZrSi_2} \cong -186000 + 21.9T \text{ (J/mol)} \quad (5\text{-}15)$$

$$\Delta G^{\circ}_{ZrSi_2} = -RT \ln \frac{a_{ZrSi_2(s)}}{a_{Zr(l) \text{ in Si-Cu melt}} \cdot a^{2}_{Si(s) \text{ in Si-Cu melt}}} \quad (5\text{-}16)$$

$$= RT \ln a_{Zr(l) \text{ in Si-Cu melt}}$$

Based on FactSage calculation, $\gamma_{B(l) \text{ in Si-Cu melt}}$ and $\gamma_{Zr(l) \text{ in Si-Cu melt}}$ at 1345 K in Zr- and Si-saturated Si-50 atom% Cu melt were estimated as 4.97 and 0.0028, respectively. Consequently, k_B was concluded become smaller in Si-Cu system (0.29 at 1345 K) than that in pure Si system (0.80 at 1687 K) [5-17] and continuous decreasing with increasing in Zr addition content (0.21 when 915 ppmw Zr was added), as shown in Fig. 5-10, which consistent with previous analysis.

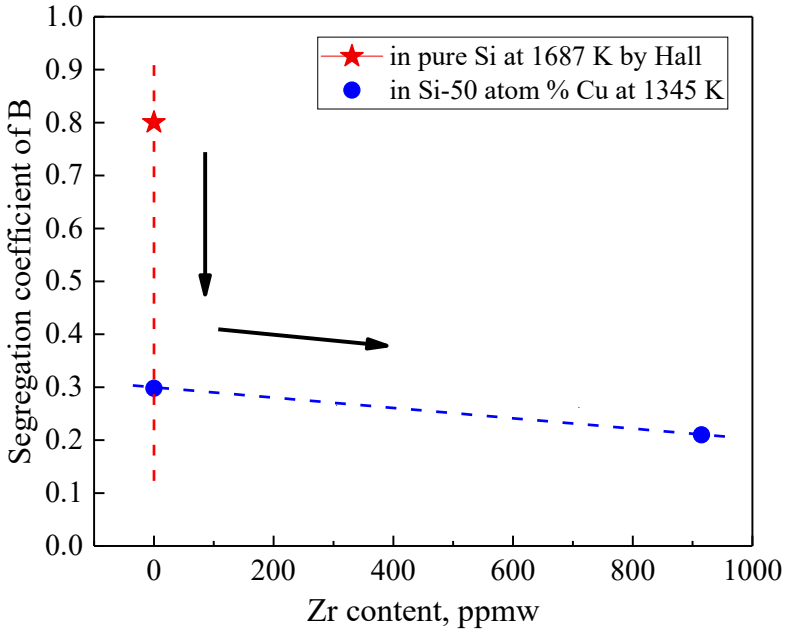

Fig. 5-10. Effect of Zr addition content on the B-segregation coefficient in the Si-Cu melt at 1345 K compared with that in pure Si system.

Therefore, the main reason of the enhancement of the B removal by the Zr addition was the decrease in the segregation coefficient of B between the solid Si and the liquid Si–Cu melt, *i.e.*, k_B. Additionally, the Zr addition significantly reduced the content of B in the molten Si–Cu, as concluded in previous work; thus, the content of B in the solid Si can also be reduced significantly, according to the definition of k_B given by Eq. (5-7).

5.4. Short Summary

Based on the conclusion of Chapter IV, a series of experiments of directional solidification refining using Si-Cu solvent with Zr addition were carried out.

The experimental results show that: (i) the B-removal fraction was improved significantly as expected, the highest of which is 93.4%; (ii) Large area of bulk Si was obtained by upwards, and highest Si enrichment percentage is 99.2%; and (iii) the residual Cu content can be reduced to a relative low level, the molar fraction of which ranging from 0.00099 to 0.00191 (slightly higher than the value of solid solubility of Cu in Si).

It is concluded that the reason for the high removal fraction of B in the Si-Cu system is not only the small solubility products of Zr and B mentioned in Chapter IV, but also the smaller segregation coefficient of B in the Si-Cu system rather than in the pure Si system. However, the lowest B content in the experiment is still 5.3 ppmw, which needs to be further reduced to meet the requirements of solar grade Si.

References

5-1 Y. Ren, S. Ueda, and K. Morita, Formation Mechanism of ZrB_2 in a Si-Cu Melt and its Potential Application for Refining Si and Recycling Si Waste. *ACS Sustainable Chem. Eng.,* 7 (2019) 20107−20113. https://doi.org/10.1021/acssuschemeng.9b05986

5-2 C.P. Khattak, D.B. Joyce, F. Schmid: *Report, Crystal Systems, Inc.*, Massachusetts, December (1999).

5-3 大嶋 陽介: 東京大学修士論文 (2012).

5-4 Hopkins, R. H.; Rohatgi, A. Impurity effects in silicon for high efficiency solar cells, *J. Cryst. Growth*, 75 (1986) 67-79.

5-5 Huang, L.; Chen, J.; Danaei, A.; Thomas, S.; Huang, L.; Luo, X.; Barati, M. Effect of Ti addition to Cu-Si alloy on the boron distribution in various phases. *J. Alloys Compd.,* 734 (2018) 235-242.

5-6 F.A. Trumbore, Solid solubilities of impurity elements in germanium and silicon. *Bell Syst. Tech. J.,* 39 (1960) 206–233.

5-7 Y. Ren, H. Wang, and K. Morita, Growth control and enrichment of Si crystals from Si-Sn melt by directional solidification. *Vacuum*, 158 (2018) 86-92.

5-8 Y. Ren, H. Wang, and K. Morita, Effect of Zr addition on B-removal behavior during solidification purification of Si with Si-Sn solvent. *Vacuum*, 167 (2019) 319-328.

5-9 Lei, Y.; et al., Mechanism of ZrB_2 Formation in Al–Si Alloy and Application in Si Purification. *ACS Sustainable Chem. Eng*., 7 (2019) 12990–12996.

5-10 E.T. Turkdogan, *Physical Chemistry of High-temperature Technology*, Academic Press, New York, (1980) 5.

5-11 Yoshikawa, T.; Morita, K. Thermodynamic property of B in molten Si and phase relations in the Si–Al–B system, *Mater. Trans.*, 46 (2005) 1335–1340.

5-12 Khajavi, L.T.; et al., Thermodynamics of boron distribution in solvent refining of silicon using ferrosilicon alloys. *J. Alloys Compd.*, 619 (2015) 634-638.

5-13 Barin, I. Thermochemical Data of Pure Substances, *VCH, Weinheim*, 1989, p.1384, 1523, 1708.

5-14 Chen, H.; Zheng, F.; Liu, H.; Liu, L.; Jin, Z. Thermodynamic assessment of B-Zr and Si-Zr binary systems, *J. Alloys Compd.,* 468 (2009) 209-216.

5-15Turkdogan, E.T. Physical Chemistry of High-temperature Technology, *Academic Press*, New York, 1980, p. 20, 21, 24.

5-16 Lei, Y.; Ma, W.; Sun, L.; Dai, Y.; Morita, K. B removal by Zr addition in electromagnetic solidification refinement of Si with Si-Al melt, *Metall. Mat. Trans. B*, 47 (2016) 27-31.

5-17Hall, R.N. Segregation of impurities during the growth of germanium and silicon, *J. Phys. Chem. A.,* 57 (1953) 836-839.

Chapter VI. B Removal Using Si-Sn-Cu Ternary Solvent with Zr addition

6.1. Introduction

Based on the previous experimental results (Chapter III and IV), a single solvent refining treatment can not obtain perfect B removal fraction (final B contents in refined Si are 42.5 and 5.3 ppmw for Si-Sn and Si-Cu system, respectively); thus, combined purification systems are necessary to increase the purification efficiency.

Note that, Si–Al and Si–Sn solvent refining were combined to refine MG-Si by considering their respective characteristics has been reported by Lei, H *et al*. [6-1] The theoretical basis of their experiment are (i) the Si–Al alloy exhibits a low alloy melting point and (ii) the Si–Sn system is relatively effective for Si separation because of the larger density difference between Si ($\rho_{Si\ (300\ K)} \approx 2.33\ g/cm^3$) and Sn ($\rho_{Sn\ (1555\ K)} \approx 6.32\ g/cm^3$) than that between Si and Al.

The results indicate that P can be removed as P-containing phases such as Al–Ca–Mg–Si–P and Al–Si–P, which precipitate on the surface of primary Si during the solidification process. Its final content can be reduced to 0.46 ppmw, representing a removal efficiency of 99.8%. Similarly, the formation of binary silicides such as Fe_3Si_7 and $Mn_{11}Si_{19}$ or multicomponent phases such as the Ca–Mg–Si phase, which segregate on the grain boundaries or attach onto the surface of Si, can lead to a high removal efficiency of metallic impurities. Finally, their final total removal efficiencies are greater than 99.9%.

Based on the results discussed above, in this Chapter, I try to use Si-based ternary solvent (**Si-Sn-Cu**) method to further strengthen the B removal.

6.2. Principle

From Chapter II to Chapter V, I have studied the enrichment of primary Si and the addition of Zr to remove B in the systems of Si-Sn and Si-Cu. The characteristics of the two systems are summarized as follows;

Si-Sn: (i) the Si-Sn system has a moderate liquidus slope, [6-2] which indicates a large amount of precipitated Si at equilibrium; [6-3] (ii) the precipitated primary Si can grow and float easily due to the buoyancy caused by the significant density difference between primary Si and liquid Si-Sn ($\rho_{Si(300\ K)}$ = 2.33 g/cm^3, $\rho_{Sn(1555\ K)}$ = 6.32 g/cm^3 [6-4]); (iii) the activity coefficient of B in the Sn-rich side is three orders of magnitude larger than that in the Si-rich side, so B becomes thermodynamically more unstable in the Si-Sn alloy melts. [6-5] Therefore, additives (such as Zr and Ti) which have strong affinity for B can be used to enhance the B removal fraction during the solidification refining process; (iv) Sn is an electrical inactivity element in solar cells [6-6] which means that it can tolerate relative high content of Sn in refined Si; and (v) Sn has a higher vapor pressure than Si that means the remaining Sn in Si can be removed by vacuum melting. While, the liquidus temperature is higher that is not conductive for the formation of boride.

Si-Cu: (i) it has very small solid solubility in Si, [6-7] (ii) there is an obvious difference in density between primary Si ($\rho_{Si\ (300\ K)}$ = 2.33 g/cm^3) [6-8] and liquid Si-Cu ($\rho_{Cu\ (1358\ K)}$ = 8.96 g/cm^3), [6-9] and because (iii) it has a much lower liquidus temperature than a Si-Sn system, but a similar liquidus temperature compared to a Si-Al system. However, the region of primary Si is relatively short.

6.3. Experiment

Table 6-1. Properties of Si, Sn, Cu, and their molar ratio.

Element	Melting point (℃)	Density (×10^3 kg/m^3)	Atomic weight	Mole number
Si	1414	2.33	28.08	2
Sn	231.89	6.54	118.71	1
Cu	1084.6	8.96	63.55	1

30 g of bulk Si, Sn grain and Cu powder (Si: Sn: Cu = 2:1:1 in molar ratio, as listed in Table 6-1), together with different amounts of pre-melted Si-1 mass% B and Si-1 mass% Zr alloys (same raw materials as introduced in Chapter III section 3.3.1), were placed in a B-type graphite crucible (20 mm outer diameter (OD), 14 mm inner diameter (ID), 70 mm length) to prepare the Si-25at.% Sn- 25at.% Cu alloys with target amount of B (153ppma) and Zr (211 ppma).

The projection diagram of the Si-Sn-Cu ternary system can be generated from FactSage, as shown in Fig. 6-1. Also the cooling path diagram of Si-25at.% Sn-25at.% Cu can be estimated as in Fig. 6-2. From Fig. 6-2, it can be seen that the primary Si began to precipitate at about 1210℃, so I set three holding temperatures (1230, 1200, 1170℃, respectively) in the process of directional solidification. The upwards moving rate is 0.01mm/min and the moving distance is 10 cm, the experimental process is shown in Fig. 6-3.

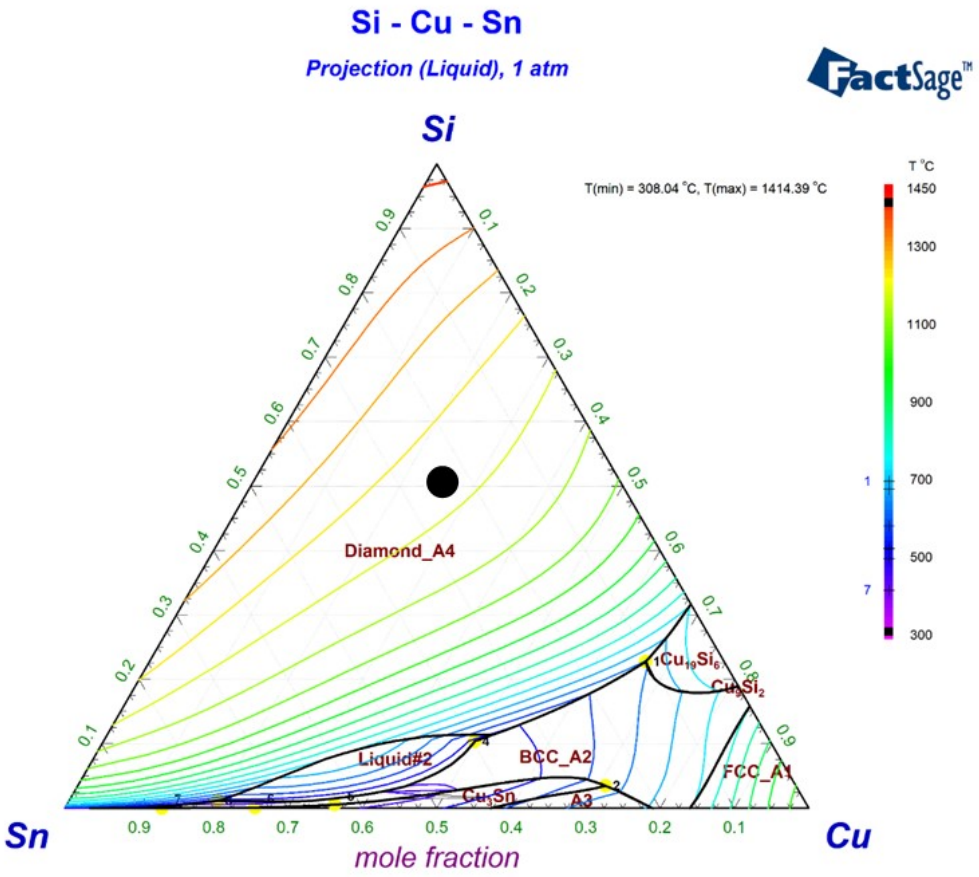

Fig. 6-1. Projection diagram of the Si-Sn-Cu ternary system.

The samples were cut open along the longitudinal section when the solidification was completed. After polished using standard metallographic techniques, a digital camera and a scanning electron microscope equipped with an energy-dispersive spectrometer (SEM-EDS) were used to observe the macroscopic and microscopic morphology of the samples.

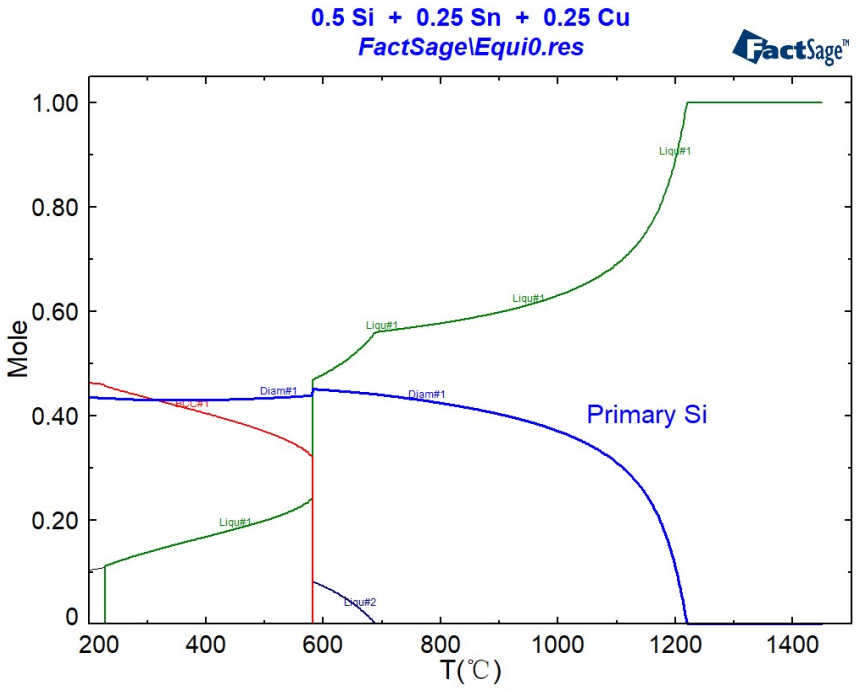

Fig. 6-2. Primary Si began to precipitate at about 1210 ℃.

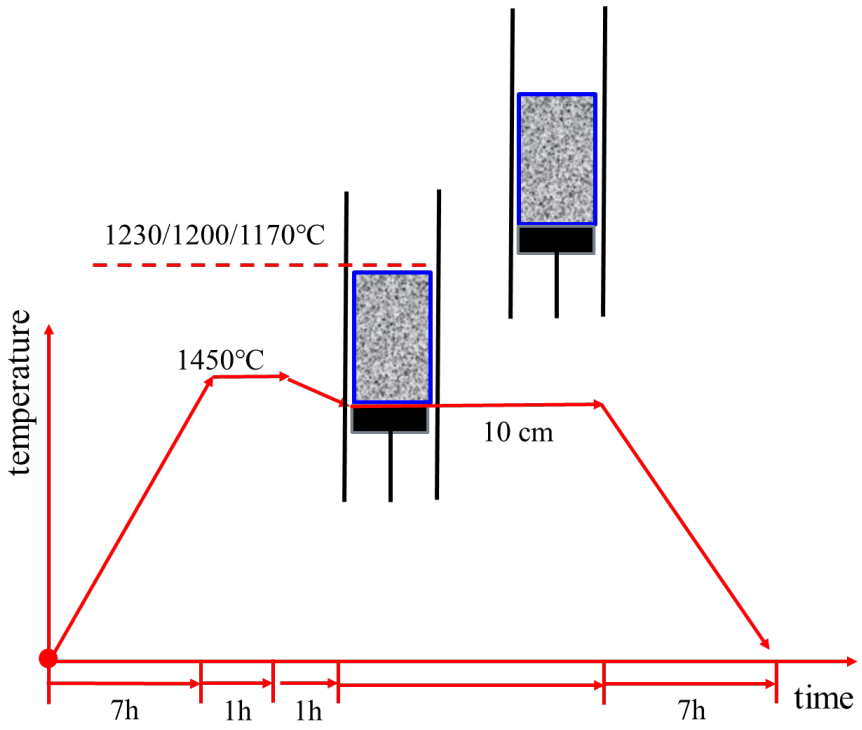

Fig. 6-3. Experimental process.

The enriched Si part was cut off along the interface, subsequently subjected to ultrasonic cleaning with acetone, ground into powders in an agate mortar, and then sifted using a 200 mesh sieve (particle diameter < 75 μm). Furthermore, the mass of

the powder was precisely determined and recorded as m_1. Afterward, the powder was dissolved using concentrated mixed acid (HNO_3 + H_2SO_4 + HCl) to remove Sn and Cu in the intergranular and liquid phases, followed by filtration and drying. The mass of the dried powder was also measured and recorded as m_2. Therefore, the enrichment Si percentage (ω) could be calculated by $m_2/m_1 \times 100\%$. Finally, after the dissolution of dried powder, the B content in the enriched Si part was analysed by an inductively coupled plasma optical emission spectrometer (ICP-OES).

6.4. Results and Discussion

6.4.1. Si Enrichment and Separation

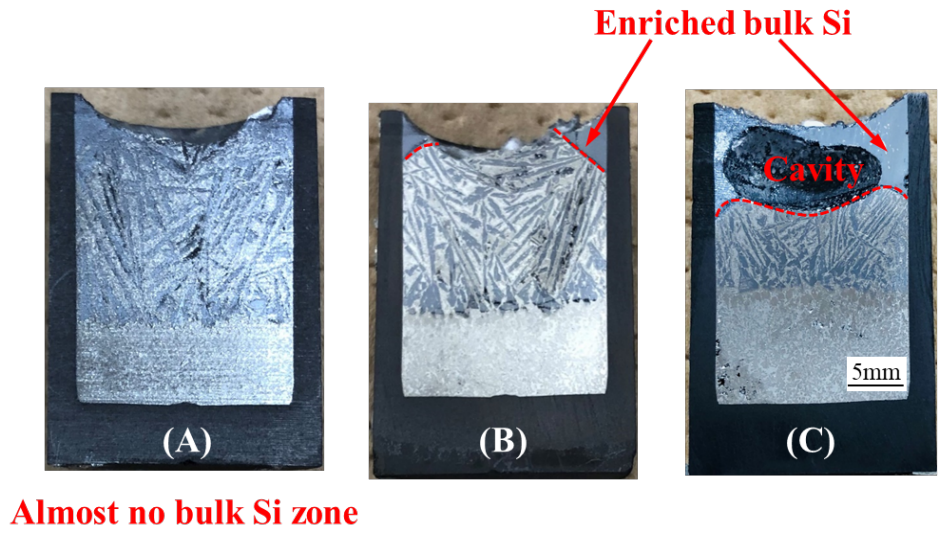

Fig. 6-4. Cross section of Si-25at.%Sn-25at.%Cu samples at different holding temperature. (A) 1230℃, (B) 1200℃, (C) 1170℃.

We know, effective temperature control during directional solidification is the key factor to obtain larger area of bulk Si. To confirm the temperature at which a large area of Si enrichment can be achieved, the experimental temperature was set at 1230, 1200, and 1170 ℃, respectively.

The upwards moving rate is 0.01mm/min and the moving distance is 10 cm. The cross sections of the samples are shown in Fig. 6-4(A)-(C). The experiment results showed that the amount of precipitated Si increased with the decrease in holding temperature. Especially for sample C, the bulk Si can be clearly seen with naked eye.

It should be mentioned that the upwards process also involved a flat interface and a stable mushy-zone in Si-Sn-Cu ternary system.

The sample in Fig. 6-4-(B) was analysed using a SEM-EDS instrument to reveal the morphology changes of the solidified alloy. The SEM image and mapping analysis results are presented in Fig. 6-5. It was determined that the cross section of the sample consisted of three parts: a Si rich zone, a mushy-zone (transition region), and a Sn-Cu rich zone. It can be clearly seen that the amount of Sn and Cu in the Si enriched area is very low.

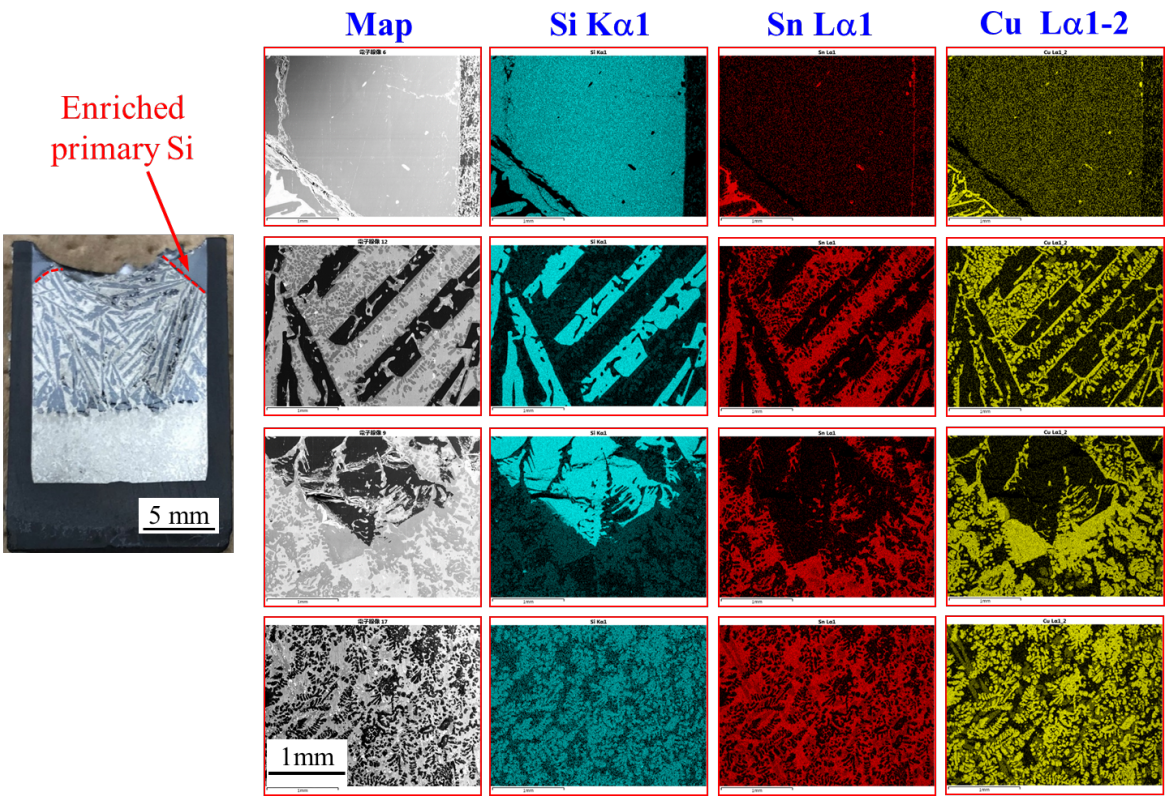

Fig. 6-5. Cross section of sample (B) in Fig. 6-4
and SEM-EDS maps for each element.

After removing Sn and Cu in the intergranular and liquid phases using concentrated mixed acid (HNO_3 + H_2SO_4 + HCl), the Si enrichment percentage can be calculated, the calculation process is shown in Fig. 6-6, and the detailed data are listed in Table 6-2.

Here I choose sample 6-4 (C) for analysis to obtain Si enrichment percentage because it has a relatively large area of bulk Si. In Table 6-2, comparison were made

with the previous enrichment experiments under the same conditions of binary system (Si-Sn, and Si-Cu). The results of the comparison are shown in Fig. 6-7.

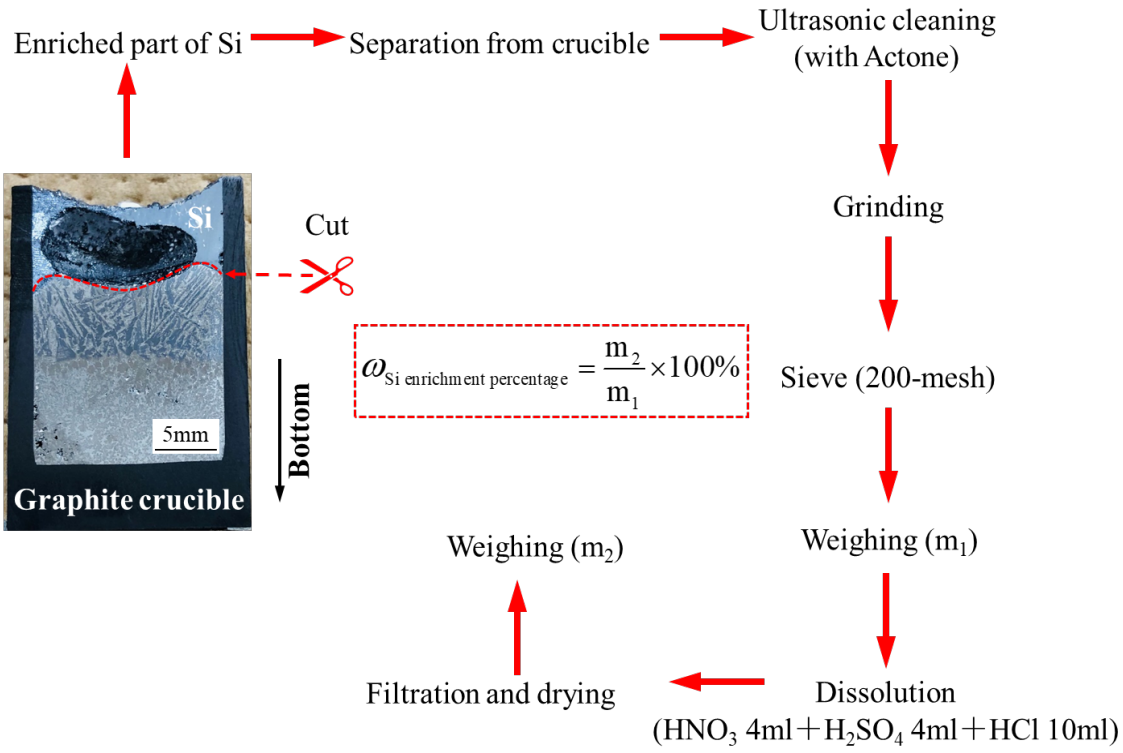

Fig. 6-6. Calculation process of Si enrichment percentage.

Table 6-2. Si enrichment percentage in different solvent systems at 0.01 mm/min upward moving rate.

Sample	Alloy system			Acid	m_1	m_2	Si enrichment percentage (%)
	Si (at.%)	Sn (at.%)	Cu (at.%)				
1	50	50	0	HCl	1.2839	1.2663	98.6
2	50	0	50	HNO_3+H_2SO_4 +HCl	1.2128	1.2031	99.2
3	50	25	25	HNO_3+H_2SO_4 +HCl	1.3746	1.3637	99.2

From Fig. 6-7, it can be seen that the Si enrichment percentage obtained by using ternary system (Si-Sn-Cu) as solvent is 99.2%, which is similar to that (99.2%) obtained by using binary system of Si-Cu, slightly higher than that (98.6%) obtained by using Si-Sn system.

This shows that the use of ternary system does not increase the difficulty of obtaining large area of bulk Si, as long as the holding temperature is slightly higher than the liquidus temperature of alloy composition during directional solidification (it can be concluded that the liquidus temperature is about 1170 ℃ for Si-25at.% Sn-25at.% Cu alloy).

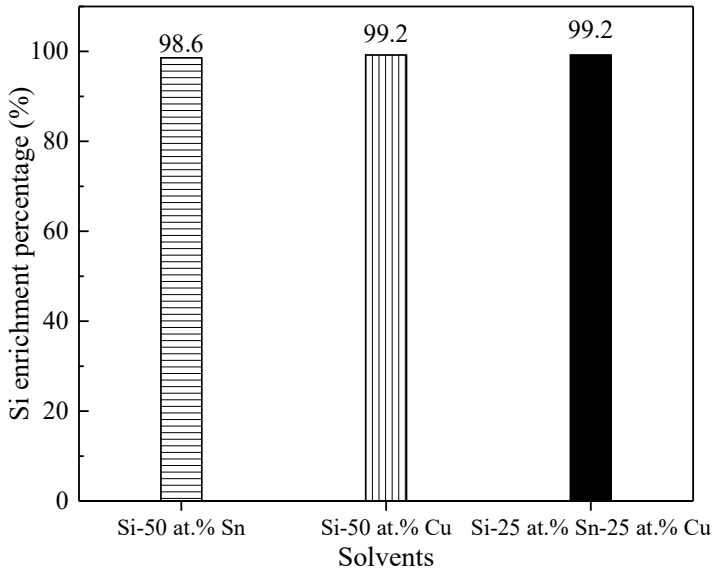

Fig. 6-7. Si enrichment percentage in different solvent systems.

6.4.2. Purification (B Removal from Si)

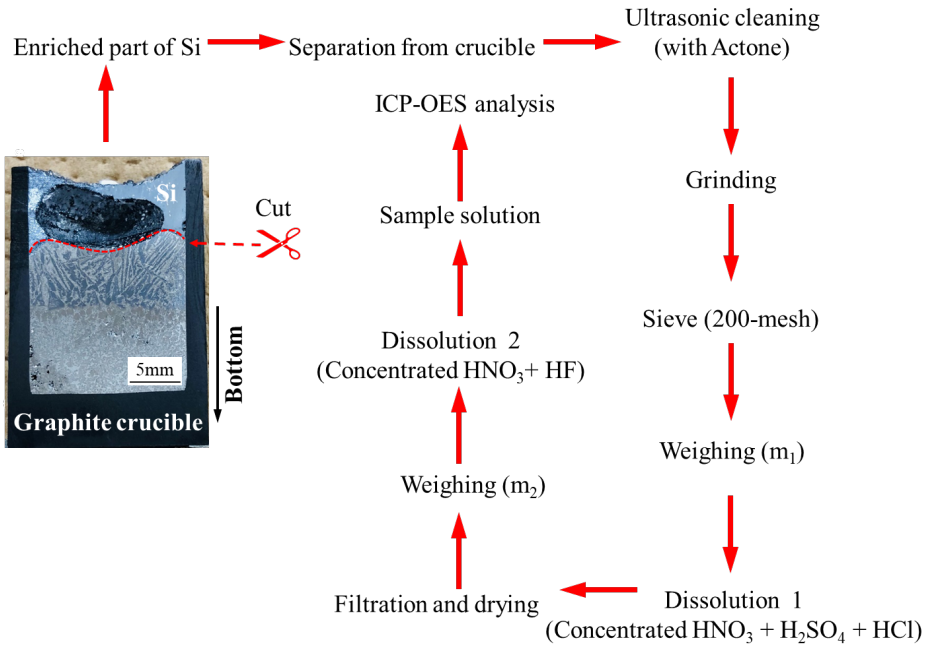

Fig. 6-8. ICP-OES analysis of enriched Si part.

After calculating the Si enrichment percentage, the dried Si powder was dissolved using a mixture of HNO_3 and HF (HNO_3:HF = 1:1 in volume ratio, where HF was added drop by drop to prevent a drastic reaction between Si and the acids) to analyse the B content by ICP-OES. The analysis process is shown in the Fig. 6-8, and the result of sample (C) in Fig. 6-4 is listed in Table 6-3.

In Table 6-3, comparison were made with the previous B-removal experiments under the same conditions of binary system (Si-Sn, and Si-Cu). The results of the comparison are presented in Fig. 6-9.

Table 6-3. B removal fraction in different solvent systems at 0.01 mm/min upward moving rate.

Sample	Alloy system			Initial B content (ppma/ppmw)	Zr content (ppma/ppmw)	Final B content (ppmw)	B removal fraction (%)
	Si (at.%)	Sn (at.%)	Cu (at.%)				
1	50	50	0	153/120	211/1370	42.5	64.6
2	50	0	50	153/80	211/915	5.3	93.4
3	50	25	25	153/100	211/1140	4.7	95.3

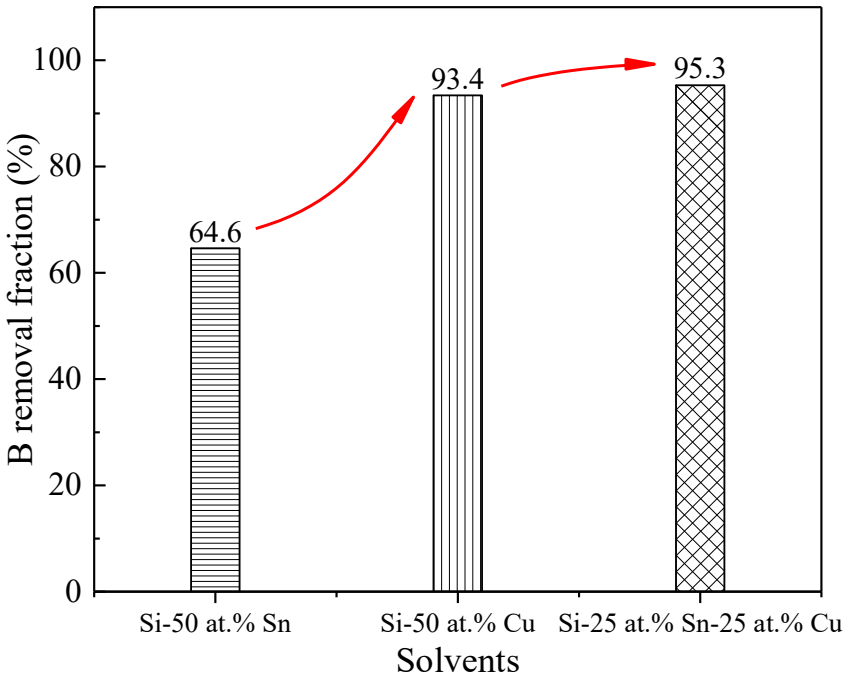

Fig. 6-9. B removal fraction in different solvent systems with Zr addition.

In order to make the removal rate of B comparable under different systems, I guarantee that the atomic fraction of the initial B content and the added Zr content are the same, which are 153 and 211ppma respectively.

From Fig. 6-9, it can be seen that under the same conditions, the effect of adding Zr to remove B was the lowest in Si-Sn system, with a removal fraction of only 64.6%; when the system was replaced by Si-Cu system, the removal fraction of B increased sharply, which reached 93.4%; then using ternary Si-Sn-Cu system, the removal fraction of B further increased to 95.3%, and the content of remaining B can be reduced to about 4.7 ppmw.

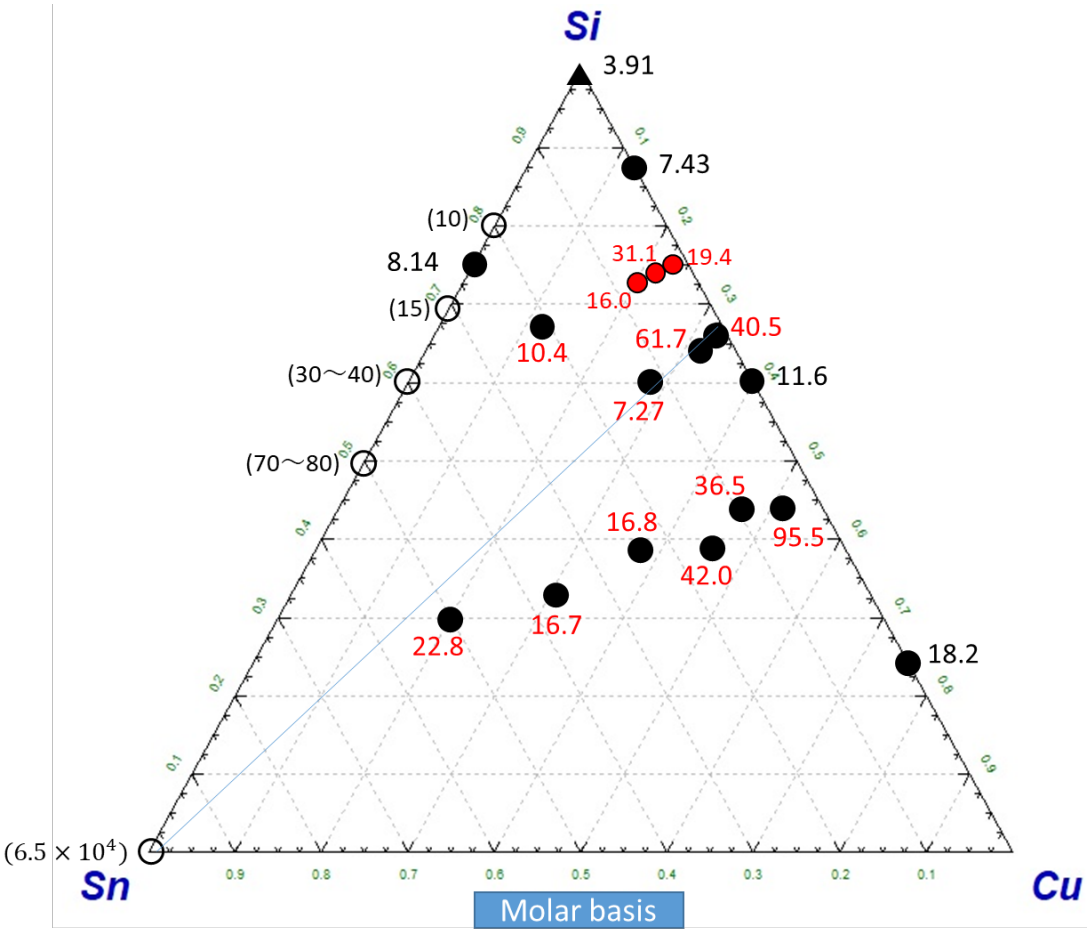

Fig. 6-10. Activity coefficient of B in Si-Sn-Cu ternary system measured by Mr. Mizutani. [6-10]

Compared with the binary Si-Cu system, the absolute content of B is further reduced (5.3 ppmw in Si-Cu), but it is still higher than the standard of SOG (0.3 ppmw). Therefore, the next step is to use the alloy composition with high activity coefficient of B in the ternary system as the solvent for refining.

For the measurement of activity coefficient, Mr. Mizutani, a member of our research group, has measured this data in a series of alloy compositions, as shown in Fig. 6-10. [6-10] While, in the process of selecting composition, we should also consider the liquidus temperature, the range of primary crystal region of Si, and the proportion of Si in it, *etc*.

6.5. Short Summary

From Chapter II to Chapter V, I have studied the enrichment of primary Si and the addition of Zr to remove B in the systems of Si-Sn and Si-Cu. In order to make full use of the advantages of aforementioned Si-Sn and Si-Cu system, I tried to use Si-based ternary alloy (**Si-Sn-Cu**) method. The separation of Si and B removal fraction were investigated using Si-25at.% Sn-25at.% Cu alloy.

Si enrichment percentage obtained by using ternary system (Si-Sn-Cu) as solvent is 99.2%, which is similar to that (99.2%) obtained by using binary system of Si-Cu, slightly higher than that (98.6%) obtained by using Si-Sn system.

Compared with the binary Si-Cu system, the absolute content of B (4.7 ppmw) is further reduced (5.3 ppmw in Si-Cu), but it is still higher than the standard of SOG (0.3 ppmw). Therefore, the next step is to use the alloy composition with high activity coefficient of B in the ternary system as the solvent for refining.

References

6-1 Lei, H.; Zhi, W.; Xuzhong, G.; Zhancheng, G.; Hu, Z. Impurities Removal from Metallurgical-Grade Silicon by Combined Sn-Si and Al-Si Refining Processes. *Metall. Mater. Trans. B,* 44 (2013) 828–836.

6-2 R.W. Olesinski, G.J. Abbaschian, The Si-Sn (Silicon-Tin) System. Bulletin of Alloy Phase Diagrams, 5 (1984) 273–276.

6-3 X.D. Ma, T. Yoshikawa, and K. Morita, Si growth by directional solidification of Si–Sn alloys to produce solar-grade Si [J]. *J. Cryst. Growth*, 377 (2013) 192-196.

6-4 B.B. Alchagirov and A.M. Chochaeva, Temperature dependence of the density of liquid tin. *High Temp.*, 38 (2000) 44-48.

6-5 X. Ma, T. Yoshikawa, K. Morita, Phase relations and thermodynamic property of boron in the silicon-tin melt at 1673 K, *J. Alloy. Compd*., 529 (2012) 12–16.

6-6 R. H. Hopkins and A. Rohatgi, Impurity effects in silicon for high efficiency solar cells, *J. Cryst. Growth*, 75 (1986), 67-79.

6-7 Trumbore, F.A. Solid solubilities of impurity elements in germanium and silicon. *Bell Syst. Tech. J.,* 39 (1960) 206–233.

6-8 http://www.rsc.org/periodic-table/element/14/silicon (accessed November 6, 2019).

6-9 http://www.rsc.org/periodic-table/element/29/copper (accessed November 6, 2019)

6-10 水谷智洋，森田一樹．溶融 Si-Cu-Sn 合金中 B の熱力学的性質，2019 年第 177 回春季講演大会ポスター，東京電機大学，日本東京.

Chapter VII. Conclusion and Outlook

7.1. Conclusion

In order to explore a more efficient process for realizing the mass production of SOG-Si with relative low cost, in this dissertation, the physical chemistry on B removal from Si using Si-Sn-Cu solvent with Zr addition was investigated.

In Chapter 1, under the policies of supporting renewable energy and reducing CO_2 emissions to solve the energy crisis and global warming, the PV industry has developed rapidly in the past decades. Currently, the improved Siemens and fluidized bed methods serve as mainstream techniques to produce SOG-Si. Nevertheless, these methods are energy-intensive with high cost. The metallurgical refining route enables the purification of metallurgical grade Si (MG-Si) to SOG-Si as a sustainable process, and it has advantages of mass productivity and relatively low cost. Solvent refining, can be applied at a considerably low temperature that is more conducive to B removal. Moreover, if B can be removed by adding additives which have strong affinity for B to enhance the formation and precipitation of boride, it would become more effective and practical. The objective of this study is to clarify the mechanism of (i) separation of bulk Si by flotation based on the significant density difference, and (ii) enhancing B-removal fraction by using additives (Zr, Ti *etc*) in the solidification process of Si with the Si-Sn(-Cu) solvent.

In Chapter 2, to confirm whether the upwards or downwards motion generated better Si enrichment results, the growth control and enrichment of Si crystals from the Si-50.0 at.% Sn melt were conducted in the 1605–1505 K temperature range, under different moving directions, and at different rates ranging from 0.01-0.10mm/min.

The upwards process was more favorable than the downwards one: the amount of precipitated Si increased and floated upwards easily due to the buoyancy caused by the significant difference in density between solidified Si and the Si-Sn melt during the upwards process.

The Si enrichment percentage increased with the decrease of the moving rates. The largest Si enrichment percentage reached 98.6% at the 0.01 mm/min upwards moving rate. After HCl leaching, the residual Sn (molar fraction) in the enriched Si area could be easily reduced to the 0.00132-0.00163 range, which was almost the same as but slightly higher than the range of the solid solubility of Sn in Si. The obtained bulk Si is polycrystalline Si, and the priority growth direction is from crucible wall based on the EBSD results. And a model was established to simulate the Si growth process using COMSOL Multiphysics 5.2, which explained the defects (grain boundaries and dislocations) formation and residual Sn content in the enriched Si part dependence on the width of S/L interface, caused by the moving rate. The most critical first step for using Si based alloy solvent refining to produce SOG-Si was analyzed in this Chapter.

In Chapter 3, after determining the advantage of the upwards motion in the separation of bulk Si during the directional solidification process, the effect of Zr/Ti addition on B removal fraction was compared. The B-removal mechanism is discussed from the aspects of theoretical analysis and experimental design. The effects of different variables, such as the moving direction, moving rate, Zr/Ti addition content, and initial Sn content in Si-Sn alloys, on the B-removal fraction were observed.

Although the removal fraction of B has been improved, it is not as significant as expected (highest B-removal fraction was 73.6% with 1057ppma/6857 ppmw Zr addition, B: 120 → 31.2 ppmw). To further explain this phenomenon, the distribution behavior of B and Zr in the directional solidification refining process was studied by SEM-EDS. B- and Zr-enriched areas were found only in the mushy zone, but not combined to form B-Zr intermediate compounds.

Furthermore, the solubility product (Ksp) of Zr and B in Si-Sn melt was also measured using equilibrium technology. The constants were determined as $\geq 9.62 \times 10^{-10}$ (1605 K, Si-50 at.% Sn) and $\geq 3.32 \times 10^{-10}$ (1575 K, Si-65 at.% Sn), which were 100 times higher than those in the Si-Al melt measured by Yoshikawa et al. A high refining temperature was responsible for the lower removal fraction of B when the Si-Sn alloy was employed as the refining solvent.

Finally, a series of comparative experiments were carried out by adding Ti additive. The results showed that the effect of B removal by adding Ti was very weak, even worse than that by adding Zr. It can be explained by that ZrB_2 is more stable at low temperature and the solubility product constant of ZrB_2 is smaller than TiB_2, based on the activity coefficients of Zr and Ti in Si-Sn melt. I concluded that the refining process should be carried out at a low temperature, which is more conducive to boride formation.

In Chapter 4, based on (i) the low liquidus temperature of Si-Cu systems, (ii) low solubility of Cu in solid Si, and (iii) strong affinity of Zr to B for the enhanced boride formation, a novel attempt to remove B from Si using Zr as a trapping agent via a Si-Cu solvent was developed. Therefore, this chapter aimed to clarify the formation mechanisms of ZrB_2 in a Si-Cu melt by using chemical equilibrium technology and to measure important thermodynamic data (such as solubility products).

Firstly, the SEM-EDS result showed that B-bearing polygonal ZrB_x precipitations found at the bottom of test samples, and further were confirmed as ZrB_2 by electron probe microanalysis. Thermodynamic analysis revealed that the solubility products of ZrB_2 in a Si-Cu melt were 2.50×10^{-12} (1258 K, Si-57.0 at.% Cu) and 4.11×10^{-12} (1345 K, Si-50.0 at.% Cu).

Finally, the compositions of Si-Cu alloys that can form stable ZrB_2 particles were estimated by calculating the solubility products of ZrB_2, and the equilibrium contents between B and Zr at different corresponding liquidus temperatures ranging from 1133 to 1450 K. B in a Si-Cu melt at 1133 K can be reduced to a content less than 10 ppma when adding an amount of Zr greater than 1000 ppma, which is lower than the content estimated by Lei in a Si-Al melt at the same temperature. All of the results above indicate that a Si-Cu system forms ZrB_2 more easily than a Si-Al system.

In Chapter 5, after confirming that B in a Si-Cu melt can be reduced by precipitating ZrB_2 via Zr addition, the solidification refining of Si using Si-Cu solvent with Zr addition was studied. A series of experiments of directional solidification refining were carried out.

The B-removal fraction, bulk Si enrichment percentage, and residual Cu content in refined Si were investigated. The results showed that (i) the B-removal fraction was improved significantly as expected, the highest of which is 93.4% (80 → 5.3 ppmw with 211ppma/915 ppmw Zr addition); (ii) Large area of bulk Si was obtained by upwards, and highest Si enrichment percentage is 99.2%; (iii) the residual Cu content can be reduced to a relative low level, the molar fraction of which ranging from 0.00099 to 0.00191; and (iv) k_B was concluded become smaller in Si-Cu system (0.29 at 1345 K) than that in pure Si system (0.80 at 1687 K) and continuous decreasing with increasing in Zr addition content (0.21 when 915 ppmw Zr was added).

It is concluded that the reason for the high removal fraction of B in the Si-Cu system is not only the small solubility products of Zr and B mentioned in Chapter IV, but also the smaller segregation coefficient of B in the Si-Cu system rather than in the pure Si system and continuous decreasing with increasing in Zr addition content.

Finally, in Chapter 6, to further enhancing B removal fraction and make full use of the advantages of aforementioned Si-Sn and Si-Cu system, I tried to use Si-based ternary alloy (Si-Sn-Cu) method. The separation of Si and B removal fraction were investigated using Si-25at.% Sn-25at.% Cu alloy.

Based on the FactSage results, the primary Si began to precipitate at about 1210℃, so I set three holding temperatures (1230, 1200, 1170℃, respectively) in the process of directional solidification to confirm which is closer to its real liquidus temperature. The upwards moving rate was 0.01mm/min and the moving distance was 10 cm, and initial B and Zr content were set as 100 ppmw and 211ppma/1140 ppmw, respectively.

The results showed that the liquidus temperature was determined at about 1170 ℃, the Si enrichment percentage can reach 99.2%, and the B removal fraction was 95.3% (100 → 4.7 ppmw). Although the B removal fraction has been further improved, but the absolute content of B still needs to be further reduced by subsequent process to meet the requirements of SOG-Si (≤ 0.3ppmw).

7.2. Outlook

For future researchers, the use of Si-based alloy solvent method combined with boron-affinity additives to enhance boron removal should pay attention to the following issues:

1). the elements used for alloying should be cheap metals;

2). large area polysilicon should be easily separated from the Si-based alloy melt;

3). the alloyed elements and additives should remain in the enriched (or refined) Si as little as possible;

4). the liquidus temperature of the alloy system should be as low as possible;

5). the solubility product of borides should be as small as possible;

6). the segregation behavior of boron or boride during directional solidification should be examined further, *etc*.

Acknowledgements

I would like to express my gratitude to all those who helped me through difficulties and setbacks during my Ph.D. study and research.

Foremost, I would like to express my sincerest gratitude to my supervisor Prof. Kazuki Morita, for his patience, encouragement, enthusiasm, immense knowledge, and continuous support. In the preparation of the dissertation and papers, he had spent much time reading through each draft and provided me inspiring advice. Without his patient instruction, insightful criticism and expert guidance, the completion of these workloads and achievements would not have been possible.

I would like to thank my dissertation committee: Prof. Toru H. Okabe, Prof. Hiroshi Fujioka, Assoc. Prof. Takeshi Yoshikawa and Assoc. Prof. Hiroyuki Matsuura, for their constructive critics and insightful comments.

I am greatly indebted to the Ministry of Education, Science, Sports, and Culture, Government of Japan (Monbukagakusho Project: MEXT), for the financial support as the doctoral scholarship that gave me the great opportunity to pursue my studies and Ph.D. degree in Japan.

I also wish to acknowledge the numerous assistances of Assis. Prof. Shirayama, Mr. Eguchi, Mr. Kimura and Ms. Nakaya on the daily routine in the lab.

Thanks to all members of the Materials Production and Recycling Engineering Laboratory (Morita Lab) with whom I spent memorable time during three and a half years. They are Dr. You, Dr. Ueda, Mr. Chen, Mr. Kawamoto, Mr. Fukada, Mr. Nagata, Mr. Maegawa, Mr. Mizutani, Mr. Aoki, Mr. Luo, Ms. He, Ms. Lorena, Mr. Takeuchi, and Ms. Nakajima. Special thanks for their warm friendship, knowledge exchange, valuable discussion and help throughout the life in Japan.

Meanwhile, I would like to express my gratitude to Dr. Xiaodong Ma of University of Queensland, Dr. Yun Lei of Kunming University of Science and Technology, Dr. Ye Wang of Sichuan University, Dr. Minggang Li of Mitsui Mining & Smelting Co., Ltd., and Dr. Zhao Ding of Illinois Institute of Technology for their useful discussion, Dr. Hongpo Wang of Chongqing University for his aid in EPMA

analysis, Dr. Jianmeng Jiao of Norwegian University Science and Technology for his aid in FactSage computations, and Mr. Nakamura of the University of Tokyo for his guidance on the operation of SEM-EDS and EBSD analysis.

Finally, I would like to thank to my whole family (my father Hongbo Ren, mother Fengyun Cui, brother Yongjie Ren, sister Xiaoling Ren, and other relatives) for their always encouragements and dual support at the material and spiritual levels. Thanks my kind friends for giving me endless understanding and supports.

Ren Yongsheng

任 永生

November 2019

Appendix I HEA Method for B Removal

ZrTiHfCuNi High-entropy Alloy as Additive to Remove B from Si

High Entropy Alloys (HEAs) are alloys which contain at least five principal elements with each concentration ranges from 5 to 35 at.% and therefore have a high entropy of mixing during the liquid state. [A-1, 2] The alloys are divided by many scientists into three types according to the values of entropy of mixing, as is shown in Fig. A-1. For alloys with entropy of mixing smaller than R, they are classified as Low-entropy alloys. For alloys with entropy of mixing between R and 1.5R, they are classified as Medium-entropy alloys. And for alloys with entropy of mixing larger than 1.5R, they are classified as High-entropy alloys.

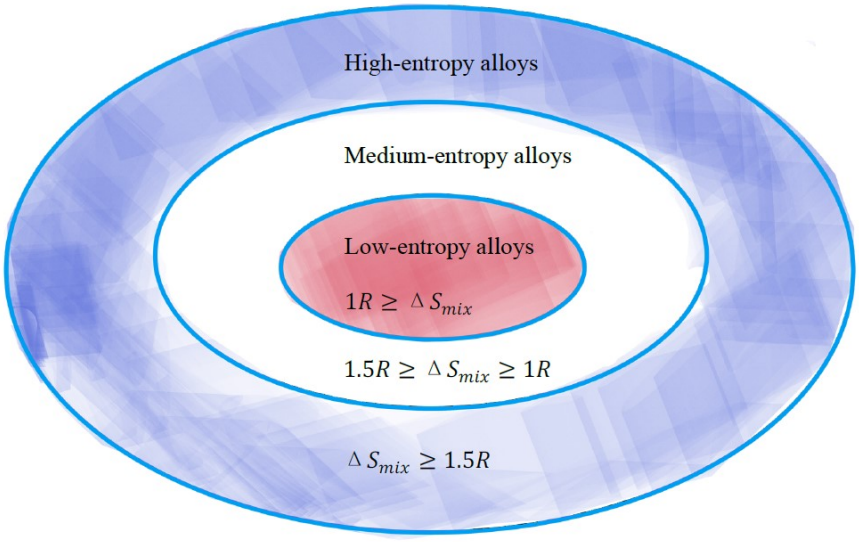

Fig. A-1. Classification of alloys according to the entropy of mixing. [A-3]

Plenty of unique experimental phenomenon and characteristics of high entropy alloys have been reported over the intensive researches up to now, which were not observed before in conventional alloys. These characteristics were summarized into four aspects that are known as the four core effects of HEAs, including High Entropy Effect, Sluggish Diffusion Effect, Lattice Distortion Effect, and Cocktail Effect. In this part, the High Entropy Effect will be introduced and discussed.

The High Entropy Effect is the most fundamental characteristic of HEAs since it arises from their definition. It implies the huge entropy of mixing during phase configuration process, meaning that Gibbs free energy will be very low.

To utilize the high entropy effect and cocktail effect of high entropy alloy, the effect of using TiZrHfCuNi high entropy alloy as additive on B removal behavior was tried. Here, it was considered as the additive because (i) the phase of ZrHfTiCuNi is amorphous [A-4] as listed in Table A-1, (ii) Zr, Hf, Ti have strong affinity for B as shown in Fig. A-2.

Table A-1. Parameters of each HEAs.

Calculated parameters δ, ΔH_{mix}, S_c, VEC, φ, and ε_{RMS}.

Alloy composition	δ	ΔH_{mix} (kJ/mol)	S_c (k_B per atom)	φ	ε_{RMS}	VEC	Phase detected
$Al_{0.5}CoCrCuFeNiTi_{0.2}$	4.93	−4.15	1.86	17.41	0.0487	8.12	FCC [76]
$Al_{0.3}CoCrFeNi$	3.76	−7.27	1.54	19.99	0.0370	7.88	FCC [77]
$Al_{0.5}CrCuFeNi_2$	4.20	−2.51	1.52	20.44	0.0414	8.45	FCC [78]
ZrHfTiCuNi	10.34	−27.36	1.61	−0.27	0.1049	6.60	Amorphous [96]
ZrHfTiCuFe	10.43	−15.84	1.61	1.73	0.1059	6.20	Amorphous [96]
ZrHfTiCuCo	10.24	−23.52	1.61	0.42	0.1039	6.40	Amorphous [96]

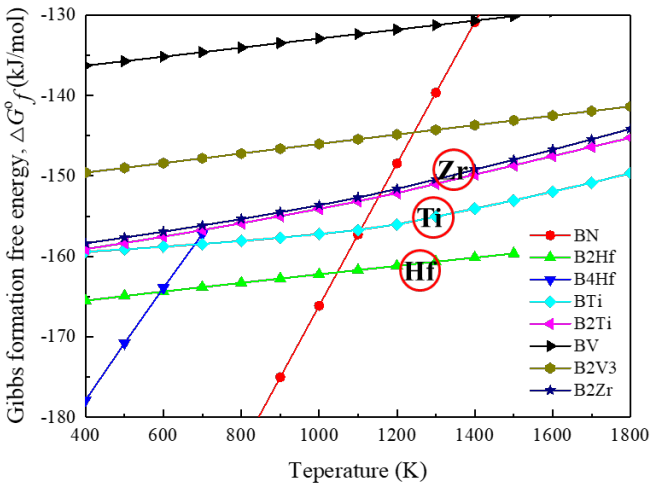

Fig. A-2. Ellingham diagram for some borides.

Therefore, I hope that the process diagram of B removal can be shown in Fig. A-3.

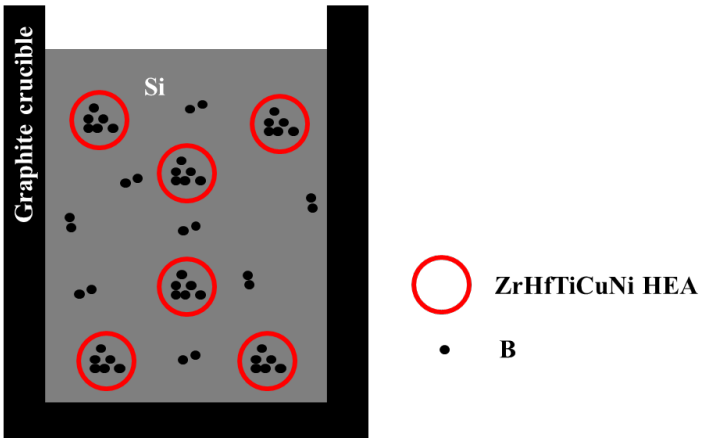

Fig. A-3. Schematic diagram of the process of B removal.

Here, make sure that the mass ration of Si and B is 99:1, and the molar ration of each HEA elements to B is 1:1, in total 10g, as listed in Table A-2. The sample was melted with induction furnace, holding at 1600℃ for 2h, as shown in Fig. A-4.

Table A-2. Properties of various substances and the amount of experimental use.

Element	Melting point (℃)	Density ($\times 10^3$ kg/m^3)	Atomic weight	Mole number	Mass	In total 10g
Si	1414	2.33	28.08		1070.19	7.03693
B	2300	2.34	10.81	1	10.81	0.07108
Zr	1852	6.49	91.22	1	91.22	0.59981
Hf	2227	13.31	178.49	1	178.49	1.17364
Ti	1660	4.54	47.87	1	47.87	0.31476
Cu	1084.6	8.96	63.55	1	63.55	0.41787
Ni	1453	8.9	58.69	1	58.69	0.38591

Mass ratio of Si:B =99:1

Then inlay with curing agent, cut the sample in half along the longitudinal direction, as shown in Fig. A-5. After polished using standard metallographic techniques, a digital camera and a scanning electron microscope equipped with an energy-dispersive spectrometer (SEM-EDS) were used to observe the macroscopic and microscopic morphology of the samples. The SEM-EDS results are shown in A-6, from which we can see that although boride was not found, B was adsorbed near HEA and not exist in Si. This provides a perspective for B removal by using pure Si system with B-friendly high entropy alloy as additive. However, further study is needed to explain the specific mechanism.

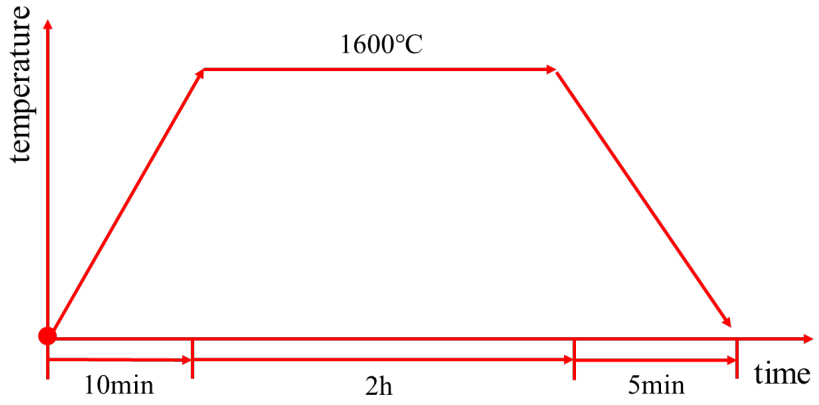

Fig. A-4. Experimental process.

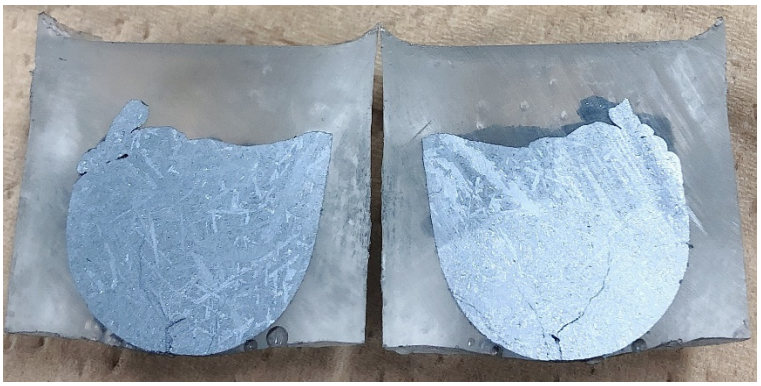

Fig. A-5. Longitudinal section of HEA

Inlay with curing agent (エポマウント硬化剤＋エポキシ樹脂).

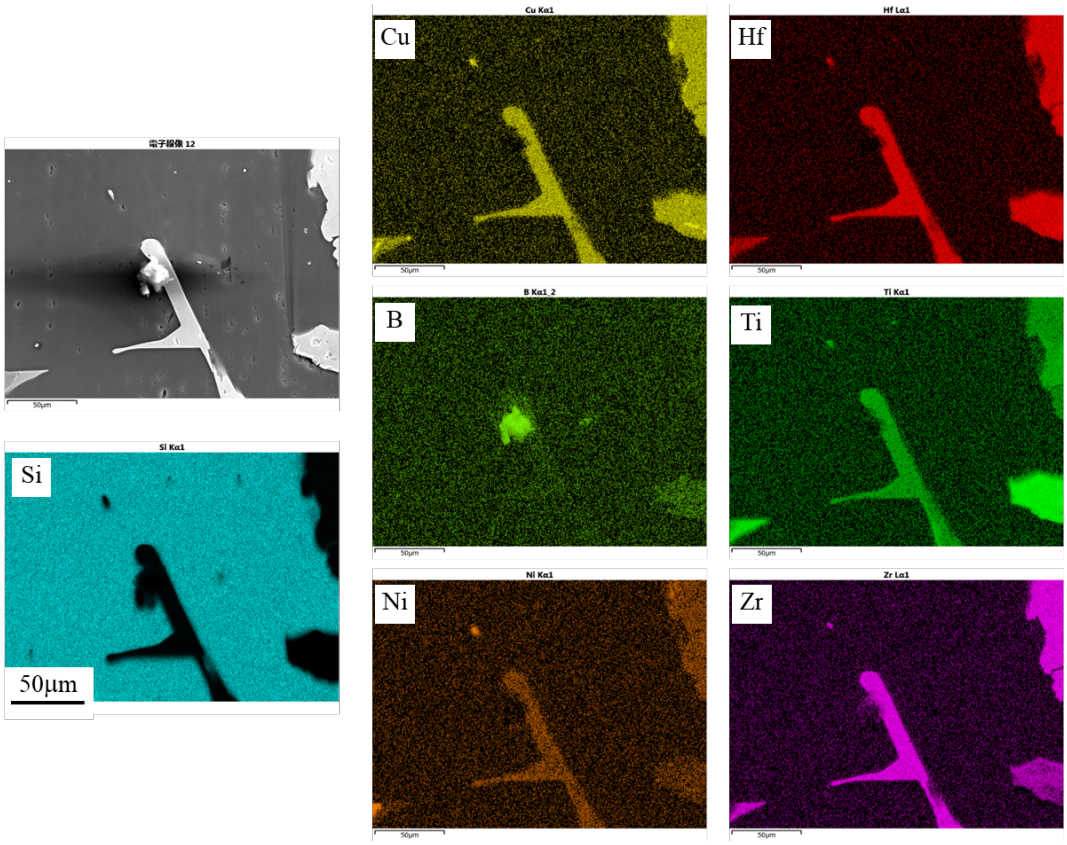

Fig. A-6. SEM-EDS analysis results of HEA (ZrTiHfCuNi) as additive for Si refining.

References

A-1 M.-H. Tsai, J.-W. Yeh, High-entropy alloys: a critical review, *Mater. Res. Lett.,* 2 *(*2014) 107.

A-2 J.-W. Yeh, S.-K. Chen, S.-J. Lin, J.-Y. Gan, T.-S. Chin, T.-T. Shun, C.-H. Tsau, S.-Y. Chang, Nanostructured high-entropy alloys with multiple principal elements: novel alloy design concepts and outcomes, *Adv. Eng. Mater.,* 6 (2004) 299.

A-3 J.-W. Yeh, Alloy design strategies and future trends in high-entropy alloys, *JOM,* 65 (2013) 1759.

A-4 L. Ma, L. Wang, T. Zhang, and A. Inoue, Bulk Glass Formation of Ti-Zr-Hf-Cu-M (M = Fe Co, Ni) Alloys, *Mater. Trans.,* 43 (2002) 277-280.

Appendix II CV

Basic Information

Name：**Yongsheng Ren (任　永生)**
Laboratory name：Morita Lab
Native Place：Henan, China
E-mail：ryssdy@wood3.t.u-tokyo.ac.jp
Gender: Male
Applied Degree：Ph.D.
Phone：(+81)-080-4957-2016
Address：7-3-1 Hongo, Bunkyo-ku, Tokyo

Education Background

2008/09 — 2012/07	***Kunming University of Science and Technology*** ***(China)*** ● Bachelor Degree of Engineering Major: Metallurgy Engineering Faculty of Metallurgical and Energy Engineering
2010/09 — 2011/07*	***Northeastern University*** ***(China)*** ● Exchange Student* Major: Metallurgical Physical Chemistry School of Materials and Metallurgy
2012/09 — 2015/07	***Kunming University of Science and Technology*** ***(China)*** ● Master Degree of Engineering Major: Non-ferrous Metallurgy Faculty of Metallurgical and Energy Engineering
2015/10 — 2016/08	***Northeast Normal University*** ***(China)*** ● MEXT Scholarship Student Training Center of Education Ministry Preparatory School for Chinese Students to Japan
2016/10 — 2017/03	***The University of Tokyo*** ***(Japan)*** ● International Research Student Department of Materials Engineering Graduate School of Engineering
2017/04 — present	***The University of Tokyo*** ***(Japan)*** ● PhD Candidate Department of Materials Engineering Graduate School of Engineering

Academic Projects

2011/09 — 2012/07	**Si refining** → Bubble Adsorption for Refining Si from Al-Si System under the Electromagnetic Field (**Undergraduate** thesis)
2012/09 — 2015/07	**Al alloy purification** → Degassing of Al-Si Alloy during the Electromagnetic Directional Solidification (**Master's** thesis)
2017/04 — present	**Si refining** → Physical Chemistry on B Removal from Si Using Si-Sn-Cu Solvent with Additives (**Doctoral** dissertation)